Karlsruher Institut für Technologie

Confining the Higgs sector via the investigation of di-tau final states with LHC Run II data

---

Zur Erlangung des akademischen Grades eines

DOKTORS DER NATURWISSENSCHAFTEN (Dr. rer. nat.)

von der KIT-Fakultät für Physik des
Karlsruher Instituts für Technologie (KIT)
angenommene

DISSERTATION

von

M.Sc. René Caspart
aus Stuttgart

Tag der mündlichen Prüfung: 27. Oktober 2017

Referent: Priv.-Doz. Dr. Roger Wolf
Korreferent: Prof. Dr. Günter Quast

Abstract

Common extensions to the Standard Model Higgs sector, such as two-Higgs-doublet models as for example the Minimal Supersymmetric Standard Model, predict the presence of additional Higgs bosons. In these extensions the coupling of the additional Higgs bosons to down-type fermions, such as τ-leptons, is enlarged for large parameter spaces. As a result, the decay of these Higgs bosons into a pair of τ-leptons is one of the most promising channels to search for new physics. In this thesis, this decay channel is explored using data recorded by the CMS experiment in the year 2016 at a center-of-mass energy of $\sqrt{s} = 13\,\mathrm{TeV}$. The analysis methods, selection criteria and the resulting uncertainty model are detailed. No evidence for additional Higgs bosons is found and exclusion limits on the cross section times branching ratio for further Higgs bosons are set. These exclusion limits constrain the phase space for possible deviations from the Standard Model Higgs sector. Examples of scenario-specific exclusion limits are given and possibilities for interpretations in the context of further scenarios based on the results of this analysis are discussed.

Zusammenfassung

Erweiterungen des Higgs-Sektors im Standardmodell, wie zum Beispiel Modelle mit zwei Higgs-Dubletts, etwa das Minimale Supersymmetrische Standardmodell, sagen weitere Higgs-Bosonen voraus. In diesen Erweiterungen ist die Kopplung der weiteren Higgs-Bosonen an down-artige Fermionen, wie etwa τ-Leptonen, erhöht in einem großen Phasenraum. Daraus folgend ist der Zerfall dieser Higgs-Bosonen in Paare von τ-Leptonen einer der viel versprechensden Kanäle für die Suche nach neuer Physik. In dieser Arbeit wird dieser Zerfallkanal mit Daten, die mit dem CMS Experiment im Jahr 2016 bei einer Schwerpunktsenergie von $\sqrt{s} = 13\,\mathrm{TeV}$ aufgenommen wurden, untersucht. Die Analysemethoden, Selektionskriterien und das resultierende Unsicherheitsmodell werden dargestellt. Es wurde kein Hinweis auf zusätzliche Higgs-Bosonen gefunden. Entsprechende Ausschlussgrenzen werden auf das Produkt aus Wirkungsquerschnitt und Verzweigungsverhältnis für weitere Higgs-Bosonen bestimmt. Diese Ausschlussgrenzen schränken den Phasenraum für mögliche Abweichungen vom Higgs-Sektor des Standardmodells ein. Ausschlussgrenzen für exemplarische Szenarien werden bestimmt und Möglichkeiten zur Interpretation der Ergebnisse dieser Analyse im Kontext von weiteren Szenarien werden diskutiert.

Contents

Introduction

The Large Hadron Collider is the most powerful particle accelerator currently operated. In combination with some of the most sophisticated detectors in particle physics, one of them being the Compact Muon Solenoid, it offers unprecedented possibilities for precision measurements as well as for searches for new physics beyond the Standard Model.

One major field of study at these detectors is the Higgs sector. With the discovery of a new particle with a mass close to 125 GeV and properties compatible with those of a Standard Model Higgs boson an important milestone was reached. However, many open questions related to this discovery remain. Are the properties of the found Higgs boson identical to those predicted for the Higgs boson of the Standard Model? Are there additional heavier or lighter Higgs bosons, which can give clues towards physics beyond the Standard Model?

Since the discovery of the Higgs boson, these two questions are being tackled in parallel. With increasing amount of recorded data and better understanding of the detector, more precise measurements of the properties of the found Higgs boson are being performed. The aim of these measurements is to either confirm the Standard Model predictions or find deviations from its predicted properties. Any such deviation might be a sign for physics beyond the Standard Model. Complementary to these measurements, searches for additional Higgs bosons are being performed.

Many suggested models beyond the Standard Model predict an enhanced coupling from additional Higgs bosons to down-type fermions, like the τ-lepton. As a result, the direct searches for additional Higgs bosons decaying into τ-leptons are flagship analyses offering the farthest reach into the Higgs sector for those models. These searches are carried out for charged Higgs bosons decaying into a single τ-lepton [1, 2] as well as neutral Higgs bosons decaying into a pair of τ-leptons [3–5]. The results of several direct searches for additional Higgs boson performed by the CMS collaboration based on the data recorded in the years 2011 and 2012 at center-of-mass energies of 7 and 8 TeV respectively, is shown in figure 1.1.

In the first full year of data taking at a center-of-mass energy of 13 TeV, data corresponding to $35.9\,\text{fb}^{-1}$ was recorded. With this increase in the amount of recorded data and center-of-mass energy compared to the previous data taking, an even further reach of searches for additional Higgs bosons can be achieved. An analysis performed using this
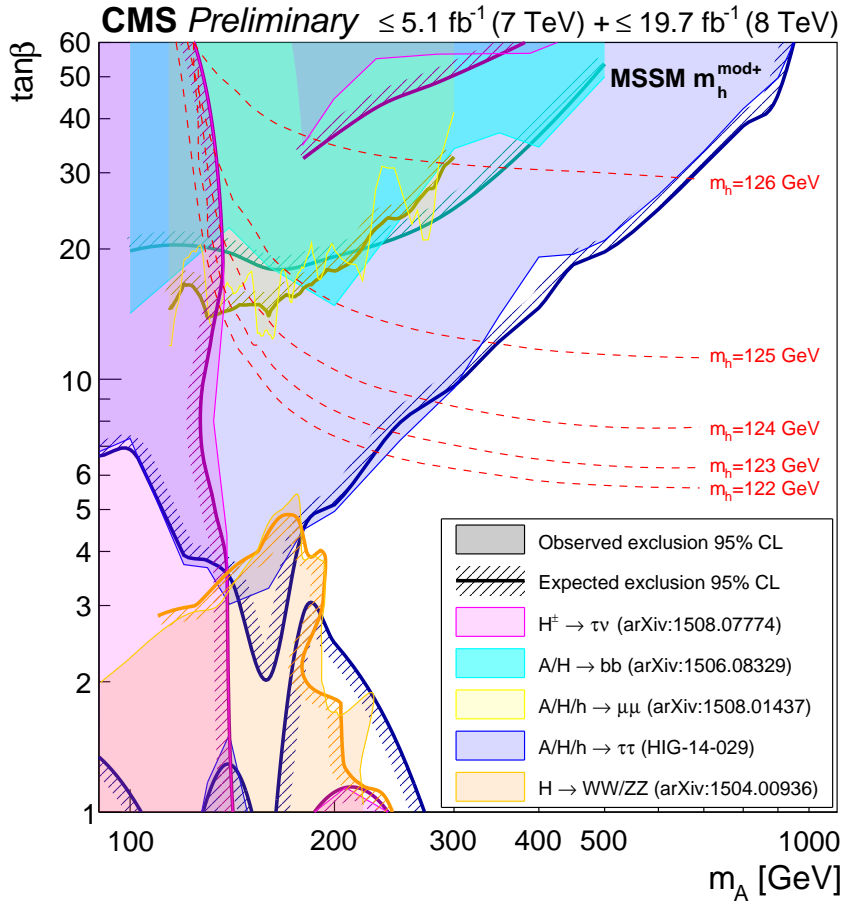
Figure 1.1: Exclusion limits in a possible scenario predicting an extension of the Higgs sector compared to the Standard Model, the $m_h^{\text{mod}+}$ scenario of the MSSM. The two free parameters of this model, m_A and $\tan\beta$, span the plane in which the exclusion limits are derived. The results are derived using the data recorded by the CMS experiment in the years 2011 and 2012 at center-of-mass energies of 7 and 8 TeV respectively. The search for additional neutral Higgs bosons decaying into a pair of τ-leptons offers the farthest reach in this plane [6].

data to search for additional Higgs bosons decaying into a pair of τ-leptons is presented in this thesis.

In chapter 2, an overview of the Higgs mechanism in the Standard Model of particle physics and extensions is given. The Statistical basis and methods used in this thesis are introduced in chapter 3. Subsequently, the concept and design of the Large Hadron Collider and Compact Muon Solenoid detector are introduced in chapter 4. Furthermore, in chapter 4, a brief overview of the basics for event and object reconstruction used for the recorded events is given. In chapter 5, the performed analysis is detailed. Object selections, background estimations as well as correction factors and considered uncertainties are discussed. Finally, the results of this analysis using the methods introduced in chapter 3 are given in chapter 6.

The Higgs Sector in the Standard Model and Beyond

This chapter introduces the theoretical background on which this thesis resides. In the first section, a brief introduction to the Standard Model of Particle Physics is given. The Higgs mechanism, which gives mass to the particles in the Standard Model is introduced and the properties of the resulting Higgs boson are stated. Motivations for extensions to the Standard Model are given and a minimal extension to the Standard Model is introduced. The Higgs sector in this extension of the Standard Model is discussed.

For all notations in this thesis the natural unit notation is used. This means that the reduced Planck's constant $\hbar$ and the speed of light c are normalized to 1. The units for all quantities are expressed in terms of the energy unit eV.

2.1 The Standard Model of Particle Physics

The *Standard Model of Particle Physics* (SM) is the fundamental theory used to describe fundamental particles and the interactions between them. The interactions in the SM are related to three fundamental forces, each acting on particles with different properties and differing in strength and reach.

The three forces are identified as the electromagnetic, weak and strong interaction. The electromagnetic force describes the interaction between electrically charged particles, the weak force the interaction of subatomic particles causing radioactive decays and the strong force the interaction between color charged particles. In the SM each force is mediated by *gauge bosons* of spin 1. A summary of the gauge bosons and their properties is given in table 2.1.

In addition to the gauge bosons, the SM contains twelve fermions with spin $\frac{1}{2}$ (see table 2.2). They can be grouped into color neutral particles, the *leptons*, and color charged particles, the *quarks*. Leptons carry an electric charge of 0 or ± 1, whereas quarks are the only particles with a non-integer electric charge of $\pm 1/3$ or $\pm 2/3$. However, isolated quarks can not be observed on their own but only in states with integer electric charge. Based on the weak isospin, leptons and quarks can be separated into *up-type* fermions, with a weak isospin of $+\frac{1}{2}$, and *down-type* fermions with a weak isospin of $-\frac{1}{2}$.

Table 2.1: Gauge bosons in the Standard Model mediating the electromagnetic, weak and strong forces. For each gauge boson the corresponding electric charge, spin and parity transformation J^P and mass is given [7].

Interaction	Gauge boson	Charge	J^P	Mass
electromagnetic	Photon (γ)	0	1^-	$0\,\text{GeV}$
weak	Z^0	0	1	$91.1876 \pm 0.0021\,\text{GeV}$
weak	$W^\pm$	± 1	1	$80.385 \pm 0.015\,\text{GeV}$
strong	Gluon (g)	0	1^-	$0\,\text{GeV}$

Table 2.2: Fermions in the Standard Model. They can be grouped into *up-* and *down-type* particles based on their weak isospin [7].

	Generation 1	2	3	charge	Weak Isospin	color charge
Leptons	e	μ	τ	-1	$-\frac{1}{2}$	no
	ν_e	ν_μ	ν_τ	0	$+\frac{1}{2}$	no
Quarks	u	c	t	2/3	$+\frac{1}{2}$	yes
	d	s	b	-1/3	$-\frac{1}{2}$	yes

2.1.1 The Higgs sector in the Standard Model

In the original gauge ansatz from which the SM evolves the gauge bosons are required to be massless particles. However, as mentioned before, the W and Z bosons have been found to be massive [8–11]. A new mechanism needs to be introduced in order to explain these masses in the context of the SM. This mechanism is referred to as the Higgs mechanism [12–17]. In the following, a brief introduction to the Higgs mechanism is given. Interested readers can find further details in [18, 19].

In a first step, the Higgs mechanism in the case of a $U(1)$ theory, as for example quantum electrodynamics, is discussed. In this case, the Higgs mechanism is introduced via a complex scalar field ϕ, the Higgs field, with a characteristic potential $V(\phi)$, as illustrated in figure 2.1, which is given by

$$V(\phi) = \mu^2 \phi\phi^* + \lambda \left(\phi\phi^*\right)^2, \ \mu^2 < 0, \lambda > 0. \tag{2.1}$$

The Lagrangian density corresponding to this system is given by

$$\mathcal{L} = [\partial^\mu \phi^*][\partial_\mu \phi] - V(\phi) \tag{2.2}$$

and is covariant under phase transformations and hence has a $U(1)$ symmetry.

The potential $V(\phi)$ has degenerate ground states which are composed of all states satisfying the condition

$$|\phi_0| = \sqrt{\phi_1^2 + \phi_2^2} = \sqrt{\frac{-\mu^2}{2\lambda}} = \frac{v}{\sqrt{2}}, \tag{2.3}$$
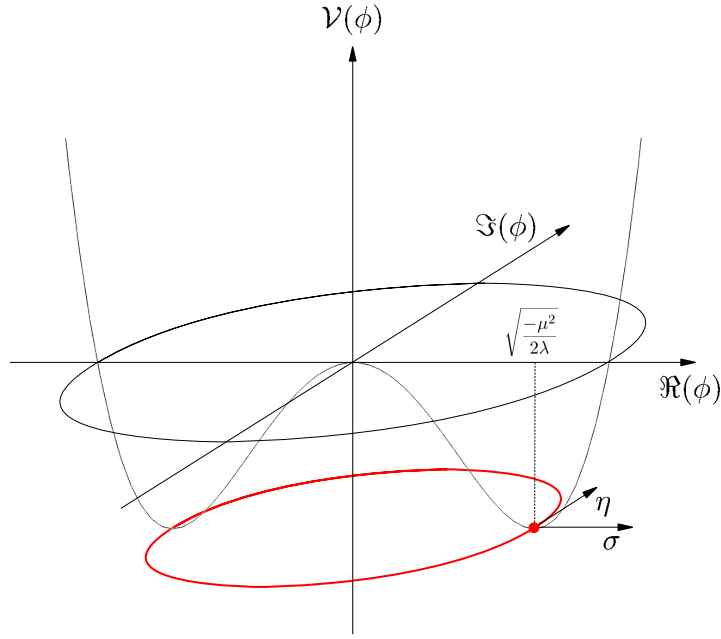
Figure 2.1: Illustration of the symmetric Higgs potential [20]. It has degenerate ground states indicated by the red circle. The complex Higgs field can be expressed using the two real scalar fields σ and η.

with the expression $\frac{v}{\sqrt{2}}$ being referred to as the *vacuum expectation value.* None of those degenerate ground states does satisfy the $U(1)$ symmetry and hence the symmetry is said to be spontaneously broken in the ground state.

For the following considerations the ground state after spontaneous symmetry breaking is chosen to be real and positive with $\phi_0 = v/\sqrt{2}$. Using two real scalar fields σ and η, which vanish in the ground state, the Higgs field can then be expressed as

$$\phi = \frac{1}{\sqrt{2}}(v + \sigma + i\eta). \tag{2.4}$$

Using this formulation in the Lagrangian given in equation 2.2 leads to

$$\mathcal{L} = \frac{1}{2}[\partial^\mu \sigma][\partial_\mu \sigma] - \frac{1}{2}(2\lambda v^2)\sigma^2 + \frac{1}{2}[\partial^\mu \eta][\partial_\mu \eta] + \mathcal{L}_I \tag{2.5}$$

where the term $\mathcal{L}_I$ sums up all terms of cubic or higher order in the fields σ and η. The first and second term correspond to a free scalar boson σ with a mass of $\sqrt{2\lambda v^2}$. The third term corresponds to a massless free scalar boson η.

To enforce the gauge invariant transformation of $D_\mu A^\mu$, the covariant derivative D_μ is used instead of the partial derivative ∂_μ. In the case of a U(1) symmetry, the covariant derivative is given by

$$D_\mu = \partial_\mu - ieA_\mu \tag{2.6}$$

with the gauge field A_μ. With the covariant derivative the Lagrangian given in equation 2.5 becomes

$$\mathcal{L} = \frac{1}{2}[\partial^\mu \sigma][\partial_\mu \sigma] - \frac{1}{2}(2\lambda v^2)\sigma^2 + \frac{1}{2}[\partial^\mu \eta][\partial_\mu \eta] + \frac{1}{2}e^2 v^2 A_\mu A^\mu - ev A_\mu \partial^\mu \eta + \mathcal{L}_I. \quad (2.7)$$

In this Lagrangian, a massive gauge boson A with the mass-term $\frac{1}{2}e^2 v^2 A_\mu A^\mu$ and consequently the mass $m_A = ev$ can be identified. As a final point, the number of degrees of freedom needs to be addressed. At the beginning of the considerations detailed before, four degrees of freedom were present, two for the field A and two for the field ϕ. In contrast to this, the Lagrangian in equation 2.7 has five degrees of freedom, one for the field σ, one for the field η and three for the massive gauge boson A. This shortcoming can be addressed by finding a gauge in which the field η vanishes and only the physical fields remain. This gauge is referred to as *unitary gauge.*

The previous considerations introduced a massive gauge boson in a U(1) symmetry using the Higgs mechanism. For the application of this mechanism in the electroweak sector of the Standard Model, which has a SU(2) × U(1) symmetry, a different starting point needs to be considered. A weak isospin doublet ϕ, referred to as the *Higgs doublet,* whose components are both complex scalar Higgs fields is chosen:

$$\phi = \begin{pmatrix} \phi_1 \\ \phi_2 \end{pmatrix}. \quad (2.8)$$

As before, the potential $V(\phi)$, sharing the SU(2) × U(1) symmetry, is defined as

$$V(\phi) = \mu^2 \phi^\dagger \phi + \lambda[\phi^\dagger \phi]^2, \ \mu^2 < 0, \lambda > 0 \quad (2.9)$$

with the ground states given by

$$\phi_0^\dagger \phi_0 = |\phi_1^0|^2 + |\phi_2^0|^2 = \frac{v^2}{2}. \quad (2.10)$$

Without loss of generality, the ground state is chosen to be

$$\phi_0 = \begin{pmatrix} 0 \\ v/\sqrt{2} \end{pmatrix} \quad (2.11)$$

and the Higgs doublet can be expressed using four real scalar fields, vanishing in the ground state:

$$\phi_0 = \frac{1}{\sqrt{2}} \begin{pmatrix} \eta_1 + i\eta_2 \\ v + \sigma + i\eta_3 \end{pmatrix} \quad (2.12)$$

It can be shown that the same considerations presented before for the case of a complex scalar Higgs field with the U(1) symmetry can also be applied for the doublet of complex scalar fields. In the following, only the results of these considerations for the SM are presented. For an explicit calculation, interested readers are referred to [18, 19]. As a result of the spontaneous breaking of the SU(2) × U(1) symmetry one finds a Lagrangian

in which mass terms for the $W^{\pm}$ and Z gauge bosons can be identified and the photon remains massless. The resulting masses for the gauge bosons and the massive Higgs boson are

$$m_{W^{\pm}} = \frac{1}{2}vg_2, \quad m_Z = \frac{1}{2}v\sqrt{g_1^2 + g_2^2}, \quad m_{\gamma} = 0, \quad m_H = \sqrt{2\lambda}v. \tag{2.13}$$

Up to now only the introduction of masses for the gauge bosons has been discussed. Masses of fermions can be introduced in the SM via an interaction between the fermions and the Higgs field. This coupling is expressed as a Yukawa coupling for which the Lagrangian is given by

$$\mathcal{L}_{\text{Yukawa}} = -\lambda_f \bar{\psi}\phi\psi \tag{2.14}$$

with the fermion field ψ.

As a result of the non-vanishing vacuum expectation value one obtains the Lagrangian

$$\mathcal{L}_{\text{Yukawa}} = -\frac{1}{\sqrt{2}}\lambda_f v \bar{f}_{\text{L}} f_{\text{R}} - \frac{1}{\sqrt{2}}\lambda_f \sigma \bar{f}_{\text{L}} f_{\text{R}} \tag{2.15}$$

where the first term can be identified as the Lagrangian of a massive fermion f with the mass $m_f = \lambda v/\sqrt{2}$. The second term of the Lagrangian can be identified as a coupling term between the fermion and the Higgs field σ. Likewise in the case of the gauge bosons an interaction between the gauge bosons and the Higgs field can be found. The corresponding coupling constants are given as

$$g_{Hff} = m_f/v, \qquad g_{HVV} = 2m_V^2/v, \tag{2.16}$$

meaning that for fermions and vector bosons the coupling to the Higgs boson is proportional to the mass and mass squared respectively.

2.2 Extensions to the Standard Model

Up to now, the SM was found to be a theory which is able to explain experimental findings with astonishing accuracy. However, several open questions exist, for which the SM does not have any or only unsatisfactory answers. One of these open questions is the problem of *fine tuning*. This refers to the problem of quadratically divergent corrections to the Higgs mass which, especially at high energies, have to be handled by very specific choices of the parameters of the SM.

Additional open questions arise from the field of cosmology. One of these questions is the origin of matter in the universe. The current universe is dominated by matter. However, it is expected that equal amounts of matter and anti-matter existed at the early stages of the universe. A small portion of this asymmetry can be explained by the CP violation in the SM. However, this effect is too small to explain the extent of the asymmetry observed today.

A second open question is the presence of *dark matter* [21–23] and *dark energy* [24]. In cosmological observations, the universe was found to consist of only about 5 % visible matter. About 25 % consist of dark matter, which does not interact electromagnetically and hence has never been observed directly. The existence of dark matter and its properties

are interfered from observations of gravitational interactions, such as the rotational speed of galaxies and gravitational lensing. The remaining 75 % consists of dark energy. Like the dark matter dark energy has not been observed directly and is only postulated as a possible solution to explain the accelerating expansion rate of the universe. In the SM neutrinos are the only potential candidates for dark matter. However, in most dark matter models these are not sufficient to describe this sector. No explanation for the dark energy is available in the SM.

In order to account for these limitations of the SM, extensions of the SM are proposed. A common example for a theory beyond the SM is the Minimal Supersymmetric Standard Model (MSSM). This model introduces a new symmetry between fermions and bosons. New particles, the so-called superpartners of the SM particles, are predicted as a result of this symmetry.

2.2.1 The Higgs sector in the MSSM

Extensions of the SM, such as the MSSM, also predict extended Higgs sectors compared to the SM Higgs sector. In this section a brief introduction to the Higgs sector in the MSSM and its implication for the couplings of the predicted Higgs bosons are given. A more detailed description can be found in [25].

A common extension of the Higgs sector is installed by introducing two Higgs doublets instead of a single one. The MSSM is a special type of two-Higgs-doublet model imposing additional constraints. For a two-Higgs-doublet model, the two doublets can be expressed as

$$\phi_1 = \begin{pmatrix} \phi_1^0 \\ \phi_1^- \end{pmatrix} \text{ with } Y_{\phi_1} = -1, \qquad \phi_2 = \begin{pmatrix} \phi_2^+ \\ \phi_2^0 \end{pmatrix} \text{ with } Y_{\phi_2} = +1. \tag{2.17}$$

The vacuum expectation values of the neutral components of these Higgs fields are defined as

$$\langle \phi_1 \rangle = \frac{v_1}{\sqrt{2}}, \qquad \langle \phi_2 \rangle = \frac{v_2}{\sqrt{2}} \tag{2.18}$$

and the parameter $\tan \beta$ is defined as the ratio of the vacuum expectation values of the two doublets:

$$\tan \beta = \frac{v_2}{v_1} \tag{2.19}$$

As a result of the spontaneous symmetry breaking five massive Higgs boson are predicted:

$$h, H, A, H^+, H^- \tag{2.20}$$

Two of these Higgs bosons, h and H, are neutral scalar particles and one, A is a neutral, pseudoscalar particle. The remaining two predicted Higgs bosons, H^+ and H^-, are charged Higgs bosons with equal mass. At leading order, the masses of these five Higgs bosons can be fully described using two free parameters. These two parameters are commonly chosen as $\tan \beta$ and m_A. The resulting masses of the Higgs bosons then are given as

$$m_{H^\pm} = m_A^2 + m_W^2 \tag{2.21}$$

$$m_{h,H}^2 = \frac{1}{2} \left[m_A^2 + m_Z^2 \mp \sqrt{\left(m_A^2 + m_Z^2 \right)^2 - 4m_A^2 m_Z^2 \cos^2 2\beta} \right] \tag{2.22}$$

As can be inferred from these equations, the mass of the light neutral scalar Higgs boson h is required to fulfill $m_h \leq \min(m_A, m_Z) \cdot \cos 2\beta \leq m_Z$. In addition, the heavy scalar Higgs boson H is required to fulfill $m_H > \max(m_A, m_Z)$. Given these masses and the properties of the light scalar Higgs boson, it should have been observed in precision measurements at LEP. As no observation of this particle has been made, the mass of the light scalar Higgs boson needs to be higher and out of the reach of LEP [26]. For this increase of the mass, higher order radiative corrections need to be taken into account.

These higher order corrections introduce additional parameters, on which the Higgs sector in the MSSM depends. However, although the corrections themselves can be large, they usually do not significantly alter the general description of the Higgs sector. For searches exploring this sector the parameters associated with higher order corrections are usually set to predefined values leaving m_A and $\tan\beta$ as free parameters. Each set of these values is referred to as *benchmark scenario*, with each of the benchmark scenarios emphasizing a different aspect of the Higgs sector and MSSM. A selection of different benchmark scenarios can be found in [27]. For the results presented later in this thesis the $m_{\mathrm{h}}^{\mathrm{mod}+}$ benchmark scenario is used as a representative benchmark scenario. In this scenario a large fraction of the phase space is compatible with the observed Higgs boson at 125 GeV within theoretical uncertainties.

As an alternative possible description of the MSSM Higgs sector the hMSSM [28] is used. The hMSSM incorporates the Higgs boson found with a mass close to 125 GeV. It describes the Higgs sector using the parameter entering at tree level, m_A and $\tan\beta$, and the mass of the observed Higgs boson. Higher order corrections to the neutral Higgs boson mixing matrix are traded against the mass of the Higgs boson and the experimental uncertainties on the mass measurement. As a result of this approach, the hMSSM naturally predicts the existence of a Higgs boson compatible with the observed Higgs boson for all values of the parameters m_A and $\tan\beta$. The difference in the predicted masses of the Higgs bosons between the $m_{\mathrm{h}}^{\mathrm{mod}+}$ scenario and the hMSSM can also be seen in figure 2.2, where the masses of the five Higgs bosons are illustrated for the $m_{\mathrm{h}}^{\mathrm{mod}+}$ and hMSSM scenario as a function of m_A for two values of $\tan\beta$.

Similar to the masses of the Higgs boson, the coupling structure can also be fully described using two parameters. These parameters are chosen to be $\tan\beta$ and the mixing angle of the states ϕ_1^0 and ϕ_2^0, α. Using the parameters β, m_A and m_Z, the parameter α can be expressed as

$$\alpha = \frac{1}{2}\arctan\left(\tan(2\beta)\frac{m_A^2 + m_Z^2}{m_A^2 - m_Z^2}\right). \tag{2.23}$$

In the *decoupling limit*, which is the case if $m_A \gg m_Z$, the parameter α follows the relation

$$\alpha \to \beta - \frac{\pi}{2}. \tag{2.24}$$

The coupling structure of the light neutral scalar Higgs boson in the decoupling limit converges to the coupling structure of the Standard Model Higgs boson. A similar coupling structure is predicted for both the heavy neutral scalar and the pseudoscalar Higgs boson. The coupling to down-type fermions, for example the bottom quark or τ-lepton, is modified by $\tan\beta$, whereas the coupling to up-type fermions is modified by $1/\tan\beta$
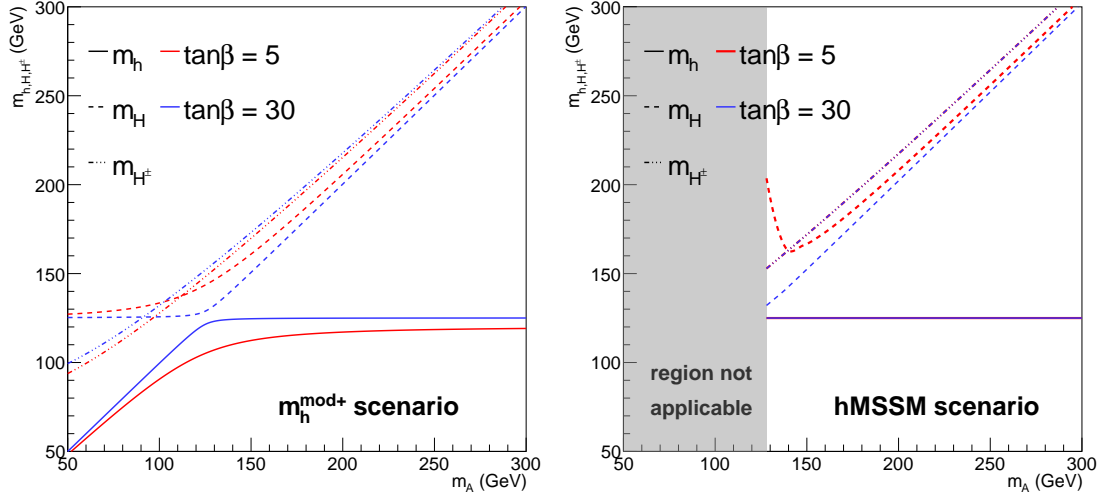
Figure 2.2: Masses of the neutral scalar and charged Higgs boson predicted in the MSSM as a function of the mass of the pseudoscalar Higgs boson m_A. The masses are shown for the values $\tan\beta = 5$ and $\tan\beta = 30$ in the $m_h^{\text{mod+}}$ (left) and hMSSM (right) scenario. In the hMSSM scenario the masses of the light scalar and charged Higgs bosons are the same for both values of $\tan\beta$. The shaded gray indicated the region where the hMSSM scenario is not applicable. For the $m_h^{\text{mod+}}$ scenario the masses are derived using Feynhiggs [29–34]. For the hMSSM scenario inputs provided by the LHC Higgs cross section working group are used [35].

with respect to the Standard Model coupling. For vector-bosons, no coupling to the pseudoscalar and a coupling converging to 0 for the heavy neutral Higgs boson is predicted. The coupling structures are given in table 2.3.

For the heavy neutral scalar and pseudoscalar Higgs boson the two dominant production mechanisms are the gluon-fusion and bottom quark associated production. Both are shown in figure 2.3 as a function of m_A for two values of $\tan\beta$. The relative importance of both production mechanisms largely depends on the value of $\tan\beta$. For higher values of $\tan\beta$ the bottom quark associated production mechanism dominates. At lower values the gluon-fusion production has a larger cross section. This is compatible with the expectation based on the coupling structure discussed before. Due to the coupling between bottom quarks and both Higgs bosons being enhanced with $\tan\beta$, also the cross section of the bottom quark associated production mechanism increases with increasing $\tan\beta$. For the gluon-fusion both bottom and top quark contribute in the quark loop, resulting in a non-trivial dependence of the cross section on $\tan\beta$.

The branching ratios for each of the three neutral Higgs bosons can be determined based on the prediction for the Higgs boson masses, coupling structure as well as the coupling to additional particles in the MSSM. In figure 2.4 the branching ratios for the decay of any of the Higgs bosons into SM particles are illustrated for two values of $\tan\beta$. For the light neutral scalar Higgs boson only a minor dependence on the $\tan\beta$ value is
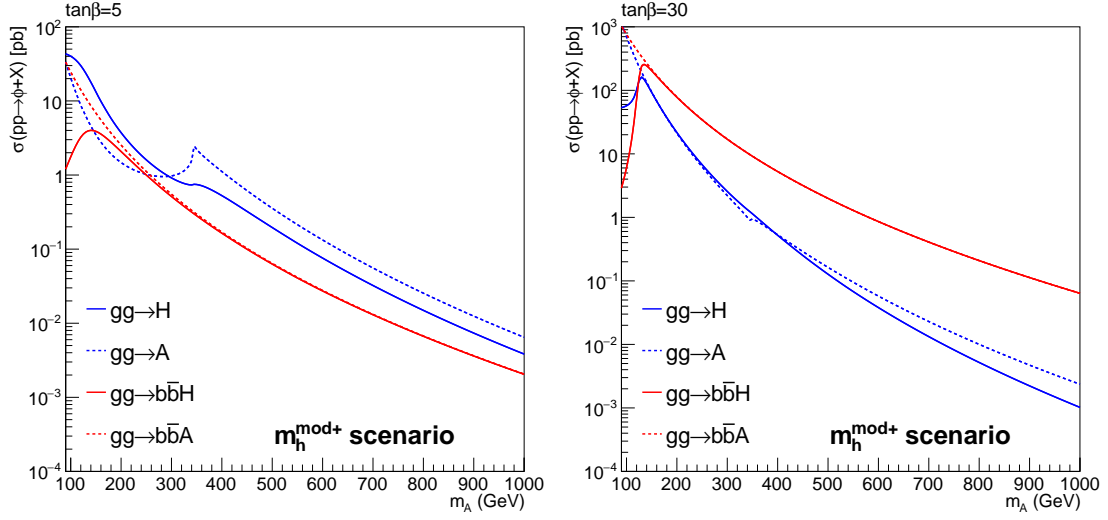
Figure 2.3: Production cross sections for gluon fusion and bottom quark associated production of a heavy scalar and pseudoscalar Higgs boson in the $m_{\mathrm{h}}^{\mathrm{mod+}}$ scenario. The cross sections are given for $\tan\beta = 5$ (left) and $\tan\beta = 30$ (right) using inputs provided by the LHC Higgs cross section working group [35]. For higher values of $\tan\beta$ the bottom quark associated production dominates due to the scaling of the coupling between the bottom quark and the Higgs boson with $\tan\beta$.

Table 2.3: Coupling structure of the three neutral Higgs bosons in the MSSM, h, H, A. The coupling to vector-bosons, up-type fermions and down-type fermions is given normalized to the coupling of a SM Higgs boson. The coupling structure is given for the general case as well as the decoupling limit. In the decoupling limits the coupling of the h converges to the coupling of the SM Higgs boson and the coupling of H, A to down-type fermions is enhanced by $\tan\beta$.

"reduced coupling" to	h	H	A
vector boson	$\sin(\beta - \alpha) \to 1$	$\cos(\beta - \alpha) \to 0$	0
up-type fermion	$\dfrac{\cos\alpha}{\sin\beta} \to 1$	$\dfrac{\sin\alpha}{\sin\beta} \to \dfrac{1}{\tan\beta}$	$\dfrac{1}{\tan\beta}$
down-type fermion	$\dfrac{\sin\alpha}{\cos\beta} \to 1$	$\dfrac{\cos\alpha}{\cos\beta} \to \tan\beta$	$\tan\beta$

observed. On the other hand, for both the heavy neutral scalar and the pseudoscalar Higgs boson the expected enhancement of the branching ratio into down-type fermions with higher values of $\tan\beta$ is can be seen.
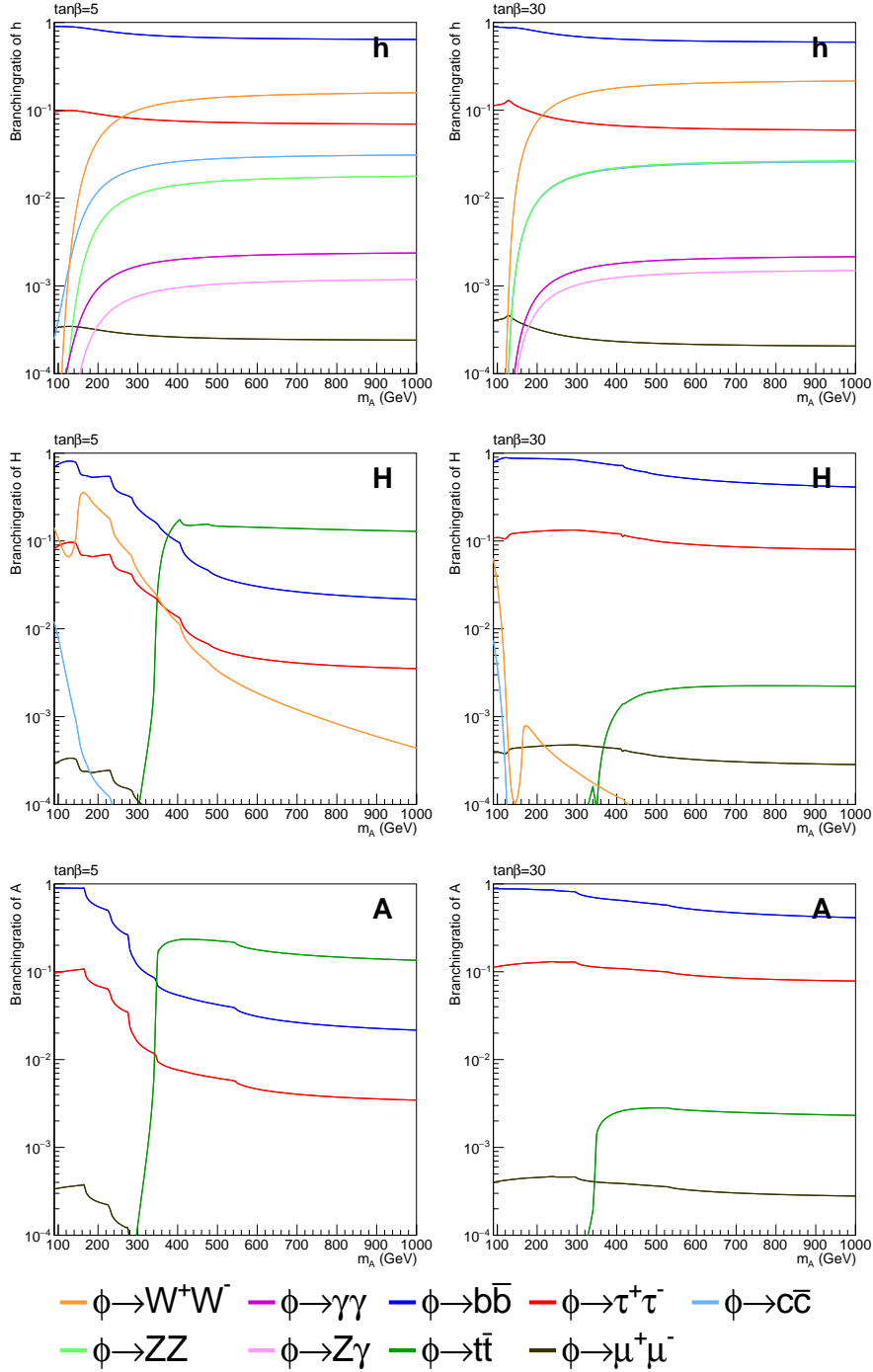
Figure 2.4: Branching ratios for the decay of the light scalar Higgs boson h (top), heavy scalar Higgs boson H (middle) and pseudoscalar Higgs boson A (bottom) in Standard Model particles. Decays into supersymmetric particles are included in the calculation but not shown. The branching ratios are shown for $\tan\beta = 5$ (left) and $\tan\beta = 30$ (right) in the $m_{\text{h}}^{\text{mod+}}$ scenario using inputs provided by the LHC Higgs cross section working group [35].

Statistical inference

The major goal of any search for new physics is to quantify the agreement or disagreement of these results with a given prediction. This chapter introduces the methods and techniques used for deriving the interpretation of the data as presented in chapter 6. First, the basic principles of the likelihood function and the inclusion of systematic uncertainties are discussed. In the second part, the application of such likelihood functions to perform hypothesis tests and determine upper limits on parameters is detailed. As an example the procedure for deriving exclusion limits for a specific MSSM scenario as they are presented in chapter 6 is highlighted. A more detailed description of these basics and methods can be found in [36, 37].

3.1 Basic principles

For this thesis the analysis is performed in binned histograms corresponding to independent counting experiments in each bin. The probability for an outcome of a counting experiment can be described using the Poisson distribution

$$P(n|\nu) = \frac{\nu^n e^{-\nu}}{n!} \equiv \text{Poisson}(n|\nu) \tag{3.1}$$

where n is the observed and ν the predicted number of occurrences.

Similarly, a process following a Gaussian distribution can be described with the Gaussian probability density function (PDF)

$$P(n|\nu,\sigma) = \frac{1}{\sqrt{2\pi}\sigma} e^{-\frac{(n-\nu)^2}{2\sigma^2}} \equiv \text{Gaussian}(n|\nu,\sigma) \tag{3.2}$$

where in addition to the previously defined parameters ν and n, σ represents the standard deviation of the distribution.

In the context of searches for new particles the prediction ν can be expressed as $\nu = s + b$ with b being the predicted number of events for all known backgrounds and s the predicted number of signal events. In the likelihood the prediction further depends on additional parameters θ. The likelihood function is then expressed as a function of the observation, prediction and additional parameters

$$L(n|s,b,\theta) \tag{3.3}$$

3.2 Systematic uncertainties

Generally, the predictions for s and b are known only within a given uncertainty. In the following the incorporating of this uncertainty on the background b in the likelihood function is discussed. The uncertainty on the background prediction is introduced in the likelihood function using a nuisance parameter θ_b with a corresponding PDF $P(\theta_b)$. The prediction for the background b is then written as

$$b \rightarrow b \cdot (1 + \theta_b) \tag{3.4}$$

Leading to a resulting likelihood function of

$$L(n|s, b, \theta_b) = \mathrm{Poisson}(n|s + b \cdot (1 + \theta_b))P(\theta_b). \tag{3.5}$$

In typical particle physics applications, more than one source of uncertainty needs to be taken into account. This leads to the introduction of one nuisance parameter θ_b^i for each uncertainty with a corresponding PDF $P(\theta_b^i)$. The background prediction can then be expressed as

$$b \rightarrow b \prod_{i=1}^{N} (1 + \theta_b^i). \tag{3.6}$$

The specific choices of the PDFs for the nuisance parameter θ_b^i depend on the nature of the uncertainty. Typically however, they all need to be constrained to values larger than -1 in order to prevent non-physical negative contributions to the expected event count. This is for example achieved by the choice of log-normal or truncated Gaussian distributions.

Typical analyses have contributions from more than one background process. In the likelihood formulation this is obtained by expressing the background prediction b as the sum over all backgrounds b_j.

$$b \rightarrow \sum_{j} b_j \prod_{i=1}^{N} (1 + \theta_b^{i,j}). \tag{3.7}$$

Up to this point, only uncertainties uncorrelated between different background contributions have been considered. To fully describe a measurement, correlations across different background contributions need to be taken into account. For simplicity, only fully correlated or uncorrelated uncertainties are introduced. Partial correlations are split into their fundamental correlated and uncorrelated parts, which are accounted for by means of dedicated nuisance parameters.

A correlated uncertainty means that multiple backgrounds b_i are affected by one uncertainty in a common way. To account for this a common nuisance parameter θ^c and corresponding PDF $P(\theta^c)$ are introduced. Different magnitudes of the effect of this common nuisance parameter on the individual backgrounds b_i are accounted for by a scaling factor

$$f_i = \frac{\sigma_i}{\sigma_c}, \tag{3.8}$$

with σ_c corresponding to the uncertainty of the PDF of the common nuisance parameter and σ_i corresponding to the uncertainty for the background i. In the case of two background contributions with one fully correlated uncertainty, the resulting background predictions are given by

$$b_1 \rightarrow b_1(1 + \theta_b^c f_1) \qquad \text{and} \qquad b_2 \rightarrow b_2(1 + \theta_b^c f_2). \qquad (3.9)$$

Positive values of f_i denote a positive correlation, while negative values imply an anti-correlation. The considerations presented before for the background b can also be applied to the signal prediction s by substituting b and θ_b by s and θ_s respectively.

Up to now, only a single independent counting experiment has been discussed. In the case of histograms, with each bin of a given histogram being a single counting experiment, the likelihood function can be described as a combination of many counting experiments:

$$L(\vec{n}|\vec{s}, \vec{b}, \vec{\theta}) = \prod_{i=1}^{N} P(n_i|s_i(\vec{\theta}) + b_i(\vec{\theta})) \times \prod_{j=1}^{M} P(\theta_j) \qquad (3.10)$$

where $\vec{n}$, $\vec{s}$ and $\vec{b}$ correspond to vectors of the individual observations, signal and background predictions respectively. The systematic uncertainties on the individual contributions s_i and b_i are incorporated in this likelihood function as discussed before taking into account the correlation between them.

In the search for upper limits on cross sections, as presented in section 6.4, a common approach is to introduce a global signal strength value μ relative to the predicted signal, which is given by $\mu = 1$. The signal prediction is then expressed as μs_i. Leading to the resulting likelihood function given by

$$L(\vec{n}|\mu, \vec{s}, \vec{b}, \vec{\theta}) = \prod_{i=1}^{N} P(n_i|\mu s_i(\vec{\theta}) + b_i(\vec{\theta})) \times \prod_{j=1}^{M} P(\theta_j). \qquad (3.11)$$

3.3 Maximum likelihood fit

Using the likelihood function given in equation 3.11 a maximum likelihood fit can be performed. In this fit the values of the nuisance parameters $\vec{\theta}$ and the parameter μ maximizing the likelihood function are determined.

A common approach to simplify the procedure is to maximize the logarithm of the likelihood function $\log L(\vec{n}|\mu, \vec{s}, \vec{b}, \vec{\theta})$ instead of the likelihood function itself.

$$\log L(\vec{n}|\mu, \vec{s}, \vec{b}, \vec{\theta}) = \sum_{i=1}^{N} \log P(n_i|\mu s_i(\vec{\theta}) + b_i(\vec{\theta})) \times \sum_{j=1}^{M} \log P(\theta_j) \qquad (3.12)$$

This approach offers the advantage that instead of deriving the maximum for a product of terms, the maximum only needs to be derived for a sum of terms.

3.4 Hypothesis testing and the test statistic

To perform a hypothesis test discriminating between two hypotheses the *profile likelihood ratio* λ is introduced. The profile likelihood ratio is given as the ratio of the likelihood for the signal-plus-background (s+b) hypothesis and the likelihood for the background-only (b-only) hypothesis:

$$\lambda(\mu) = \frac{L(n|\mu, \hat{\theta}_\mu)}{L(n|0, \hat{\theta}_0)} \tag{3.13}$$

Values of λ larger than 1 favor the s+b hypothesis, whereas lower values favor the b-only hypothesis. The simple likelihood ratio only quantifies the discrimination between the s+b and b-only hypothesis based on the observation. For the following considerations the *text statistic* q_μ is constructed as

$$q_\mu = -2\log\lambda(\mu). \tag{3.14}$$

Based on the distribution of the test statistic for the s+b case $f(q_\mu|\mu)$ and b-only case $f(q_\mu|0)$ the confidence levels $\mathrm{CL}_{\mathrm{S+B}}$ and CL_{B} are calculated (see figure 3.1). The $\mathrm{CL}_{\mathrm{S+B}}$ value is obtained by integrating the distribution of $f(q_\mu|\mu)$ from the observed value to $+\infty$, corresponding to the probability to find a less s+b-like value of the test statistic. Likewise, the value for CL_{B} is obtained by integrating from the observed value to $+\infty$, corresponding to the probability to find a more b-only-like value of the test statistic.

$$\mathrm{CL}_{\mathrm{S+B}}(\mu) = \int_{q_\mu^{\mathrm{obs}}}^{\infty} f(q_\mu|\mu)\,\mathrm{d}q_\mu \tag{3.15}$$

$$\mathrm{CL}_{\mathrm{B}} = \int_{q_\mu^{\mathrm{obs}}}^{\infty} f(q_\mu|0)\,\mathrm{d}q_\mu. \tag{3.16}$$

The $\mathrm{CL}_{\mathrm{S+B}}$ does, however, not take into account how well the s+b and b-only hypotheses can be separated. This is taken into account in the CL_{S} method [38, 39] used by the LEP experiments and ATLAS and CMS for setting upper limits on parameters. In this approach the $\mathrm{CL}_{\mathrm{S+B}}$ and CL_{B} measures are combined in the CL_{S} value, which is defined as

$$\mathrm{CL}_{\mathrm{S}}(\mu) = \frac{\mathrm{CL}_{\mathrm{S+B}}(\mu)}{\mathrm{CL}_{\mathrm{B}}}. \tag{3.17}$$

Due to the normalization to the CL_{B} value this measure takes into account how well the s+b and b-only hypothesis can be separated.

The upper limits at a confidence level α on the parameter μ is then found for the value of μ for which the CL_{S} value satisfies

$$\mathrm{CL}_{\mathrm{S}}(\mu^{\mathrm{up}}) = 1 - \alpha. \tag{3.18}$$

Common choices for the confidence level are 95 %.

For the determination of the CL_{S} value the distributions of the test statistic $f(q_\mu|\mu)$ and $f(q_\mu|0)$ need to be determined. These can be derived based on toys, for which the observation n is replaced with toy observations drawn according to the given hypothesis.
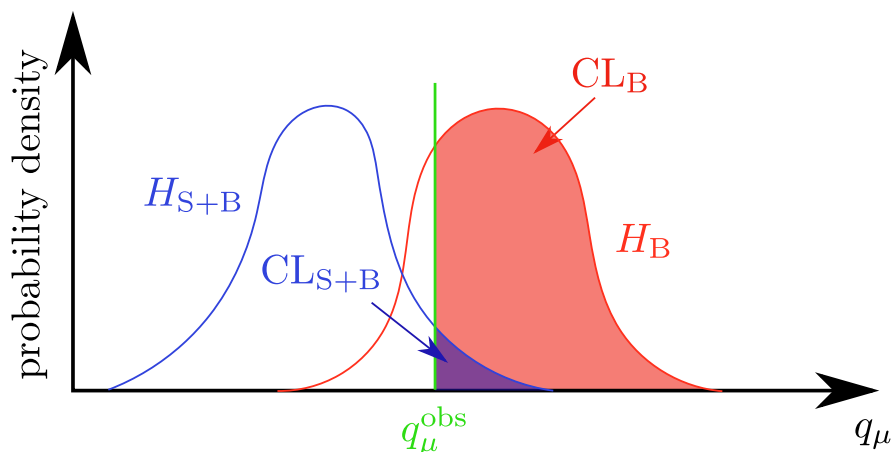
Figure 3.1: Illustration of the test statistic distribution for the background-only (H_B) and signal-plus-background (H_{S+B}) hypotheses. The regions of the CL_B and CL_{S+B} values correspond to the integrals of the corresponding distributions from the observed value of the test statistic q_μ^{obs} to ∞.

However, this can be computing resource expensive. By ATLAS and CMS a modified approach is used. In this approach the profile likelihood ratio is not normalized to the likelihood for the b-only hypothesis, but to the global maximum of the likelihood-function. It is given by

$$\lambda(\mu) = \frac{L(n|\mu, \hat{\hat{\theta}}_\mu)}{L(n|\hat{\mu}, \hat{\theta})}, \ 0 \leq \hat{\mu} < \mu \tag{3.19}$$

where $\hat{\mu}$ and $\hat{\theta}$ are the values of μ and θ which globally maximize the likelihood function and $\hat{\hat{\theta}}_\mu$ are the parameters which maximize the likelihood function for a given fixed choice of μ. The corresponding test statistic q_μ is then given as

$$q_\mu = \begin{cases} -2\log\lambda(\mu) & \mu \geq \hat{\mu} \\ 0 & \mu < \hat{\mu} \end{cases} \tag{3.20}$$

Using this definition of the profile likelihood and test statistic asymptotic formulae [40, 41] can be used for deriving the distribution of the test statistic. In the case of sufficiently large number of events these are found to provide good descriptions of the test statistic distribution.

3.5 Exclusion limits in the m_A-tan β plane

The methods described before are used to set exclusion limits for a specific MSSM scenario in the m_A-tan β plane. For these limits the MSSM hypothesis needs to be distinguished from the SM hypothesis. The corresponding profile likelihood ratio is given by

$$\lambda = \frac{L(BG + MSSM)}{L(BG + SM)} \tag{3.21}$$

For the methods presented in the previous section and especially to ensure the applicability of asymptotic formulae, a likelihood function being able to express both probed hypotheses needs to be found. As the hypotheses being probed do not depend on each other, a dedicated method needs to be applied to merge both hypotheses into a single likelihood function. The method used as well as advantages and disadvantages of this approach are discussed in [42]. The chosen likelihood function is

$$L(x) = L\left(x \cdot s_{\text{MSSM}} + (1 - x) \cdot s_{\text{SM}} + \text{BG}\right), 0 \leq x \leq 1 \tag{3.22}$$

with the parameter of interest x. For $x = 0$ this likelihood function corresponding to the SM+BG case, whereas for $x = 1$ the MSSM+BG hypothesis is described. However, while for the values $x = 0$ and $x = 1$ the described model is physically meaningful, values of x in between 0 and 1 do not correspond to a physical model. Nonetheless, they are well defined from a statistical point of view and can be used for the calculations presented in the previous section.

When using the profile likelihood ratio given in equation 3.21 no asymptotic description of the test statistic distribution is available. Consequently, these distributions need to be derived in a toy based approach. For the exclusion limits in the m_{A}-$\tan\beta$ plane this means that for each parameter point in this plane the corresponding distributions need to be derived. An illustration of the grid of points used for deriving the exclusion limits is shown in figure 3.2. In order to reduce the computational efforts needed for these limits the points on the grid are chosen such that they have the highest density close to the expected exclusion limits and its uncertainties, while only few points are probed farther away. Values for parameter points in between the probed points are interpolated.

As the toy based approach is computationally intensive an approach employing the LHC test statistic given in equation 3.20 and corresponding asymptotic formulae are used for the results presented in chapter 6. This approach was studied in [43] and the difference of the results to the fully toy based approach were found to be small for the central values of the expectation and observation and yield similar uncertainties for the expectation.
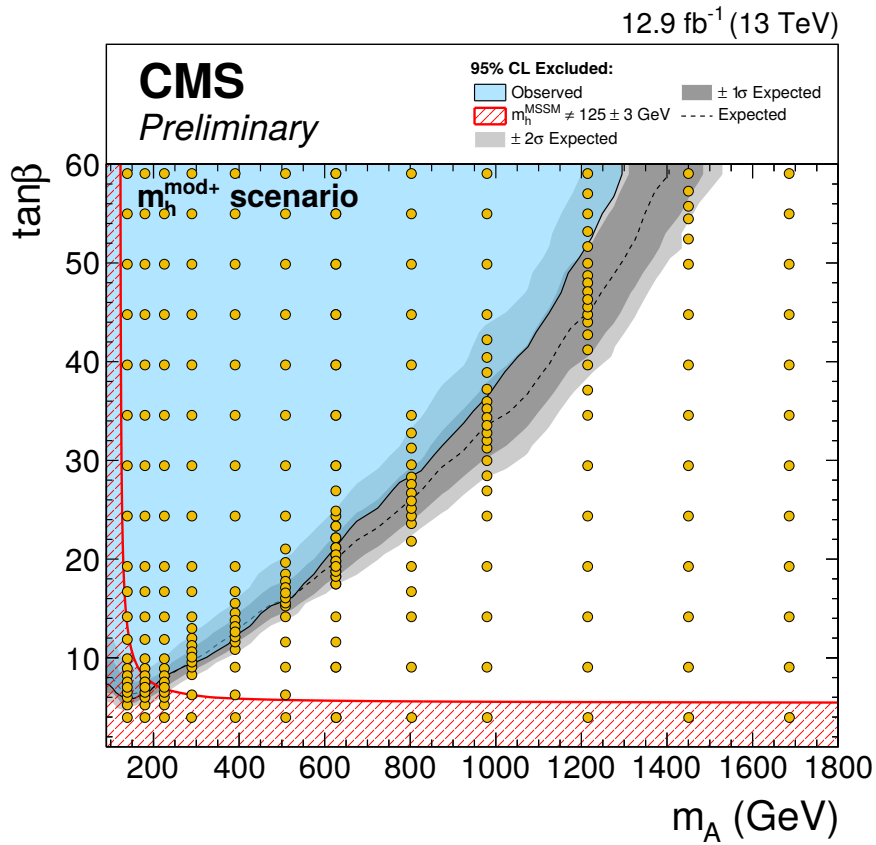
Figure 3.2: Illustration of the grid in the m_A-tan β plane. Each yellow point corresponds to a single point for which the test statistic distribution is derived and the CL_S value is computed. The grid has a higher density in regions close to the exclusion contours in order to improve their resolution. For illustrational purpose the underlying plot is taken from [5].

Experimental Setup

This section gives an overview of the experimental setup and environment of this thesis. Section 4.1 gives an overview of the accelerator complex at CERN and the parameters of its largest accelerator, the Large Hadron Collider (LHC). Section 4.2 introduces the design and components of the Compact Muon Solenoid Experiment (CMS). The computing environment and the Worldwide LHC Computing Grid are sketched in section 4.3. Eventually, section 4.4 introduces the techniques and algorithms used to reconstruct and identify particles at the CMS experiment.

4.1 The Large Hadron Collider

The LHC [44] is the worlds most powerful particle accelerator. The accelerator with a circumfence of 27 km is build up in the tunnel of its predecessor, the Large Electron Positron Collider (LEP), close to the CERN main site in Meyrin at a depth between 50 and 175 m. Using more than 1000 dipole magnets with a magnetic field of 8.3 T to bend the proton beams onto the circular trajectory and around 400 quadrupole magnets to focus the proton beams, the LHC is operated to accelerate protons up to an energy of 6.5 TeV.

Two beams inside the LHC are collided at four interaction points, where the four LHC experiments - ALICE, ATLAS, LHCb and CMS - are located. The ALICE experiment is designed to study the quark-gluon plasma using data collected during the heavy ion operation on the LHC. These measurements are designed to draw conclusions about the initial state of the universe. LHCb focuses on precisely measuring B-meson decays and CP-violating processes. CMS and ATLAS are the two general purpose experiments at the LHC build for studying a broad range of physics processes. These studies include precision measurements of Standard Model processes and parameters, thereby deepening our knowledge and understanding of the Standard Model. In addition, major fields of study are searches for the Higgs bosons and study of their properties and searches for physics beyond the Standard Model.

Prior to the injection into the LHC, the protons pass through a series of smaller accelerators [45]. Starting from a bottle of hydrogen, the initial acceleration of the protons up to an energy of 50 MeV takes place in a linear accelerator (LINAC2). From there
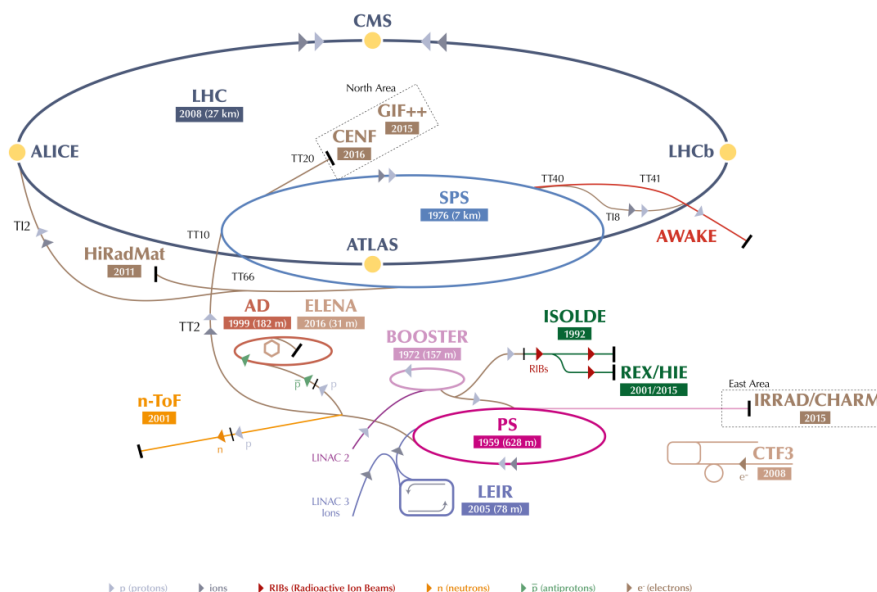
Figure 4.1: The CERN accelerator complex consists of several particle accelerators which are chained to accelerate the protons up to the energy with which they are injected into the LHC. Alongside these accelerators further experiments are located serving a broad range of physics. Taken from [46]

the protons are transferred to and further accelerated by four circular accelerators with increasing size. The Proton Synchrotron Booster with a circumfence of 157 m accelerates the protons up to an energy of 1.4 GeV. From there on the protons are transferred to the Proton Synchrotron (PS) with a circumfence of 628 m where the energy is increased to 25 GeV. The 7 km long Super Proton Synchrotron (SPS) is the final step in this chain. There the protons are accelerated to an energy of 450 GeV and eventually injected into the LHC ring. In addition to feeding the LHC, these accelerators are also used for other physics experiments on the CERN site like the Antiproton decelerator (AD), see figure 4.1.

4.2 The Compact Muon Solenoid Experiment

The data analyzed in this thesis has been taken with the CMS detector in the year 2016. The CMS detector is build up in a barrel-like design around the interaction point of the proton beams delivered by the LHC. The detector can be separated into two main parts, the central part of the detector, referred to as barrel and the two sections closing the detector in the direction of the LHC beampipe, referred to as endcaps.

The CMS experiment consists of four different subdetectors, each targeting a different kind of measurement. The combination of these subdetectors allows to detect and measure the properties of most stable particles being produced in proton-proton or heavy ion collisions (see figure 4.2).
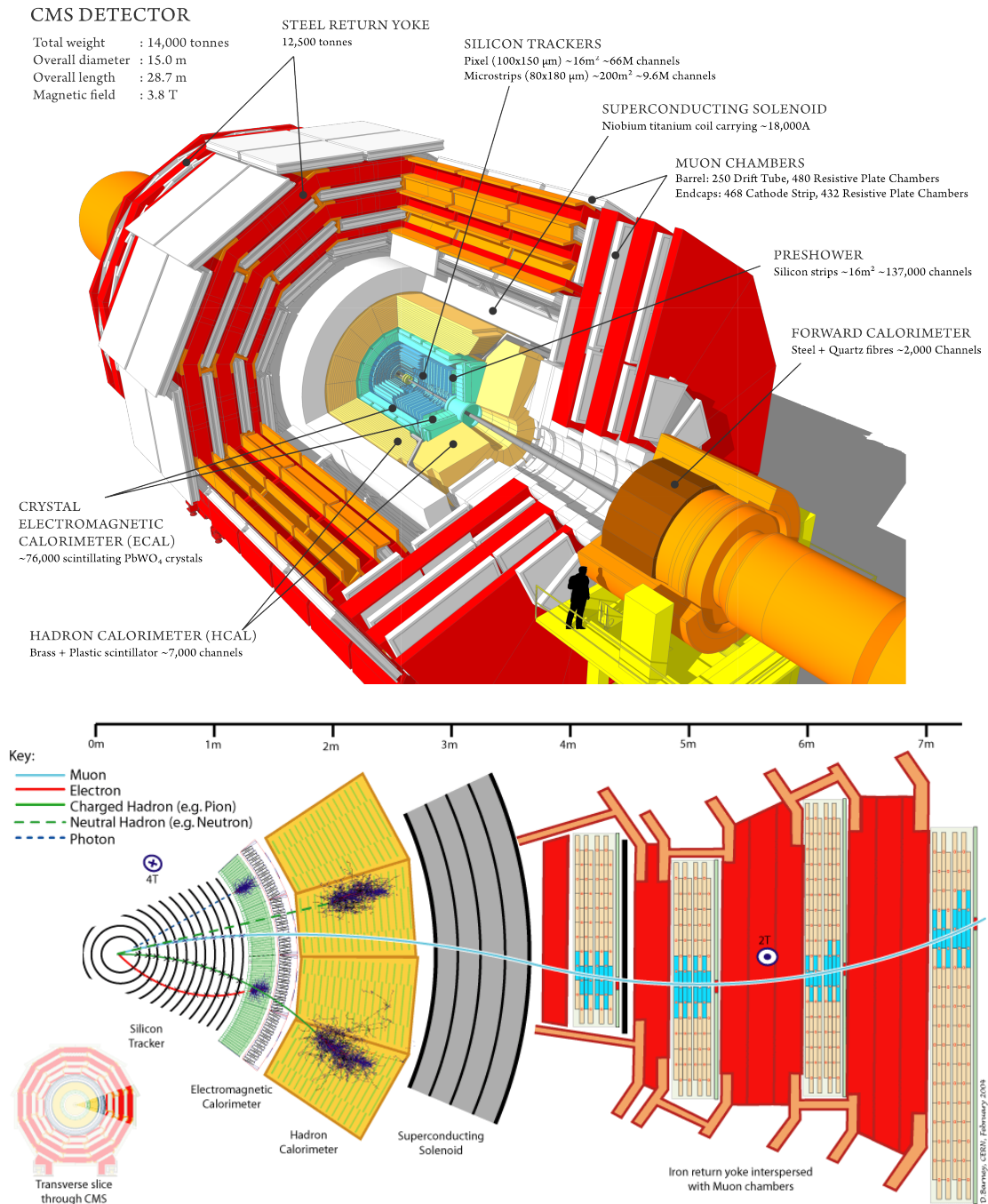
CMS DETECTOR
Total weight   : 14,000 tonnes
Overall diameter : 15.0 m
Overall length   : 28.7 m
Magnetic field   : 3.8 T

STEEL RETURN YOKE
12,500 tonnes

SILICON TRACKERS
Pixel (100x150 μm) ~16m² ~66M channels
Microstrips (80x180 μm) ~200m² ~9.6M channels

SUPERCONDUCTING SOLENOID
Niobium titanium coil carrying ~18,000A

MUON CHAMBERS
Barrel: 250 Drift Tube, 480 Resistive Plate Chambers
Endcaps: 468 Cathode Strip, 432 Resistive Plate Chambers

PRESHOWER
Silicon strips ~16m² ~137,000 channels

FORWARD CALORIMETER
Steel + Quartz fibres ~2,000 Channels

CRYSTAL
ELECTROMAGNETIC
CALORIMETER (ECAL)
~76,000 scintillating PbWO₄ crystals

HADRON CALORIMETER (HCAL)
Brass + Plastic scintillator ~7,000 channels

Figure 4.2: Illustration of the CMS detector (top) [47] and cross section of the barrel region of the CMS detector (bottom) [48]. The components of the subdetectors are highlighted. In the bottom figure the trajectories and energy deposits for five classes of particles observed in the final state of proton-proton collisions are shown.

25

First, the coordinate system used to describe interactions recorded with the CMS detector is introduced in this section. Afterwards, a brief description of the individual subdetectors of the CMS experiment is given. More details on the setup of the CMS experiment can be found in [49–53].

Coordinate system at CMS

To describe interactions within the CMS detector an orthogonal right handed coordinate system is used. The x axis of this coordinate system points towards the center of the LHC ring, the y axis upwards orthogonal to the plane of the accelerator and the z axis counterclockwise in the direction of the beam pipe. In addition, the two angles ϕ, defined as the azimuthal angle to the x axis in the x-y plane, and θ, the polar angle measured from the z axis, are used. The x-y plane is also referred to as the transverse plane.

Instead of the angle θ commonly the pseudorapidity η which is defined as

$$\eta = -\ln\left[\tan\left(\frac{\theta}{2}\right)\right] \tag{4.1}$$

is used. In the limit of massless particles, the pseudorapidity has the advantage of being covariant under boosts along the z axis.

As a measure of the distance between two objects the metric ΔR is introduced, which is defined as

$$\Delta R = \sqrt{\Delta\phi^2 + \Delta\eta^2}. \tag{4.2}$$

Inner Tracking System

The inner tracking system is used for measuring the trajectory of charged particles, such as charged leptons and charged hadrons (see figure 4.2), passing through the detector. In combination with the magnetic field of the superconducting solenoid, this enables a measurement of the momentum of these particles based on the curvature of the track. The super conducting solenoid is located outside of the electromagnetic calorimeter and generates a magnetic field of 3.8 T.

The inner tracking system itself is the first layer of the CMS detector located directly around the beam pipe. This positioning as close as possible to the interaction point allows to measure the interaction vertices and tracks with the best achievable resolution. The tracking system used in the CMS experiment is built out of silicon based semiconductor detectors. Two different types of detectors are used. For the innermost layers silicon pixel detectors, which allow the best resolution for particle hits in the detector are used. This setup is completed by layers of strip detectors used for the outer layers. The combination of silicon pixel and strip detectors allows for a precise measurement of the trajectories close to the interaction point.

The CMS tracking system covers the detector region up to $|\eta| = 2.5$ and has a resolution of up to 10 µm in the x-y direction and 20 µm in the z direction. The transverse momentum of tracks can be measured with a resolution of 1-2 % for muons with a p_T of 100 GeV.

Electromagnetic Calorimeter

The electromagnetic calorimeter (ECAL) is designed to measure the energy of electrons and photons. It consists of 75000 lead tungstate (PbWO4) crystals. Lead tungstate is chosen as material due to its radiation hardness, high density ($8.28 \, \text{g cm}^{-3}$) and therefore short radiation length (0.89 cm). It consists of two parts, the ECAL barrel (EB) extending up to $|\eta| < 1.479$, the ECAL endcap (EE) covering $1.479 < |\eta| < 3.0$. The crystals of the EB are arranged in a cylindrical shape with an inner radius of 1.29 meter. Each crystal in the EB has a depth of 23 cm, which corresponds to 25.8 radiation lengths X_0, and is $2.2 \, \text{cm} \times 2.2 \, \text{cm}$ large, covering an area of 1° in the $\eta - \phi$ plane.

The EE is made up from similar lead tungstate crystals with a depth of 22 cm, corresponding to $25X_0$, and a size of $2.86 \, \text{cm} \times 2.86 \, \text{cm}$. In front of the EE an additional preshower (ES) is installed in the region $1.653 < |\eta| < 2.6$. The ES allows for a precise measurement of the position of electromagnetic showers, thereby allowing an improved differentiation between the signatures of electrons and photons from π^0 decays. The ES consists of one layer of lead absorber followed by a layer of plastic scintillators. Both layers have a total thickness of $4X_0$.

The resolution of the ECAL is characterized by three components:

$$\frac{\sigma_E}{E} = \frac{S}{\sqrt{E}} \oplus \frac{N}{E} \oplus C \tag{4.3}$$

where S corresponds to the stochastic part of the uncertainty for example due to statistical fluctuations in the photon emission in the crystals. N represents the contribution to the uncertainty due to noise in the electronics or pile-up. The constant term C accounts among other effects for the uncertainty due to leakage of the energy from showers extending beyond the end of the crystals. In a test beam setup, the terms have been measured as $S = 0.028 \sqrt{\text{GeV}}$, $N = 0.12 \, \text{GeV}$ and $C = 0.003$ [53].

Hadron Calorimeter

The hadron calorimeter (HCAL) is designed to measure the energy of hadrons originating from the collisions in the detector. It covers the region up to $|\eta| < 3$ and consists of alternating layers of brass and plastic scintillators. It is 5.8 interaction lengths (λ_I) thick. Combined with an additional system outside of the solenoid coil a total thickness of $\approx 11.8\lambda_\text{I}$ is reached.

In the forward and backward direction, the hadron calorimeter is completed by an additional calorimeter covering small opening angles up to $|\eta| < 5.2$. Due to the high particle fluxes in these regions this calorimeter is made up from radiation hard quartz fibers embedded in steel.

The resolution of the hadron calorimeter is characterized by a term proportional to the square root of the energy and a constant, described as

$$\frac{\sigma_E}{E} = \frac{84.7 \, \%}{\sqrt{E/\text{GeV}}} \oplus 7.4 \, \% \tag{4.4}$$

Muon System

The muon system is the largest subdetector at the CMS experiment located outside of the superconducting solenoid. Three different types of detectors are employed in the muon system. In the barrel region of the CMS detector up to $|\eta| \approx 1.3$ drift tubes and in the endcap regions, for $0.9 < |\eta| < 2.4$, cathode strip chambers are used. Both of these detectors allow to measure the trajectories of muons passing through the detector and hence, combined with the information of the inner tracking system, provide a precise measurement of the muon momentum.

In addition, resistive plate chambers are employed in both the barrel and endcap region up to $|\eta| = 2.1$. These types of detectors offer a poor spatial resolution in the order of a few cm but provide a good time resolution of $\approx 3 \, \text{ns}$. The resistive plate chambers are used to provide a dedicated signal for triggering events with muons.

Triggering at CMS

Proton-proton collisions at the LHC take place once every 25 ns. Due to this high inter-action rate, the data recorded by the detector can not be fully stored at a computing center. In order to account for this, a tiered triggering approach is used by the CMS collaboration. In a first step, the *level 1* trigger is used to reduce the event rate to 100 kHz. The level 1 triggering system is based on dedicated hardware, allowing for a fast enough decision.

Events accepted by the level 1 trigger are sent on to the *high level trigger*. The high level trigger is entirely software based and is run on a dedicated server farm. At the high level trigger step, an initial reconstruction of each event is performed. This allows the trigger to use high-level objects such as reconstructed τ-leptons.

Using the high level trigger, the event rate gets reduced to 100 Hz. These events are then transferred to the computing center at CERN, reconstructed and made available for analyses.

4.3 Computing environment and the Worldwide LHC Computing Grid

Despite of the high level triggering and similar techniques employed by the CMS experiment and other large scale experiments, they still produce large amounts of data. The CMS experiment alone produced approximately 16 PB of data in the year 2016 [54]. Connected with this huge amount of data, a large amount of computing power is needed. To account for this need of storage and provide corresponding computing facilities, the experiments at the LHC make use of the worldwide LHC computing grid (WLCG).

The WLCG is a tiered structure connecting in the order of 170 computing centers to provide the necessary storage and computing facilities (see figure 4.3). The primary computing centers of the WLCG are located at the CERN site in Meyrin and the Wigner datacenter in Budapest. It provides the initial reconstruction of recorded events and storage for the obtained datasets. The tier 1 data centers are mainly used for generating
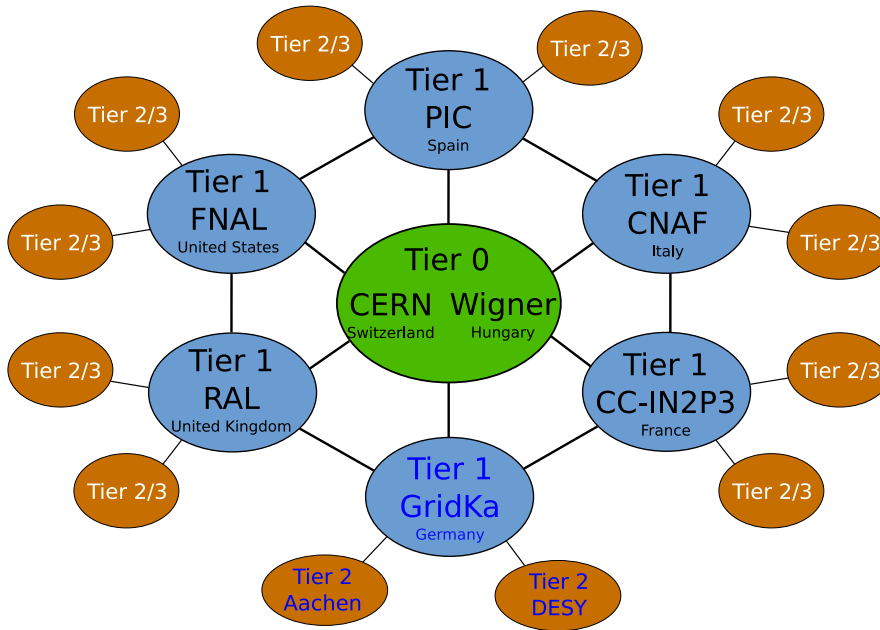
Figure 4.3: The worldwide LHC computing grid (WLCG) provides the storage and computing resources needed to process the data recorded by the CMS experiment and to provide them to the users. The WLCG is organized in a tiered structure with the tier 0 being located at CERN and Budapest. One of the six tier 1 datacenters is operated in Karlsruhe, Germany

simulated events and storing a copy of the raw data. Together with the tier 2 facilities the tier 1 centers provide access to the simulated and measured data to the users. Finally, at the tier 2 and tier 3 facilities analysis jobs of users of the WLCG can be run and the results stored for further processing.

4.4 Object identification and reconstruction

CMS uses a particle flow approach for reconstructing and identifying particles. In this approach, the information of all sub detectors is combined for the reconstruction of the events. This allows for a more precise and reliable reconstruction compared to using the information only from individual subdetectors. In the following section, the principle of the reconstruction and identification which are used for particles most important for the analysis - jets, electrons, muons and τ-leptons - is introduced. Further information on the particle-flow approach employed at CMS can be found in [55].

General comment on the recorded data

An important aspect of the data recorded by the CMS experiment is the number of collisions happening in a single crossing. Among these interactions, only a single one is of interest, with the remaining ones leading to additional signatures in the detector. These

additional interactions are referred to as pile-up. In the year 2016 on average around 23 collisions were recorded per crossing. The place within in the detector at which the interaction takes place is reconstructed as vertex. Based on the sum of the transverse momenta of all particles associated with each vertex and criteria for the quality of the reconstruction and identification of each vertex, a single vertex, referred to as primary-vertex, is selected among those. This primary vertex is used as basis for the object and event reconstruction.

Jet reconstruction

Jets are reconstructed from particle-flow candidates, resembling trajectories in the tracker and energy deposits in the electromagnetic and hadronic calorimeter. For the purpose of the analysis presented in this thesis, jets are clustered using the anti-k_t clustering algorithm [56] with a cone size of 0.4. The clustering algorithm determines how the contributions of individual particles and initial jets are combined in order to arrive at the final jet selection.

A dedicated method is applied to mitigate the effect of pile-up. This is done by removing the contribution from charged hadrons which, based on their track, are identified to originate from other interaction vertices than the primary vertex.

B-tagging

A special class of jets are jets originating from bottom quarks. Hadrons containing bottom quarks have a long enough lifetime to lead to a secondary decay vertex which is displaced with respect to the primary vertex. The mean displacement is in the order of a few millimeters. To differentiate between jets originating from bottom quarks and jets originating from light quarks or gluons, b-tagging algorithms are used. Using a likelihood or multi-variate approach, these algorithms exploit the lifetime of hadrons containing bottom quarks to differentiate between these classes of jets.

For the analysis presented in this thesis the *combined secondary vertex version 2* (CSVv2) b-tagging algorithm is used. This algorithm combines the information of displaced tracks and reconstructed secondary vertices of the decay of hadrons containing b quarks using a multivariate technique [57]. Three working points, loose, medium and tight, are defined for the CSVv2 algorithm. The working points correspond to probabilities of 10, 1 and 0.1 % to mistag jets from light quarks as jets originating from bottom quarks respectively. The efficiency to correctly identify jets originating from bottom quarks is determined as 83, 69 and 49 % for the respective working point. The distribution of the CSVv2 discriminator is shown in figure 4.4. The values of the discriminator corresponding to the three working points are 0.46, 0.8 and 0.935 respectively.

Muon reconstruction and isolation

The muon reconstruction is based on the information from the tracking and muon system. In a first step, an independent reconstruction of tracks of muons is performed for both subdetectors. After this, two compatible tracks are searched for in the results of the
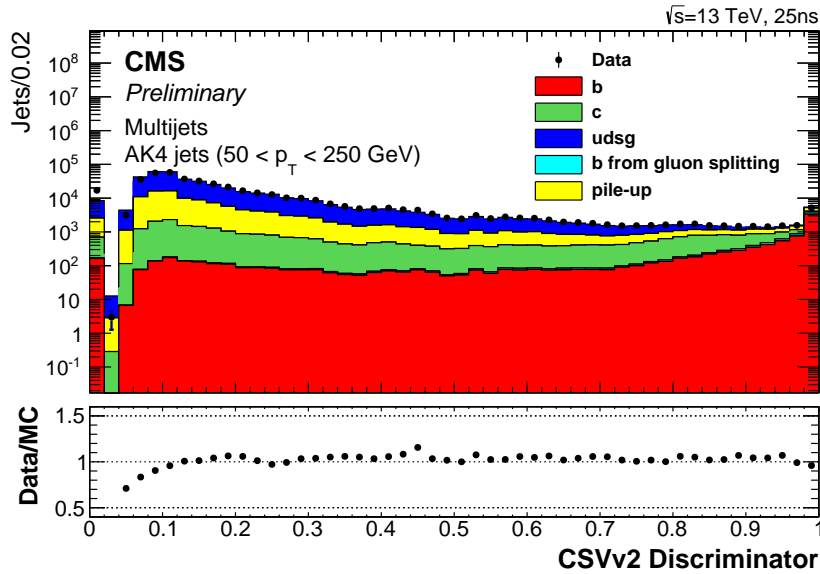
Figure 4.4: Distribution of the CSVv2 discriminator. The medium working point corresponds to a value of 0.8 [57].

individual reconstructions. A combined reconstruction of a muon is then performed using the information from both subdetectors. The combination of both sources of information leads to an improved resolution of the muon reconstruction.

Leptons from the hard interaction are expected to have little other activity in the vicinity around them. In contrast to this, leptons originating from a cascade of hadronic activity are expected to be less isolated from additional activity in the detector due to the confinement. The amount of additional activity in the vicinity of leptons is referred to as the isolation of a lepton. For both muons and electrons, an isolation based on the output of the particle flow algorithm is used. It is defined as the energy deposited in a cone with radius ΔR centered on the lepton and calculated as

$$I_{\mathrm{L}} = \sum_{\mathrm{charged,PV}} p_{\mathrm{T}} + \max\left(0.0, \sum_{\mathrm{neutral}} p_{\mathrm{T}} - \Delta\beta\right) \tag{4.5}$$

where the first term is the sum of the transverse momentum of all charged particles associated to the same primary vertex, which contribute in the cone around the lepton. The second term sums the contribution of all neutral particles. As neutral particles can not be associated to the primary vertex this sum also includes contributions from pile-up vertices. Finally, the $\Delta\beta$ term is introduced to take this into account. It is given by

$$\Delta\beta = 0.5 \sum_{\mathrm{charged,PU}} p_{\mathrm{T}} \tag{4.6}$$

where the factor of 0.5 is given by the expectation that pile-up contributions consist of

equal contributions from charged and neutral particles and the sum is performed over all charged particles within the cone not associated to the primary vertex.

A more common metric for the isolation of leptons is the relative isolation. It is derived by dividing the isolation as defined above by the transverse momentum of the lepton:

$$I_{\mathrm{L}}^{\mathrm{rel}} = \frac{I_{\mathrm{L}}}{p_{\mathrm{T}}^{L}}. \tag{4.7}$$

Electron reconstruction and isolation

Electrons in the CMS detector are reconstructed based on their energy deposition in the electromagnetic calorimeter and a track in the tracking system. The matching is complicated by the fact that electrons while traversing the inner tracking system can radiate off photons as bremsstrahlung. These photons then in turn may convert to an e^+e^- pair. On average $35\,\%$ of the electrons radiate off $70\,\%$ of their energy in this way before reaching the ECAL. To account for this dedicated "superclustering" algorithms are employed combining the energy deposited by an electron and its respective bremsstrahlung photons. As discussed before for electrons the lepton isolation given in equation 4.5 is used.

Identification and reconstruction of hadronically decaying τ-leptons

The hadronic decay of a τ-lepton generally produces a jet with a narrow cone consisting of one or three charged hadrons ($\pi^\pm$) as well as additional neutral hadrons and tau neutrinos. As neutrinos pass the detector without interacting with the detector material they contribute to the $\not{E}_{\mathrm{T}}$ in the given event (see next section). The reconstruction of hadronically decaying τ-leptons at CMS uses the "hadron-plus-strip" algorithm as described in [58, 59]. In this algorithm, one charged hadron, reconstructed using the particle-flow information, is combined with neutral pions, reconstructed from strips of clusters in the electromagnetic calorimeter. All particles of the τ-lepton decay are required to be contained within the same jet, which is clustered using the anti-k_t algorithm with a cone size of $\Delta R = 0.5$.

Strips are formed following the following iterative procedure.

- the electron or photon (e/γ) with the highest p_{T} not included in any strip is selected as seed for a new strip

- The e/γ with the next highest p_{T} within a $\Delta\eta$-$\Delta\phi$ window is searched. The window is defined as $\Delta\eta = 0.2 \left(\left(p_{\mathrm{T}}^{e/\gamma}/\mathrm{GeV} \right)^{-0.66} + \left(p_{\mathrm{T}}^{\mathrm{strip}}/\mathrm{GeV} \right)^{-0.66} \right)$ with a maximum of 0.3 and a minimum of 0.05 and $\Delta\phi = 0.35 \left(\left(p_{\mathrm{T}}^{e/\gamma}/\mathrm{GeV} \right)^{-0.71} + \left(p_{\mathrm{T}}^{\mathrm{strip}}/\mathrm{GeV} \right)^{-0.71} \right)$ with a maximum of 0.15 and a minimum of 0.05. Where $p_{\mathrm{T}}^{\mathrm{strip}}$ corresponds to the sum of the p_{T} of all e/γ assigned to the strip. These parameters have been obtained based on simulated τ-lepton decays.

Table 4.1: Decay modes of a hadronic τ decays. In decays which are via an intermediate meson resonance the resonance and its respective mass are given [7]

Decay Mode	Resonance	Mass [MeV]	Branching fraction [%]
$\tau^{\pm} \to \pi^{\pm}\nu_{\tau}$			11.6
$\tau^{\pm} \to \pi^{\pm}\pi^0\nu_{\tau}$	ρ	770	26.0
$\tau^{\pm} \to \pi^{\pm}\pi^0\pi^0\nu_{\tau}$	a_1	1260	10.8
$\tau^{\pm} \to \pi^{\pm}\pi^{\pm}\pi^{\mp}\nu_{\tau}$	a_1	1260	9.8
$\tau^{\pm} \to \pi^{\pm}\pi^{\pm}\pi^{\mp}\pi^0\nu_{\tau}$			4.8

- The position of the strip is recomputed as p_{T} weighted average of all e/γ assigned to the strip.

For the reconstruction of hadronic τ decays, four decay modes are considered accounting for a total of 63 % of all τ-lepton decays (see table 4.1).

- One charged hadron: reconstructed as decay $\tau^{\pm} \to \pi^{\pm}\nu_{\tau}$.

- One charged hadron and one strip: The invariant mass of the combination of hadron and strip is required to suffice $0.3\,\mathrm{GeV} - \Delta m_{\tau} < m < 1.3\,\mathrm{GeV}\sqrt{p_{\mathrm{T}}/100\,\mathrm{GeV}} + \Delta m_{\tau}$. The mass cut selects $\tau^{\pm} \to \pi^{\pm}\pi^0\nu_{\tau}$ decays with an intermediate ρ meson.

- One charged hadron and two strips: the mass of the combination of the hadrons is required to suffice $0.4\,\mathrm{GeV} - \Delta m_{\tau} < m < 1.2\,\mathrm{GeV}\sqrt{p_{\mathrm{T}}/100\,\mathrm{GeV}} + \Delta m_{\tau}$. Leading to the decay being identified and reconstructed as the decay of a a_1 meson resonance, $\tau^{\pm} \to a_1\nu_{\tau} \to \pi^{\pm}\pi^0\pi^0\nu_{\tau}$.

- Three charged hadrons: the invariant mass of the combination of the hadrons is required to suffice $0.8\,\mathrm{GeV} - \Delta m_{\tau} < m < 1.5\,\mathrm{GeV} + \Delta m_{\tau}$. This leads to the decay kinematics being compatible with the decay of an a_1 meson resonance. The decay is identified as $\tau^{\pm} \to a_1\nu_{\tau} \to \pi^{\pm}\pi^{\pm}\pi^{\mp}\nu_{\tau}$ decay.

The variable Δm_{τ} accounts for the change in mass of the reconstructed τ-lepton due to the strip reconstruction performed before and depends on the energy and momenta of the reconstructed τ-lepton and the strip.

All of the charged hadrons and strips are required to be within a cone with a radius of

$$\Delta R = \begin{cases} 0.1 & \text{if } p_{\mathrm{T}} < 28\,\mathrm{GeV} \\ \frac{2.8\,\mathrm{GeV}}{p_{\mathrm{T}}} & \text{if } 28 < p_{\mathrm{T}} < 56\,\mathrm{GeV} \\ 0.05 & \text{if } p_{\mathrm{T}} > 56\,\mathrm{GeV} \end{cases} \quad . \tag{4.8}$$

After this selection, jets and other leptons can still be misidentified as hadronic τ decays. One way to reduce the contributions of these misidentified objects is to require the τ-lepton candidate to pass an isolation requirement.
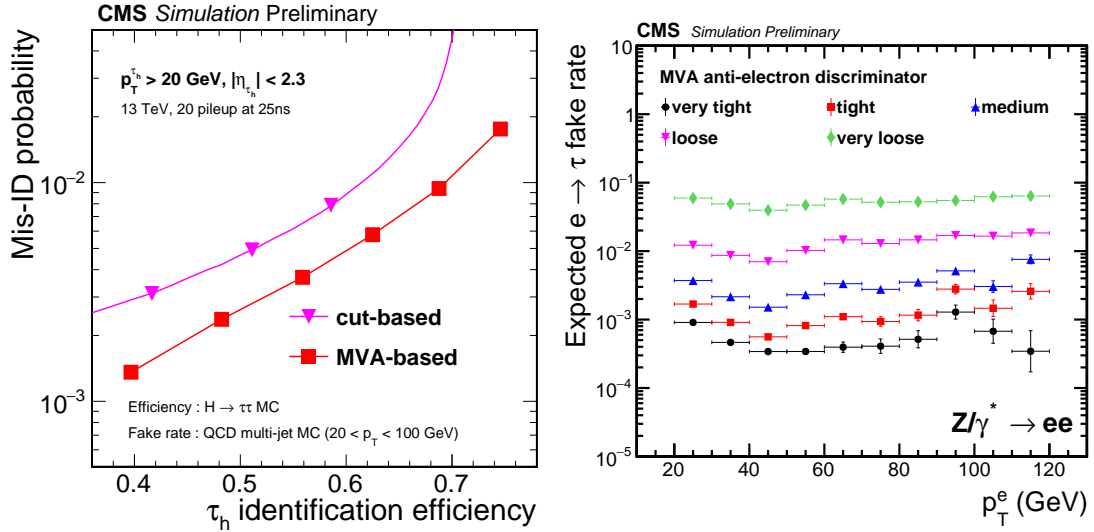
Figure 4.5: *(left)* Performance of the available isolation and identification definitions for hadronically decaying τ-leptons. The MVA based identification offers a better discimination against jets compared to the cut-based particle-flow isolation. For the MVA-based identification the working points very loose, loose, medium, tight, very tight and very very tight are defined with signal efficiencies ranging from 40 to 75 %.
(right) Performance of the MVA based anti-electron discriminator. The rate of electrons misidentified as hadronic τ decays is shown as a function of the transverse momentum of the electron for the five defined working points [59].

For hadronically decaying τ-leptons a modified particle-flow isolation as given in equation 4.5 is used. This approach is modified by requiring a maximum distance from the τ production vertex in the z direction of $d_z < 0.2\,\mathrm{cm}$ for the sum over the charged particles. The contribution from pileup $\Delta\beta$ is estimated by summing over the objects within a cone with radius $\Delta R = 0.8$ and a minimal distance to the τ vertex of $d_z > 0.2\,\mathrm{cm}$. To account for this modification, the factor for the pileup correction is adapted to 0.2 resulting in the following isolation definition

$$I_{\tau_\mathrm{h}} = \sum_{\mathrm{charged,PV}} p_\mathrm{T}(d_z < 0.2\,\mathrm{cm}) + \max\left(0.0, \sum_{\mathrm{neutral}} p_\mathrm{T} - 0.2\sum_{\mathrm{PU}} p_\mathrm{T}(d_z > 0.2\,\mathrm{cm})\right) \quad (4.9)$$

To improve the identification of hadronic τ decays and improve the discrimination against jets a multivariate discriminator is used. This discriminator combines the information from the particle-flow isolation with information about the lifetime of the τ-lepton. Six working points, very loose to very very tight, with τ-lepton identification efficiencies ranging from 75 to 40 % are defined (see figure 4.5).

Additional methods are available to suppress the amount of muons or electrons misidentified as hadronic τ decays. For muons, the discrimination is based on the presence of signals in the muon system in the proximity of the τ-lepton [58]. Two working points are defined for this discriminator

Loose:

    The τ-lepton is vetoed when more than two track segments in the muon system are found within a cone with $\Delta R = 0.3$ centered on the τ-lepton. It is also vetoed when the energy deposition in the ECAL and HCAL identified as originating from the τ-lepton amounts to less than $20\,\%$ of the momentum of the track of the τ-lepton.

Tight:

    Requires the τ-lepton to pass the loose working point and in addition no hits in the two outermost layers of the muon system within a cone of $\Delta R = 0.3$ around the τ-lepton.

For the discrimination against misidentified electrons, an MVA based method is available [59, 60]. This method uses information about the energy deposit in the ECAL and HCAL, observables related to the bremsstrahlung and particle multiplicities to distinguish between hadronic τ decays and electrons. Five working points with misidentification rates for electrons ranging from 0.001 to 0.1 are defined (see figure 4.5).

Missing transverse energy

Due to the topology and symmetry of the LHC setup and the design of the CMS detector each event is expected to be balanced in the transverse plane. This means that the transverse momenta of all particles originating from a given vertex sum up to 0. As not all particles can be detected by the CMS detector, this does not hold true when considering the reconstructed particles.

For this unmeasured momentum the quantity *missing transverse energy* $\not{E}_\mathrm{T}$ is introduced. In the particle-flow approach, it is defined as the negative sum of the momenta of all reconstructed particles

$$\vec{\not{E}}_\mathrm{T} = -\sum_i \vec{p}_\mathrm{T}. \tag{4.10}$$

Corrections to the measured energy of jets are propagated to the calculation of the $\not{E}_\mathrm{T}$ [61].

Search for additional heavy Higgs bosons decaying into two τ-leptons

The $H \to \tau\tau$ decays can be divided into three different decay channels based on the number of hadronically decaying τ-leptons, in the following referred to as hadronic τ-lepton, in the final state. These decay channels have none, one or two hadronic τ-leptons in the final state. For the analysis presented in this thesis only the latter two decay channels are considered. These decay channels sum up to approximately 88 % of all $H \to \tau\tau$ decays (see figure 5.1).
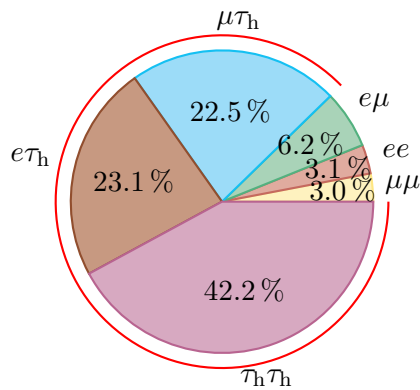
Figure 5.1: Branching ratios of the decay of the di-τ system. The outer red segment indicates the final states which are studied in this analysis [7].

Due to the different background compositions, the decay channels with one hadronic τ-lepton in the final state are further divided into two decay channels with either one electron or one muon in the final state. The former decay channel is referred to as $e\tau_\mathrm{h}$ and the latter one as $\mu\tau_\mathrm{h}$. The fully hadronic final state is referred to as $\tau_\mathrm{h}\tau_\mathrm{h}$.

In section 5.1 the processes contributing to the studied final states are described. In section 5.2 the event selection for the studied final states is given. The kinematic selection is motivated by the requirements of the high level triggers employed during data taking as well as the optimisation of the signal efficiency and background rejection for each of the final states.

The methods used to estimate the contributions from the individual processes are described in section 5.3. For backgrounds involving jets which are misidentified as hadronic

τ decays two independent estimation methods are presented. These two methods are also used to cross-check each other.

The corrections employed in this analysis to improve the description of measured data by the simulation are detailed in section 5.4. The uncertainties associated with these corrections as well as further uncertainties due to the background estimations, experimental setup and theory predictions which are considered in the statistical model are given in section 5.5.

5.1 Considered processes

The final states studied in the analysis presented in this thesis are characterized by one or two candidates for hadronic τ-leptons in the $e\tau_\mathrm{h}$, $\mu\tau_\mathrm{h}$ or $\tau_\mathrm{h}\tau_\mathrm{h}$ decay channel respectively. In the $e\tau_\mathrm{h}$ or $\mu\tau_\mathrm{h}$ decay channels one additional electron or muon candidate is expected.

The processes contributing to these final states can be separated into two classes based on the presence of a genuine hadronic τ decay or another object which is misidentified as a hadronic τ decay. The latter case can further be divided into processes with misidentified leptons or jets.

In this section, the processes contributing to the studied final states and the available simulated events of these processes are given. A summary of the event generators used for generating these processes and the corresponding cross sections is given in table A.3. A general overview of Standard Model processes measured by the CMS collaboration, from which most contribute to the studied final state, can be found in figure 5.2.

5.1.1 Higgs boson production

The Higgs boson production serves two purposes in this analysis. One on side Higgs boson production processes in the context of the MSSM serve as signal hypothesis for this analysis. One the other side the production of the Standard Model Higgs boson serves as an alternative hypothesis against which the MSSM hypothesis is discriminated.

MSSM Higgs boson production

As mentioned in section 2.2.1, in the MSSM the two dominant production processes for a Higgs boson are gluon-fusion and bottom quark associated production (see figure 5.3). These two production processes are important for all three predicted neutral Higgs boson h, H, A. In the following ϕ resembles any of these three Higgs bosons.

The simulated events used for these processes are generated at leading order using the `PYTHIA 8` generator [63]. For the results presented in chapter 6 the production cross sections and branching ratios are provided by the LHC Higgs cross section working group for the different MSSM scenarios [64]. These numbers are calculated taking into account corrections up to next-to-next-to-leading-order. For the calculation `SusHi` [65], `HIGLU` [66], `bbH@nnlo` [67], `HDECAY` [68, 69], `FeynHiggs` [29–34] and `PROPHECY4f` are used.
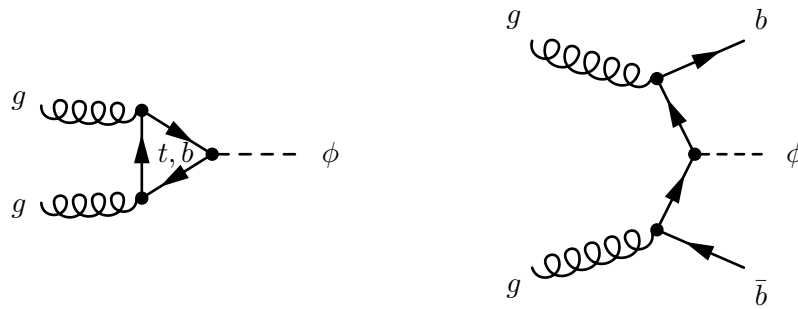
Figure 5.2: Production cross sections of important Standard Model processes measured by the CMS experiment based on pp collision data at center of mass energies of 7, 8 and 13 TeV and their corresponding theory predictions [62]. Many of these processes, as for example the production of W or Z-bosons are important backgrounds for the $H \rightarrow \tau\tau$ searches.

Figure 5.3: Gluon-fusion (left) and bottom quark associated production (right) of a super symmetric Higgs boson ϕ at leading order.
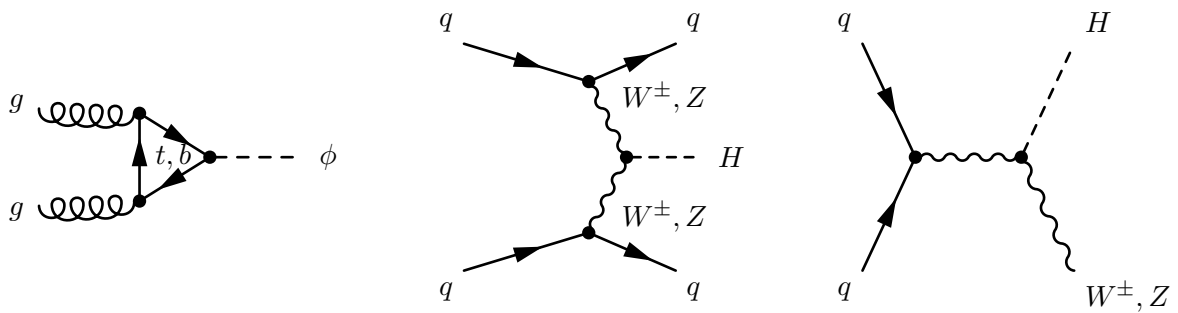
Figure 5.4: Gluon-fusion (left), vector-boson fusion (middle) and vector-boson associated production (right) of a Standard Model Higgs boson in hadron collisions at leading order.

Standard Model Higgs boson production

In the presented searches in the context of the MSSM the Standard Model Higgs boson serves as an alternate hypothesis against which the signal hypotheses are tested (see chapter 6). The three main production mechanisms for the Standard Model Higgs boson are the gluon-fusion, vector-boson fusion and vector-boson associated production (see figure 5.4). These three production processes are generated at next-to-leading-order precision using POWHEG [70].

5.1.2 Background processes

The studied final state includes contributions from further processes in addition to the production of a Higgs boson, either in the MSSM or the SM. In the following section the SM processes contributing to this final state are detailed.

Z boson production

The *Z* boson was discovered at the SPS in 1983 [10, 11] and its mass and decay width measured with high precision at LEP to be $m_Z = 91.187\,\text{GeV}$, $\Gamma_Z = 2.495\,\text{GeV}$ [7].

The major production mechanism at hadron colliders is the Drell-Yan process (see figure 5.5). The *Z* boson decay contributes to the final state studied in this analysis in two ways: via genuine τ-leptons, $Z \to \tau\tau$, as well as misidentified leptons and jets. For the $e\tau_\text{h}$ and $\mu\tau_\text{h}$ decay channels a significant contribution comes from the $Z \to ll$ decay where one of the leptons is misidentified as hadronic τ decay.

In order to sufficiently populate all kinematic regions used in this analysis, dedicated events are simulated where up to four additional partons are required to be present on the hard interaction level. *Z* boson events are generated using MADGRAPH with leading-order precision for the corresponding parton multiplicity.
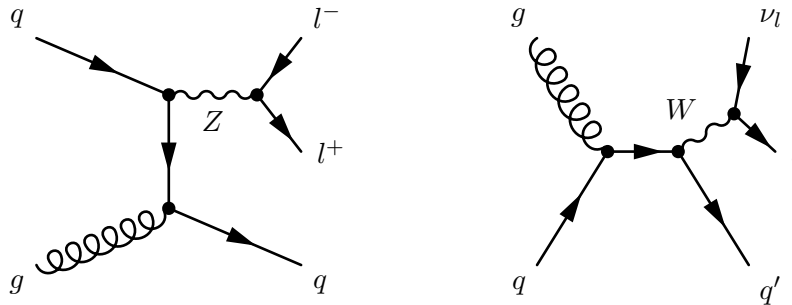
Figure 5.5: Examplary feynman graphs for Drell-Yan *Z* boson production (left) and *W* boson production (right) including one additional quark jet in the final state.

W boson production in association with jets

Like the *Z* boson, the *W* boson was discovered at the SPS in 1983 [8, 9]. It has a mass of 80.385 GeV [7]. As the decay of the *W* boson by itself does not lead to the final state studied in this analysis, the dominant contribution comes from *W* boson production in association with a jet, which is referred to as W+jets (see figure 5.5). In these events, the associated jet is misidentified as a hadronic τ decay. As for the *Z* boson, dedicated events are produced to improve the population of relevant kinematic regions. The events for this background are simulated at leading order in the respective parton multiplicity using the MADGRAPH generator.

Top quark pair production

The top quark was discovered at the Tevatron in 1995 [71, 72] and its mass is measured as 173.21 GeV [7]. The production of a top-anti-top quark pair, further referred to as $t\bar{t}$, is a significant contribution to the studied final states. The production can take place either via gluon-fusion or quark anti-quark annihilation (see figure 5.6). It decays predominantly into two W bosons and two bottom quarks in the final state. Hence the final state closely resembling the final state of a di-τ pair decay. Most specifically due to the bottom quarks it is also a significant background in searches for the bottom quark associated production. $t\bar{t}$ events are generated using the POWHEG generator at next-to-leading-order precision.
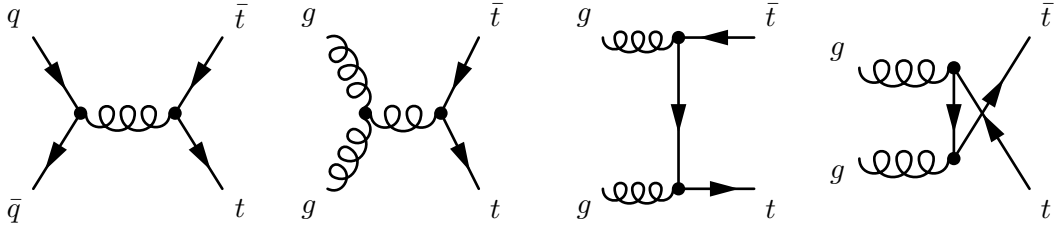
Figure 5.6: Production of a top quark pair at leading order.

Single top quark production

In addition to the $t\bar{t}$ process also the production of a single top quark contributes to the studied final states (see figure 5.7). The corresponding events are generated using the POWHEG generator at next-to-leading-order precision.
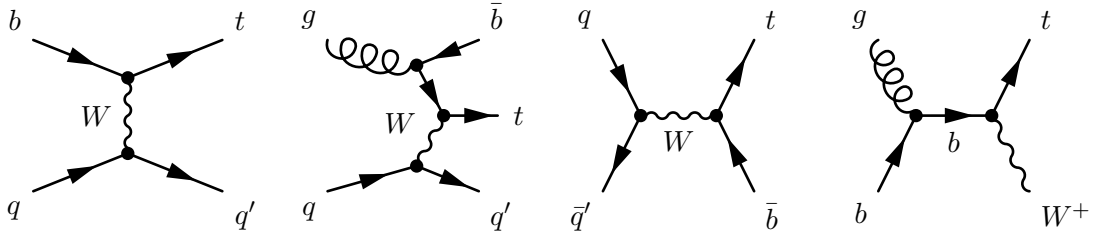
Figure 5.7: Production of a single top quark at leading order.

Di-boson

The Di-boson contribution comprises WW, ZZ and WZ production processes. With decays involving either τ-leptons directly or electrons, muons and jets which can be misidentified as τ decays, these processes contribute to the studied final states. The events are simulated using the AMC@NLO generator [73]. The sum of Single top quark production and Di-boson processes are also referred to as electroweak contributions in the following.

QCD multi-jet

Remaining processes involving more multiple jets in the final state are summed up as QCD multi-jet. These processes feature both jets, which can be misidentified as hadronic τ decays, and non isolated leptons from leptonic decays in the final state. For the QCD multi-jet processes no sufficient coverage with simulated events is available. As a result, methods using observed data to estimate the contribution of QCD multi-jet are employed (see section 5.3).

5.2 Event selection

The selection of relevant events from the large amount of data recorded by the CMS experiment is the first step for any analysis. For this analysis, the selection is split into two parts. In the first step, valid events are selected based on the presence of leptons passing kinematic requirements. Afterwards, two leptons are selected as candidates for the decay of a Higgs boson and additional vetoes are applied to increase the sensitivity of the analysis.

5.2.1 Lepton and di-τ pair selection

The event selection and selection of the di-τ pair which is considered for a given event is based on a tiered approach. The individual selection requirements for each decay channel are given in table 5.1. As a first step valid leptons are selected from all leptons by applying kinematic requirements which are motivated by the high level trigger selection applied later in the process. Electrons are required to have a transverse momentum $p_{\mathrm{T}}^{\mathrm{e}}$ larger than 26 GeV and a pseudorapidity smaller than 2.1. Furthermore, electrons are required to pass identification criteria with an 80 % efficiency [74]. Muons are selected with $p_{\mathrm{T}}^{\mu} > 23$ GeV, $|\eta^{\mu}| < 2.1$ and passing a medium muon identification requirement with about 99 % efficiency [75].

Further requirements are placed on the distance between the leptons and the primary vertex, also referred to as impact parameter. For muons and electrons criteria are applied in the x-y and z plane with $|\mathrm{d}_{\mathrm{xy}}^{\mu,\mathrm{e}}| < 0.045$ cm and $|\mathrm{d}_{\mathrm{z}}^{\mu,\mathrm{e}}| < 0.2$ cm. For hadronic τ-leptons a requirement is imposed only in the z plane with $|\mathrm{d}_{\mathrm{z}}^{\mathrm{Th}}| < 0.2$ cm.

After selecting the valid leptons based on the kinematic cuts all possible combinations of one electron and one hadronic τ-lepton, one muon and one hadronic τ-lepton or

two hadronic τ-leptons are formed for the $e\tau_\mathrm{h}$, $\mu\tau_\mathrm{h}$ and $\tau_\mathrm{h}\tau_\mathrm{h}$ decay channel respectively. Lepton pairs passing a minimum separation requirement between the two leptons of $\Delta R_\mathrm{ll} > 0.5$ are further considered as di-τ pair candidates. Events without any valid di-τ pair candidate are not considered any further for the respective decay channel.

On average approximately 1.5 di-τ pair candidates with a maximum of 7 are found in a single event. In case more than one di-τ pair candidate is found the di-τ pair with the more isolated electron or muon is chosen in the $e\tau_\mathrm{h}$ and $\mu\tau_\mathrm{h}$ decay channel respectively. If this selection is ambiguous the di-τ pair with the higher transverse momentum of the electron or muon is chosen. In case this does not lead to a unique decision the di-τ pair candidate with the more isolated hadronic τ-lepton and as a final criterion, the higher transverse momentum of the hadronic τ-lepton is chosen. For the $\tau_\mathrm{h}\tau_\mathrm{h}$ decay channel the di-τ pair candidate which has the more isolated hadronic τ-lepton with a higher transverse momentum and in case of ambiguities with the more isolated second hadronic τ-lepton is chosen.

The leptons of the chosen di-τ pair are required to pass isolation requirements. For the electron and muon the relative isolation introduced in section 4.4 and for the hadronic τ-leptons the MVA based identification detailed in section 4.4 are used. These isolation and identification variables are shown in figure 5.8. The muon is required to pass $I_\mu^\mathrm{rel} < 0.15$ with the isolation being calculated for a cone of $\Delta R = 0.4$. For electrons an isolation requirement of $I_\mathrm{e}^\mathrm{rel} < 0.1$ with an isolation cone of $\Delta R = 0.3$ is used. In the $e\tau_\mathrm{h}$ and $\mu\tau_\mathrm{h}$ decay channels the hadronic τ-lepton is required to pass a tight identification requirement and in the $\tau_\mathrm{h}\tau_\mathrm{h}$ channel both hadronic τ-leptons need to pass a medium identification requirement.

5.2.2 Additional selection

After a single di-τ pair is selected for each event further selection criteria are applied. To reduce the number of leptons misidentified as hadronic τ-lepton additional discriminators are applied (see section 4.4). For the $\mu\tau_\mathrm{h}$ channel, a natural abundance of muons which can be misidentified as hadronic τ-lepton is present, for example in the Drell-Yan Z boson production with the Z boson decaying into a pair of muons. As a result, the tight anti-muon discriminator working point is chosen. In contrast to this only few events with electrons misidentified as hadronic τ-lepton pass the selection for this channel. Consequently, the very loose working point is chosen for the anti-electron discriminator to uphold an as high as possible efficiency for the hadronic τ-lepton identification. For the $e\tau_\mathrm{h}$ channel the same considerations apply with inverted roles of muon and electron leading to the choice of the tight working point for the anti-electron and the loose working point for the anti-muon discriminator.

In the $\tau_\mathrm{h}\tau_\mathrm{h}$ channel the number of events with electrons or muons misidentified as hadronic τ-lepton is small. Consequently for both the anti-electron and the anti-muon discriminator the working points with the highest efficiency for the identification of genuine hadronic τ-leptons are chosen. These are the very loose and the loose working points respectively.
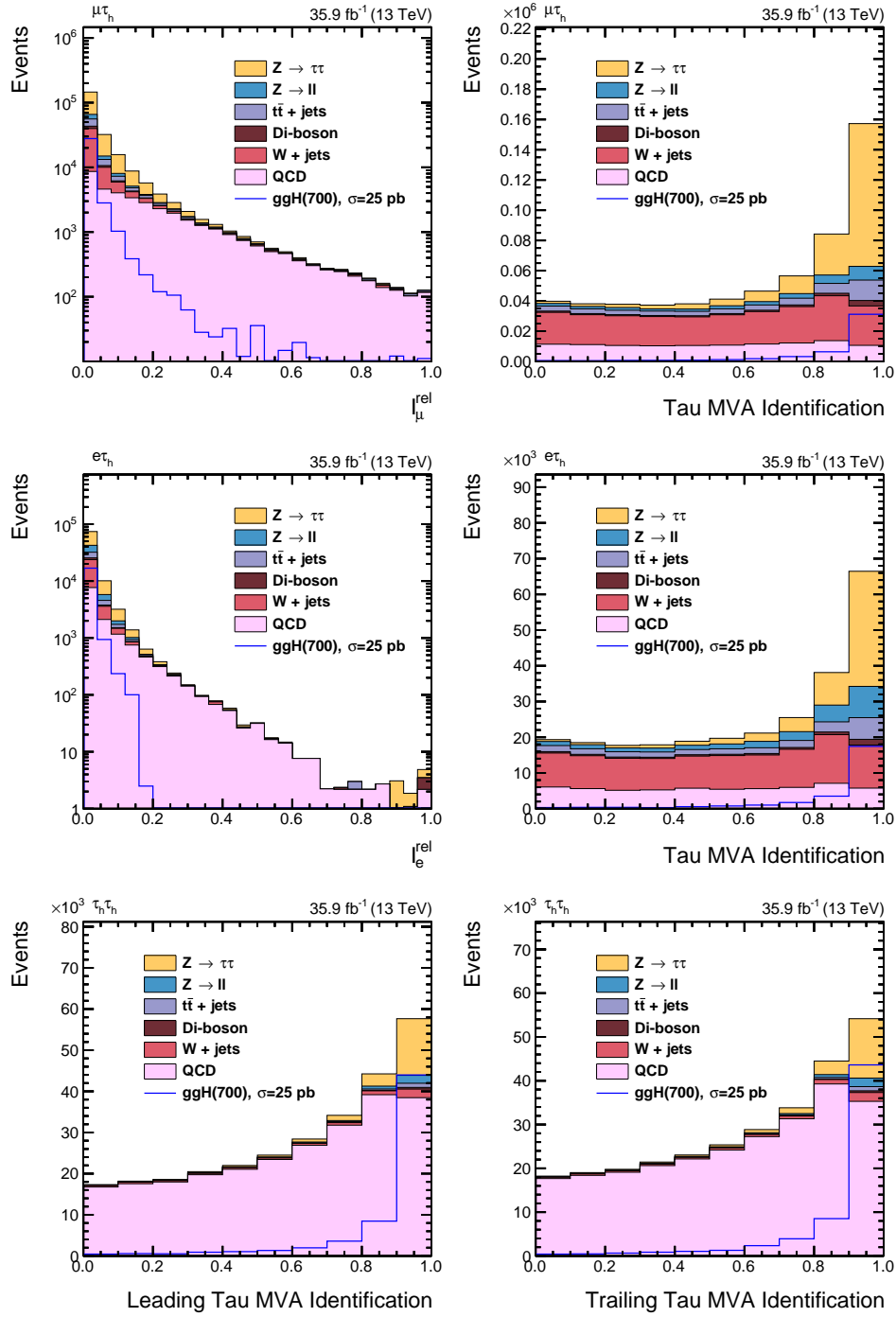
Figure 5.8: Distributions of the relative isolation of the muon (I_μ^{rel}) and MVA based identification of the hadronic τ-lepton in the $\mu\tau_{\mathrm{h}}$ decay channel (top), relative isolation of the electron ($I_{\mathrm{e}}^{\mathrm{rel}}$) and MVA based identification of the hadronic τ-lepton in the $e\tau_{\mathrm{h}}$ decay channel (middle) and MVA based identification of the leading and subleading hadronic τ-lepton in the $\tau_{\mathrm{h}}\tau_{\mathrm{h}}$ decay channel (bottom).

Table 5.1: Event selection in the $e\tau_\text{h}$, $\mu\tau_\text{h}$ and $\tau_\text{h}\tau_\text{h}$ decay channels. After an initial selection of leptons for each event di-τ pair candidates are formed. The leptons in these pairs are required to pass additional isolation requirements and anti-lepton discriminators. Further vetos to suppress background contributions are applied based on the presence of additional leptons in the event. Loose e and μ refer to electrons or muons passing a looser selection requirement compared to the selection given in this table.

	$e\tau_\text{h}$	$\mu\tau_\text{h}$	$\tau_\text{h}\tau_\text{h}$
First lepton	$p_\text{T}^\text{e} > 26\,\text{GeV}$, $\|\eta^e\| < 2.1$	$p_\text{T}^\mu > 23\,\text{GeV}$, $\|\eta^\mu\| < 2.1$	$p_\text{T}^{\tau_\text{h}} > 40\,\text{GeV}$, $\|\eta^{\tau_\text{h}}\| < 2.1$
Second lepton	$p_\text{T}^{\tau_\text{h}} > 30\,\text{GeV}$, $\|\eta^{\tau_\text{h}}\| < 2.3$	$p_\text{T}^{\tau_\text{h}} > 30\,\text{GeV}$, $\|\eta^{\tau_\text{h}}\| < 2.3$	$p_\text{T}^{\tau_\text{h}} > 40\,\text{GeV}$, $\|\eta^{\tau_\text{h}}\| < 2.1$
Lepton identification	80 % ID tight I_{τ_h}	medium ID tight I_{τ_h}	medium I_{τ_h} medium I_{τ_h}
Impact parameter	$\|\text{d}_\text{xy}^\text{e}\| < 0.045\,\text{cm}$ $\|\text{d}_\text{z}^\text{e}\| < 0.2\,\text{cm}$ $\|\text{d}_\text{z}^{\tau_\text{h}}\| < 0.2\,\text{cm}$	$\|\text{d}_\text{xy}^\mu\| < 0.045\,\text{cm}$ $\|\text{d}_\text{z}^\mu\| < 0.2\,\text{cm}$ $\|\text{d}_\text{z}^{\tau_\text{h}}\| < 0.2\,\text{cm}$	$\|\text{d}_\text{z}^{\tau_\text{h}}\| < 0.2\,\text{cm}$ $\|\text{d}_\text{z}^{\tau_\text{h}}\| < 0.2\,\text{cm}$
Trigger (threshold in GeV)	e(25)	μ(22)	τ_h(35)&τ_h(35)
Lepton isolation	$I_\text{e}^\text{rel} < 0.1$ –	$I_\mu^\text{rel} < 0.15$ –	– –
τ anti-lepton discriminator	anti-μ: loose anti-e: tight	anti-μ: tight anti-e: very loose	anti-μ: loose anti-e: very loose
Lepton vetos	No loose e^+e^- pair with $p_\text{T}^\text{e} > 15\,\text{GeV}$	No loose $\mu^+\mu^-$ pair with $p_\text{T}^\mu > 15\,\text{GeV}$	–
	No additional loose e with $p_\text{T}^\text{e} > 10\,\text{GeV}$ and $\|\eta^\text{e}\| < 2.5$		
	No additional loose μ with $p_\text{T}^\mu > 10\,\text{GeV}$ and $\|\eta^\mu\| < 2.4$		

To further suppress the contribution from resonant di-electron or di-muon pair production dedicated event vetos are defined for the $e\tau_\text{h}$ and $\mu\tau_\text{h}$ decay channel. Electrons used for this veto are defined by $p_\text{T}^\text{e} > 15\,\text{GeV}$, $\|\eta^\text{e}\| < 2.5$ and $I_\text{e}^\text{rel} < 0.3$. Furthermore, these electrons are required to pass the identification requirements with 95 % signal efficiency. Muons are defined by $p_\text{T}^\mu > 15\,\text{GeV}$, $\|\eta^\mu\| < 2.4$ and $I_\mu^\text{rel} < 0.3$. Both muons and electrons are required to pass the impact parameter selection defined before. In case a pair of electrons or muons with opposite charge, which are separated by at least $\Delta R = 0.15$, is found for the $e\tau_\text{h}$ or $\mu\tau_\text{h}$ decay channel respectively the event is vetoed.

To exclude a single event being selected for multiple decay channels any event with additional electrons or muons passing a looser selection requirement than the one detailed in section 5.2.1 are vetoed. The selection for these electrons is given as $p_\text{T}^\text{e} > 10\,\text{GeV}$, $\|\eta^\text{e}\| < 2.5$, $I_\text{e}^\text{rel} < 0.3$ and in addition passing a predefined electron identification with an efficiency of 90 % and quality requirements on the reconstructed track of

the electron. Muons are required to pass the medium muon identification and $p_T^\mu >$ 10 GeV, $|\eta^\mu| < 2.4$, $I_\mu^{rel} < 0.3$. Both muons and electrons are also required to pass the impact parameter requirements given before.

As detailed in section 4.2 CMS employs triggering techniques to reduce the rate of stored data and prefilter it for processing. Dedicated high level triggers are available for events including electrons, muons and hadronic τ-leptons. For this analysis in the $e\tau_h$ channel a trigger for a single electron with a triggering threshold of $p_T^e > 25$ GeV, $|\eta^e| < 2.1$ and passing a tight identification is used[1]. In the $\mu\tau_h$ channel, the combination of four triggers each with a triggering threshold of $p_T^\mu > 22$ GeV but differing $|\eta^\mu|$ thresholds and identification requirements is considered[2]. For the $\tau_h\tau_h$ channel two different triggers each for different run periods are used. They both require two τ-leptons with $p_T^{\tau_h} > 35$ GeV and $|\eta^{\tau_h}| < 2.1$ passing a medium identification working point[3]. For each of the events, the electron or muon identified as part of the di-τ pair in the $e\tau_h$ and $\mu\tau_h$ decay channel respectively is required to be matched with the object firing the high level trigger within $\Delta R < 0.5$. In the $\tau_h\tau_h$ decay channel both τ-leptons need to be matched to one object firing the high level trigger each. The matching between reconstructed lepton and the object firing the trigger in this cone has an efficiency of about 99 %.

5.2.3 Categorisation and final discriminator

Events with at least one di-τ pair passing the selection are further categorized to improve the sensitivity of the analysis. For all three decay channels, a common categorisation is applied based on the presence of b-tagged jets in the event. A b-tagged jet is defined as a jet with $p_T^j > 20$ GeV, $|\eta^j| < 2.4$ and passing the medium working point of the CSVv2 b-tagging algorithm described in section 4.4. In the category vetoing events with b-tagged jets, referred to as *no b-tag*, the acceptance for the gluon-gluon fusion and the bottom quark associated production processes is about the same, with the relative fraction of the acceptance for the gluon-gluon fusion production varying between about 60 % for low and 45 % for high Higgs boson masses. The second category, referred to as *b-tag*, is targeting the bottom quark associated production process and requires at least on b-tagged jet in the event. The relative fraction of the acceptance for the bottom quark associated production in this category ranges between 75 % for low and 85 % for high Higgs boson masses.

In the $e\tau_h$ and $\mu\tau_h$ decay channel, a further categorisation is applied based on the transverse mass of the electron or muon and the missing transverse energy $\not{E}_T$. The transverse mass m_T^l for the lepton l is defined as

$$m_T^l = \sqrt{2p_T^l \not{E}_T (1 - \cos\Delta\phi)} \tag{5.1}$$

where $\Delta\phi$ is the difference in the azimuthal angle between the lepton and the vector of the missing transverse momentum $\not{p}_T$.

---

[1] `HLT_Ele25_eta2p1_WPTight_Gsf`

[2] `HLT_IsoMu22` or `HLT_IsoTkMu22` or `HLT_IsoMu22_eta2p1` or `HLT_IsoTkMu22_eta2p1`

[3] `HLT_DoubleMediumIsoPFTau35_Trk1_eta2p1_Reg` or `HLT_DoubleMediumCombinedIsoPFTau35_Trk1_-`
`eta2p1_Reg`

(a) $\mu\tau_h$ **(b)** $e\tau_h$
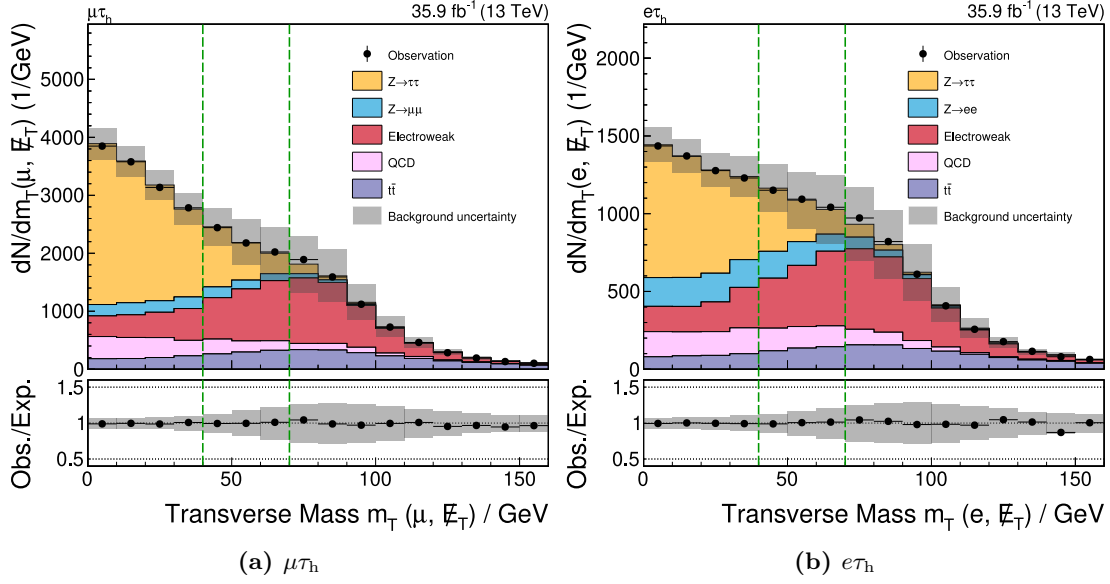
Figure 5.9: Distributions of the transverse mass in the $\mu\tau_h$ (left) and $e\tau_h$ (right) decay channel. The dashed lines indicate the selection requirements for the tight and loose mT categories. The upper cut on the transverse mass significantly reduces the contribution from the W+jets background.

The two considered categories are defined as $m_T < 40\,\text{GeV}$, referred to as *tight*, and $40\,\text{GeV} < m_T < 70\,\text{GeV}$, referred to as *loose mT* (see figure 5.9). The upper cut on the transverse mass is used to suppress a large fraction of the contributions of the W+jets background. The resulting categorisation is given in figure 5.10.

The statistical inference leading to the results presented in chapter 6, is performed using the variable m_T^{tot} as final discriminator. It is defined as the square root of the sum of the squared transverse masses of the leptons in the di-τ pair and the $\not{E}_T$:

$$m_T^{\text{tot}} = \sqrt{m_T^2(l_1, \not{E}_T) + m_T^2(l_1, \not{E}_T) + m_T^2(l_1, l_2)} \tag{5.2}$$

With the transverse mass being defined as

$$m_T(p_1, p_2) = \sqrt{2p_T^1 p_T^2 (1 - \cos\Delta\phi)} \tag{5.3}$$

where $p_T^{1,2}$ are the transverse components of the momenta $p_{1,2}$ and $\Delta\phi$ is the difference in the azimuthal angle between the momenta. For muons and electrons the momentum of the reconstructed objects are used and the definition corresponds to the transverse mass given in equation 5.1. For hadronic τ decays the momentum of the visible decay products of the reconstructed τ-lepton is used. In studies the variable m_T^{tot} was found to give an improved separation between the signal processes and the background contribution from QCD multi-jet events [5].
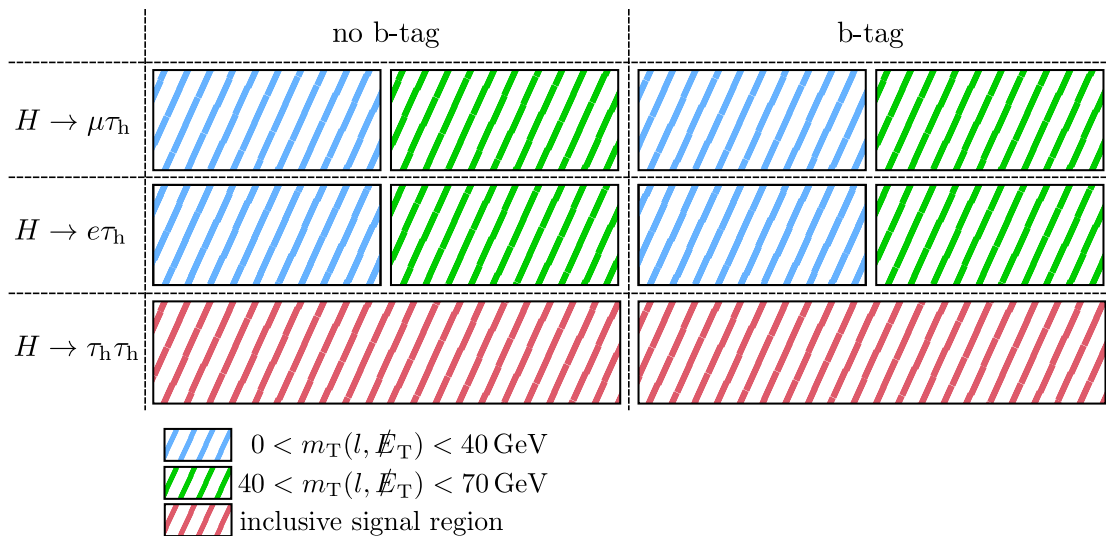
Figure 5.10: Categories used in the analysis. For all decay channels a categorisation based on the presence of b-tagged jets in the event is applied. The semileptonic decay channels $e\tau_{\mathrm{h}}$ and $\mu\tau_{\mathrm{h}}$ are further divided into two categories using the transverse mass m_{T}. For the $\tau_{\mathrm{h}}\tau_{\mathrm{h}}$ decay channel no further catgorisation is applied.

5.3 Background estimation

The simplest method for estimating the contribution of a given background is to estimate it based on simulated events of the given process. However, for a part of the considered processes these simulated events are not available or do not agree well with the measured data. In this analysis simulated events are used for all background processes which have genuine hadronic τ-leptons or leptons misidentified as hadronic τ-leptons in the final state. This applies to the $Z \to \tau\tau$ process and parts of the $Z \to ll$, Di-boson, Single top quark production and $t\bar{t}$ processes.

For the processes having jets misidentified as hadronic τ-leptons in the final state two methods can be used to estimate the contribution. The first method relies on simulated events to describe large extends of these contributions and introduces a data driven approach to estimate the contribution of the W+jets and QCD multi-jet background. In a second approach, the complete contribution from misidentified jets is estimated based on control regions.

As both methods provide independent approaches for estimating the contribution of these backgrounds, the results presented in chapter 6 for the individual approaches are also used as a cross check of the methods.

5.3.1 Simulation based estimation method

W+jets and QCD multi-jet estimation in the $e\tau_\mathrm{h}$ and $\mu\tau_\mathrm{h}$ decay channels

In the $e\tau_\mathrm{h}$ and $\mu\tau_\mathrm{h}$ decay channels the yield and the shape of the W+jets background are estimated independently from each other. The shape is estimated based on simulated events. For estimating the yield two control regions are used (see figure 5.11). These control regions are defined by requiring $m_\mathrm{T}^{\mu,\mathrm{e}} > 70\,\mathrm{GeV}$ and both leptons in the di-τ pair to have opposite or same charge respectively. The contribution of W+jets in these control regions is enriched compared to the signal region and amounts to about 50 %.

To estimate W+jets the other background contributions, which are estimated based on simulated events, are subtracted from the observed data in these regions. The backgrounds which are subtracted are Drell-Yan, Di-boson, Single top quark production and $t\bar{t}$. The resulting difference corresponds to the sum of the contribution from W+jets and QCD multi-jet events. To derive the contribution from W+jets alone additional information on the ratio of QCD multi-jet and W+jets events in the same charge and opposite charge selection is needed. For W+jets this ratio is derived from simulated events, whereas for QCD multi-jet a dedicated measurement detailed in the next section is performed.

The estimate for the W+jets contribution is derived by solving the linear equation given by

$$D_\mathrm{CR,SS} = N_\mathrm{CR,SS}^\mathrm{W} + N_\mathrm{CR,SS}^\mathrm{QCD} \tag{5.4}$$

$$D_\mathrm{CR,OS} = N_\mathrm{CR,OS}^\mathrm{W} + N_\mathrm{CR,OS}^\mathrm{QCD} \tag{5.5}$$

$$= R_\mathrm{OS,SS}^\mathrm{W} \cdot N_\mathrm{CR,SS}^\mathrm{W} + R_\mathrm{OS,SS}^\mathrm{QCD} \cdot N_\mathrm{CR,OS}^\mathrm{QCD} \tag{5.6}$$

where D corresponds to the result of subtracting simulated events from observed data as detailed above, N corresponds to the contribution from a given background and $R_\mathrm{OS,SS}$ correspond to the ratios of the number of opposite charge to same charge events. Quantities denoted with SS are taken from the selection requiring both leptons in the di-τ pair to have the same charge whereas OS refers to requiring opposite charge for both. The resulting estimate for W+jets in the signal region is then given by

$$N_\mathrm{SR}^\mathrm{W} = R_\mathrm{SR,CR}^\mathrm{W} R_\mathrm{OS,SS}^\mathrm{W} \frac{D_\mathrm{CR,OS} - R_\mathrm{OS,SS}^\mathrm{QCD} \cdot D_\mathrm{CR,SS}}{R_\mathrm{OS,SS}^\mathrm{W} - R_\mathrm{OS,SS}^\mathrm{QCD}} \tag{5.7}$$

where $R_\mathrm{SR,CR}^\mathrm{W}$ is the extrapolation factor from the control region to the respective signal region derived from simulated events. The values and statistical uncertainties of the extrapolation factors are given in table 5.2.

In the b-tag category the region defined by $m_\mathrm{T}^{\mu,\mathrm{e}} > 70\,\mathrm{GeV}$ is populated to a large fraction with $t\bar{t}$ events. W+jets events contribute about 4 % in this region (see figure 5.12). In order to define a region with higher fraction of the W+jets contribution the requirement of at least one b-tagged jet in the event is relaxed to requiring at least one jet with $p_\mathrm{T}^\mathrm{j} > 20\,\mathrm{GeV}$ and $|\eta^\mathrm{j}| < 4.7$ which does not need to pass any further b-tagging selections. In this relaxed selection, W+jets events contribute about 45 %. The resulting

Table 5.2: Extrapolation factors for the determination of the W+jets background in the $e\tau_\text{h}$ and $\mu\tau_\text{h}$ decay channel. The factors are determined from simulated events with the selection for the no b-tag (top) and b-tag categories (bottom). The given uncertainties correspond to the statistical uncertainty for these factors and are used to estimate the uncertainty incorporated in the fit (see section 5.5). For the b-tag categories an additional extrapolation factor is determined for a relaxed selection requiring the presence of at least one jet with $p_\text{T}^\text{j} > 20\,\text{GeV}$ and $|\eta^\text{j}| < 4.7$. The resulting correction to the yield of W+jets events is given.

	$e\tau_\text{h}$		$\mu\tau_\text{h}$	
	tight	loose mT	tight	loose mT
$R_\text{OS,SS}^\text{W}$	4.59 ± 0.05		4.50 ± 0.04	
$R_\text{SR,CR}^\text{W}$	0.386 ± 0.005	0.613 ± 0.007	0.443 ± 0.004	0.707 ± 0.006
Correction	0.91 ± 0.02	0.91 ± 0.02	0.94 ± 0.02	0.94 ± 0.01

(a) no b-tag

	$e\tau_\text{h}$		$\mu\tau_\text{h}$	
	tight	loose mT	tight	loose mT
$R_\text{OS,SS}^\text{W}$	4.16 ± 0.06		3.86 ± 0.04	
$R_\text{SR,CR}^\text{W}$	0.371 ± 0.006	0.584 ± 0.009	0.447 ± 0.005	0.685 ± 0.007
$R_\text{relaxed}^\text{W}$	0.027 ± 0.002	0.028 ± 0.002	0.030 ± 0.002	0.025 ± 0.001
Correction	0.82 ± 0.10	0.82 ± 0.08	0.90 ± 0.08	0.90 ± 0.07

(b) b-tag

W+jets estimate is then given by

$$N_\text{SR}^\text{W} = R_\text{relaxed}^\text{W} R_\text{SR,CR}^\text{W} R_\text{OS,SS}^\text{W} \frac{D_\text{CR,OS} - R_\text{OS,SS}^\text{QCD} \cdot D_\text{CR,SS}}{R_\text{OS,SS}^\text{W} - R_\text{OS,SS}^\text{QCD}} \tag{5.8}$$

where $R_\text{relaxed}^\text{W}$ corresponds to the extrapolation factor from the relaxed selection to the selection requiring at least one b-tagged jet which is derived based on simulated events. This extrapolation factor ranges between 0.025 and 0.03 (see table 5.2). The correction for the W+jets yield derived with this method ranges between 0.82 in the $e\tau_\text{h}$ b-tag categories and 0.94 in the $\mu\tau_\text{h}$ no b-tag categories.

The contribution from QCD multi-jet processes is estimated based on a control region requiring both leptons in the di-τ pair to have the same charge. From the data in this control region the contributions from all other backgrounds estimated from simulated events, with the W+jets contribution being corrected as described above, are subtracted. The resulting estimate is scaled by an extrapolation factor from this control region to the signal region $R_\text{OS,SS}^\text{QCD}$. The determination of this factor is detailed in the next section. The final estimate for QCD in the signal region is then given by

$$N_\text{SR}^\text{QCD} = R_\text{OS,SS}^\text{QCD} \cdot D_\text{CR,SS}. \tag{5.9}$$
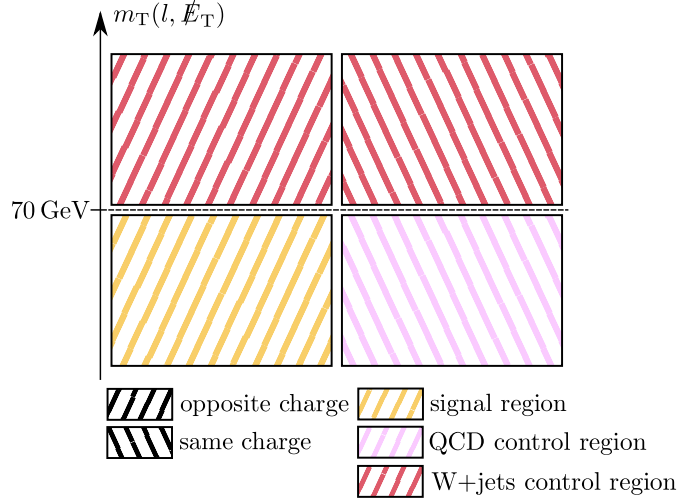
Figure 5.11: Control regions for the estimation of the QCD and W+jets background in the $\mu\tau_\mathrm{h}$ and $e\tau_\mathrm{h}$ decay channels. The control regions are chosen by inverting the opposite charge requirement and the transverse mass requirement

Deriving the QCD multi-jet opposite charge to same charge extrapolation factor

To derive the QCD multi-jet opposite charge to same charge extrapolation factor, control regions which are orthogonal to the signal region in both the opposite and same charge selection are studied. As seen in figure 5.8 requiring a looser relative isolation of the muon (electron) in the $\mu\tau_\mathrm{h}$ ($e\tau_\mathrm{h}$) decay channel enriches the fraction of QCD multi-jet events in the selection.

The extrapolation factor is determined by a fit of the spectrum of the invariant mass of the visible decay products of the di-τ system. For the QCD multi-jet process the initial contribution is derived in a same charge control region with otherwise identical selections by subtracting the other background contributions from the measured data. W+jets, Drell-Yan, Di-boson, Single top quark production and $t\bar{t}$ contributions are estimated from simulated events. The normalisation of the QCD multi-jet contribution relative to the initial normalisation from the same charge region is chosen as parameter of interest. In appendix A.1 the uncertainties considered in the fit are detailed.

The fits are performed in three sideband regions of the relative isolation which are given by $0.15 < I_\mu^\mathrm{rel} < 0.25$, $0.25 < I_\mu^\mathrm{rel} < 0.5$ and $0.15 < I_\mu^\mathrm{rel} < 0.5$ in the $\mu\tau_\mathrm{h}$ and $0.1 < I_\mathrm{e}^\mathrm{rel} < 0.2$, $0.2 < I_\mathrm{e}^\mathrm{rel} < 0.5$ and $0.1 < I_\mathrm{e}^\mathrm{rel} < 0.5$ in the $e\tau_\mathrm{h}$ decay channel. In figure 5.13 the pre- and postfit distributions are given for the b-tag category in the $\mu\tau_\mathrm{h}$ and the no b-tag category in the $e\tau_\mathrm{h}$ decay channel. The corresponding figures for the other regions are given in appendix A.1. The resulting extrapolation factors are given in table 5.3.

For the inclusive and no b-tag selection the extrapolation factors derived in the sidebands with $0.15 < I_\mu^\mathrm{rel} < 0.25$ and $0.1 < I_\mathrm{e}^\mathrm{rel} < 0.2$ are used for the QCD estimation. Due to the low acceptance for passing the b-tagged jet veto and this tight isolation re-
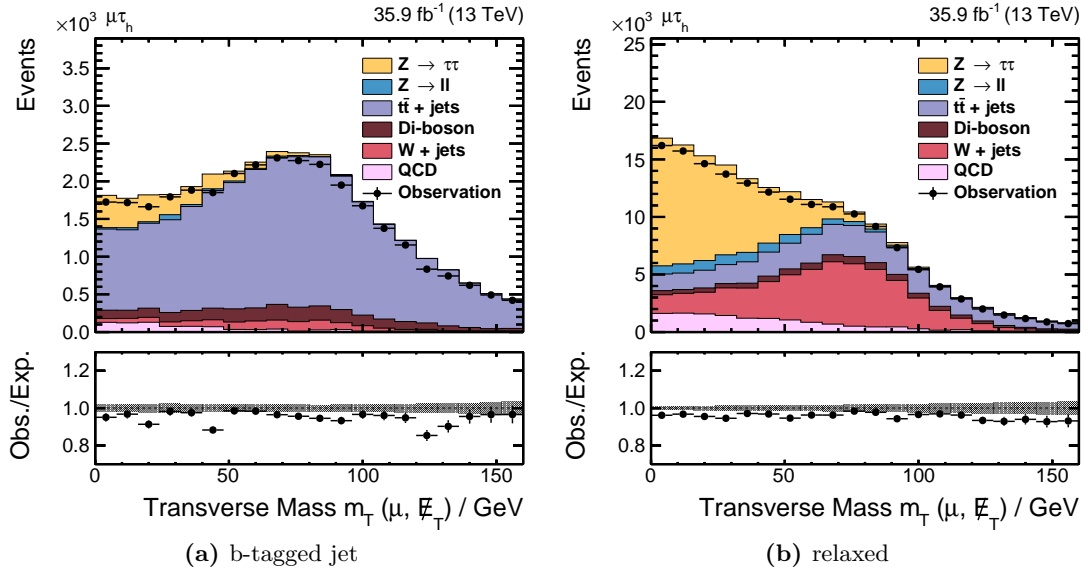
Figure 5.12: Distributions of the transverse mass in $\mu\tau_\mathrm{h}$ decay channel requiring at least one b-tagged jet (left) or at least one jet with $p_\mathrm{T}^\mathrm{j} > 20\,\mathrm{GeV}$ and $|\eta^\mathrm{j}| < 4.7$ (right) in the event. For this figure the contribution of W+jets events is estimated based on simulated events. In the selection with at least one b-tagged jet the region with $m_\mathrm{T} > 70\,\mathrm{GeV}$ is dominated by $t\bar{t}$ events. Requiring the relaxed selection increases the fraction of W+jets in this region from about $4\,\%$ to about $45\,\%$.

quirement, the extrapolation factors derived in the $0.15 < I_\mu^\mathrm{rel} < 0.5$ and $0.1 < I_\mathrm{e}^\mathrm{rel} < 0.5$ regions are chosen for the b-tag category instead. Based on the results from the other sidebands an uncertainty on this extrapolation factor is derived which is used for the signal extraction (see section 5.5).

QCD multi-jet estimation in the $\tau_\mathrm{h}\tau_\mathrm{h}$ channel

In the $\tau_\mathrm{h}\tau_\mathrm{h}$ channel the W+jets background has only a small contribution compared to the QCD multi-jet background. Consequently, it is estimated based on simulated events without further data-driven corrections.

The estimation of the QCD multi-jet background is based on a control region requiring the trailing τ-lepton to pass a very loose and fail a medium identification requirement (see figure 5.15). This region consists to about $94\,\%$ of QCD multi-jet events. The QCD multi-jet contribution is estimated by subtracting the predicted W+jets, Drell-Yan, Di-boson, Single top quark production and $t\bar{t}$ contributions from the measured data in this region (see figure 5.14).

A scale factor $R_\mathrm{anti\text{-}iso,SR}$ from the loosely isolated to the signal region is derived in the regions requiring the two τ-lepton candidates to have the same charge. The final

(a) $\mu\tau_\mathrm{h}$, Prefit

(b) $\mu\tau_\mathrm{h}$, Postfit

(c) $e\tau_\mathrm{h}$, Prefit

(d) $e\tau_\mathrm{h}$, Postfit
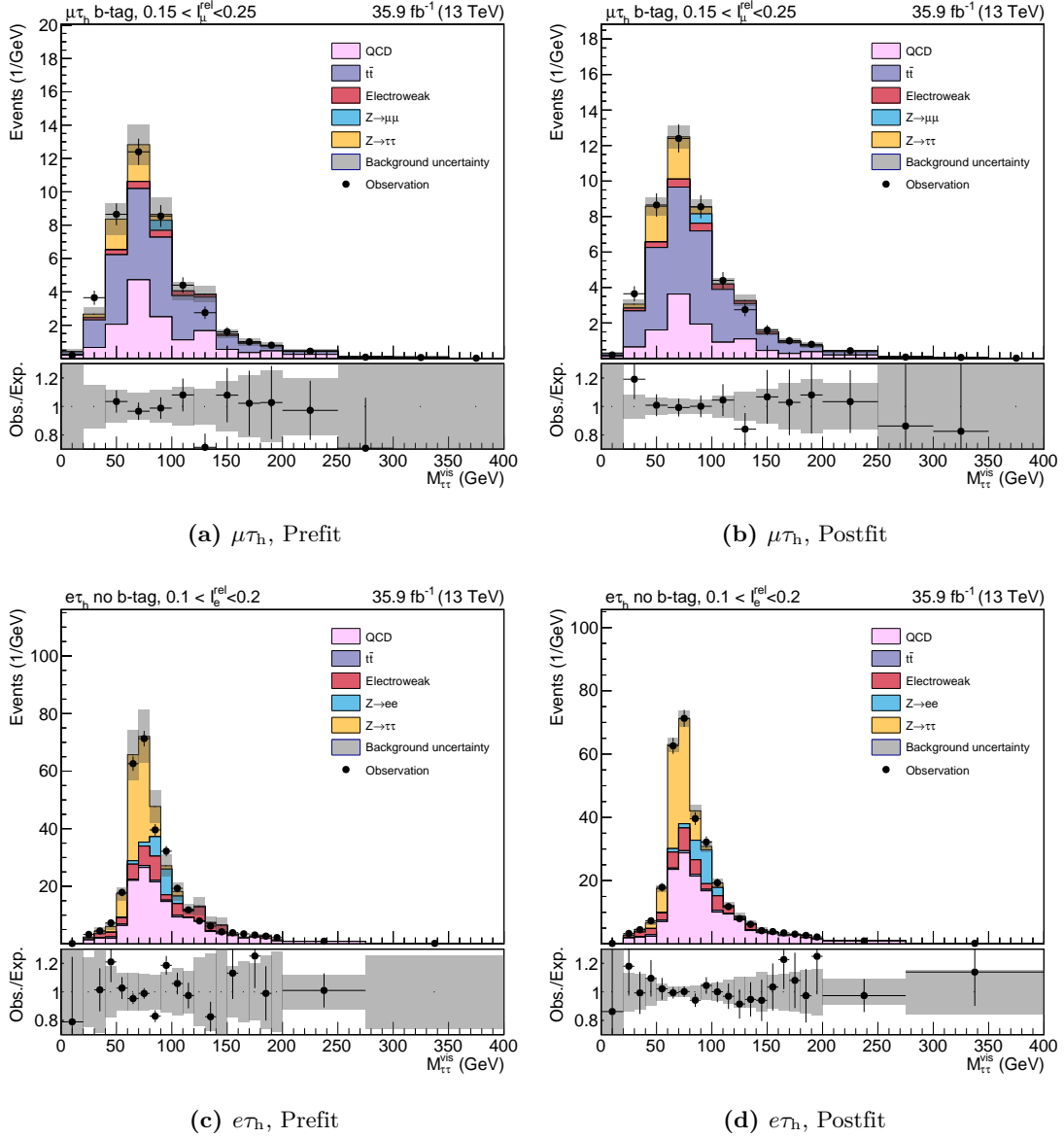
Figure 5.13: Distributions of the invariant mass of the τ-lepton decay products in the opposite charge regions with relaxed relative isolation in the $\mu\tau_\mathrm{h}$ (top) and $e\tau_\mathrm{h}$ decay channels (bottom). The distributions are shown for a selection requiring a relative isolation of $0.15 < I_\mu^\mathrm{rel} < 0.25$ in the $\mu\tau_\mathrm{h}$ decay channel requiring at least one b-tagged jet. For the $e\tau_\mathrm{h}$ decay channel the isolation sideband region defined by $0.1 < I_\mathrm{e}^\mathrm{rel} < 0.2$ and vetoing events with b-tagged jets is shown. The distributions are shown prior to (left) and after (right) performing the fit of the QCD contribution.

Table 5.3: Extrapolation factors from the same charge to the opposite charge for the QCD process in the $\mu\tau_\mathrm{h}$ (top) and $e\tau_\mathrm{h}$ (bottom) decay channels. Dedicated extrapolation factors are determined using three different selections of I_μ^rel ($I_\mathrm{e}^\mathrm{rel}$) and for selections with different requirements on the number of b-tagged jets.

	$0.15 < I_\mu^\mathrm{rel} < 0.25$	$0.25 < I_\mu^\mathrm{rel} < 0.5$	$0.15 < I_\mu^\mathrm{rel} < 0.5$
inclusive	1.10 ± 0.05	1.17 ± 0.04	1.13 ± 0.03
no b-tag	1.10 ± 0.05	1.17 ± 0.04	1.13 ± 0.03
b-tag	0.77 ± 0.26	1.17 ± 0.35	1.05 ± 0.15

(a) $\mu\tau_\mathrm{h}$

	$0.1 < I_\mathrm{e}^\mathrm{rel} < 0.2$	$0.2 < I_\mathrm{e}^\mathrm{rel} < 0.5$	$0.1 < I_\mathrm{e}^\mathrm{rel} < 0.5$
inclusive	1.09 ± 0.09	0.97 ± 0.06	1.03 ± 0.06
no b-tag	1.07 ± 0.08	0.94 ± 0.06	1.00 ± 0.06
b-tag	1.17 ± 0.65	1.28 ± 0.27	1.19 ± 0.31

(b) $e\tau_\mathrm{h}$

estimate for the QCD process is then given as:

$$N_\mathrm{SR}^\mathrm{QCD} = D_\mathrm{anti\text{-}iso} R_\mathrm{anti\text{-}iso,SR} \tag{5.10}$$

$$R_\mathrm{anti\text{-}iso,SR} = \frac{D_\mathrm{SR,SS}}{D_\mathrm{anti\text{-}iso,SS}} \tag{5.11}$$

where D refers to the simulated events subtracted from the observed data in a given region.

It was found that a constant scale factor is not sufficient to describe the QCD multi-jet contribution in the signal region. To account for this the scale factor $R_\mathrm{anti-iso,SR}$ is derived in bins of the transverse momentum of the leading hadronic τ-lepton $p_\mathrm{T}^{\tau_\mathrm{h},1}$ and the invariant mass of the visible decay products of the di-τ pair $m_{\tau\tau}^\mathrm{vis}$ (see figure 5.16). The binning used to derive these extrapolation factors is chosen to reflect the available statistic in the control region. This is done in order to minimize the impact of statistical uncertainties on these factors.

5.3.2 Fake factor method

The fake factor method is an alternative approach to estimate the contribution of all backgrounds where jets are misidentified as hadronic τ-leptons. This includes both W+jets and QCD multi-jet events as well as parts of the Drell-Yan, $t\bar{t}$ and Di-boson backgrounds.

The basis of the fake factor method is to estimate extrapolation factors from a control region with a looser identification requirement on the hadronic τ-lepton (*aSR*), which has an enriched contribution from jets misidentified as hadronic τ-leptons, to the signal
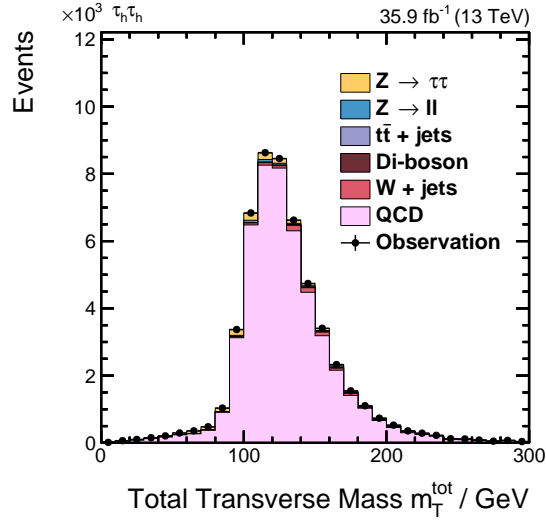
Figure 5.14: Distribution of the total transverse mass in the control region with relaxed identification requirement for the trailing hadronic τ-lepton. The control regions consist to about 94 % of QCD multi-jet events. The estimate for the QCD contribution is derived by subtracting the remaining background contributions from the observed data.

regions. These extrapolation factors are referred to as fake factors. The identification requirements for the aSR in the $e\tau_h$, $\mu\tau_h$ and $\tau_h\tau_h$ decay channels are given as

- $e\tau_h$ and $\mu\tau_h$: hadronic τ-lepton failing the tight but passing the very loose identification working point.

- $\tau_h\tau_h$: the leading hadronic τ-lepton passing the same identification working points as for the signal region, which is chosen as the medium identification working point. The trailing hadronic τ-lepton failing the medium but pass the very loose identification working point. All di-τ pairs are considered twice with switched isolation requirements for both τ-leptons. The result using both permutations is weighted with a factor of 0.5 each.

As the fake factors differ for individual background contributions, independent fake factors FF_i are derived for the W+jets, $t\bar{t}$ and QCD multi-jet process. Due to the similar properties of Drell-Yan and W+jets events with a jet misidentified as hadronic τ-lepton the W+jets fake factor is taken as estimate for the Drell-Yan fake factor. The combined fake factor FF is then obtained by weighting the individual fake factors by their respective expected fraction f_i in the aSR.

$$FF = \sum_i f_i \cdot FF_i. \tag{5.12}$$

The fractions f_i are determined based on simulated events for the W+jets, Drell-Yan and $t\bar{t}$ process. The fraction for QCD multi-jet is chosen such that the fractions sum up to 1.
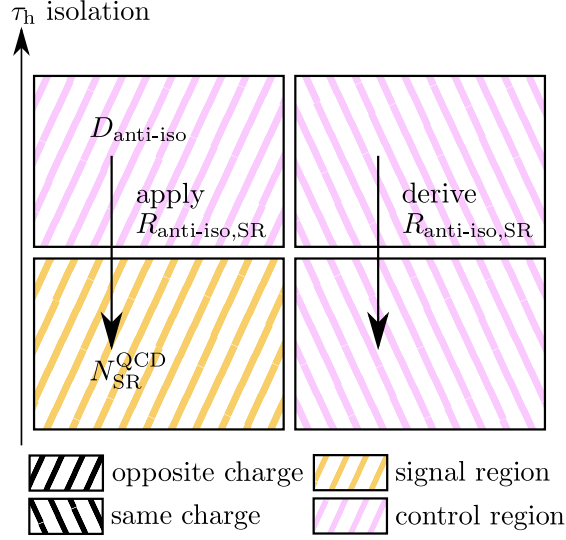
Figure 5.15: Estimation method for the QCD multi-jet background in the $\tau_h\tau_h$ channel. The control regions are chosen by inverting the opposite charge requirement and relaxing the identification requirement for the trailing hadronic τ-lepton

The principle of deriving the fake factors is similar for each background contribution. As a first step, a control region which is dominated by the desired background is defined. This control region is split into two by requiring for one the identification of the hadronic τ-lepton as defined for the signal region and on the other hand the identification as defined for the aSR region. A first estimate of the fake factors $\mathrm{FF}_{\mathrm{raw}}$ is derived by determining the fraction of events where the hadronic τ-lepton passes the nominal identification requirement of the signal region $N_{\mathrm{isoSR}}^{\mathrm{CR}}$ to the number of events where it passes the identification of the aSR region $N_{\mathrm{aSR}}^{\mathrm{CR}}$

$$\mathrm{FF}_{\mathrm{raw}} = \frac{N_{\mathrm{isoSR}}^{\mathrm{CR}}}{N_{\mathrm{aSR}}^{\mathrm{CR}}}. \tag{5.13}$$

The number of events referred to as N is given as the number of observed events minus the number of expected events for the remaining processes. When the fake factors are derived from simulated events, N refers to the plain number of events predicted in the simulation. This is the case for the $t\bar{t}$ fake factors. The initial determination of the fake factors is performed differentially in bins of the transverse momentum of the hadronic τ-lepton. To further refine the raw fake factors additional corrections detailed below are applied as detailed in the following. The fake factors including the corrections depend on the p_{T} and the reconstructed decay mode of the hadronic τ-lepton, the number of jets in the event, m_{vis}, m_{T}^{l} and the relative isolation of the lepton for the $e\tau_h$ and $\mu\tau_h$ decay channel. For the $\tau_h\tau_h$ decay channel, the fake factors depend on the p_{T} of both τ-leptons, the reconstructed decay mode of the misidentified τ-lepton, the number of jets, m_{vis} and $m_{\mathrm{T}}^{\mathrm{tot}}$.
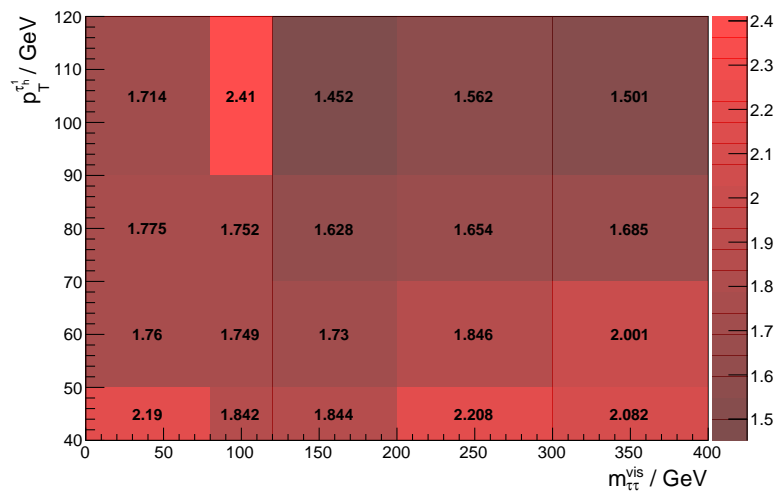
(a) no b-tag
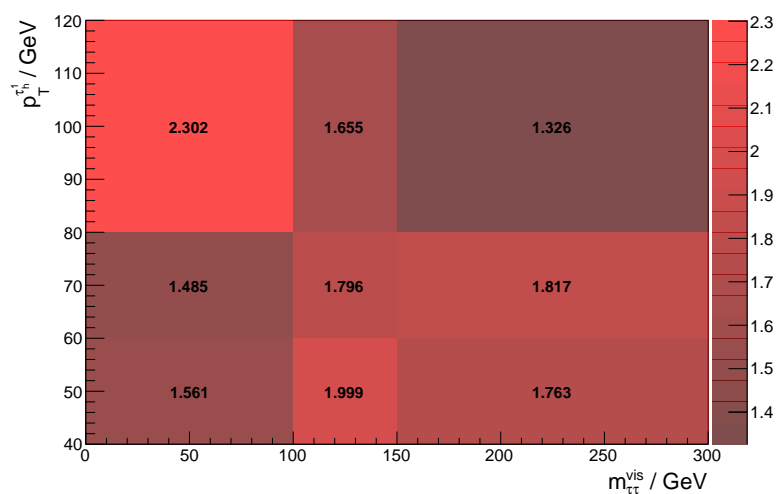
(b) b-tag

Figure 5.16: Extrapolation factors from the anti-isolated to the signal region for the QCD multi-jet contribution in the $\tau_h\tau_h$ decay channel. The extrapolation factors are determined in bins of the transverse momentum of the leading hadronic τ-lepton $p_T^{\tau_h^1}$ and the invariant mass of the visible decay products of the di-τ pair $m_{\tau\tau}^{vis}$.

For the $e\tau_\mathrm{h}$ and $\mu\tau_\mathrm{h}$ channel, fake factors are derived for the W+jets, QCD multi-jet and $t\bar{t}$ processes. For the $\tau_\mathrm{h}\tau_\mathrm{h}$ channel, QCD multi-jet is by far the leading background contribution. Consequently, fake factors are solely derived for the QCD multi-jet background contribution and differences due to the contribution of other backgrounds are introduced by uncertainties. In the following the regions and corrections used to derive these fake factors are given.

W+jets fake factors in the $e\tau_\mathrm{h}$ and $\mu\tau_\mathrm{h}$ decay channel

The control region for the W+jets fake factor method is defined as the signal region but requiring a transverse mass of $m_\mathrm{T} > 70\,\mathrm{GeV}$ and no b-tagged jet in the event. The raw fake factor estimate is corrected for two effects. First, a non-closure correction as a function of m_vis is applied. This correction is determined by applying the raw fake factors in the control region and comparing it to the observed distribution. A smoothing using a Gaussian kernel is applied to the ratio of these two distributions which is then used as correction.

A second correction is derived for the transverse mass spectrum. For this purpose, fake factors and non-closure corrections are derived based on simulated W+jets events rather than observed data. These fake factors are then applied to the simulated W+jets events and the spectrum of the transverse mass is compared to that of the simulated W+jets events. After applying a smoothing the ratio of both is used as a correction for the W+jets fake factors.

QCD multi-jet fake factors in the $e\tau_\mathrm{h}$ and $\mu\tau_\mathrm{h}$ decay channel

QCD multi-jet fake factors are derived in a control region requiring both di-τ pair constituents to have the same charge. In addition, the relative isolation of the muon or electron is required to suffice $0.05 < I_{\mu,\mathrm{e}}^\mathrm{rel} < 0.15$ and the transverse mass is required to be smaller than $40\,\mathrm{GeV}$ to further increase the purity of the control region.

Just like for the W+jets fake factors first a non-closure correction as a function of m_vis is derived in this control region. An additional correction is derived based on the isolation of the electron or muon. To derive this correction the background is estimated using the corrected fake factors in the control region as defined before excluding the requirement on the lepton isolation. The resulting distribution is compared to the observed data in the control region as a function of the lepton isolation. As the contamination of other backgrounds extends up to $50\,\%$ depending on the lepton isolation, an estimation of these backgrounds based on simulated events is subtracted from the observation before computing the ratio. The smoothed ratio is applied as a correction to the fake factors. The contamination by other backgrounds in the control region is further taken into account in the uncertainty model for the fake factor method (see section 5.5).

A final correction for the QCD multi-jet fake factors is derived for the same to opposite charge extrapolation. For this correction, the fake factors are derived in regions requiring the same charge for the di-τ pair constituents and passing $0.15 < I_\mu^\mathrm{rel} < 0.25$ or $0.1 < I_\mathrm{e}^\mathrm{rel} < 0.2$ for the $\mu\tau_\mathrm{h}$ and $e\tau_\mathrm{h}$ channel respectively. A non closure correction as described before is applied to these fake factors. The resulting fake factors are then applied

in the region requiring an opposite charge to derive an estimate for the background in this region. This estimate is compared to the observed data as a function of the visible mass and the smoothed ratio of both is applied as a correction.

QCD multi-jet fake factors in $\tau_\mathrm{h}\tau_\mathrm{h}$

In the $\tau_\mathrm{h}\tau_\mathrm{h}$ channel the control region for deriving the QCD multi-jet fake factors is defined by requiring the same charge for both di-τ pair constituents. The non closure correction is derived and applied as detailed before. A further correction is derived as a function of the transverse momentum of the trailing hadronic τ-lepton. The correction is determined as the smoothed ratio of the observed data and the estimate of the background determined using the raw fake factors in the control region. The opposite to same charge extrapolation correction is derived as a function of m_vis as for the $e\tau_\mathrm{h}$ and $\mu\tau_\mathrm{h}$ case but applying the aSR identification requirement.

Fake factors for the $t\bar{t}$ contribution in the $e\tau_\mathrm{h}$ and $\mu\tau_\mathrm{h}$ decay channel

As no suitable control region with similar properties as the signal region was found for the $t\bar{t}$ background a different approach is used. Fake factors for the $t\bar{t}$ background are derived based on simulated $t\bar{t}$ events and are then corrected based on a $t\bar{t}$ control region. Due to the generally smaller contribution of $t\bar{t}$ events compared to that of W+jets and QCD multi-jet events, this is taken as a sufficient estimation and differences are accounted for by assigning corresponding uncertainties.

The $t\bar{t}$ control region for deriving the correction is chosen as having the same selection as the signal region detailed in section 5.2 with the modification of requiring at least one b-tagged jet in the event and not vetoing events with additional leptons but instead requiring at least one isolated muon and one isolated electron in the event. In this region fake factors are derived for observed data and simulated $t\bar{t}$ events and the ratio of both is taken as correction for the initial fake factors. This correction was found to be independent of the transverse momentum within uncertainties and only depends on the decay mode of the hadronic τ-lepton. The resulting corrections c for each decay mode are given by

$$c_{\mu\tau_\mathrm{h}}^{1\pi^\pm} = 0.81 \qquad c_{\mu\tau_\mathrm{h}}^{3\pi^\pm} = 0.74$$
$$c_{e\tau_\mathrm{h}}^{1\pi^\pm} = 0.68 \qquad c_{e\tau_\mathrm{h}}^{3\pi^\pm} = 0.82$$

An additional non closure correction is derived by comparing the $t\bar{t}$ events estimated by applying the fake factors to the simulated $t\bar{t}$ events passing the aSR identification to the simulated $t\bar{t}$ events passing the signal region identification. The ratio of both is smoothed and applied as a correction.

5.4 Corrections for simulated events

Although extensive time is spent on developing and refining the simulation of events recorded with the CMS detector, differences between the simulated events and observed data remain. To minimize these differences corrections are applied to the simulated events.

Pile-up corrections

The simulated events for signal and background processes are usually produced prior to or at the same time as the data taking to allow analysts to prepare for the recorded data. However, this comes with the disadvantage that one has to choose pile-up conditions for this simulation before knowing the actual conditions during data taking. Ideally, these pile-up conditions are chosen to resemble the conditions at data-taking as close as possible. Nonetheless, especially when studying data from extensive data taking periods, such as the data taken during the whole year of 2016, differences remain. These differences are for example driven by changing machine conditions allowing the experiments to collect more data than anticipated before. To correct for these differences a reweighting technique is used. This technique is based on the pile-up profile used for the simulated events and the pile-up profile measured in data.

Corrections of the lepton triggering, isolation and identification efficiencies

The efficiency ϵ for a lepton, in this case electron or muon, to pass the requirements for triggering, isolation or the identification differ in observed data and simulated events. To account for this a correction given by $\epsilon_{\text{data}}/\epsilon_{\text{sim}}$ is applied. These corrections are determined in bins of the p_{T} and $|\eta|$ of the lepton (see figure 5.17). In addition, isolation and triggering corrections are determined for three different isolation requirements used for the measurements detailed in section 5.3.1. The efficiencies for observed data and simulated events are determined in a factorized approach. This means that for the measurement of the efficiencies of the isolation requirement the leptons are required to have passed the identification requirement. Likewise, for the measurement of the triggering efficiency the leptons are required to pass both the isolation and identification requirement. The corrections range up to 5 % for muons and 10 % for electrons. The largest corrections, albeit with the largest uncertainties, are found for the triggering in the phase space with large p_{T} and $|\eta|$.

The measurement of the efficiencies is performed using a tag-and-probe approach which is briefly described in the following. Further details on this measurement can be found in [20]. The tag-and-probe measurement is performed for candidates of Z boson decays. This means that each event is required to contain at least two electrons or muons and the invariant mass of both needs to be in a window around the Z boson mass. The advantage of this is to have little contamination from processes other than $Z \rightarrow ll$ in the selection.

For the purpose of this measurement one of the leptons, referred to as *tag*, is required to pass the full set of selection requirements. The second lepton, referred to as *probe*,
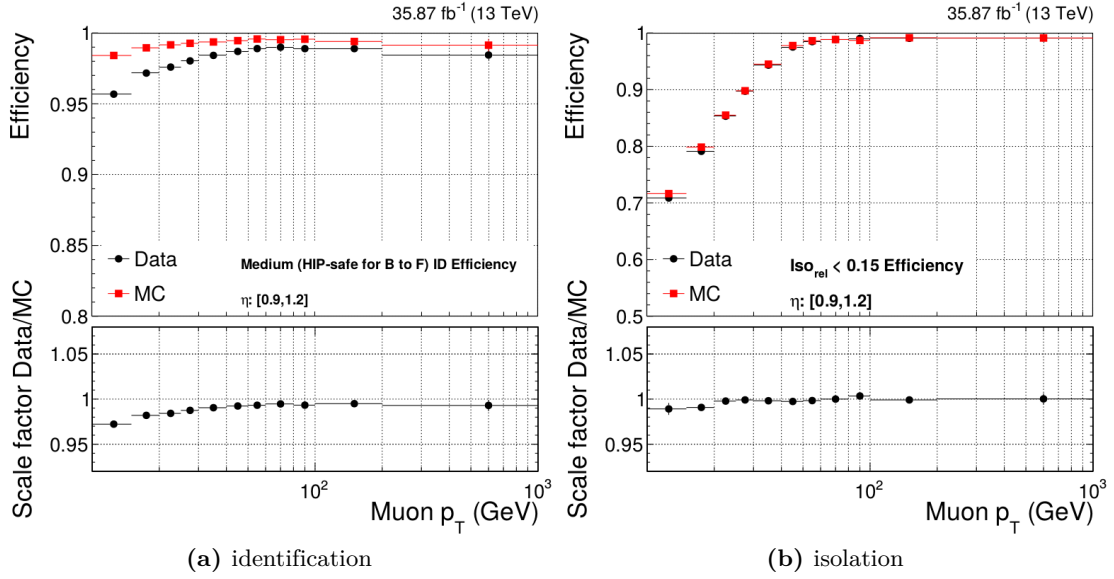
Figure 5.17: Results of the measurement of the efficiency for the identification (left) and isolation (right) for muons with $0.9 < |\eta^\mu| < 1.2$ as a function of p_T^μ using the tag-and-probe method. The ratio given in the lower part is applied as a correction [20].

is required to pass all selections up to the selection for which the efficiency is being determined for. Based on whether the probe lepton passes or fails the requirement on the property which is being tested the *pass* and *fail* region respectively are populated. The extraction of the efficiency is then performed using a maximum likelihood fit of the invariant mass spectrum in both regions, where the pass region is scaled by ϵ and the fail region is scaled by $1 - \epsilon$.

Corrections of the identification and triggering of hadronic τ-leptons

For hadronic τ-leptons a discrepancy between observed data and simulated events is observed for the triggering and identification requirement. The correction for the identification definition differs for the individual working points. For the tight working point used in the $e\tau_h$ and $\mu\tau_h$ decay channel the correction is 0.95 and for the medium working point used in the $\tau_h\tau_h$ decay channel 0.97 [59].

For the trigger used in the $\tau_h\tau_h$ decay channels correction factors are derived depending on the transverse momentum and pseudorapidity of the two hadronic τ-leptons. Dedicated corrections are available for genuine hadronic τ-leptons and objects misidentified as τ-leptons [76].

Table 5.4: Energy corrections for reconstructed hadronic τ-leptons. Depending on the original particle which is identified as a hadronic τ-lepton dedicated corrections are applied [59, 76].

decay mode	genuine hadronic τ-lepton	electron misidentified as hadronic τ-lepton
$\tau^\pm \to \pi^\pm \nu_\tau$	$-0.5\,\%$	$2.4\,\%$
$\tau^\pm \to \pi^\pm \pi^0 \nu_\tau$	$1.1\,\%$	$7.6\,\%$
$\tau^\pm \to \pi^\pm \pi^\pm \pi^\mp \nu_\tau$	$0.6\,\%$	$-$

Corrections of the measured energy of genuine hadronic τ-leptons and electrons misidentified as hadronic τ-leptons

The reconstruction of the energy of hadronic τ-leptons depends on a precise description of the CMS detector, especially the tracking and the electromagnetic calorimeter. Due to differences between the simulation and the real detector, differences in the reconstructed energy of hadronic τ-leptons in simulated events and observed data are found. To correct for these misdescriptions a shift of the energy of the respective hadronic τ-lepton is applied. This correction was found be to depend on the reconstructed decay mode of the hadronic τ-lepton as well as the object which was identified as hadronic τ-lepton. It was further found to be independent of the transverse momentum.

In the case of genuine hadronic τ-leptons the correction was found to range between $-0.5\,\%$ for the case of a reconstructed decay into a single charged pion and $1.1\,\%$ for a reconstructed decay into a single charged pion and at least one neutral pion [59]. For electrons misidentified as hadronic τ-leptons the correction was found to be between $2.4\,\%$ and $7.6\,\%$ for decays into single charged pions and single charged pions plus additional neutral pions [76]. For electrons being misidentified as a τ-lepton decay into three charged pions as well as for muons being misidentified as hadronic τ-leptons no significant energy shift was found. An overview of the corrections applied is given in table 5.4.

Anti-lepton discriminator scale factors

The $Z \to ll$ component with a lepton being misidentified as a hadronic τ-lepton is largely reduced by applying anti-muon and anti-electron discriminators. The description of these discriminators in simulated events is improved by applying a scale factor depending on $|\eta|$ of the hadronic τ-lepton candidate (see table 5.5) [59, 60].

B-tagging corrections

The CSVv2 b-tagging algorithm used in this analysis relies on the correct modelling of several variables, such as the direction and impact parameter of tracks associated with the b-tagged jet. As only the number of b-tagged jets enters the analysis an approach, referred to as *promotion-demotion method* [77], suited to correct this variable is used. The promotion-demotion method is a procedure which considers every jet in the event which passes the kinematic requirements for a b-tagged jet and reevaluates the decision

Table 5.5: Scale factors for the anti-electron and anti-muon discriminators. The scale factors depend on $|\eta|$ of the hadronic τ-lepton candidate [59].

anti-electron discriminator

$|\eta|$ range	$e\tau_{\mathrm{h}}$	$\mu\tau_{\mathrm{h}}$ and $\tau_{\mathrm{h}}\tau_{\mathrm{h}}$
$|\eta| < 1.46$	1.21 ± 0.06	1.40 ± 0.12
$|\eta| > 1.558$	1.38 ± 0.04	1.90 ± 0.30

anti-muon discriminator

$|\eta|$ range	$e\tau_{\mathrm{h}}$ and $\tau_{\mathrm{h}}\tau_{\mathrm{h}}$	$\mu\tau_{\mathrm{h}}$
$0 < |\eta| < 0.4$	1.47 ± 0.16	1.22 ± 0.04
$0.4 < |\eta| < 0.8$	1.55 ± 0.30	1.12 ± 0.04
$0.8 < |\eta| < 1.2$	1.33 ± 0.05	1.26 ± 0.04
$1.2 < |\eta| < 1.7$	1.72 ± 0.54	1.22 ± 0.15
$1.7 < |\eta| < 2.3$	2.50 ± 0.63	2.39 ± 0.16

whether this jet is to be considered b-tagged or not. It relies on correction factors for the b-tagging performance which are provided depending on the p_{T}, $|\eta|$ and the flavour of the parton from which the jet originated. Based on this information the probability for each jet originating from a light quark or gluon to be falsely considered as b-tagged is derived. Likewise, the probability for each jet originating from a bottom quark to be falsely considered as not b-tagged is evaluated. Based on the comparison with a uniform random number the decision whether to consider a non tagged jet as b-tagged, referred to as *promotion*, or to consider a b-tagged jet as not tagged, referred to as *demotion*, is taken. To ensure a full reproducibility of the analyses the random number generator used for generating the random numbers is seeded on a per-jet basis using the η value of the jet.

Top quark p_{T} reweighting

In studies of the distribution of the transverse momentum of the top quarks in $t\bar{t}$ events a misdescription was found for the used event generator [78] (see figure 5.18). The agreement is improved by applying a p_{T} dependent weight for each top quark in the event. The weight is parameterized as

$$SF(p_{\mathrm{T}}) = e^{0.156 - 0.00137 p_{\mathrm{T}}/\mathrm{GeV}}. \tag{5.14}$$

The resulting weight to be applied to each event is then given as

$$w = \sqrt{SF(p_{\mathrm{T}}^t) \cdot SF(p_{\mathrm{T}}^{\bar{t}})} \tag{5.15}$$
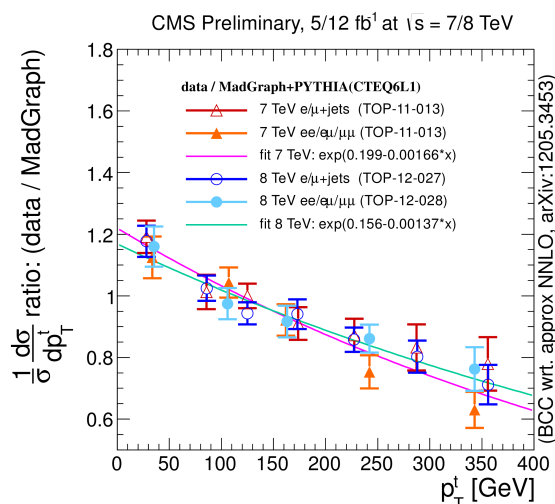
Figure 5.18: Based on the measurement and the prediction for the differential $t\bar{t}$ production cross section a correction as a function of the transverse momentum of the top quark is derived [78].

Correction of the Z boson spectrum

The Z boson spectrum is found to be mismodeled in the used leading order simulation. To account for this mismodelling correction factors depending on the mass and transverse momentum of the generated Z boson are derived in a $Z \rightarrow \mu\mu$ region [76] (see figure 5.19). The correction factors are applied for all simulated Drell-Yan events and were found to improve the description of the Z boson spectrum when comparing to higher order simulations and to observed data.

Recoil corrections

In simulated events for the Drell-Yan, W+jets and Higgs boson production processes the hadronic recoil $\vec{U}$ to the involved bosons was found to be not well modeled. This is corrected for by applying *recoil corrections*. For these corrections the hadronic recoil is split into a component parallel (U_1) and a component perpendicular (U_2) to the direction of the boson p_{T}. Corrections for these two components are derived in a $Z \rightarrow \mu\mu$ selection where no neutrinos, and hence no genuine $\not{E}_{\mathrm{T}}$, are expected. In this region a fit is performed to determine the width $\sigma(U)$ and central value $\langle U \rangle$ of the distributions of U_1 and U_2. The fitted functions are a double asymmetric Gaussian with freely floating central value and a double asymmetric Gaussian centred at 0 respectively. The values are derived for observed data and simulated events and the corrected values for U_1 and
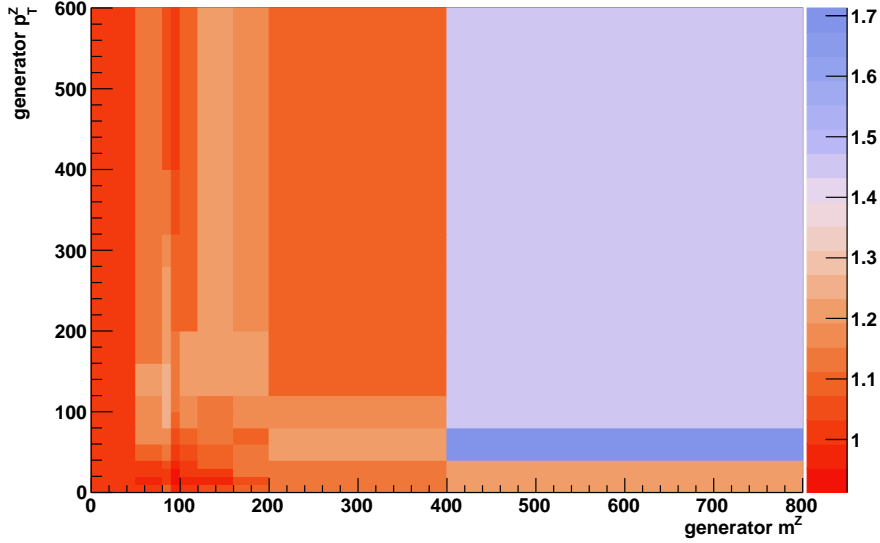
Figure 5.19: Correction factor on the Z boson leading-order spectrum. The correction factors are derived in bins of the mass and the transverse momentum of the generated Z boson.

U_2 are then given as

$$U_1' = \langle U_1 \rangle_{\text{data}} + (U_1 - \langle U_1 \rangle_{\text{sim}}) \frac{\sigma(U_1)_{\text{data}}}{\sigma(U_1)_{\text{sim}}} \tag{5.16}$$

$$U_2' = U_2 \frac{\sigma(U_2)_{\text{data}}}{\sigma(U_2)_{\text{sim}}} \tag{5.17}$$

The dependency between the hadronic recoil and the $\slashed{E}_{\text{T}}$ is given as

$$\vec{U} = \slashed{E}_{\text{T}} - \vec{p}_{\text{T}}^{\nu} \tag{5.18}$$

where $\vec{p}_{\text{T}}^{\nu}$ is the sum of the transverse momentum of the neutrinos in the final state. Corrections to the hadronic recoil are propagated to the $\slashed{E}_{\text{T}}$ using this dependency. The applied corrections and method are identical to those used in [76].

5.5 Uncertainty model

In the analysis presented in this thesis, several sources of uncertainty have to be considered which are highlighted in the following section. Tables showing the uncertainties for each category are given in appendix A.3.1. The first part of uncertainties are systematic uncertainties due to finite precision of the measurement and calibration of objects. Such uncertainties affect for example the measurement of the integrated luminosity or energy measurements for jets and leptons. In addition, systematic uncertainties are also caused by finite precision of theoretical predictions being used for this analysis. One example is

the uncertainty on the cross section for a given process which is used to normalize the simulated events.

Uncertainties can be split into two types. The first type are uncertainties which affect only the normalisation and not the shape of the $m_{\mathrm{T}}^{\mathrm{tot}}$ spectrum. These are referred to as *normalisation* uncertainties. A typical example for this type of uncertainty is the uncertainty on the luminosity measurement.

The second type of uncertainties are uncertainties which affect both the normalisation and the shape of the $m_{\mathrm{T}}^{\mathrm{tot}}$ spectrum. Such uncertainties are for example due to uncertainties on variables correlated with $m_{\mathrm{T}}^{\mathrm{tot}}$, such as the uncertainty on the energy of hadronic τ-leptons. This type of uncertainty is referred to as *shape altering* uncertainty.

A last source of uncertainty which has to be considered is the uncertainty due to the finite number of simulated events available for each process. The procedure for taking these into account and arising challenges are detailed in section 5.5.2.

5.5.1 Systematic uncertainties

Luminosity uncertainty

The luminosity of the data recorded and certified as good by the CMS collaboration corresponds to is measured by CMS with an uncertainty of 2.5 % [79]. This uncertainty is a normalisation uncertainty affecting any process which is estimated based on simulated events.

Cross section uncertainties

The cross section of the processes studied in the context of this analysis are only known with a finite precision. The magnitude of this uncertainty is driven by the order in the involved couplings, up to which the cross section calculation is performed. Cross section uncertainties are taken into account as normalisation uncertainties for all backgrounds which are not derived or corrected using methods relying on the measured data. It amounts to 6 % for the $t\bar{t}$, 4 % for the $Z \to ll$ and 5 % for the Single top quark production and Di-boson processes. In the $\tau_{\mathrm{h}}\tau_{\mathrm{h}}$ decay channel, an uncertainty of 4 % is applied for the W+jets background. For the W+jets process in the $e\tau_{\mathrm{h}}$ and $\mu\tau_{\mathrm{h}}$ decay channel as well as for the $Z \to \tau\tau$ process dedicated control regions are included in the fit (see section 5.6). Consequently, no uncertainties on the respective cross sections are included.

Lepton and hadronic τ-lepton identification uncertainty

The uncertainty on the lepton corrections described in section 5.4 amounts to 2 %. It is applied as normalisation uncertainty to all contributions which are estimated based on simulated events.

For the hadronic τ-lepton the uncertainty on the measurements amounts to 5 %. Due to differences in the composition of hadronic τ-leptons in the individual decay channels this uncertainty is broken down into a correlated and uncorrelated uncertainty. The part correlated across decay channels amounts to 4 % and the uncorrelated part to 3 % in the

(a) $Z \to \tau\tau$

(b) $Z \to ee$, with one e misidentified as τ_h
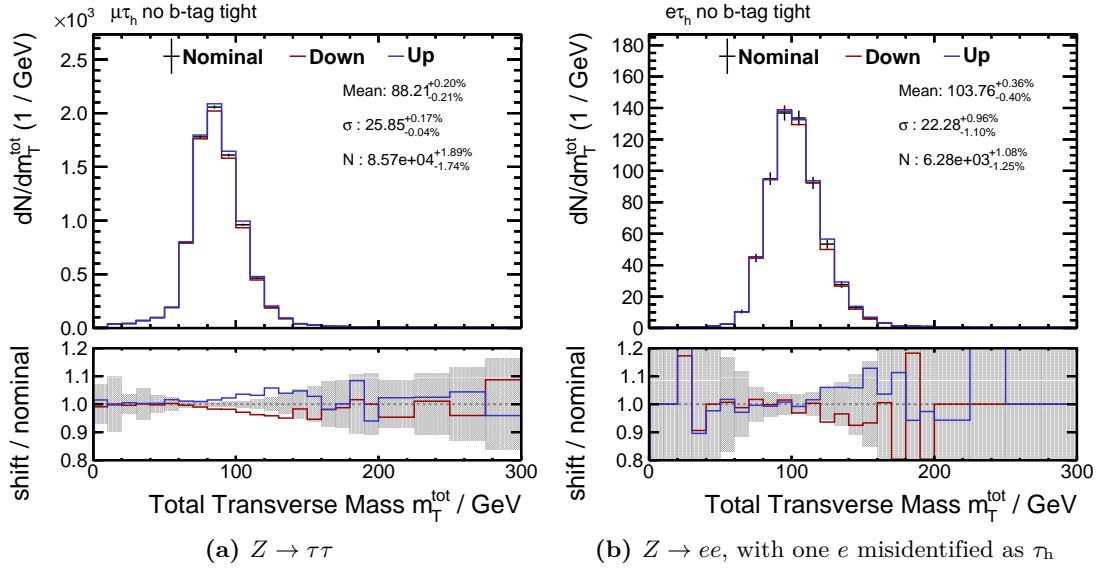
Figure 5.20: Effect of shape altering uncertainties due to the energy corrections for hadronic τ-leptons (left) and the energy corrections for electrons misidentified as hadronic τ-lepton (right) on the total transverse mass spectrum. The shaded band corresponds to the statistical uncertainty of the nominal distributions.

$e\tau_h$ and $\mu\tau_h$ channel. In the $\tau_h\tau_h$ decay channel, the part correlated across decay channels is 8 % and the uncorrelated part is 9.2 % including the uncertainty on the corrections for τ_h triggering. These uncertainties are taken into account as normalisation uncertainties.

In addition, a shape altering uncertainty is used to account for the raising uncertainty on the τ_h identification with raising p_T of the hadronic τ-lepton. This uncertainty is equal to ± 20 % per 1 TeV p_T and limited to a maximum of ± 100 %.

Energy scale of genuine hadronic τ-leptons and electrons misidentified as hadronic τ-lepton

The correction of the energy scale of genuine hadronic τ-leptons is measured with an uncertainty of 1.2 %. The uncertainty is uncorrelated between the decay modes of the τ-lepton, leading to in total three shape altering uncertainties. For electrons misidentified as hadronic τ-leptons the uncertainty is 1 % for the $\tau^\pm \to \pi^\pm \nu_\tau$ and 0.5 % for the $\tau^\pm \to \pi^\pm \pi^0 \nu_\tau$ decay mode. Two uncorrelated shape altering uncertainties are added to account for these. An illustration of the energy scales with the largest impact on the total transverse mass spectrum for the $Z \to \tau\tau$ and $Z \to ee$ processes with an electron being misidentified as hadronic τ-lepton is shown in figure 5.20.

Jet energy scale

The measured energy of jets is only weakly correlated with the total transverse mass. Consequently, uncertainties on the energy of jets are taken into account as normalisation uncertainties. These are derived by varying the measured energy of the jets by $\pm 1\sigma$ of the respective corrections [80].

Uncertainties on the recoil corrections and the $\not{E}_\mathrm{T}$

The uncertainty on the recoil corrections and the corresponding propagated uncertainty on the $\not{E}_\mathrm{T}$ is taken into account in two cases. For the $\not{E}_\mathrm{T}$ corrections described in section 5.4 a corresponding uncertainty is applied for the W+jets, Drell-Yan and Higgs boson production processes. These uncertainties are taken into account as uncorrelated normalisation uncertainties for the response and resolution corrections.

For all remaining processes the uncertainties are split into uncertainties on the $\not{E}_\mathrm{T}$ due to the jet energy scale and unclustered energy scales. They are taken into account as normalisation uncertainties [61].

Electron energy scale

The uncertainty on the measured energy of the electrons is equal to $1\,\%$ in the barrel and $2.5\,\%$ in the endcap region. This uncertainty is taken into account as a shape altering uncertainty in the $e\tau_\mathrm{h}$ decay channel.

Uncertainty due to the correction of the Z boson spectrum

The uncertainty on the correction of the Z boson spectrum described before can be broken down into three uncorrelated sources. For each of these sources, the corrections are rederived when varying the corresponding parameter by $\pm 1\sigma$. The resulting corrections are then used to derive shape altering uncertainties.

The three considered sources of uncertainty are

- The uncertainty due to the available statistics in the $Z \to \mu\mu$ control region the corrections are derived in. It was found that this effect is negligible in all but the three bins with the highest requirement on the mass of the generator level Z boson shown in figure 5.19. Consequently, in total three shape altering uncertainties, one per bin, are derived and applied.

- The major source of background contamination in the control region comes from $t\bar{t}$ events. With the dominant systematic for this process being the uncertainty on its cross section. Shape altering uncertainties are derived for the case of varying the $t\bar{t}$ cross section within its uncertainty.

- The major experimental uncertainty affecting the control region is the uncertainty on the muon energy scale of $0.2\,\%$. By varying the muon energy scale within this uncertainty and rederiving the Z boson spectrum corrections the corresponding shape altering uncertainty is derived.

B-tagging uncertainties

The uncertainties for the b-tagging and its corrections are derived following pre-defined procedures within the CMS collaboration [77]. Two dedicated uncertainties are derived accounting for the contribution of jets originating from bottom quarks not identified as b-tagged jet and other jets originating from other partons misidentified as b-tagged jets. This correction has a very minor effect on the spectrum of the total transverse mass and hence is taken into account as an normalisation uncertainty.

Top quark p_{T} reweighting

For the shape altering uncertainty due to the top quark p_{T} reweighting the up and down shifts are derived by applying the corrections described above squared and not at all respectively.

Misidentification rates of leptons and jets

Contributions where leptons are misidentified as hadronic τ-leptons are assigned an uncertainty depending on the used working point of the anti-lepton discriminator described in section 5.2.2. For misidentified muons the uncertainty amounts to $5\,\%$ in the $\tau_{\mathrm{h}}\tau_{\mathrm{h}}$ and $12\,\%$ in the $\mu\tau_{\mathrm{h}}$ decay channel. The difference of the uncertainties is due to the working points chosen for the respective decay channels. In the $e\tau_{\mathrm{h}}$ decay channel, this uncertainty is not considered due to the contribution of misidentified muons below the percent level.

In the case of misidentified electrons, the uncertainty is $11\,\%$ in the $e\tau_{\mathrm{h}}$ and $3\,\%$ in the $\tau_{\mathrm{h}}\tau_{\mathrm{h}}$ decay channel. Due to the contribution of misidentified electrons below the percent level in the $\mu\tau_{\mathrm{h}}$ channel no uncertainty is taken into account.

Theory uncertainties

On the predictions for the cross sections of the Higgs boson production processes the uncertainties provided by the LHC Higgs cross section working group are considered. These take into account the uncertainties due to variations of the renormalisation and factorisation scale and different choices of the parton distribution function.

Dedicated uncertainties for the simulation based background estimation method

Misidentification rates of jets:
    The uncertainty on jets misidentified as hadronic τ-leptons amounts to $20\,\%$. It is taken into account as normalisaion uncertainty for all processes estimated from simulated events.

p_{T} dependency of the misidentification rate of jets:
    A shape altering uncertainty is used to account for the raising uncertainty on the rate of jets being misidentified as hadronic τ-lepton. It is derived by applying a weight of $1 \pm 20\,\%/(p_{\mathrm{T}}/100\,\mathrm{GeV})$ for each hadronic τ-lepton in the event.

Background estimation for W+jets and QCD multi-jet events:

As the regions used to derive the estimates for W+jets and QCD multi-jet events are included in the fit to derive the results (see section 5.6) the statistical uncertainties are estimated in-situ during the fit. Consequently, they do not need to be added externally. However, the uncertainties on the involved extrapolation factors, both for W+jets and QCD multi-jet events, are considered. For the QCD multi-jet same charge to opposite charge extrapolation factor the uncertainty is given by the result of the fit (see section 5.3.1).

For the W+jets process the uncertainties on the same charge to opposite charge extrapolation factor is broken down into a systematic and a statistical component. The systematic part was derived in a control region requiring the hadronic τ-lepton to pass the very loose but not the tight identification working point. In this region the extrapolation factor was derived for the simulated events and compared to the extrapolation factor derived from data in a W+jets dominated region given by $120 < m_\mathrm{T} < 160\,\mathrm{GeV}$. The systematic uncertainty was found to be between 1 and 2 %. For the extrapolation factor from the W+jets control region to the signal region an uncertainty of 20 % is applied. This uncertainty is based on studies performed with the data recorded in 2015 [81].

Dedicated uncertainties for the fake factor method

Contamination uncertainties:

To account for the contribution of other backgrounds in the estimation regions dedicated normalisation uncertainties between 3 and 4 % are added.

Normalisation effect:

For all other uncertainties the effect is split into a normalisation and a shape altering effect. Two different sources of normalisation uncertainties are considered. For one the statistical uncertainty on the estimated fake factors is taken into account. To simplify the statistical model one single uncertainty is derived for each category. This uncertainty is determined by adding up the statistical uncertainties on the individual fake factors for each process in quadrature.

The effect of other systematic uncertainties is added as a single uncertainty correlated between all categories. In a first step, the effect of the individual systematic uncertainties is derived. The combined uncertainty is then calculated by adding up the individual uncertainties in quadrature.

Shape altering effects:

As shape altering effects of the uncertainties mentioned before the following sources are taken into account.

- Statistical uncertainties on the individual fake factors are treated as uncorrelated contributing to each decay channel. This adds 10 uncertainties for the $e\tau_\mathrm{h}$ and $\mu\tau_\mathrm{h}$ decay channel and four for the $\tau_\mathrm{h}\tau_\mathrm{h}$ decay channel.

- The systematic uncertainties related to the W+jets fake factors are taken into account as two uncertainties correlated among all categories in the $\mu\tau_h$ and $e\tau_h$ decay channels respectively. This comprises the effect of the uncertainty on the non-closure and transverse mass correction.

- The systematic uncertainties related to the $t\bar{t}$ fake factors are taken into account as two uncertainties correlated among all categories in the $\mu\tau_h$ and $e\tau_h$ decay channels respectively. The effects of the uncertainty on the non-closure and simulation to data corrections are considered.

- The systematic uncertainties on the QCD multi-jet fake factors are treated as fully correlated between the categories in the individual decay channels. They are formed by taking into account the effect of the uncertainty on the non-closure, lepton isolation (for the $e\tau_h$ and $\mu\tau_h$ decay channel) or p_T (for the $\tau_h\tau_h$ decay channel) and same to opposite charge correction.

- In the $\tau_h\tau_h$ decay channel the systematic uncertainties on the fraction of W+jets, Drell-Yan and $t\bar{t}$ events are taken into account as one shape altering uncertainty each.

5.5.2 Statistical uncertainty of simulated events

On top of the systematic uncertainties detailed before an additional source of uncertainty caused by the finite number of events which are simulated or estimated from control regions for a given process needs to be taken into account. This is done by introducing one dedicated uncertainty per bin, called *bin-by-bin uncertainty*, which shifts the content of this bin within its uncertainty while keeping the content of all other bins at their nominal value. Due to the large number of bins involved in this analysis this leads to 1807 uncertainties in addition to the 69 normalisation and 15 shape altering uncertainties mentioned before. This huge increase of the number of uncertainties by more than a factor of 20 significantly impacts the time needed for performing the statistical inference.

To account for this problem the number of additional uncertainties needs to be limited, thereby reducing the impact on the performance. For this the combination of the bin-by-bin uncertainties for a fraction of the individual contributions per bin is estimated by summing them up in quadrature. For example in the case that four contributions are present in one bin the largest reduction can be achieved by combining the uncertainties of all four contributions. As this method is only an approximation of taking into account all individual uncertainties, a boundary on the relative fraction of the merged uncertainties compared to the full uncertainty in the given bin is enforced.

The implementation of this method is done on a per bin basis as given below.

- For a given bin the contributions j with content x_j and uncertainty σ_j are considered and ranked according to their uncertainty.

- The total squared sum of all uncertainties $\sigma_{\text{tot}}^2 = \sum_j \sigma_j^2$ is calculated.

- Starting from the contribution with the lowest uncertainty its squared uncertainty is added to the substituted uncertainty $\sigma_{\text{sub}}^2 = \sigma_{\text{sub}}^2 + \sigma_j^2$ and set to 0.

- The previous steps are repeated until the fraction of substituted uncertainties is larger or equal to a cutoff value $\sigma^2_{\mathrm{sub}}/\sigma^2_{\mathrm{tot}} \geq \delta_{\mathrm{merge}}$.

- All remaining uncertainties are scaled by the factor $\sqrt{1/(1 - \sigma^2_{\mathrm{sub}})}$ to ensure the squared sum of all uncertainties before and after applying this procedure is the same.

The cutoff value introduced before used for this analysis is $\delta_{\mathrm{merge}} = 0.4$. Employing this procedure reduces the number of bin-by-bin uncertainties from 1807 to 421.

5.6 Control regions included in the fit

In addition to signal regions also control regions dominated by a single background contribution can be included in the fit used to derive the results later. This offers the possibility to introduce an in-situ calibration for a given background contribution while taking into account uncertainties which are correlated between the signal region and the control region. In the analysis presented in this thesis control regions for the $Z \to \tau\tau$ process are included for both the simulation based and fake factor background estimation method. For the simulation based estimation method in addition control regions for the QCD multi-jet and W+jets background are included.

$Z \to \tau\tau$ control region

To constrain the overall normalisation of the $Z \to \tau\tau$ process in simulated events using lepton universality, one control region is introduced for the no b-tag and b-tag category each. These control regions comprise di-muon events with an invariant mass of the muons close to the Z boson mass and consists to more than 99% and 89% from $Z \to \mu\mu$ events in the no b-tag and b-tag category respectively.

In the fit, the correlation between the yield of the $Z \to \tau\tau$ contribution in the signal region and the $Z \to \mu\mu$ in the control region is taken into account by introducing a fully correlated multiplicative factor allowing to change the yield of both contributions. One of these parameters is introduced for the no b-tag and b-tag category each.

Due to differences in the phase space of the Z boson leading to the di-muon pairs selected for the control region compared to the phase space of the respective di-τ pair an additional uncertainty is introduced. This uncertainty ranges between 2% in the $e\tau_{\mathrm{h}}$ and $\mu\tau_{\mathrm{h}}$ decay channels and 7% in the $\tau_{\mathrm{h}}\tau_{\mathrm{h}}$ decay channel. The larger uncertainty in the $\tau_{\mathrm{h}}\tau_{\mathrm{h}}$ decay channel is mainly caused by the higher p_{T} requirements for the τ-leptons. The uncertainty is derived based on variations of the parton density function and the factorisation and renormalisation scale used for the simulation.

W+jets and QCD multi-jet control region

The control regions for W+jets and QCD multi-jet events are taken into account in the $e\tau_{\mathrm{h}}$ and $\mu\tau_{\mathrm{h}}$ decay channel when using the simulation based background estimation method. In this estimation method the contribution of other backgrounds, such as $t\bar{t}$

and $Z \to \tau\tau$, play an important role as they are subtracted from the observed data in the control region as detailed in section 5.3.1. In the signal region, the contributions of these backgrounds are subject to uncertainties which give the fit the freedom to shift the normalisation of these backgrounds (see section 5.5). To account for the effect of these uncertainties on the W+jets and QCD multi-jet estimation the three control regions introduced for the estimation are included as additional categories. The contributions of W+jets and QCD multi-jet in these regions and the signal region are correlated as follows:

- The yield of the QCD multi-jet contribution is treated as fully correlated in categories which differ only in the opposite or same charge requirement. This leads to 6 independent QCD multi-jet event yields being considered per decay channel.

- The W+jets contribution is fully correlated in all four regions.

Taking into account the split into no b-tag and b-tag as well as in tight and loose mT categories in total 16 control regions and 16 parameters to model the correlations are introduced.

Results

Based on the results of the event selection and the uncertainties introduced in the previous chapter the results presented in this chapter are derived. For deriving the results the methods introduced in chapter 3 are used. Unless specifically stated otherwise the results shown in this chapter are derived using the simulation based background estimation method introduced in section 5.3. For selected results, the fake factor background estimation method is used to provide a cross check of the simulation based method.

In a first step, checks and tests performed to validate the uncertainty model are presented. Following this, the prefit and s+b postfit distributions of the total transverse mass $m_{\mathrm{T}}^{\mathrm{tot}}$ in the categories are discussed.

As no signal is observed, exclusion limits are derived and likelihood scans are performed. The exclusion limits can be divided into two types. Firstly, results not specific to a certain MSSM model are derived. These include exclusion limits on the cross section times branching ratio for the gluon-fusion and bottom-associated production processes of a Higgs boson. Secondly, exclusion limits for specific MSSM scenarios, like the $m_{\mathrm{h}}^{\mathrm{mod+}}$, are determined and discussed. The likelihood scans performed in the plane spanned by the cross section times branching ratios for the $gg \to \phi$ and $gg \to b\bar{b}\phi$ processes grant an easier access to compare the results of this analysis with alternative model and scenario predictions.

6.1 Pulls and constraints

The uncertainties introduced in section 5.5 are resembled by nuisance parameters in the statistical model as introduced in section 3.2. A maximum likelihood fit, as discussed in section 3.3, is performed prior to deriving the results discussed in the following sections. The results of this fit gives the best-fit values for the nuisance parameters θ_i and their constraints $\sigma_{\theta,i}$.

To quantify the difference of the best-fit values of the nuisance parameters with respect to the pre-fit ones the corresponding *pulls* are calculated. These are given by

$$\frac{\hat{\theta}_i - \theta_i}{\hat{\sigma}_{\theta,i}} \tag{6.1}$$

Table 6.1: Results of the fit of a Gaussian distribution to the post-fit pulls and number of nuisance parameters of the respective type.

	bin-by-bin	other systematics	combination
number of nuisances	422	85	507
width	1.00 ± 0.08	0.70 ± 0.21	1.00 ± 0.07
mean	0.12 ± 0.06	-0.13 ± 0.12	0.09 ± 0.06

with the initial and best-fit value of the nuisance parameter θ_i and $\hat{\theta}_i$ respectively and the corresponding best-fit constraint $\hat{\sigma}_{\theta,i}$. To illustrate the difference in constraints of the nuisance parameters in the fit this quantity is also calculated with respect to the prior constraint on the nuisance parameter $\sigma_{\theta,i}$. Pulls calculated with respect to the prior constraint and best-fit constraint are referred to as pre-fit pulls and post-fit pulls respectively.

In figure 6.1 the pulls for the involved nuisance parameters are shown. The nuisance parameters are separated into bin-by-bin uncertainties, accounting for the limited number of simulated events, and systematic uncertainties accounting for the remaining effects. The distribution of the pulls is expected to follow a Gaussian distribution centered on 0 with a width of 1, indicated by the magenta line. The distribution of the post-fit pulls follows the expected distribution, whereas for the pre-fit pulls a narrower distribution is observed. This is compatible with a conservative choice of some of the uncertainties, which are being constraint by the fit. For the post-fit pulls the results of a fit of a Gaussian to the distribution is given in table 6.1. For the bin-by-bin uncertainties and combination of all uncertainties the results are compatible with the expected distribution. For the remaining systematic uncertainties a narrower distribution is fitted. This effect is also visible in figure 6.1, where a slight excess of uncertainties with a pull around 0 is observed. It can be explained by uncertainties, which are being accounted for although the analysis has only little sensitivity to them, such as uncertainties on the Higgs boson production cross sections.

6.2 Goodness-of-fit test

To assess how well the uncertainty model corresponds to the data when performing a fit of the background-only hypothesis a goodness-of-fit test with a saturated model is performed [82]. The goodness-of-fit test relies on the evaluation of the profile likelihood λ

$$\lambda = \prod_i e^{-\frac{(d_i - f_i)^2}{2\sigma_i^2}} \tag{6.2}$$

where d_i, σ_i and f_i are the measured data, uncertainty of the measured data and prediction in bin i respectively. The evaluated value for this test is given by

$$\chi^2 = -2 \ln \lambda \tag{6.3}$$

which asymptotically follows χ^2 distribution.

(a) normalized to prior constraints

(b) normalized to post-fit constraint
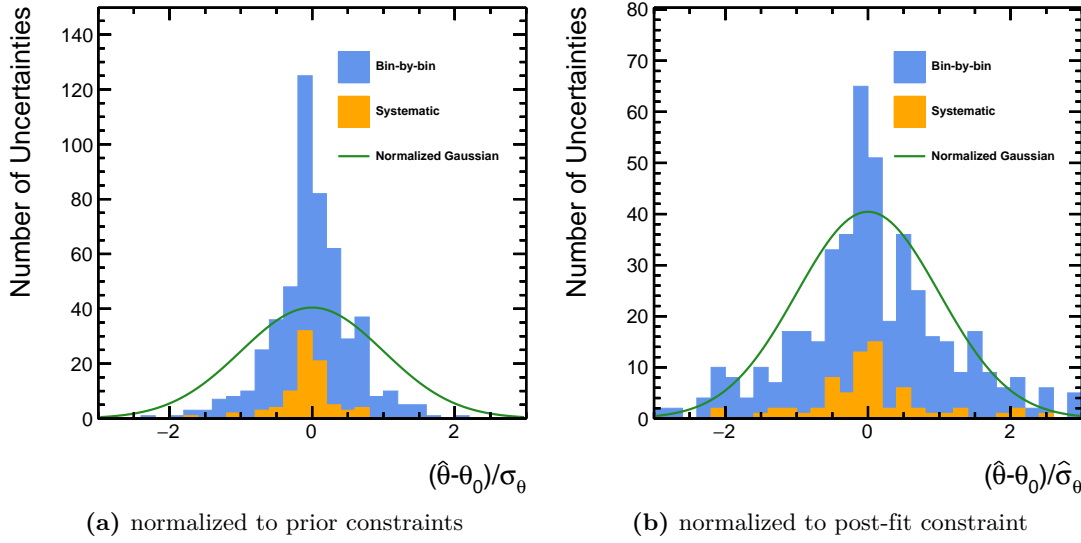
Figure 6.1: Distribution of the pulls in the s+b fit of the nuisance parameters involved in the fit. The pulls are given normalized to the prior constraint (left) and post-fit constraint (right) of the nuisance parameters. The nuisance parameters are split into bin-by-bin uncertainties resembling the uncertainty due to the limited number of simulated events per process and other systematics. The pulls are expected to follow a Gaussian distribution centered on 0 with a width of 1, which is indicated by the magenta line.

This value is evaluated for the measured data as well as for 1000 toy datasets. The toy datasets are randomly sampled from the background expectation and the corresponding uncertainty model. Based on the results of the toys the probability p to observe an at least as large value based on the background expectation is calculated. Results with a p-value of more than 5% are accepted without further investigation, confirming the chosen uncertainty model. The expected contributions from signal processes are small compared to the background processes. As a result, the presence of signal in the observed data is expected to only have a minor effect on the results of this test.

The goodness-of-fit test is performed for each category, the combination of all categories of each decay channel and the global combination of all categories and decay channels. The results per decay channel and category are given in table 6.2. The lowest p-value of 6.6% is observed in the $e\tau_h$ decay channel in the no b-tag loose mT category and is still compatible according to the criterion given before. Exemplary distributions for the two categories with the lowest and highest p-value respectively are given in figure 6.2 and the corresponding m_T^{tot} distributions are given in the top and middle of figure 6.3.

Table 6.2: Results of the goodness-of-fit test in the categories of the $e\tau_\mathrm{h}$, $\mu\tau_\mathrm{h}$ and $\tau_\mathrm{h}\tau_\mathrm{h}$ decay channels using the simulation based background estimation method. In categories with results larger than 0.05 the uncertainty model is considered to be chosen appropriately.

$e\tau_\mathrm{h}$ no b-tag tight	$e\tau_\mathrm{h}$ no b-tag loose mT	$e\tau_\mathrm{h}$ b-tag tight	$e\tau_\mathrm{h}$ b-tag loose mT
0.546	0.066	0.110	0.238

(a) $e\tau_\mathrm{h}$

$\mu\tau_\mathrm{h}$ no b-tag tight	$\mu\tau_\mathrm{h}$ no b-tag loose mT	$\mu\tau_\mathrm{h}$ b-tag tight	$\mu\tau_\mathrm{h}$ b-tag loose mT
0.463	0.266	0.984	0.993

(b) $\mu\tau_\mathrm{h}$

$\tau_\mathrm{h}\tau_\mathrm{h}$ no b-tag	$\tau_\mathrm{h}\tau_\mathrm{h}$ b-tag
0.368	0.609

(c) $\tau_\mathrm{h}\tau_\mathrm{h}$

(a) $\mu\tau_\mathrm{h}$ b-tag loose mT
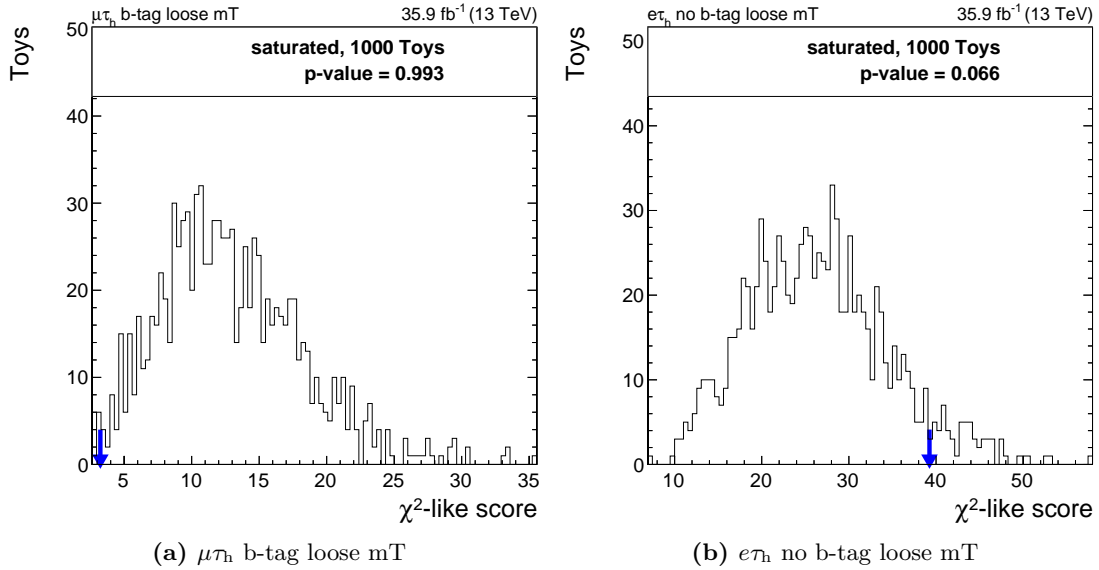
(b) $e\tau_\mathrm{h}$ no b-tag loose mT

Figure 6.2: Goodness-of-fit test performed in the $\mu\tau_\mathrm{h}$ b-tag loose mT and $e\tau_\mathrm{h}$ no b-tag loose mT categories. The distributions of the χ^2-like test statistic for 1000 toy datasets randomly generated according to the background-only model and for the observed data is shown. The p-value gives a measure of the agreement between this observation and the distribution for the toys. For the two given categories the highest and lowest p-value respectively has been obtained.

6.3 Pre- and postfit distributions

To further assess the compatibility of the observed data and the expectation, the prefit and s+b postfit distributions of $m_\mathrm{T}^\mathrm{tot}$ in the individual categories are studied. The postfit distributions and their corresponding uncertainties are derived based on the pulls and constraints of the individual nuisance parameters in a maximum likelihood fit as mentioned in section 6.1. The fit is performed for the s+b hypothesis assuming a single 700 GeV Higgs boson with a cross section of 0.1 pb for both the $gg \to \phi$ and $gg \to b\bar{b}\phi$ production processes. The prefit distributions allow to assess this agreement based solely on the selection and the corrections introduced in section 5.4 and how well disagreements are covered by the uncertainty model prior to performing the fit. The postfit distributions in addition take the pulls and constraints the fit imposes on the involved uncertainties into account.

For the $\mu\tau_\mathrm{h}$ b-tag loose mT, $e\tau_\mathrm{h}$ no b-tag loose mT and $\tau_\mathrm{h}\tau_\mathrm{h}$ no b-tag categories these plots are shown in figure 6.3. The observed data is found to be described within uncertainties by the background prediction prior to performing the fit for all categories apart from the $e\tau_\mathrm{h}$ no b-tag loose mT category. In this category, a deviation is observed in the region around $m_\mathrm{T}^\mathrm{tot} = 200$ GeV. After applying the shifts and constraints for the nuisance parameters from the s+b fit also in this category no significant deviation is found, indicating that this deviation is accounted for by the respective uncertainties and a corresponding pull larger than 1σ. In general, the observed data is found to be well described within uncertainties by the background prediction, indicating that the studied phase space in the decay channels is well understood.

6.4 Model independent exclusion limits

As a first result, exclusion limits on the cross section times branching ratio ($\sigma\mathcal{B}$) for the gluon-fusion and bottom-quark associated production processes are derived. These limits are derived assuming a single Higgs boson ϕ with mass m_ϕ using the narrow-width approximation as signal hypothesis. While deriving the result for one production process the contribution of the other process is profiled. Meaning the contribution of this production process is allowed to freely float and assume its best-fit value.

The expected limits are derived as the limits in case the predicted background is being observed. This allows to assess the sensitivity of the analysis. The sensitivity is derived for the three decay channels $e\tau_\mathrm{h}$, $\mu\tau_\mathrm{h}$ and $\tau_\mathrm{h}\tau_\mathrm{h}$ as well as the combination of them (see figure 6.4). Comparing the sensitivities of the individual decay channels allows to assess the importance of each decay channel in a given mass range.

For both production processes a similar behaviour is observed. For the high mass region the $\tau_\mathrm{h}\tau_\mathrm{h}$ decay channel is more sensitive than the $\mu\tau_\mathrm{h}$ and $e\tau_\mathrm{h}$ decay channels by approximately a factor of 3 and 6 respectively. For lower masses the semi-leptonic decay channels gain more sensitivity compared to the $\tau_\mathrm{h}\tau_\mathrm{h}$ decay channel and eventually have the higher sensitivity for masses lower than ≈ 200 GeV. This effect is driven by the signal acceptance for the respective masses. In the $\tau_\mathrm{h}\tau_\mathrm{h}$ decay channel these are
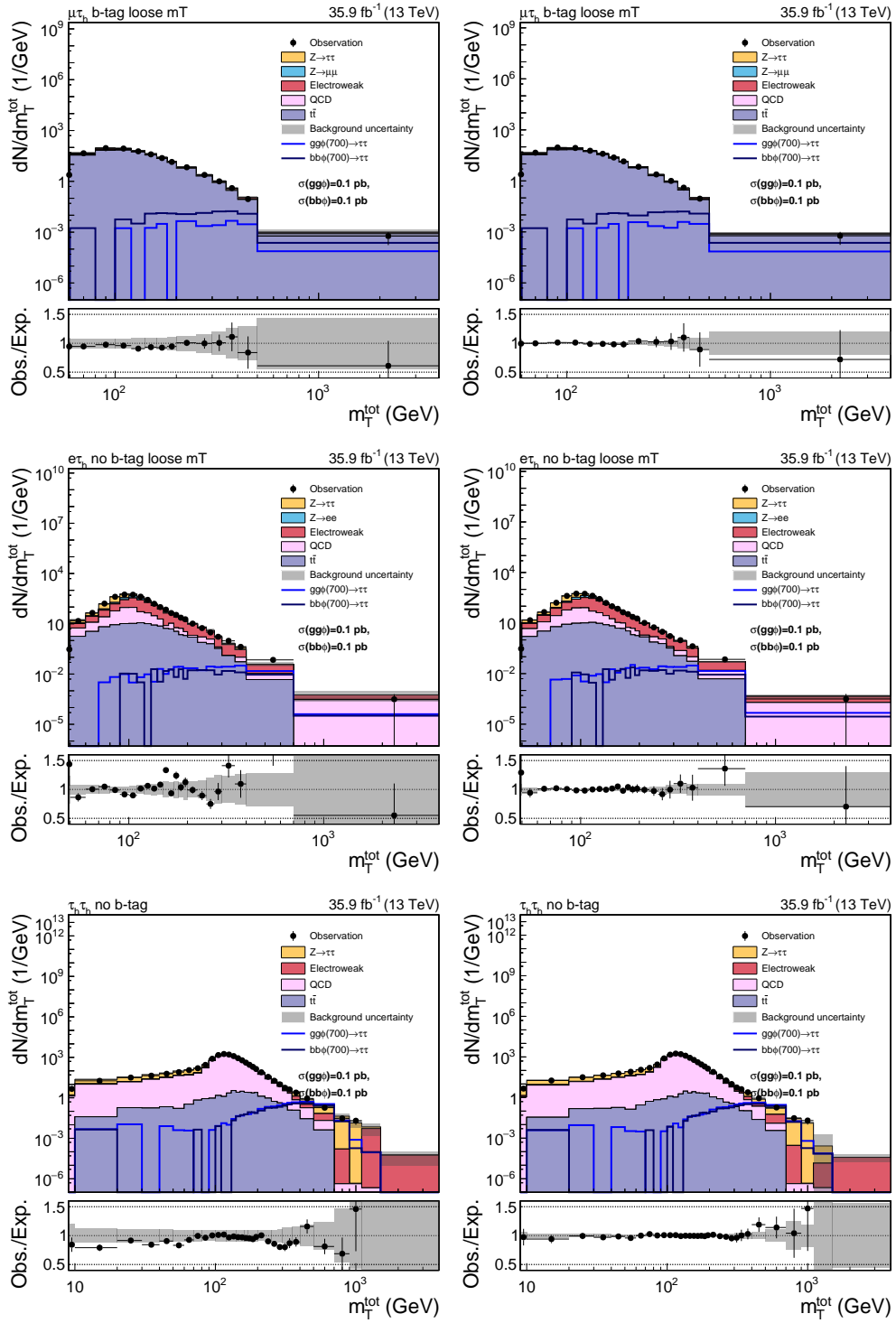
Figure 6.3: Prefit (left) and s+b postfit (right) distributions of m_T^{tot}. The postfit distributions are evaluated based on the pulls of the nuisance parameters in the s+b fit. For the uncertainty bands the full uncertainty model is considered. The distributions are given for the $\mu\tau_h$ b-tag loose mT (top), $e\tau_h$ no b-tag loose mT (middle) and $\tau_h\tau_h$ no b-tag (bottom) categories.
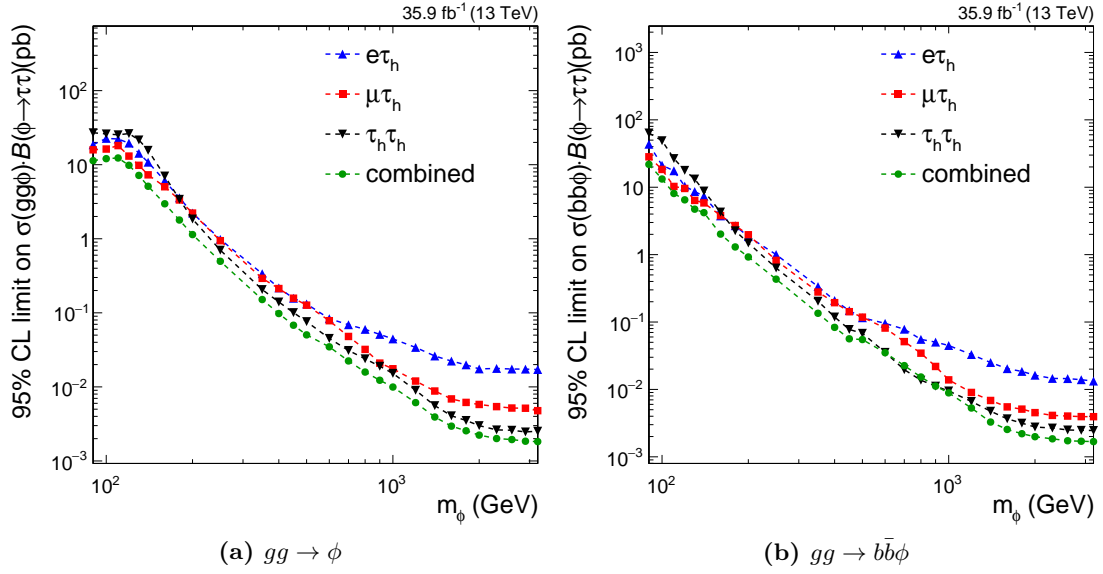
Figure 6.4: Sensitivity of the searches to a single Higgs boson with a mass m_ϕ. The sensitivity is shown for the individual decay channels $e\tau_\mathrm{h}$, $\mu\tau_\mathrm{h}$ and $\tau_\mathrm{h}\tau_\mathrm{h}$ as well as the combination of them. The sensitivity at high m_ϕ is mainly driven by the $\tau_\mathrm{h}\tau_\mathrm{h}$ decay channel while at low masses the semi-leptonic decay channels are more sensitive.

lower compared to the semi-leptonic channels due to the higher triggering threshold and resulting kinematic requirements of $p_\mathrm{T} > 40\,\mathrm{GeV}$ compared to $26\,\mathrm{GeV}$ and $23\,\mathrm{GeV}$ for the $e\tau_\mathrm{h}$ and $\mu\tau_\mathrm{h}$ decay channel respectively.

In addition to the expected sensitivity, the corresponding uncertainties and exclusion limits for the observed data are derived. The results are given in figure 6.5. The expected exclusion limit is indicated by the red line. The corresponding $\pm 1\sigma$ and $\pm 2\sigma$ uncertainties are indicated by the green and yellow bands respectively. The observed exclusion limit, represented by the black line and points, is found to be consistent with the expected exclusion limits within the $\pm 2\sigma$ band for all mass points. For the $gg \rightarrow \phi$ production process the observed exclusion limits in the mass regions up to $180\,\mathrm{GeV}$ and between 500 and $1400\,\mathrm{GeV}$ are found to be higher, within uncertainties, than the expected exclusion limit. For the remaining mass points a, within uncertainties, lower exclusion limit than expected is observed. For the $gg \rightarrow b\bar{b}\phi$ production, a within uncertainties lower exclusion limit is observed for all mass points.

The results derived using the simulation based background estimation are cross checked with those derived using the fake factor background estimation method. For the cross check the difference between observed and expected exclusion limits normalized to the $\pm 1\sigma$ uncertainty is calculated. The result is shown in figure 6.6. For both background estimation methods similar trends are seen, indicating the compatibility of the findings when using both methods.

(a) $gg \to \phi$ **(b)** $gg \to b\bar{b}\phi$
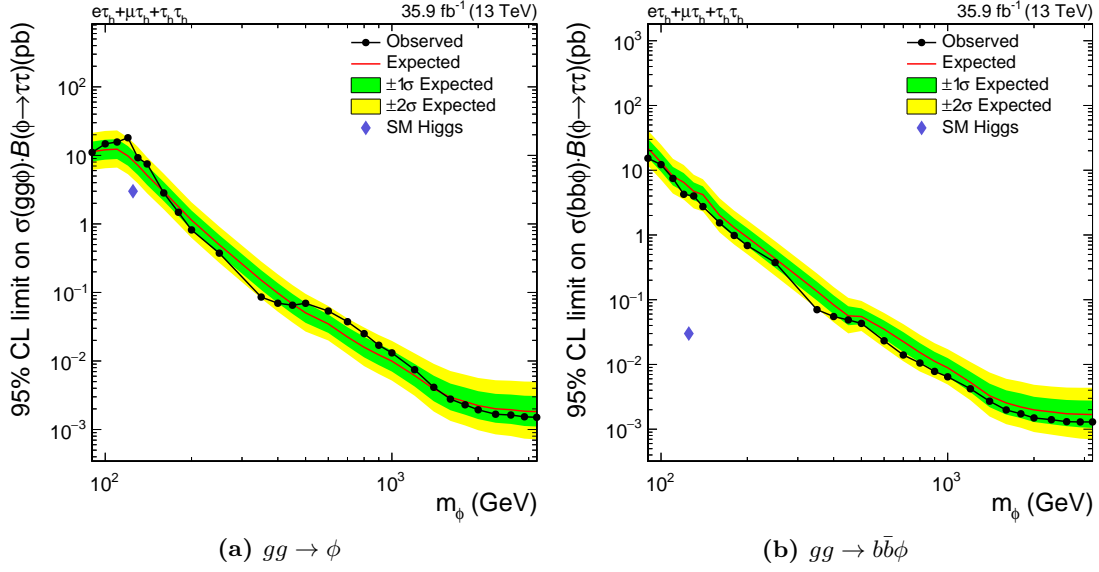
Figure 6.5: Expected and observed exclusion limits on the $\sigma\mathcal{B}$ for the $gg \to \phi$ (left) and $gg \to b\bar{b}\phi$ (right) production process. The cross section for the SM Higgs boson with a mass of $125\,\text{GeV}$ is indicated by the blue marker. For the whole mass range no significant excess of the observation compared to the expectation is observed.

(a) $gg \to \phi$ **(b)** $gg \to b\bar{b}\phi$
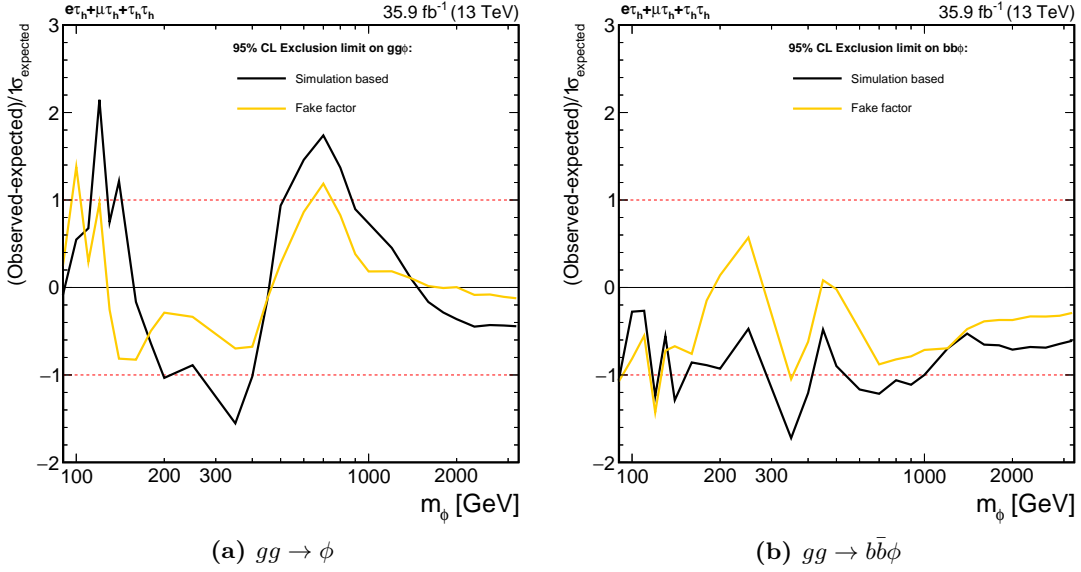
Figure 6.6: Comparison of the difference between observed and expected upper limits using the simulation based and fake factor background estimation method. The difference is expressed in multiples of 1 standard deviation as derived for the $\sigma\mathcal{B}$ of the $gg \to \phi$ (left) and $gg \to b\bar{b}\phi$ (right) production process. Both background estimation methods show compatible results, indicating similar findings using both methods.

(a) $gg \to \phi$ **(b)** $gg \to b\bar{b}\phi$
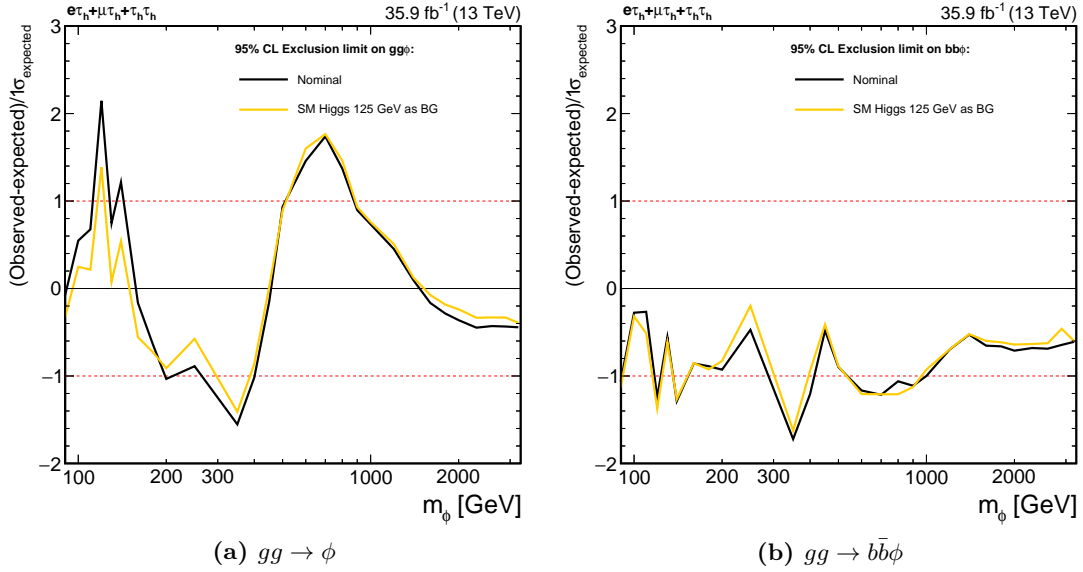
Figure 6.7: Comparison of the difference between observed and expected upper limits on the $\sigma\mathcal{B}$ of the $gg \to \phi$ (left) and $gg \to b\bar{b}\phi$ (right) process. The difference is calculated for the case of considering only the SM processes as the background hypothesis (black line) and additionally considering the SM Higgs boson as part of the background hypothesis (yellow line). The resulting limits differ mainly in the region around the mass of the Standard Model Higgs boson.

A further point to consider is the sensitivity of the derived exclusion limits to the SM Higgs boson. The derived observed exclusion limit around 125 GeV is 10 pb for the $\sigma\mathcal{B}$ of the $gg \to \phi$ production process. The corresponding $\sigma\mathcal{B}$ for the SM Higgs boson is 3 pb [64]. For the $gg \to b\bar{b}\phi$ production process the observed exclusion limit is 4 pb, whereas a $\sigma\mathcal{B}$ of 0.03 pb is expected for the SM Higgs boson. As a consequence, a small impact is expected for the $gg \to \phi$ process, whereas no impact is expected for the $gg \to b\bar{b}\phi$ process.

The comparison of the exclusion limits when considering only the SM processes as contributions to the background compared to also considering the SM Higgs boson as background contribution is shown in figure 6.7. For the $gg \to \phi$ process small differences are found in the region around the SM Higgs boson mass. For higher Higgs boson masses no deviations are found. This behaviour is expected due to the sensitivity of the m_T^{tot} spectrum to the mass of the Higgs boson. For the $gg \to b\bar{b}\phi$ production process no significant deviations are found. As detailed before this insensitivity of the exclusion limit on the $gg \to b\bar{b}\phi$ production process to the SM Higgs boson is expected due to the significantly higher exclusion limit than the expected SM Higgs boson $\sigma\mathcal{B}$.

6.5 Likelihood scan in the *ggϕ-bbϕ* plane

The exclusion limits presented before only provide a handle on one of the production processes while the other one is allowed to freely take any value. As such they are not optimally suited to allow theoreticians to test the compatibility of a new scenario or model with the results of this analysis. To provide additional information, a likelihood scan is performed for each Higgs boson mass in the plane spanned by the $\sigma\mathcal{B}$ of the $gg \rightarrow \phi$ and $gg \rightarrow b\bar{b}\phi$ processes, which is referred to as $gg\phi$-$bb\phi$ plane in the following. The likelihood value is evaluated for each pair of $\sigma\mathcal{B}$ for the $gg \rightarrow \phi$ and $gg \rightarrow b\bar{b}\phi$ production processes and Higgs boson mass.

Using these results, an estimate of the likelihood for a new model or scenario can be derived by looking up and combining the likelihood value for the production of all Higgs bosons which are predicted by this model. This combination of the likelihood values gives an estimate for the compatibility of this new model with the measurement performed in this analysis. To further ease the lookup of the likelihood values and make the results more widely usable tables of the likelihood scans are provided for the corresponding results published by the CMS collaboration [83]. These tables then also include reference likelihood values for asimov datasets representing the background-only hypothesis. One possible tool for such interpretations is `HiggsBounds` [84]. It has been shown that using this tool it is possible to derive comparable exclusion limits in already studied scenarios as well as provide exclusion limits for alternative scenarios [85].

As an additional point, the best-fit value in the $gg\phi$-$bb\phi$ plane is derived assuming the background prediction and the Higgs boson with $m_H = 125\,\text{GeV}$ as predicted by the Standard Model. The results for four exemplary mass points is shown in figure 6.8. The observed best fit is found to be compatible with the results assuming only the background processes, which is indicated by the origin in these figures, with a confidence level of at least 95 %. For the majority of mass points a compatibility with a confidence level of at least 68 % is observed. The best-fit point assuming a Standard Model Higgs boson is close to the background-only expectation for all scans with $m_\phi \gtrsim 200\,\text{GeV}$. For masses lower than this value the compatibility with this point is found to be well within the 68 % confidence level. The largest deviations between the best-fit point and the one assuming a Standard Model Higgs boson is found in the region of $m_\phi = 600\,\text{GeV}$ with a confidence level just above 68 %. This observation is compatible with the results given in section 6.4, where in this mass region an over fluctuation in the exclusion limits for the $gg \rightarrow \phi$ production process is observed.
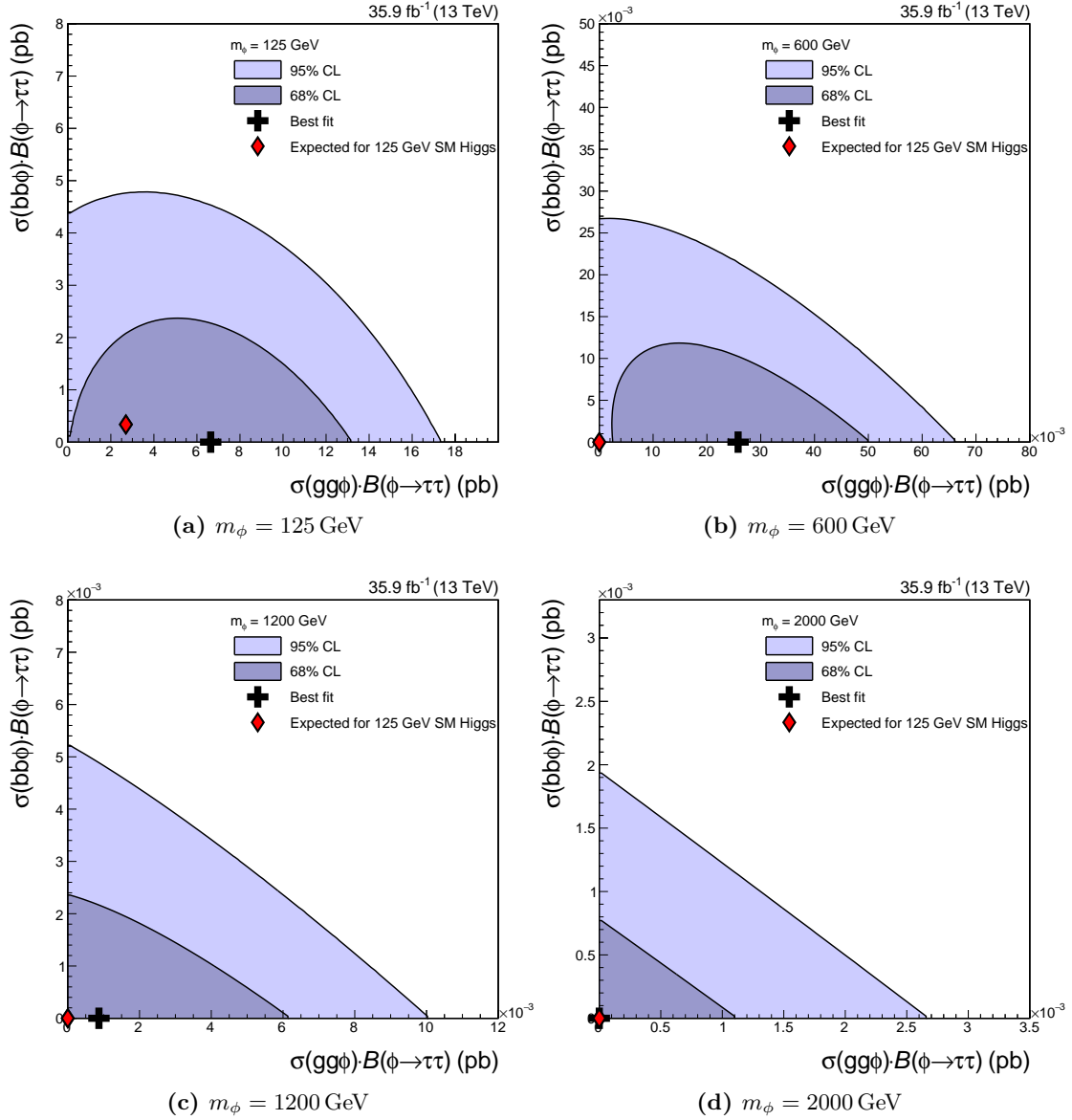
Figure 6.8: Likelihood scan in the *ggφ-bbφ* plane for four Higgs boson mass hypotheses $m_\phi = 125, 600, 1200, 2000$ GeV. The expected best-fit point in case the observation is equal to the background plus the Standard Model Higgs boson with a mass of $m_\mathrm{H} = 125$ GeV is indicated. The best fit point is found to be compatible with the Standard Model Higgs boson within at least the 95 % confidence level for all masses. The largest deviation is found for a Higgs boson mass of $m_\phi = 600$ GeV for the $gg \to \phi$ process. This behaviour is compatible with the slight excess observed in the exclusion limits around this mass.

85

6.6 Model dependent exclusion limits

As detailed in section 2.2.1, several different scenarios are available for the MSSM predicting slightly different Higgs sectors. All of these scenarios include the free parameters m_A and $\tan\beta$, which can be used to fully characterize a given model point.

For the two scenarios $m_h^{\text{mod+}}$ and hMSSM, exclusion limits are derived in the m_A-$\tan\beta$ plane. As introduced in section 3.5, these limits are derived taking the background plus Standard Model Higgs boson as null-hypothesis and background plus MSSM Higgs bosons as alternative hypothesis. Hence, taking the Higgs boson observed at $m_H \approx 125\,\text{GeV}$ into account.

The resulting exclusion contours are shown in figure 6.9. The region excluded by this analysis is indicated by the blue area. The expected exclusion if only the SM would be observed is given by the dashed gray curve. Its corresponding $\pm 1\sigma$ and $\pm 2\sigma$ uncertainty bands are indicated by the dark gray and light gray bands respectively. The excluded parameter space in the $m_h^{\text{mod+}}$ scenario extends from $\tan\beta = 6$ for m_A around $200\,\text{GeV}$ up to $\tan\beta = 60$ for $m_A = 1800\,\text{GeV}$. In the hMSSM scenario the whole $\tan\beta$ range is excluded for m_A around $300\,\text{GeV}$. For lower m_A the exclusion extends down to $\tan\beta = 6$. The highest m_A value excluded for $\tan\beta = 60$ is $1900\,\text{GeV}$. In both scenarios no deviation between the expected and observed exclusion contours larger than the 2σ uncertainty is found.

The exclusion contours in this plane using the data of analyses previously published by the CMS collaboration are also shown. These were rederived taking into account only the $e\tau_h$, $\mu\tau_h$ and $\tau_h\tau_h$ decay channels for integrated luminosities corresponding to $2.3\,\text{fb}^{-1}$ [81] and $12.9\,\text{fb}^{-1}$ [5]. The resulting exclusion limits are indicated by the brown and blue curves respectively. Comparing the exclusion limits derived in this thesis to these exclusion limits the increased sensitivity in the m_A-$\tan\beta$ plane in both scenarios due to the increased amount of data is visible.
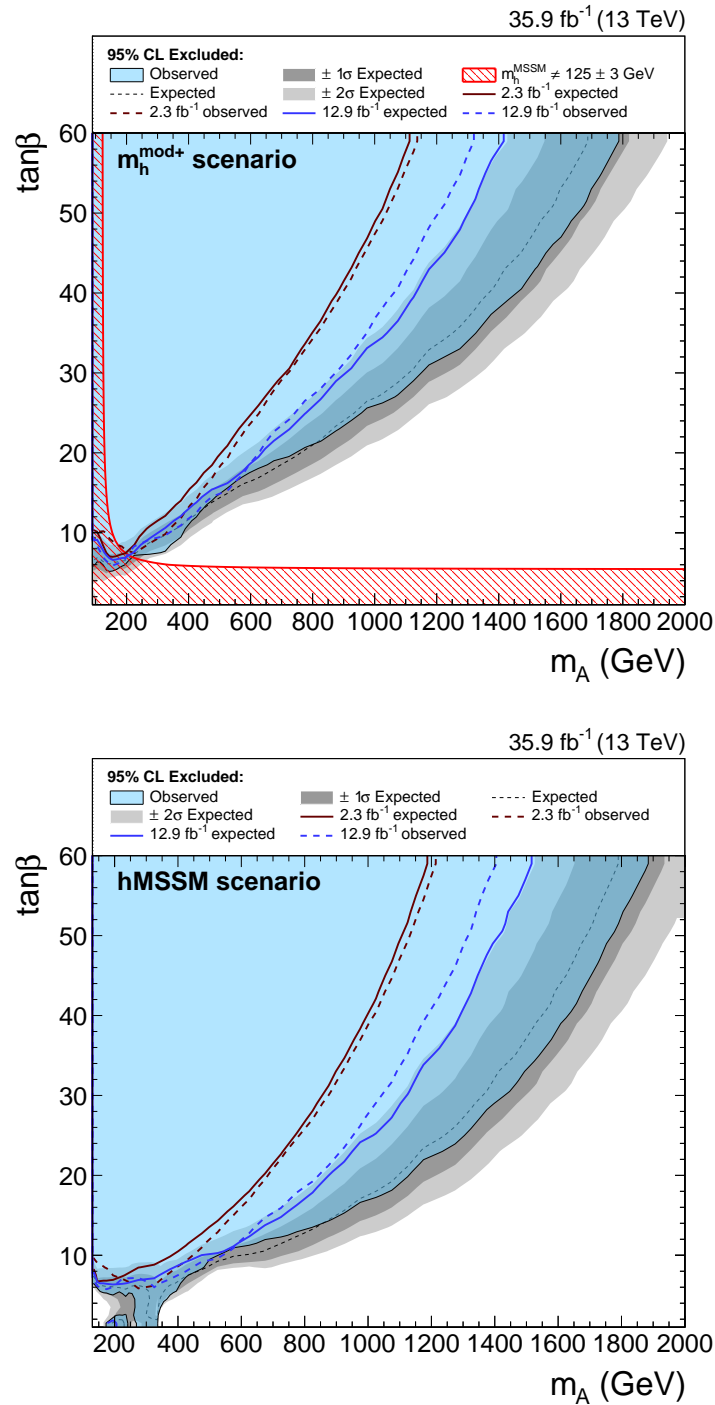
Figure 6.9: Exclusion limits in the m_A-$\tan\beta$ plane for the $m_\mathrm{h}^{\mathrm{mod+}}$ (top) and hMSSM (bottom) scenarios. The exclusion limits derived in previous analyses using less data are also shown. The results for $2.3\,\mathrm{fb}^{-1}$ are evaluated based on the results from [81] and for $12.9\,\mathrm{fb}^{-1}$ from [5]. For both analyses the results are rederived using the asymptotic approach and limiting the analyzed channels to the $e\tau_\mathrm{h}$, $\mu\tau_\mathrm{h}$ and $\tau_\mathrm{h}\tau_\mathrm{h}$ decay channel.

Conclusion

With the Run I of the LHC a new milestone in the field of particle physics has been reached. After the discovery of a Higgs boson with a mass of about 125 GeV in 2012 [86, 87], the field of analyses in the Higgs sector shifted towards conducting more extensive searches for clues for physics beyond the Standard Model, such as additional Higgs bosons.

With the outstanding performance of the LHC and the CMS experiment during the LHC Run II data taking period, it was possible to collect $35.9\,\mathrm{fb}^{-1}$ of data at a center-of-mass energy of 13 TeV suitable for analyses.

First analyses targeting the search for additional Higgs bosons decaying into a pair of τ-leptons have been conducted using a subset of this data. The results of these analyses already gave an unprecedented reach, allowing to surpass the results from Run I in a large fraction of the phase space.

In this thesis, the search for additional Higgs bosons in the decay to a pair of τ-leptons using the full 2016 dataset of $35.9\,\mathrm{fb}^{-1}$ has been presented. Background estimation methods complementary to those used in the analysis as published by CMS have been introduced. These allow an independent cross check of the published results. Correction factors for the simulated events have been either derived or common corrections, derived in the scope of the analysis published by CMS, have been used where applicable. The combination of these background estimation methods and corrections for simulated events was found to give a good description of the collected data.

No significant excess hinting at additional Higgs bosons was found. Corresponding exclusion limits for new physics in the Higgs sector are set as a result of this thesis. Model independent interpretations, in the form of upper limits on the cross sections times branching ratio into two τ-leptons for the Higgs boson production mechanisms, are derived. In addition, model dependent interpretations of the results are given for the $m_{\mathrm{h}}^{\mathrm{mod+}}$ and hMSSM scenarios. Finally, likelihood-scans in the plane span by the cross section of the gluon-fusion and bottom-quark associated production mechanisms are performed. These offer an easy access to estimate a measure for the compatibility of new models and scenarios with the analysed data.

The results derived in this thesis represent the up to now most stringent limits set in direct searches for additional Higgs bosons. Compared to the limits derived in analyses of Run I data [3] the exclusion limits are extended by a factor of two in the m_{A} range. They
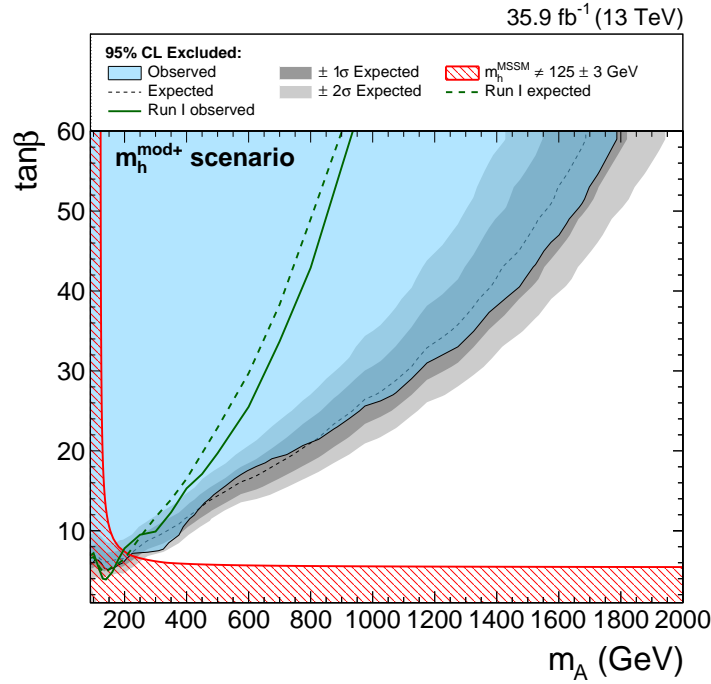
Figure 7.1: Exclusion limits for the $m_{\mathrm{h}}^{\mathrm{mod+}}$ scenario in the m_{A}-$\tan\beta$ plane. The exclusion limits derived based on the data recorded during Run I are also shown [3]. With the presented analysis of Run II data the exclusion limits are extended beyond those derived in any previous analysis.

further manifest the claim of the $\phi \to \tau\tau$ analysis as the leading analysis in searches for further Higgs bosons.

The derived results show no significant deviation from the Standard Model hypothesis. Consequently, the methods presented for estimating the background contributions in this analysis offer one of the best and furthest reaching descriptions of Standard Model processes in the di-τ final state used up to now.

Future improvements of results presented in this thesis can originate from two sources. For one the LHC is expected to be operated until the end of 2018 with similar performance as in 2016. By this time CMS is will have recorded about three times the current amount of data. With this increase of data, a significant improvement in the understanding of the detector and further improvements in the modelling of background contributions is expected. A second frontier of improvement is opened by more sophisticated analysis techniques and tools. Examples for these are multivariate analysis techniques, such as *Boosted Decision Trees*. The application of these tools and techniques is an active field of study as of today. First steps and studies towards the usage in a full analysis have already been taken and future analyses may greatly profit from these improvements.

Appendix

A.1 QCD multi-jet opposite charge to same charge extrapolation factors

Table A.1: Uncertainties used in the fit for the determination of the QCD multi-jet opposite to same charge extrapolation factors in the $e\tau_h$ and $\mu\tau_h$ decay channels. *Shape* uncertainties refer to uncertainties involving shape altering effects. VV refers to the Di-boson processes.

Systematic	Process	$\mu\tau_h$	$e\tau_h$
Luminosity uncertainty	$t\bar{t}$, VV, W+jets, Drell-Yan	6.2 %	6.2 %
Muon ID efficiency	$t\bar{t}$, VV, W+jets, Drell-Yan	2 %	-
Electron ID efficiency	$t\bar{t}$, VV, W+jets, Drell-Yan	-	2 %
Tau ID efficiency	$t\bar{t}$, VV, W+jets, Drell-Yan	8 %	8 %
τ_h energy scale	$Z \to ll$	shape	shape
$e \to \tau_h$ fake energy scale	$Z \to ll$	-	shape
top p_T reweighting	$t\bar{t}$	shape	shape
anti-μ discriminator	$Z \to ll$	30 %	-
anti-e discriminator	$Z \to ll$	-	30 %
Drell-Yan cross section uncertainty	Drell-Yan	20 %	20 %
Di-boson cross section uncertainty	Di-boson	10 %	10 %
$t\bar{t}$ cross section uncertainty	$t\bar{t}$	10 %	10 %
W+jets cross section uncertainty	W+jets	10 %	10 %
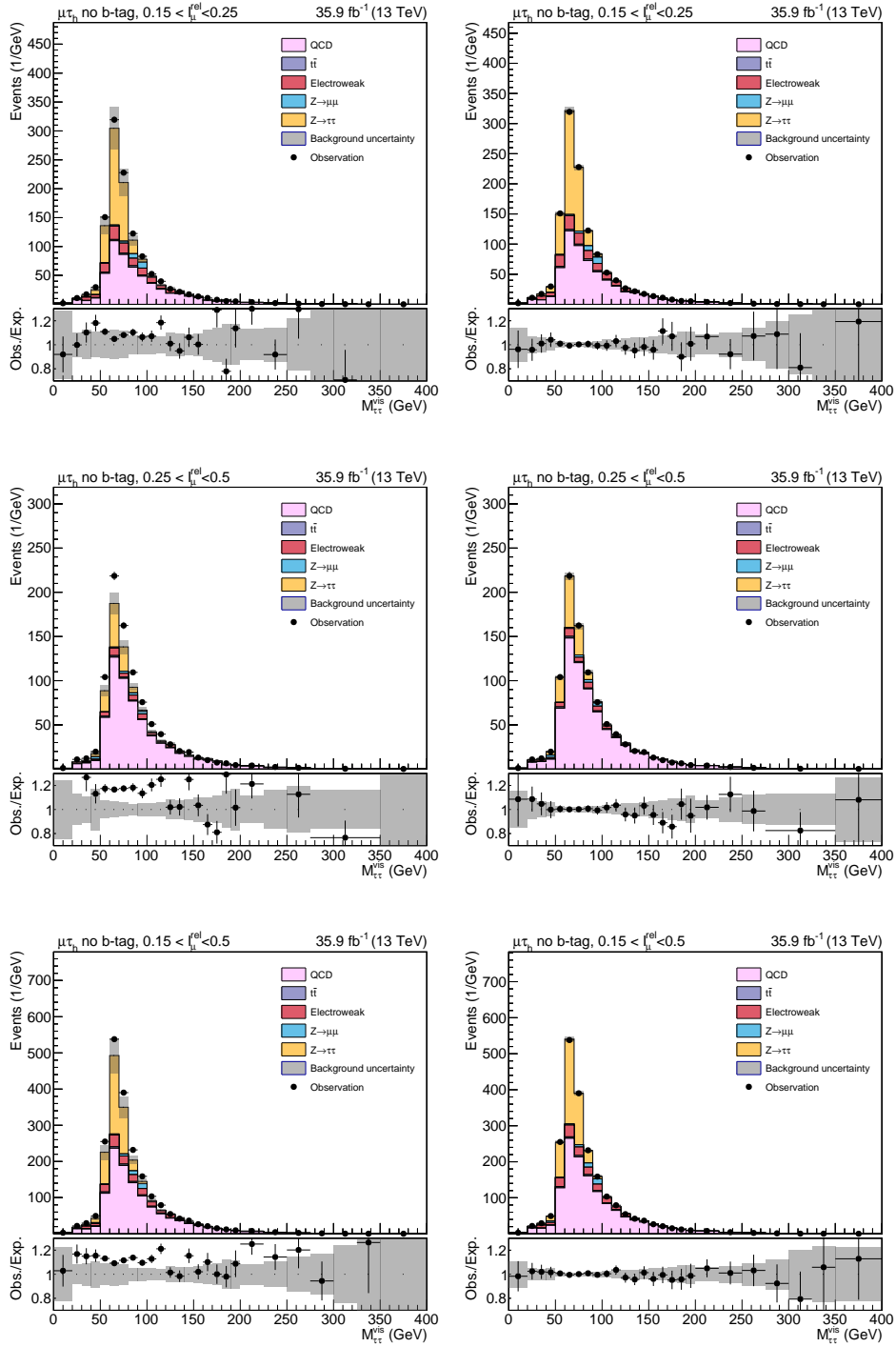
Figure A.1: Distributions of the invariant mass of the visible τ-lepton decay products in the opposite charge regions with relaxed relative isolation in the $\mu\tau_{\mathrm{h}}$ decay channel vetoing events with b-tagged jets. The distributions are shown for a selection requiring a relative isolation of $0.15 < I_\mu^{\mathrm{rel}} < 0.25$ (top), $0.25 < I_\mu^{\mathrm{rel}} < 0.5$ (middle) and $0.15 < I_\mu^{\mathrm{rel}} < 0.5$ (bottom). The distributions are shown prior to (left) and after (right) performing the fit of the QCD multi-jet contribution.
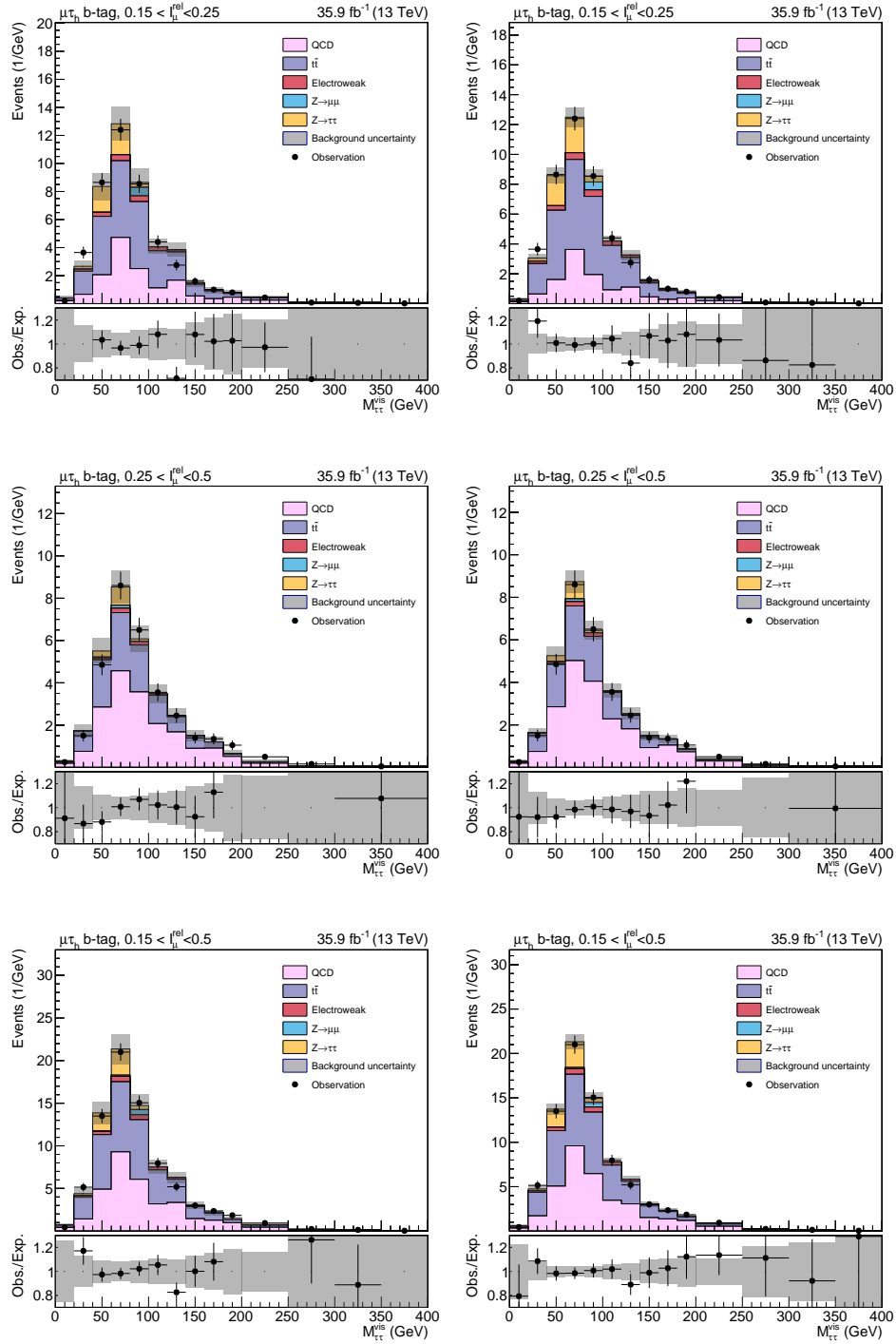
Figure A.2: Distributions of the invariant mass of the visible τ-lepton decay products in the opposite charge regions with relaxed relative isolation in the $\mu\tau_\mathrm{h}$ decay channel requiring at least one b-tagged jet in the event. The distributions are shown for a selection requiring a relative isolation of $0.15 < I_\mu^\mathrm{rel} < 0.25$ (top), $0.25 < I_\mu^\mathrm{rel} < 0.5$ (middle) and $0.15 < I_\mu^\mathrm{rel} < 0.5$ (bottom). The distributions are shown prior to (left) and after (right) performing the fit of the QCD multi-jet contribution.
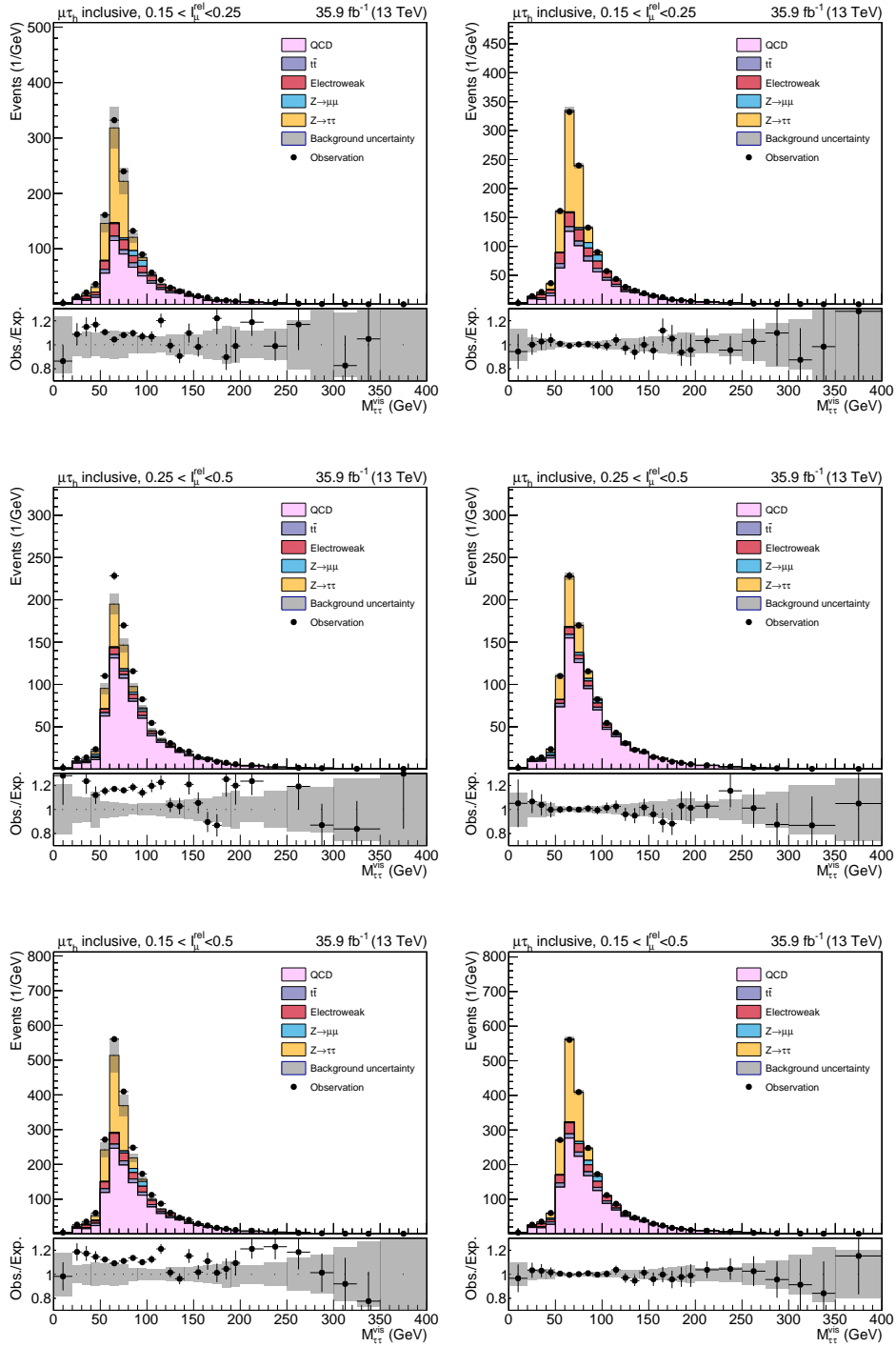
Figure A.3: Distributions of the invariant mass of the visible τ-lepton decay products in the opposite charge regions with relaxed relative isolation in the $\mu\tau_{\mathrm{h}}$ decay channel. The distributions are shown for a selection requiring a relative isolation of $0.15 < I_\mu^{\mathrm{rel}} < 0.25$ (top), $0.25 < I_\mu^{\mathrm{rel}} < 0.5$ (middle) and $0.15 < I_\mu^{\mathrm{rel}} < 0.5$ (bottom). The distributions are shown prior to (left) and after (right) performing the fit of the QCD multi-jet contribution.
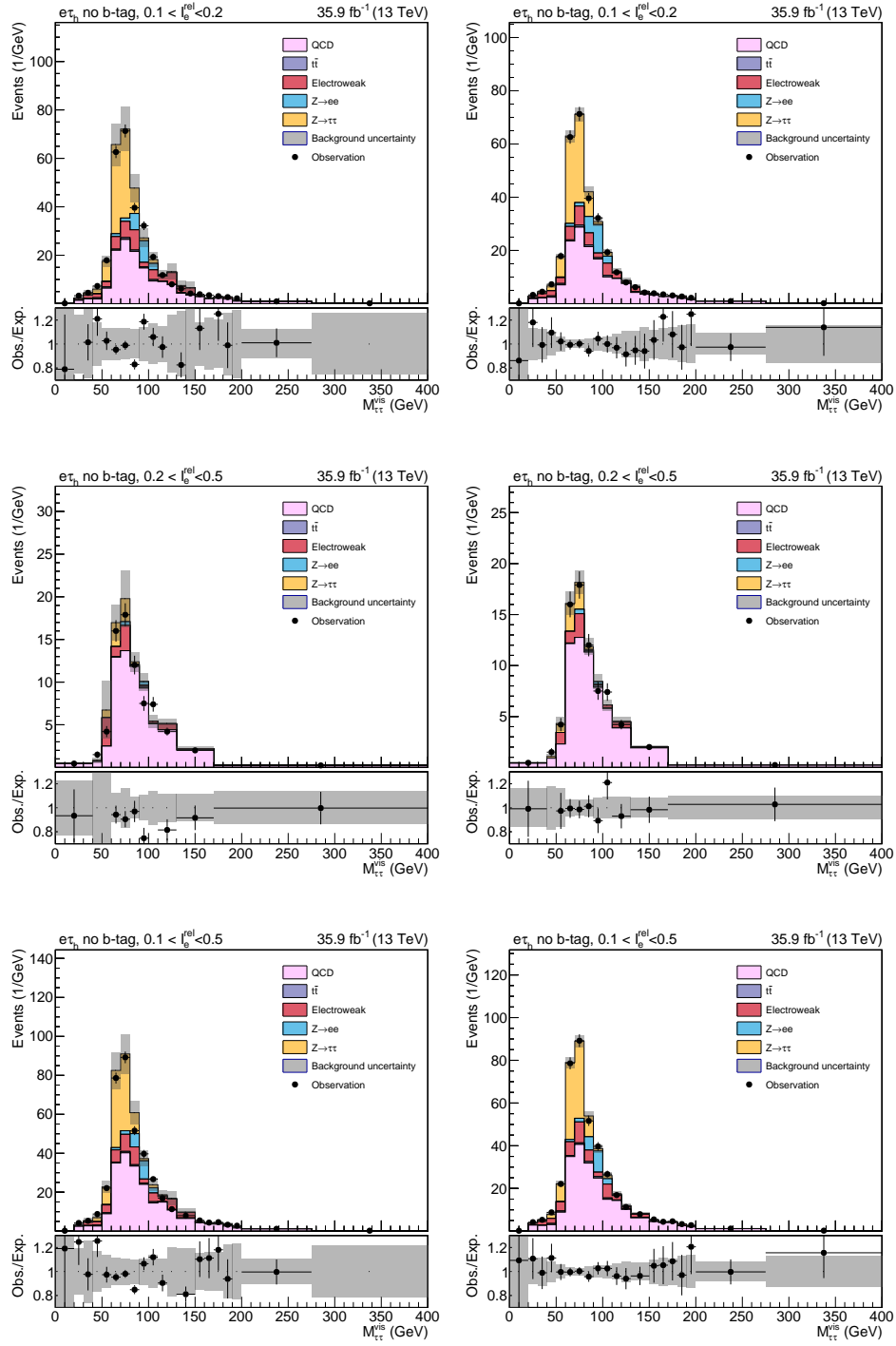
Figure A.4: Distributions of the invariant mass of the visible τ-lepton decay products in the opposite charge regions with relaxed relative isolation in the $e\tau_\mathrm{h}$ decay channel vetoing events with b-tagged jets. The distributions are shown for a selection requiring a relative isolation of $0.1 < I_\mathrm{e}^\mathrm{rel} < 0.2$ (top), $0.2 < I_\mathrm{e}^\mathrm{rel} < 0.5$ (middle) and $0.1 < I_\mathrm{e}^\mathrm{rel} < 0.5$ (bottom). The distributions are shown prior to (left) and after (right) performing the fit of the QCD multi-jet contribution.
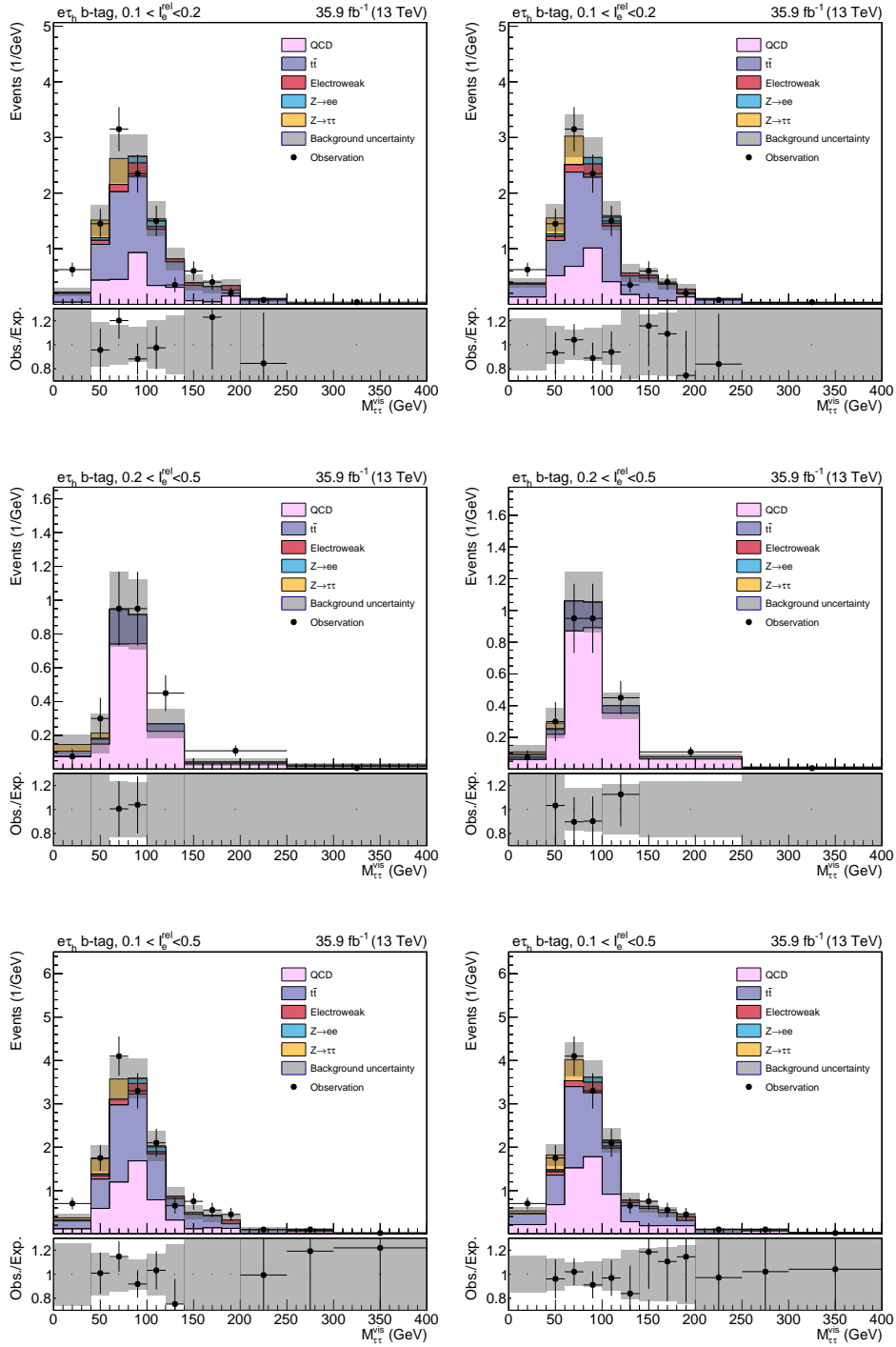
Figure A.5: Distributions of the invariant mass of the visible τ-lepton decay products in the opposite charge regions with relaxed relative isolation in the $e\tau_h$ decay channel requiring at least one b-tagged jet in the event. The distributions are shown for a selection requiring a relative isolation of $0.1 < I_e^{rel} < 0.2$ (top), $0.2 < I_e^{rel} < 0.5$ (middle) and $0.1 < I_e^{rel} < 0.5$ (bottom). The distributions are shown prior to (left) and after (right) performing the fit of the QCD multi-jet contribution.
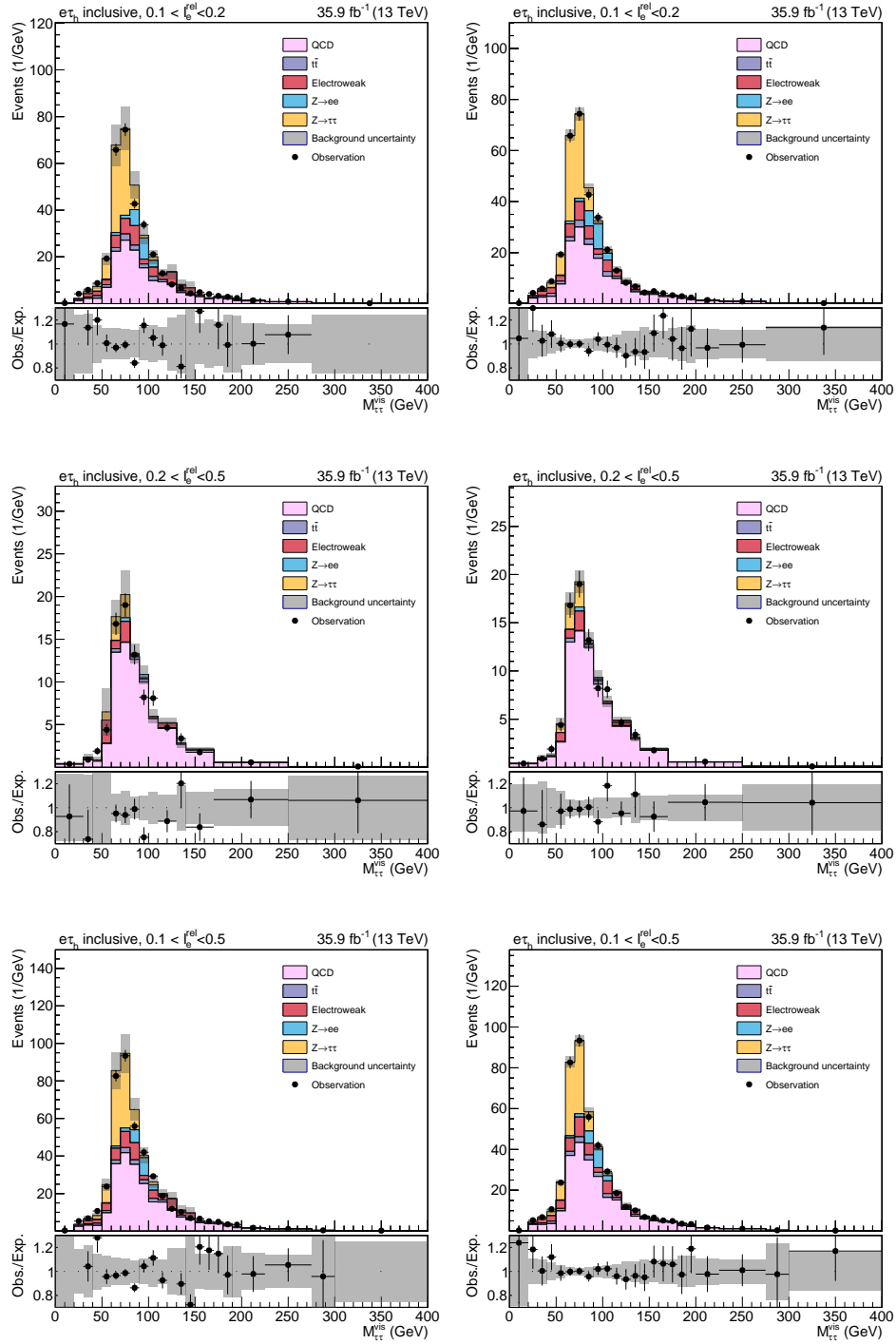
Figure A.6: Distributions of the invariant mass of the visible τ-lepton decay products in the opposite charge regions with relaxed relative isolation in the $e\tau_\mathrm{h}$ decay channel. The distributions are shown for a selection requiring a relative isolation of $0.1 < I_\mathrm{e}^\mathrm{rel} < 0.2$ (top), $0.2 < I_\mathrm{e}^\mathrm{rel} < 0.5$ (middle) and $0.1 < I_\mathrm{e}^\mathrm{rel} < 0.5$ (bottom). The distributions are shown prior to (left) and after (right) performing the fit of the QCD multi-jet contribution.

A.2 Tables of recorded datasets and generated events

Table A.2: Summary of datasets recorded by CMS during the year 2016 of the LHC Run II. The datasets are split by the objects triggered at level 1 and by run period. The corresponding integrated luminosity (int. $\mathcal{L}$) and number of recorded events are given.

Dataset	Run period	Int. $\mathcal{L}$ (fb^{-1})	Number of recorded events
Single Muon	Run 2016 B	5.788	158,145,722
Single Muon	Run 2016 C	2.573	67,441,308
Single Muon	Run 2016 D	4.248	98,017,996
Single Muon	Run 2016 E	4.009	90,963,495
Single Muon	Run 2016 F	3.102	65,489,554
Single Muon	Run 2016 G	7.540	149,916,849
Single Muon	Run 2016 H	8.606	174,035,164
Single Electron	Run 2016 B	5.788	246,440,440
Single Electron	Run 2016 C	2.573	97,259,854
Single Electron	Run 2016 D	4.248	148,167,727
Single Electron	Run 2016 E	4.009	117,321,545
Single Electron	Run 2016 F	3.102	70,593,532
Single Electron	Run 2016 G	7.540	153,330,123
Single Electron	Run 2016 H	8.606	129,018,252
Tau	Run 2016 B	5.788	68,727,458
Tau	Run 2016 C	2.573	36,931,473
Tau	Run 2016 D	4.248	56,827,771
Tau	Run 2016 E	4.009	58,348,773
Tau	Run 2016 F	3.102	40,549,716
Tau	Run 2016 G	7.540	79,557,782
Tau	Run 2016 H	8.606	76,758,754

Table A.3: Summary of generated samples for signal and background processes with their cross section and number of generated events

Process	Monte Carlo generator	$\sigma\mathcal{B}$ [pb]	Number of events
$gg \to \phi \to \tau\tau$	pythia 8	–	100,000-500,000
$gg \to b\bar{b}\phi \to \tau\tau$	pythia 8	–	100,000-500,000
$Z \to ll$, m=50 GeV	madgraph	5765.4	49,144,274
$Z \to ll$ +1 jet, m=50 GeV	madgraph	1012.5	65,485,168
$Z \to ll$ +2 jets, m=50 GeV	madgraph	332.8	19,970,551
$Z \to ll$ +3 jets, m=50 GeV	madgraph	101.8	5,856,110
$Z \to ll$ +4 jets, m=50 GeV	madgraph	54.8	4,197,868
$Z \to ll$, 10 GeV<m<50 GeV	madgraph	18610.0	49,144,274
W+jets	madgraph	61526.7	86,731,806
W+1 jet	madgraph	9644.5	42,207,819
W+2 jets	madgraph	3144.5	29,895,373
W+3 jets	madgraph	954.8	19,864,549
W+4 jets	madgraph	485.6	29,995,313
$t\bar{t}$	powheg	831.76	92,925,926
Single top quark, t-channel	powheg	136.02	67,240,808
Single anti-top quark, t-channel	powheg	80.95	38,811,017
Single top quark, tW	powheg	35.6	998,400
Single anti-top quark, $\bar{t}W$	powheg	35.6	967,600
$WW \to 1l1\nu2q$	aMC@NLO	49.997	5,176,114
$WZ \to 3l + 1\nu$+jets	aMC@NLO	4.708	1,930,828
$WZ \to 2l2q$	aMC@NLO	5.595	26,517,272
$WZ \to 1l3\nu$	aMC@NLO	3.05	1,703,772
$WZ \to 1l1\nu2q$	aMC@NLO	10.71	24,221,923
$ZZ \to 4l$	aMC@NLO	1.212	17,379,772
$ZZ \to 2l2q$	aMC@NLO	3.22	15,345,572
$VV \to 2l2\nu$	aMC@NLO	11.95	9,741,469
SM Higgs boson, $gg \to h \to \tau\tau$	powheg	3.05	1,471,061
SM Higgs boson, VBF $h \to \tau\tau$	powheg	0.237	1,499,400
SM Higgs boson, $W^+h \to \tau\tau$	powheg	0.0059	428,036
SM Higgs boson, $W^-h \to \tau\tau$	powheg	0.0037	445,200
SM Higgs boson, $Zh \to \tau\tau$	powheg	0.0594	571,597

A.3 Results using the simulation based background estimation method

A.3.1 Systematic uncertainties

Table A.4: Uncertainties used in the fit for the case of using the simulation based background estimation method in the $e\tau_h$, $\mu\tau_h$ and $\tau_h\tau_h$ decay channel. *Shape* uncertainties refer to uncertainties involving shape altering effects. VV refers to the Di-boson processes. MC represents all processes estimated based on simulated events.

Systematic	Process	$\mu\tau_h$	$e\tau_h$	$\tau_h\tau_h$
Luminosity uncertainty	MC	2.5 %	2.5 %	2.5 %
Muon ID efficiency	MC	2 %	–	–
Electron ID efficiency	MC	–	2 %	–
Tau ID efficiency, correlated	MC	4 %	4 %	8 %
Tau ID efficiency, uncorrelated	MC	3 %	3 %	9.2 %
High-pt tau ID efficiency	MC	shape	shape	shape
τ_h energy scale	$Z \to ll$	shape	shape	shape
$e \to \tau_h$ fake energy scale	$Z \to ll$	–	shape	–
electron energy scale	MC	–	shape	–
top p_T reweighting	$t\bar{t}$	shape	shape	shape
Z p_T reweighting	Drell-Yan	shape	shape	shape
anti-μ discriminator	$Z \to ll$	12 %	–	5 %
anti-e discriminator	$Z \to ll$	–	11 %	3 %
anti-jet discriminator, uncorrelated	$Z \to ll$	20 %	20 %	20 %
b-tagging efficiency	MC	1–3 %	1–4 %	1–4 %
b-tagging misstag rate	MC	1–4 %	1–3 %	1–5 %
$\not{E}_T$ resolution	Drell-Yan W+jets, signal	1–2 %	1–3 %	–
$\not{E}_T$ scale	Drell-Yan W+jets, signal	1–4 %	1–4 %	–
$\not{E}_T$ unclustered energy	$t\bar{t}$, VV	1–5 %	1–5 %	–
$\not{E}_T$ jet energy	$t\bar{t}$, VV	1–3 %	1–4 %	–
$Z \to \tau\tau$ acceptance	$Z \to \tau\tau$	1–2 %	2 %	5–7 %
QCD normalisation, syst	QCD multi-jet	4–60 %	12–60 %	12–14 %
QCD normalisation, stat	QCD multi-jet	–	–	2–20 %
W+jets OS/SS factor, syst	W+jets	1.2–2.4 %	1.9 %	–
W+jets OS/SS factor, stat	W+jets	1.8–2.2 %	2.4–2.9 %	–
W+jets m_T factor, syst	W+jets	20 %	20 %	–
W+jets m_T factor, stat	W+jets	2–14 %	2–17 %	–
Drell-Yan cross section uncertainty	Drell-Yan	4 %	4 %	4 %
Di-boson cross section uncertainty	Di-boson	5 %	5 %	5 %
$t\bar{t}$ cross section uncertainty	$t\bar{t}$	6 %	6 %	6 %
W+jets cross section uncertainty	W+jets	–	–	4 %

A.3.2 Goodness-of-fit test
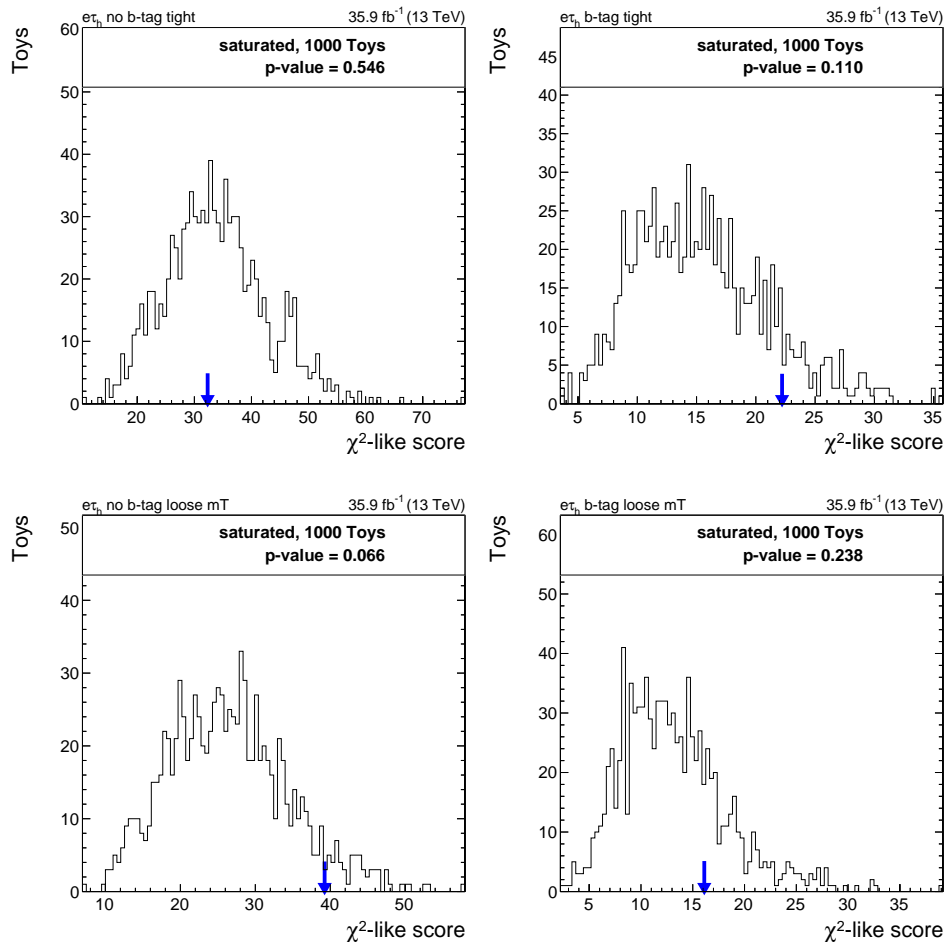
Figure A.7: Goodness of Fit in the $e\tau_h$ channel using the simulation based method and the saturated approach.
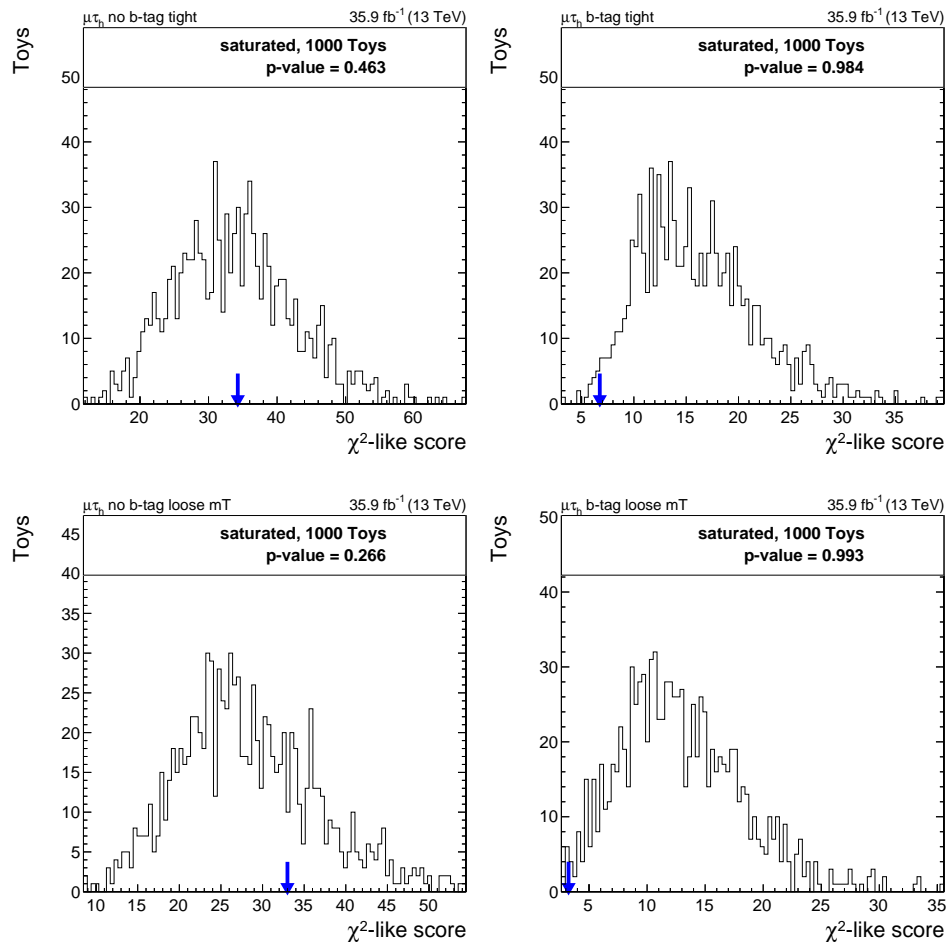
Figure A.8: Goodness of Fit in the $\mu\tau_\mathrm{h}$ channel using the simulation based method and the saturated approach.
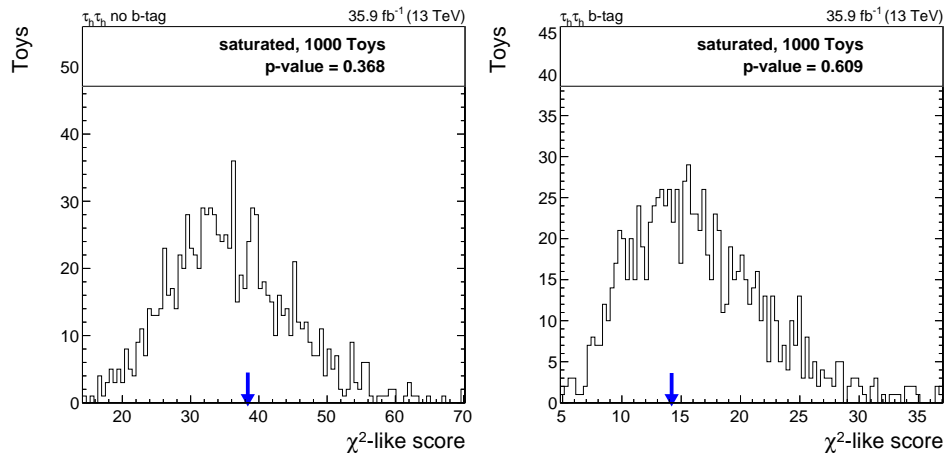
Figure A.9: Goodness of Fit in the $\tau_h\tau_h$ channel using the simulation based method and the saturated approach.

A.3.3 Prefit $m_{\mathrm{T}}^{\mathrm{tot}}$ distributions
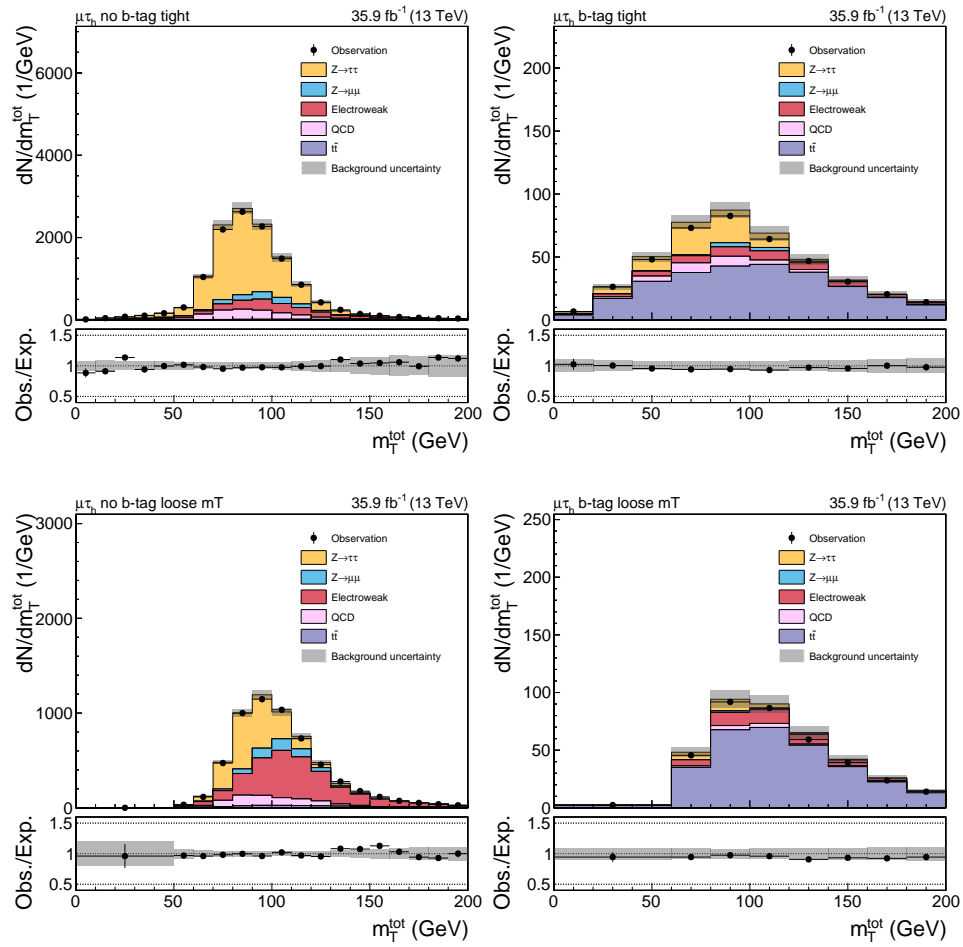
Figure A.10: Prefit distributions of $m_{\mathrm{T}}^{\mathrm{tot}}$ in the $\mu\tau_{\mathrm{h}}$ decay channel. The distributions are given for the $\mu\tau_{\mathrm{h}}$ no b-tag tight (top left), $\mu\tau_{\mathrm{h}}$ b-tag tight (top right), $\mu\tau_{\mathrm{h}}$ no b-tag loose mT (bottom left) and $\mu\tau_{\mathrm{h}}$ b-tag loose mT (bottom right) categories.
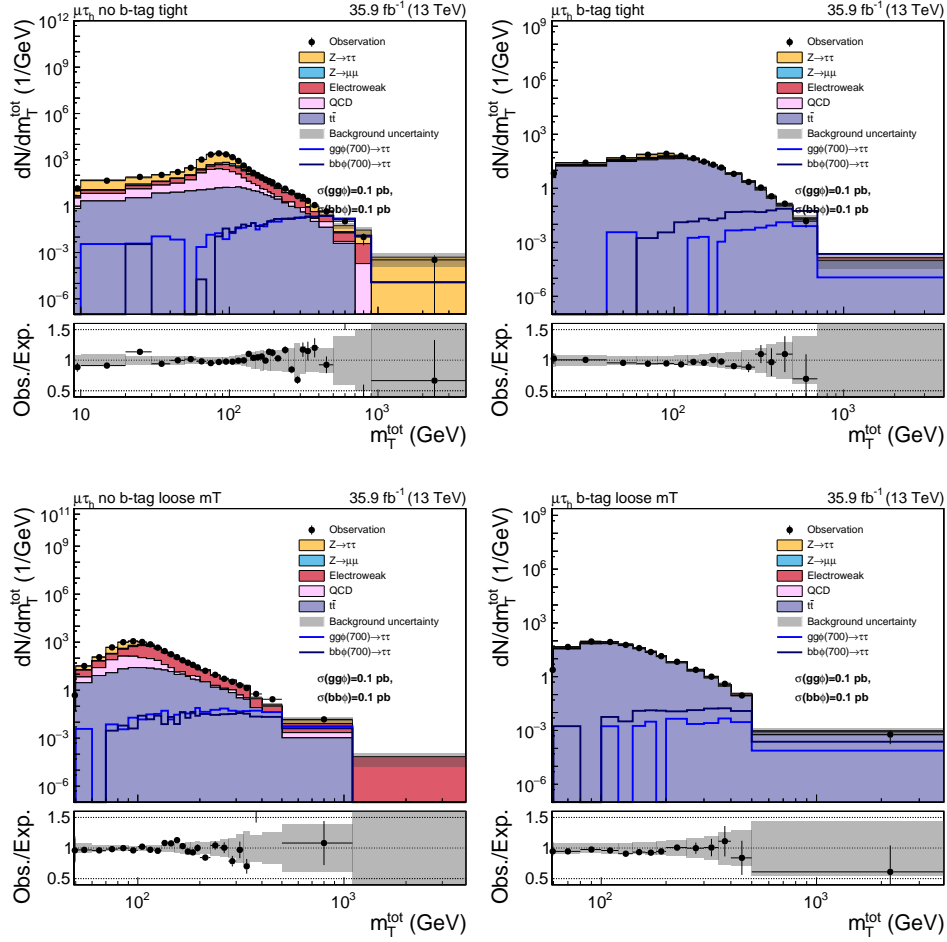
Figure A.11: Prefit distributions of m_T^{tot} in the $\mu\tau_h$ decay channel. The distributions are given for the $\mu\tau_h$ no b-tag tight (top left), $\mu\tau_h$ b-tag tight (top right), $\mu\tau_h$ no b-tag loose mT (bottom left) and $\mu\tau_h$ b-tag loose mT (bottom right) categories.
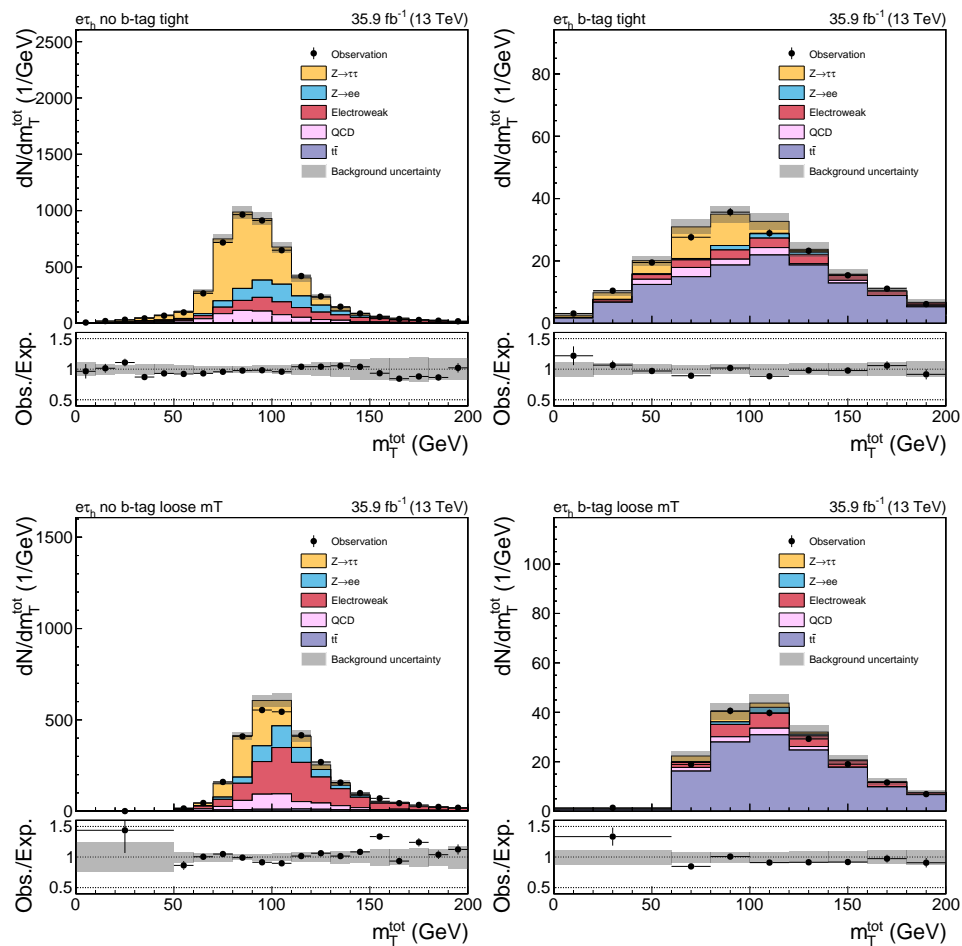
Figure A.12: Prefit distributions of $m_\mathrm{T}^\mathrm{tot}$ in the $e\tau_\mathrm{h}$ decay channel. The distributions are given for the $e\tau_\mathrm{h}$ no b-tag tight (top left), $e\tau_\mathrm{h}$ b-tag tight (top right), $e\tau_\mathrm{h}$ no b-tag loose mT (bottom left) and $e\tau_\mathrm{h}$ b-tag loose mT (bottom right) categories.
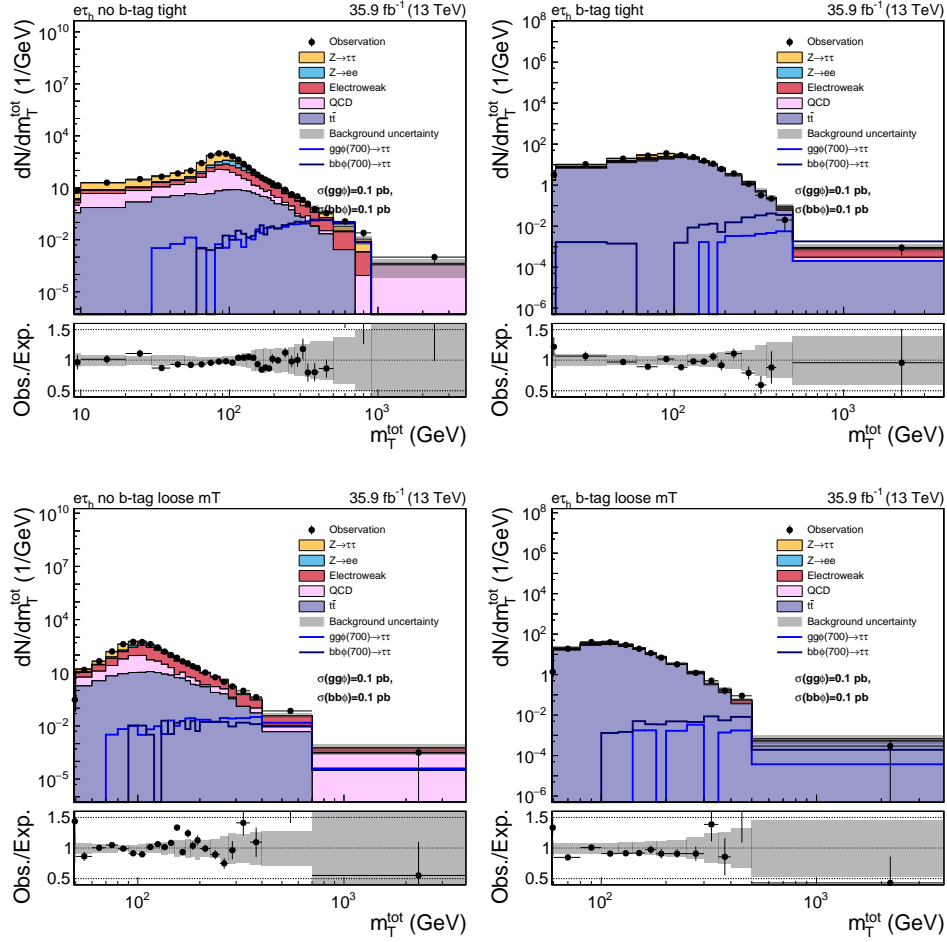
Figure A.13: Prefit distributions of m_T^{tot} in the $e\tau_h$ decay channel. The distributions are given for the $e\tau_h$ no b-tag tight (top left), $e\tau_h$ b-tag tight (top right), $e\tau_h$ no b-tag loose mT (bottom left) and $e\tau_h$ b-tag loose mT (bottom right) categories.
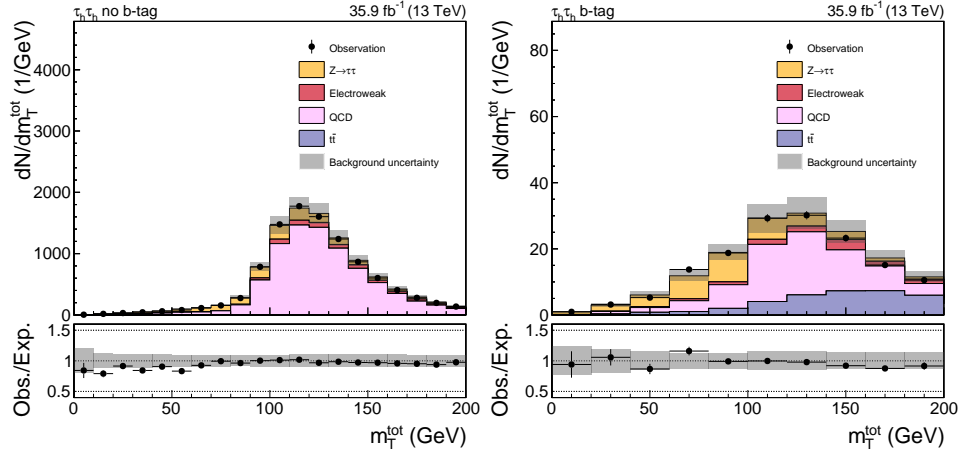
Figure A.14: Prefit distributions of m_T^{tot} in the $\tau_h\tau_h$ decay channel. The distributions are given for the $\tau_h\tau_h$ no b-tag (left) and $\tau_h\tau_h$ b-tag (right) categories.
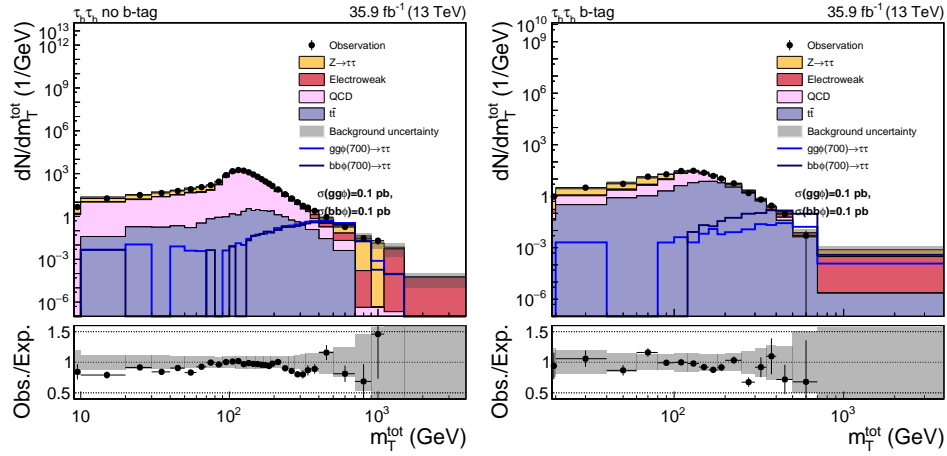
Figure A.15: Prefit distributions of m_T^{tot} in the $\tau_h\tau_h$ decay channel. The distributions are given for the $\tau_h\tau_h$ no b-tag (left) and $\tau_h\tau_h$ b-tag (right) categories.

A.3.4 Postfit $m_\mathrm{T}^\mathrm{tot}$ distributions
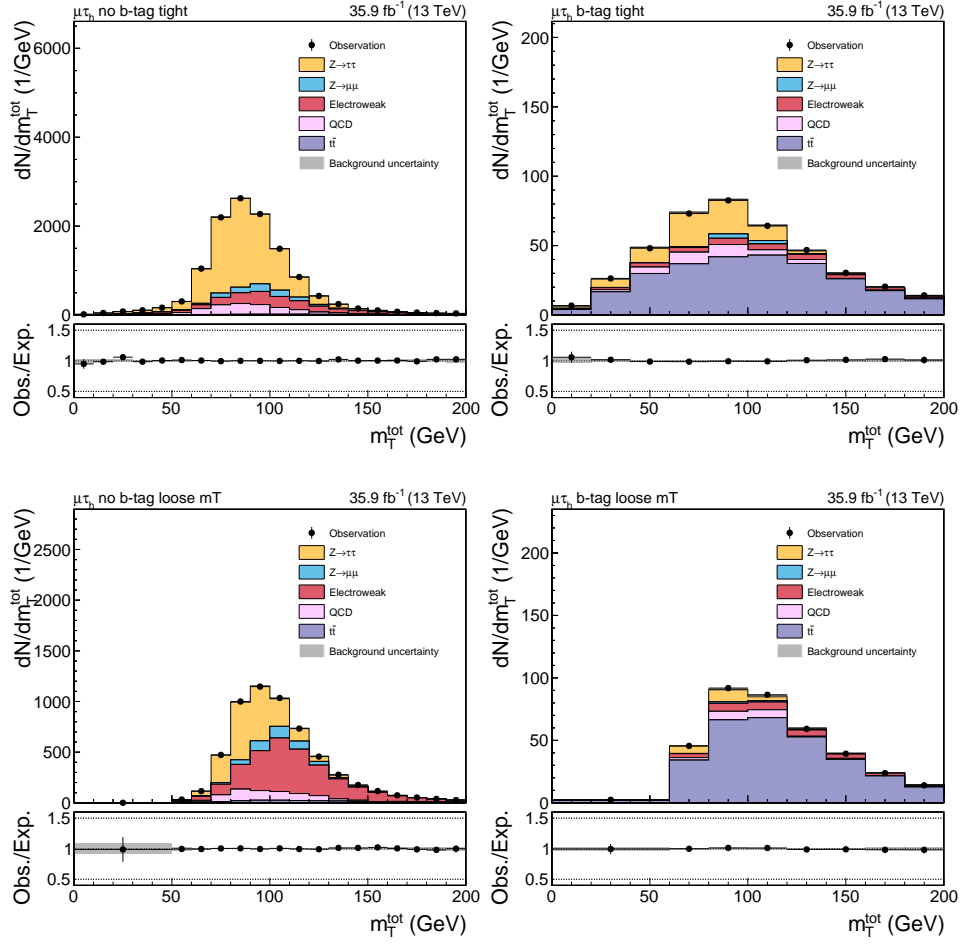
Figure A.16: Postfit distributions of $m_\mathrm{T}^\mathrm{tot}$ in the $\mu\tau_\mathrm{h}$ decay channel. The postfit distributions are evaluated based on the pulls of the nuisance parameters in the signal-plus-background fit. For the uncertainty bands the full uncertainty model is considered. The distributions are given for the $\mu\tau_\mathrm{h}$ no b-tag tight (top left), $\mu\tau_\mathrm{h}$ b-tag tight (top right), $\mu\tau_\mathrm{h}$ no b-tag loose mT (bottom left) and $\mu\tau_\mathrm{h}$ b-tag loose mT (bottom right) categories.
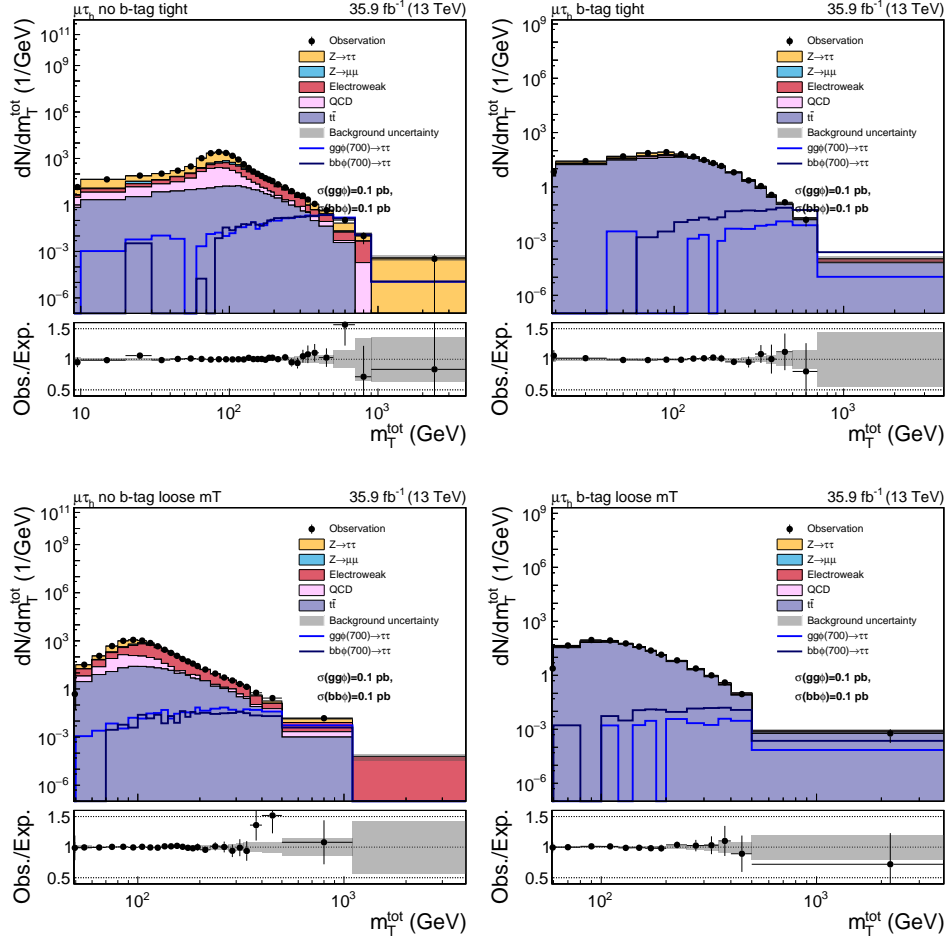
Figure A.17: Postfit distributions of m_T^{tot} in the $\mu\tau_h$ decay channel. The postfit distributions are evaluated based on the pulls of the nuisance parameters in the signal-plus-background fit. For the uncertainty bands the full uncertainty model is considered. The distributions are given for the $\mu\tau_h$ no b-tag tight (top left), $\mu\tau_h$ b-tag tight (top right), $\mu\tau_h$ no b-tag loose mT (bottom left) and $\mu\tau_h$ b-tag loose mT (bottom right) categories.
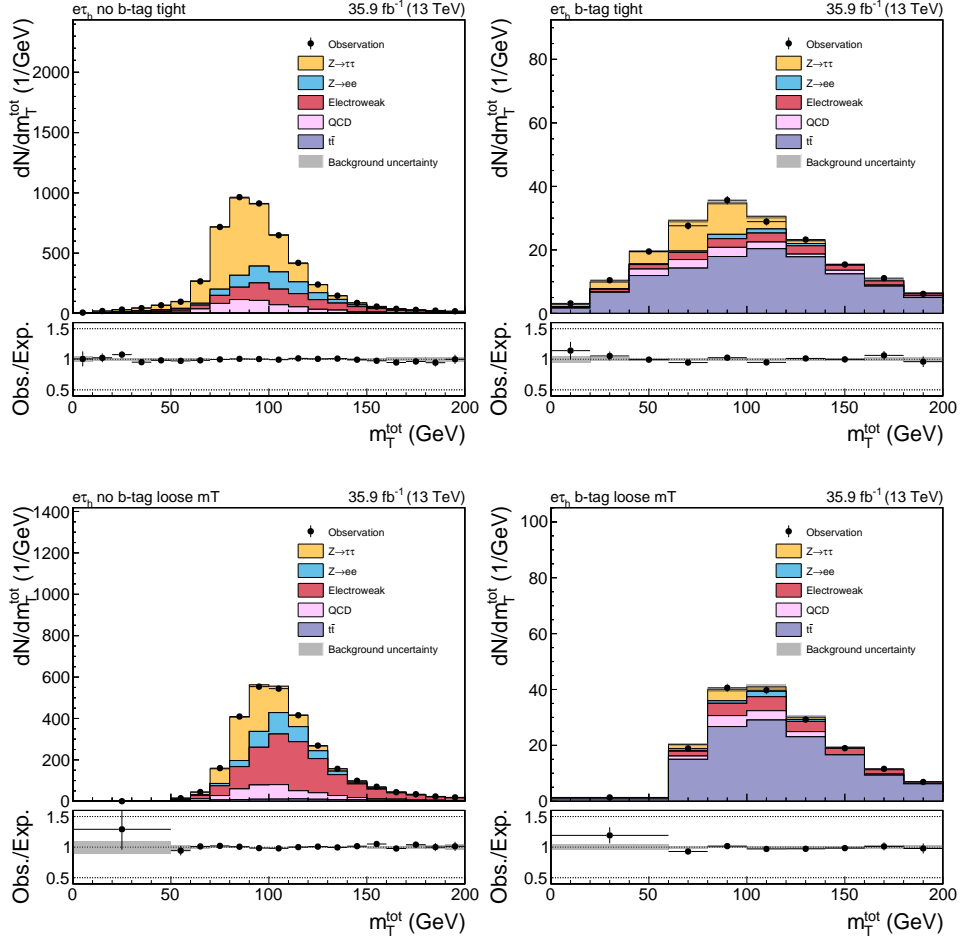
Figure A.18: Postfit distributions of m_T^{tot} in the $e\tau_h$ decay channel. The postfit distributions are evaluated based on the pulls of the nuisance parameters in the signal-plus-background fit. For the uncertainty bands the full uncertainty model is considered. The distributions are given for the $e\tau_h$ no b-tag tight (top left), $e\tau_h$ b-tag tight (top right), $e\tau_h$ no b-tag loose mT (bottom left) and $e\tau_h$ b-tag loose mT (bottom right) categories.
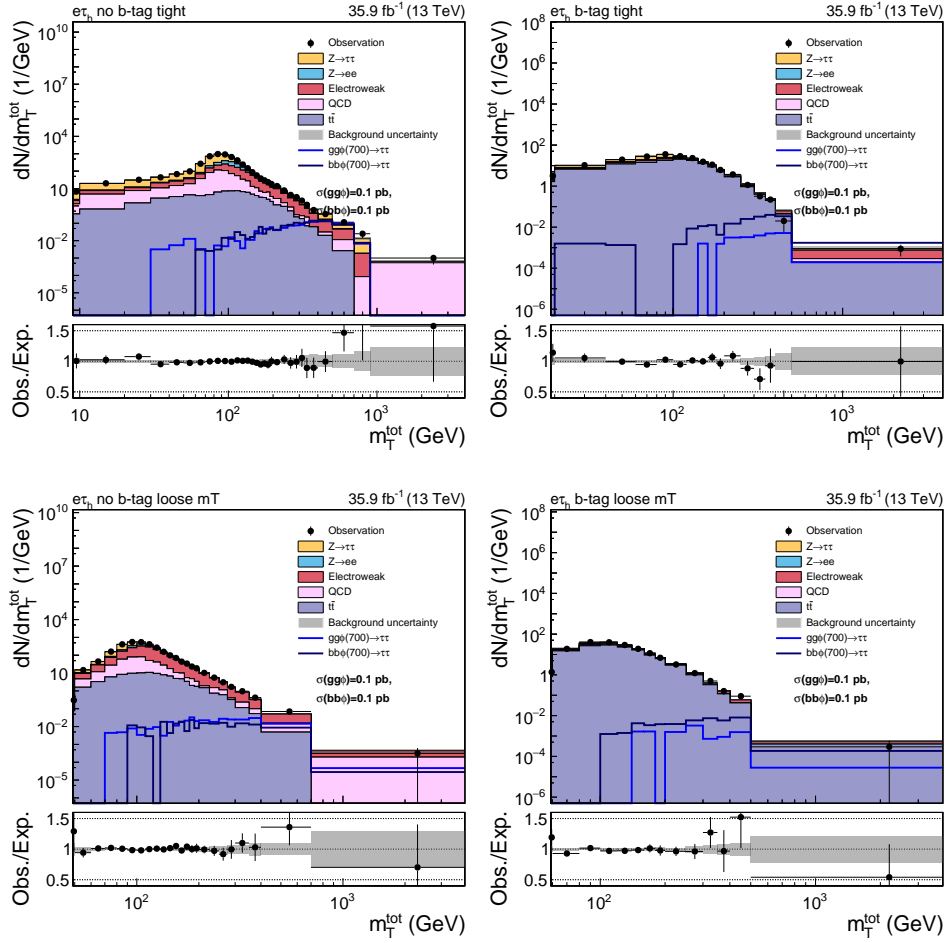
Figure A.19: Postfit distributions of m_T^{tot} in the $e\tau_h$ decay channel. The postfit distributions are evaluated based on the pulls of the nuisance parameters in the signal-plus-background fit. For the uncertainty bands the full uncertainty model is considered. The distributions are given for the $e\tau_h$ no b-tag tight (top left), $e\tau_h$ b-tag tight (top right), $e\tau_h$ no b-tag loose mT (bottom left) and $e\tau_h$ b-tag loose mT (bottom right) categories.
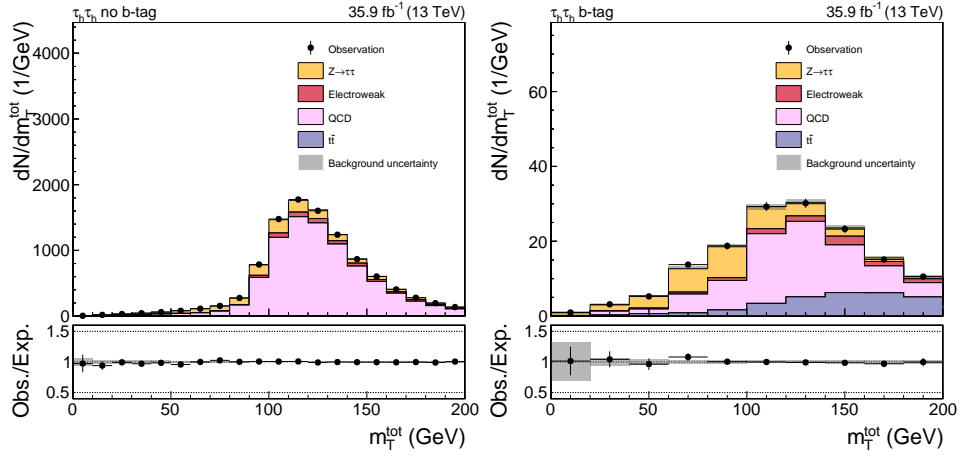
Figure A.20: Postfit distributions of $m_\mathrm{T}^\mathrm{tot}$ in the $\tau_\mathrm{h}\tau_\mathrm{h}$ decay channel. The postfit distributions are evaluated based on the pulls of the nuisance parameters in the signal-plus-background fit. For the uncertainty bands the full uncertainty model is considered. The distributions are given for the $\tau_\mathrm{h}\tau_\mathrm{h}$ no b-tag (left) and $\tau_\mathrm{h}\tau_\mathrm{h}$ b-tag (right) categories.
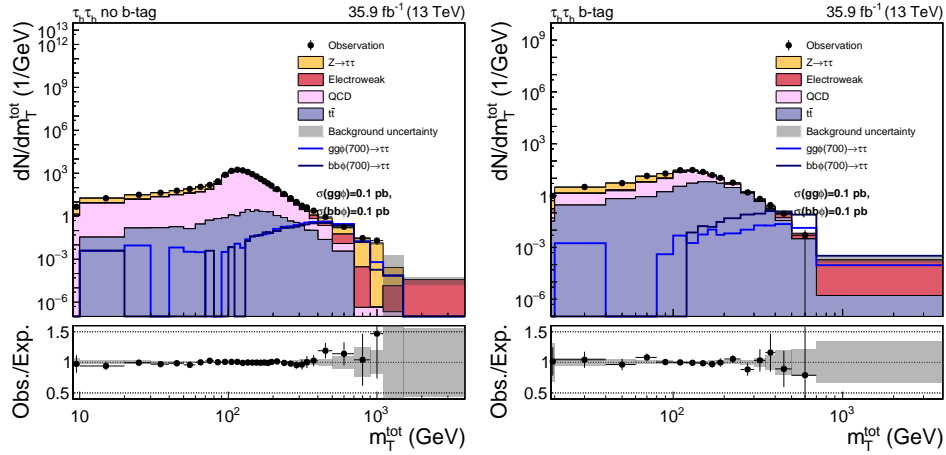
Figure A.21: Postfit distributions of $m_\mathrm{T}^\mathrm{tot}$ in the $\tau_\mathrm{h}\tau_\mathrm{h}$ decay channel. The postfit distributions are evaluated based on the pulls of the nuisance parameters in the signal-plus-background fit. For the uncertainty bands the full uncertainty model is considered. The distributions are given for the $\tau_\mathrm{h}\tau_\mathrm{h}$ no b-tag (left) and $\tau_\mathrm{h}\tau_\mathrm{h}$ b-tag (right) categories.

A.3.5 Exclusion limits

(a) $\mu\tau_{\mathrm{h}}$, $gg \to \phi$

(b) $\mu\tau_{\mathrm{h}}$, $gg \to b\bar{b}\phi$

(c) $e\tau_{\mathrm{h}}$, $gg \to \phi$

(d) $e\tau_{\mathrm{h}}$, $gg \to b\bar{b}\phi$
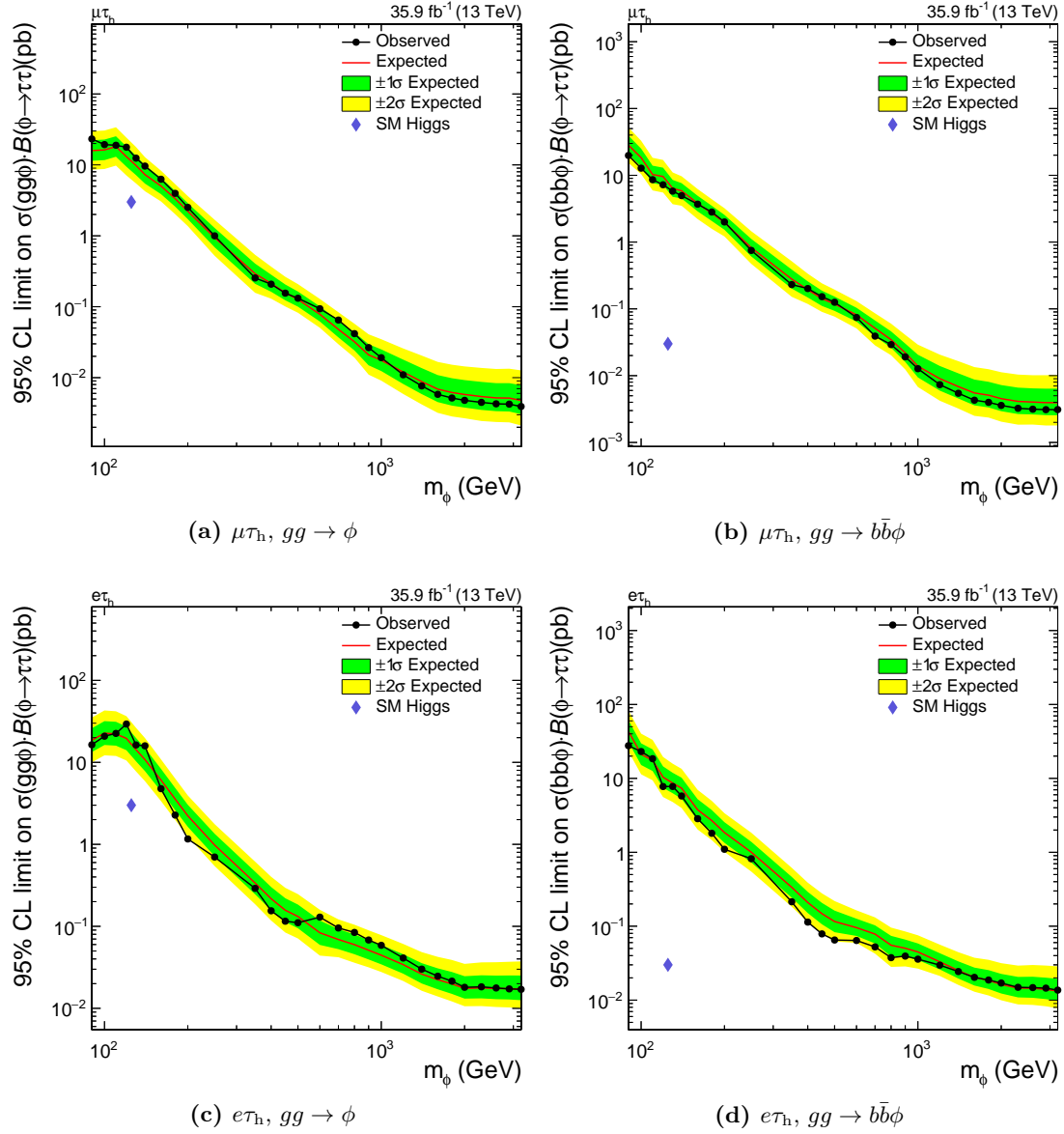
Figure A.22: Expected and observed exclusion limits at 95 % CL$_{\mathrm{S}}$ on the $\sigma\mathcal{B}$ for the $gg \to \phi$ (left) and $gg \to b\bar{b}\phi$ (right) production process. The exclusion limits are derived for the $\mu\tau_{\mathrm{h}}$ (top) and $e\tau_{\mathrm{h}}$ (bottom) decay channel. The cross section for the SM Higgs boson with a mass of 125 GeV is indicated by the blue marker. For the whole mass range no significant excess of the observation compared to the expectation is observed.

(a) $\tau_{\mathrm{h}}\tau_{\mathrm{h}}$, $gg \to \phi$ **(b)** $\tau_{\mathrm{h}}\tau_{\mathrm{h}}$, $gg \to b\bar{b}\phi$
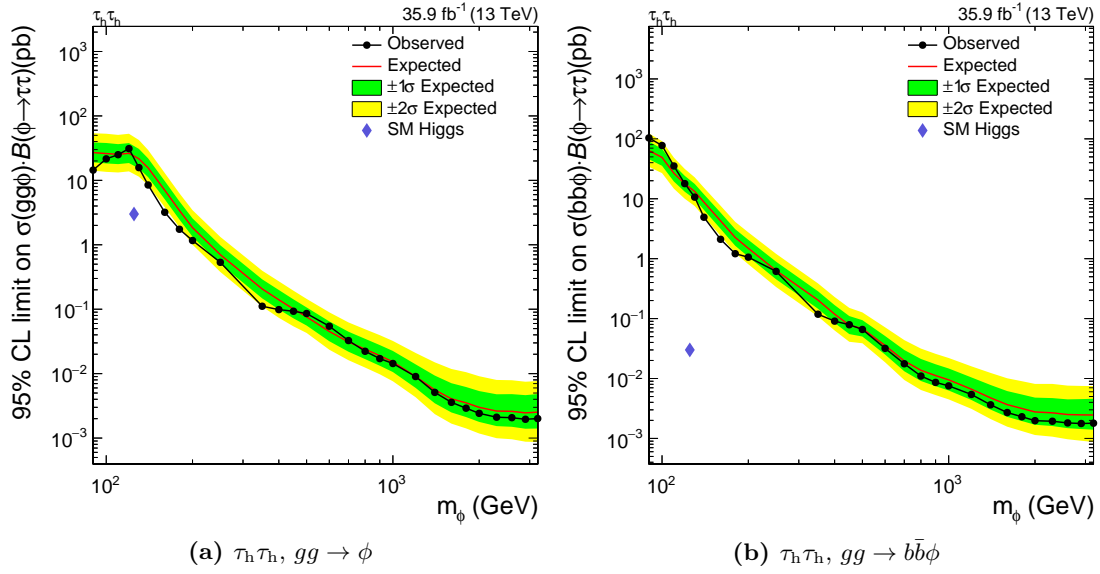
Figure A.23: Expected and observed exclusion limits at 95 % CL$_\mathrm{S}$ on the $\sigma\mathcal{B}$ for the $gg \to \phi$ (left) and $gg \to b\bar{b}\phi$ (right) production process. The exclusion limits are derived for the $\tau_{\mathrm{h}}\tau_{\mathrm{h}}$ decay channel. The cross section for the SM Higgs boson with a mass of 125 GeV is indicated by the blue marker. For the whole mass range no significant excess of the observation compared to the expectation is observed.

A.3.6 Likelihood scan in *ggφ-bbφ* plane

(a) $m_\phi = 90\,\text{GeV}$

(b) $m_\phi = 100\,\text{GeV}$

(c) $m_\phi = 110\,\text{GeV}$
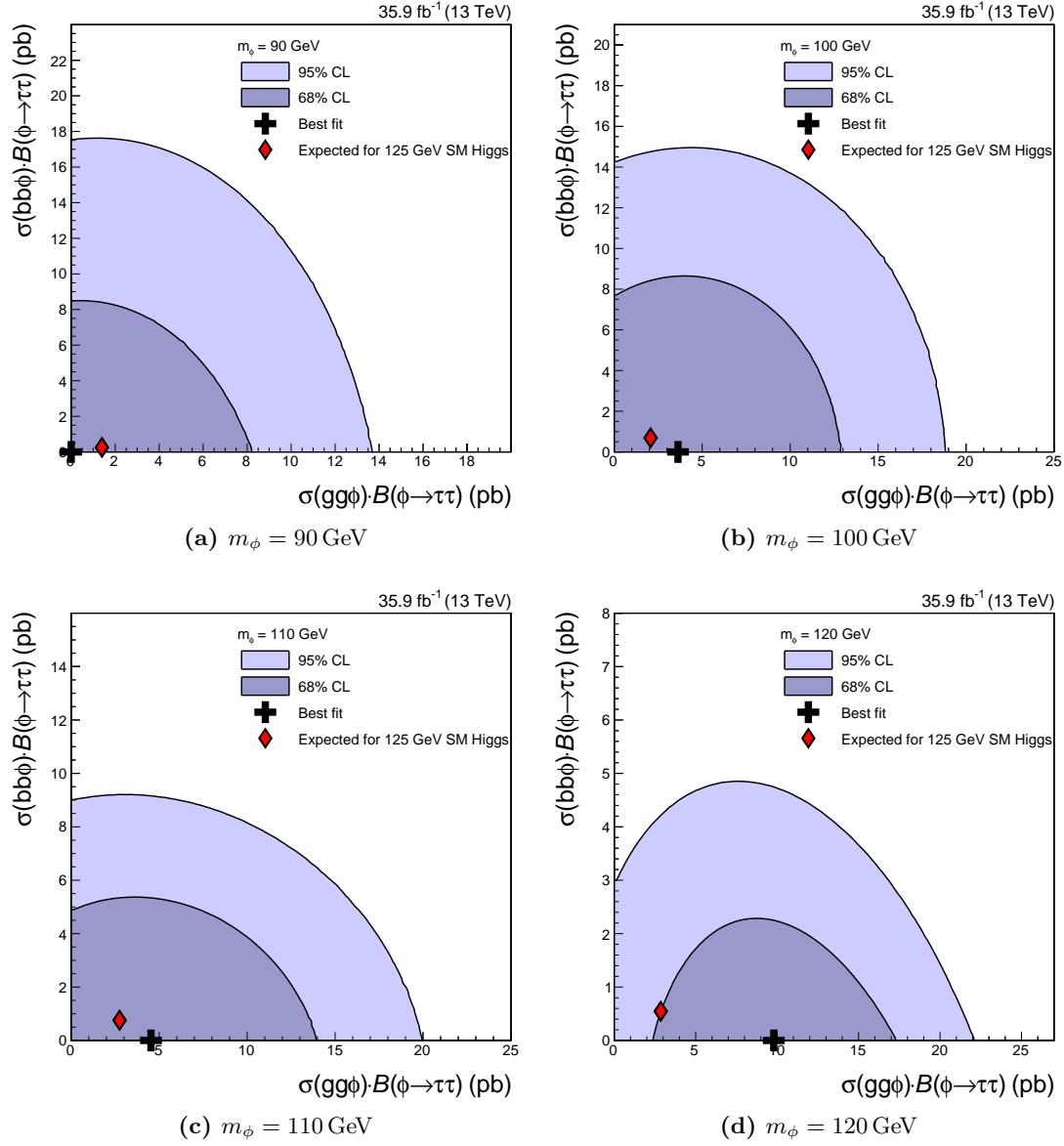
(d) $m_\phi = 120\,\text{GeV}$

Figure A.24: Likelihood scan in the *ggφ-bbφ* plane for four Higgs boson mass hypotheses $m_\phi = 90, 100, 110, 120\,\text{GeV}$. The expected best-fit point in case the observation is equal to the background and the Standard Model Higgs boson with a mass of $m_\text{H} = 125\,\text{GeV}$ is indicated. It is found to be within the 68 % confidence level for all masses but the 600 and 700 GeV point. Likewise the origin indicating no Higgs boson with the given mass is observed is compatible within the 95 % confidence level for all masses.
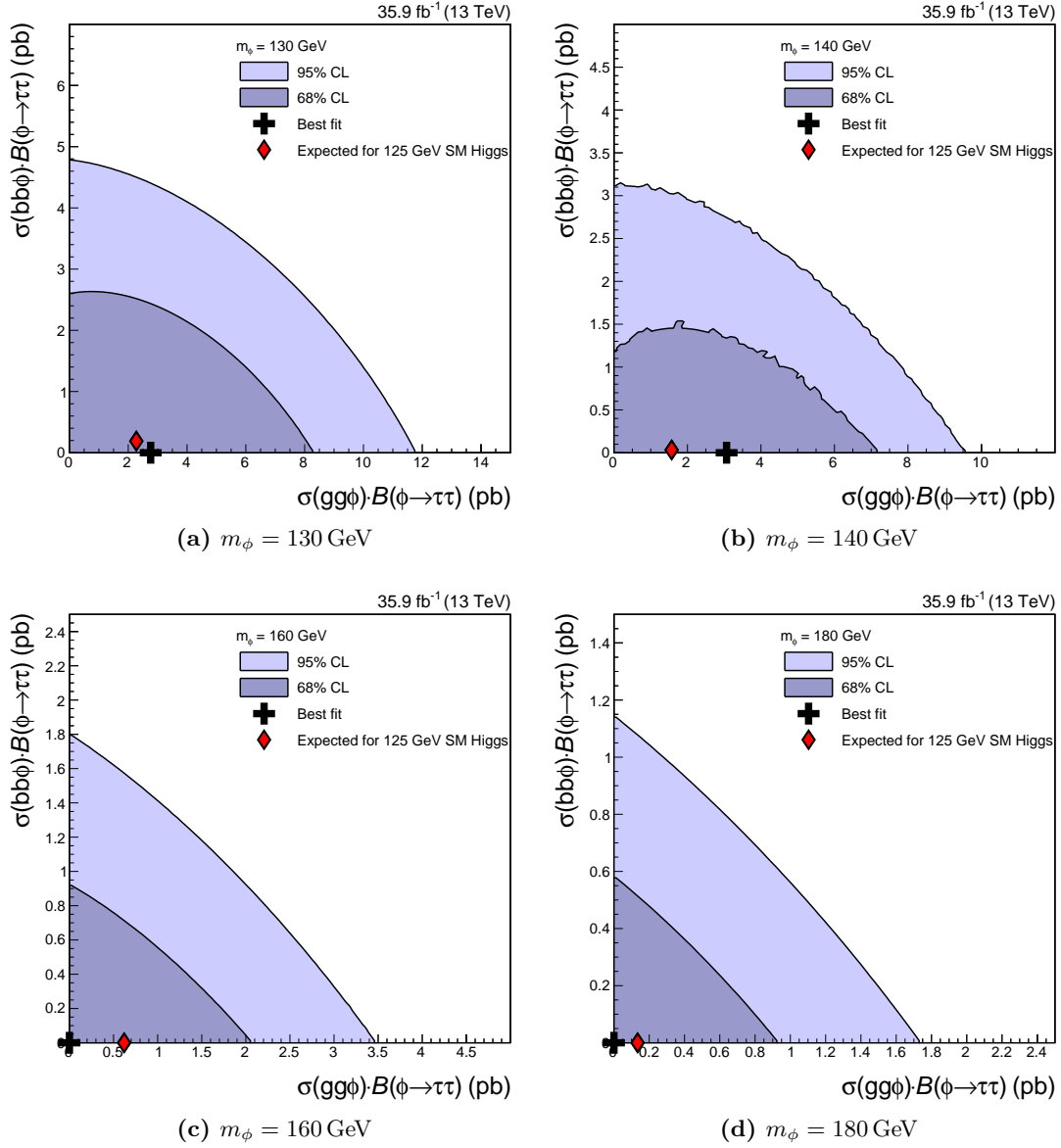
Figure A.25: Likelihood scan in the *ggφ-bbφ* plane for four Higgs boson mass hypotheses $m_\phi = 130, 140, 160, 180$ GeV. The expected best-fit point in case the observation is equal to the background and the Standard Model Higgs boson with a mass of $m_H = 125$ GeV is indicated. It is found to be within the 68 % confidence level for all masses but the 600 and 700 GeV point. Likewise the origin indicating no Higgs boson with the given mass is observed is compatible within the 95 % confidence level for all masses.
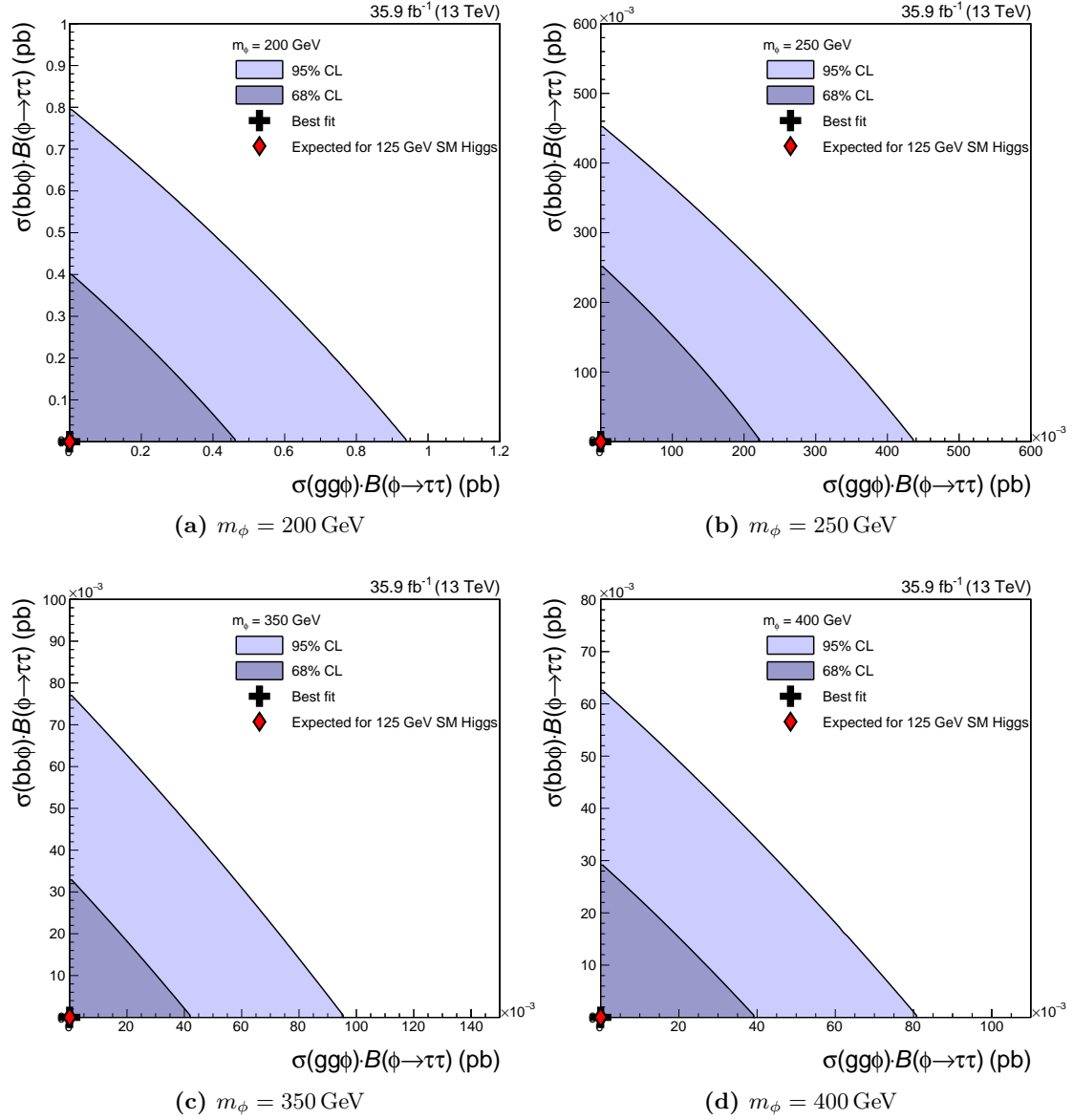
Figure A.26: Likelihood scan in the *ggφ-bbφ* plane for four Higgs boson mass hypotheses $m_\phi = 200, 250, 350, 400\,\text{GeV}$. The expected best-fit point in case the observation is equal to the background and the Standard Model Higgs boson with a mass of $m_\text{H} = 125\,\text{GeV}$ is indicated. It is found to be within the 68 % confidence level for all masses but the 600 and 700 GeV point. Likewise the origin indicating no Higgs boson with the given mass is observed is compatible within the 95 % confidence level for all masses.
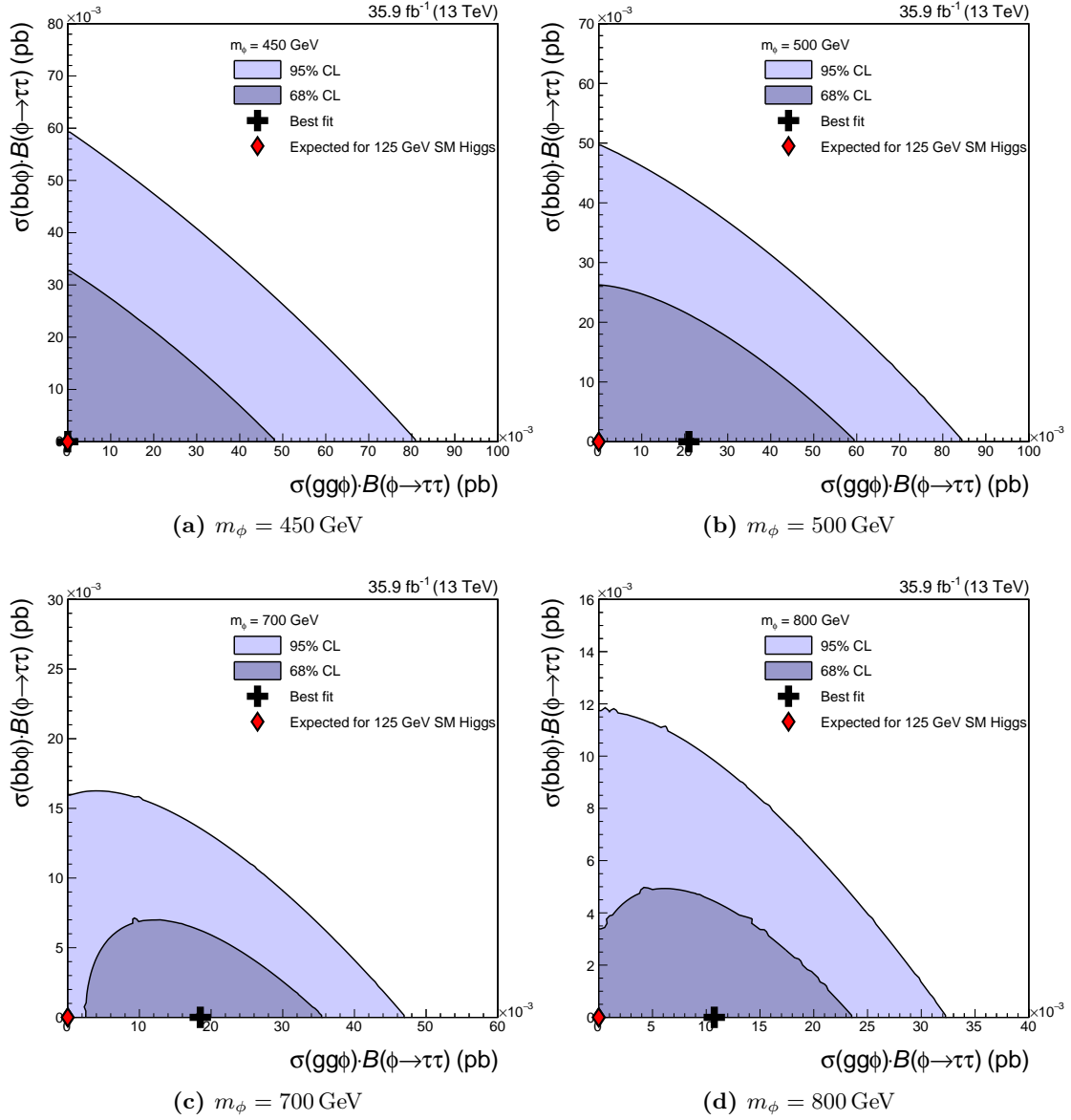
Figure A.27: Likelihood scan in the *ggφ-bbφ* plane for four Higgs boson mass hypotheses $m_\phi = 450, 500, 700, 800$ GeV. The expected best-fit point in case the observation is equal to the background and the Standard Model Higgs boson with a mass of $m_H = 125$ GeV is indicated. It is found to be within the 68 % confidence level for all masses but the 600 and 700 GeV point. Likewise the origin indicating no Higgs boson with the given mass is observed is compatible within the 95 % confidence level for all masses.
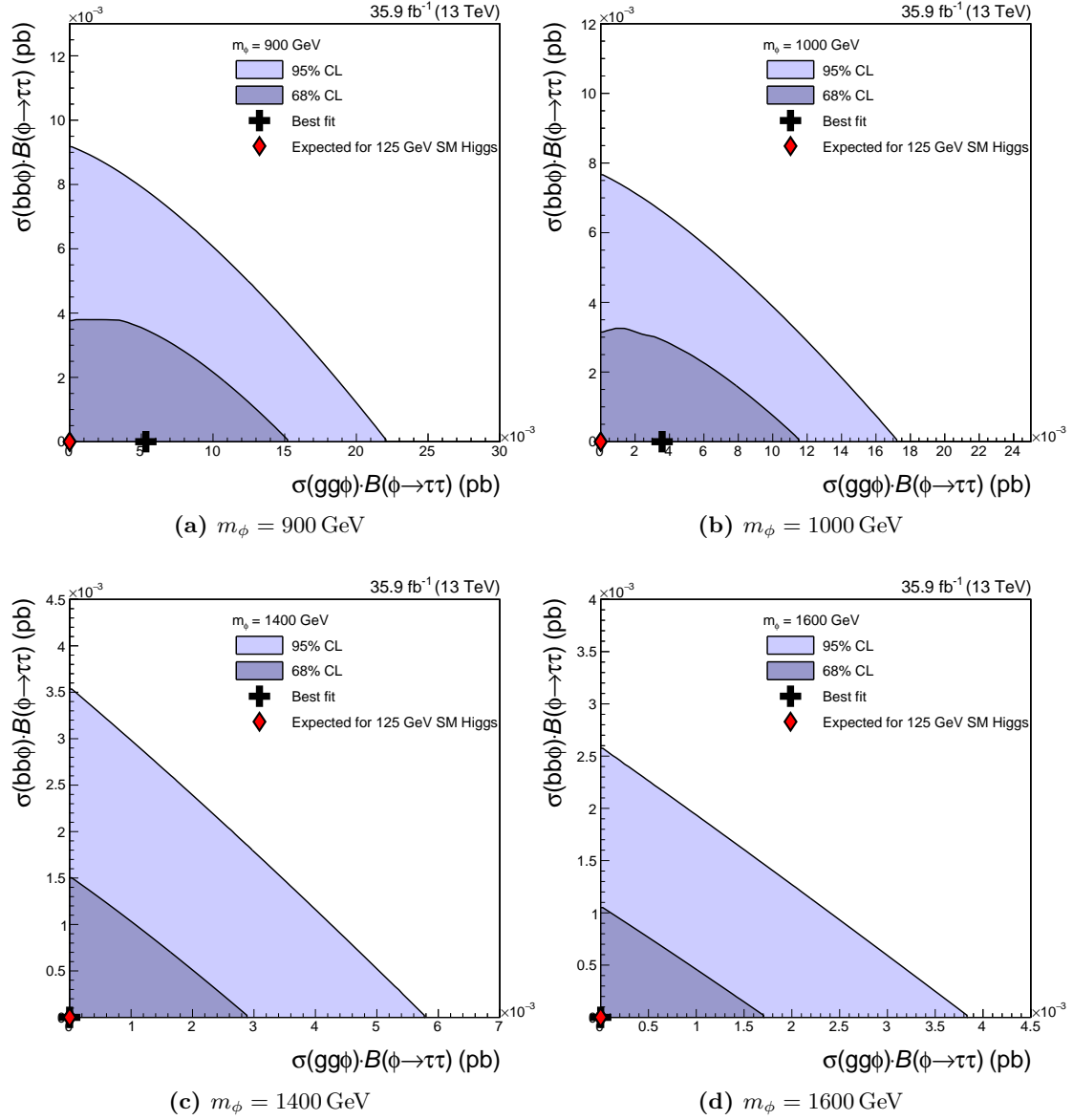
Figure A.28: Likelihood scan in the *ggφ-bbφ* plane for four Higgs boson mass hypotheses $m_\phi = 900, 1000, 1400, 1600 \, \text{GeV}$. The expected best-fit point in case the observation is equal to the background and the Standard Model Higgs boson with a mass of $m_\text{H} = 125 \, \text{GeV}$ is indicated. It is found to be within the 68 % confidence level for all masses but the 600 and 700 GeV point. Likewise the origin indicating no Higgs boson with the given mass is observed is compatible within the 95 % confidence level for all masses.
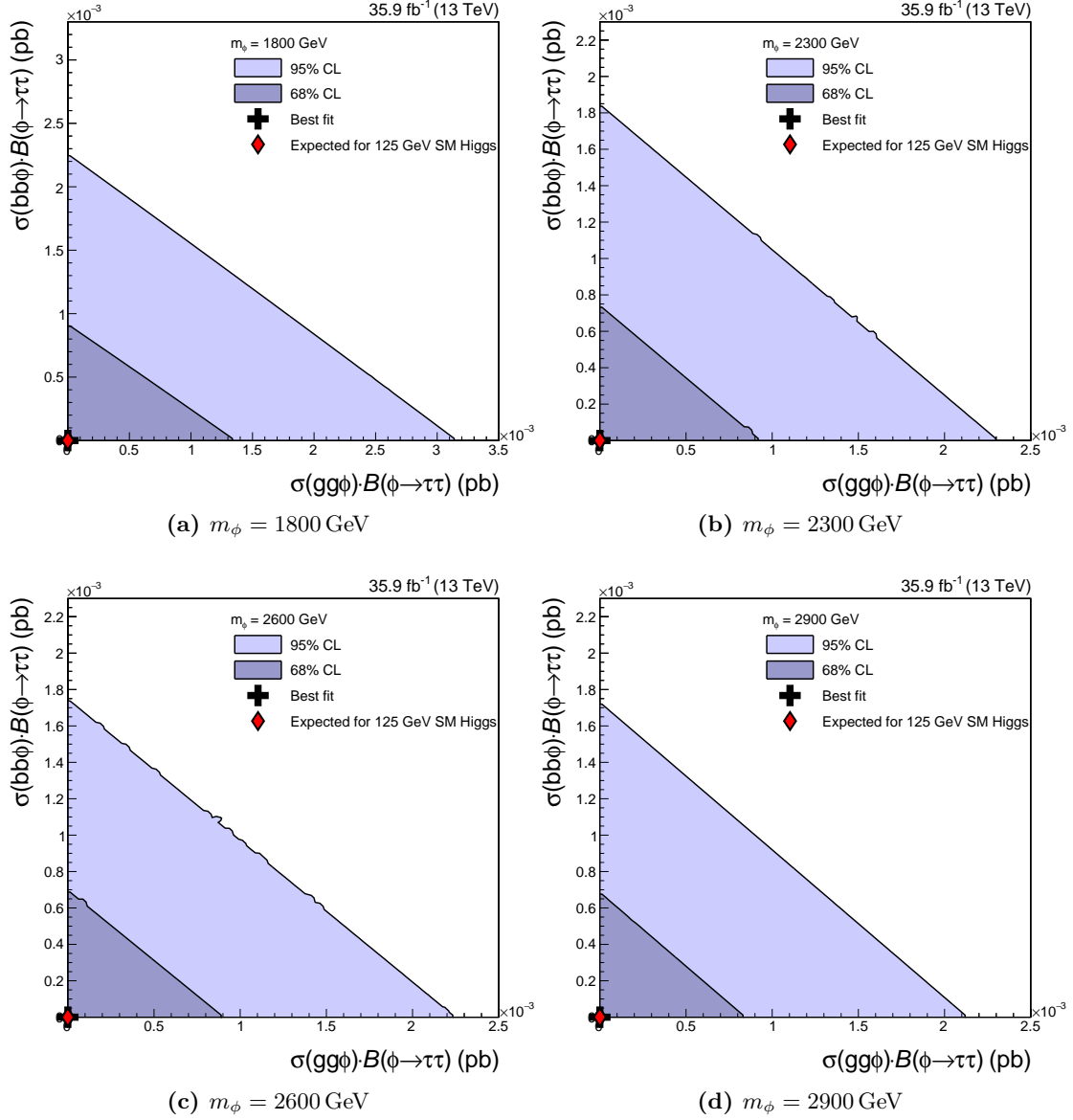
Figure A.29: Likelihood scan in the *ggφ-bbφ* plane for four Higgs boson mass hypotheses $m_\phi = 1800, 2300, 2600, 2900\,\text{GeV}$. The expected best-fit point in case the observation is equal to the background and the Standard Model Higgs boson with a mass of $m_\text{H} = 125\,\text{GeV}$ is indicated. It is found to be within the 68 % confidence level for all masses but the 600 and 700 GeV point. Likewise the origin indicating no Higgs boson with the given mass is observed is compatible within the 95 % confidence level for all masses.

A.4 Results using the fake factor background estimation method

A.4.1 Systematic uncertainties

Table A.5: Uncertainties used in the fit for case of using the fake factor background estimation method in the $e\tau_h$, $\mu\tau_h$ and $\tau_h\tau_h$ decay channels. *Shape* uncertainties refer to uncertainties involving shape altering effects. VV refers to the Di-boson processes. MC represents all processes estimated based on simulated events.

Systematic	Process	$\mu\tau_h$	$e\tau_h$	$\tau_h\tau_h$
Luminosity uncertainty	MC	2.5 %	2.5 %	2.5 %
Muon ID efficiency	MC	2 %	–	–
Electron ID efficiency	MC	–	2 %	–
Tau ID efficiency, correlated	MC	4 %	4 %	8 %
Tau ID efficiency, uncorrelated	MC	3 %	3 %	9.2 %
High-pt tau ID efficiency	MC	shape	shape	shape
τ_h energy scale	$Z \to ll$	shape	shape	shape
$e \to \tau_h$ fake energy scale	$Z \to ll$	–	shape	–
electron energy scale	MC	–	shape	–
top p_T reweighting	$t\bar{t}$	shape	shape	shape
Z p_T reweighting	Drell-Yan	shape	shape	shape
anti-μ discriminator	$Z \to ll$	12 %	–	5 %
anti-e discriminator	$Z \to ll$	–	11 %	3 %
anti-jet discriminator, uncorrelated	$Z \to ll$	20 %	20 %	20 %
b-tagging efficiency	MC	1–3 %	1–4 %	1–4 %
b-tagging misstag rate	MC	1–4 %	1–3 %	1–5 %
$\not{E}_T$ resolution	$Z \to \tau\tau$, signal	1–2 %	1–3 %	–
$\not{E}_T$ scale	$Z \to \tau\tau$, signal	1–4 %	1–4 %	–
$\not{E}_T$ unclustered energy	$t\bar{t}$, VV	1–5 %	1–5 %	–
$\not{E}_T$ jet energy	$t\bar{t}$, VV	1–3 %	1–4 %	–
$Z \to \tau\tau$ acceptance	$Z \to \tau\tau$	1–2 %	2 %	5–7 %
Drell-Yan cross section uncertainty	Drell-Yan	4 %	4 %	4 %
Di-boson cross section uncertainty	Di-boson	5 %	5 %	5 %
$t\bar{t}$ cross section uncertainty	$t\bar{t}$	6 %	6 %	6 %

Table A.6: Continuation of table A.5. The uncertainties due to the fake factor background estimation are given. jet $\to \tau_h$ fakes denotes the background contribution estimated using the fake factor method.

Systematic	Process	$\mu\tau_h$	$e\tau_h$	$\tau_h\tau_h$
fake factor QCD contribution stat, dm $= 0$, $n_{\text{jet}} = 0$	jet $\to \tau_h$ fakes	shape	shape	shape
fake factor QCD contribution stat, dm $= 0$, $n_{\text{jet}} >= 1$	jet $\to \tau_h$ fakes	shape	shape	shape
fake factor QCD contribution stat, dm $= 1$, $n_{\text{jet}} = 0$	jet $\to \tau_h$ fakes	shape	shape	shape
fake factor QCD contribution stat, dm $= 1$, $n_{\text{jet}} >= 1$	jet $\to \tau_h$ fakes	shape	shape	shape
fake factor W+jets contribution stat, dm $= 0$, $n_{\text{jet}} = 0$	jet $\to \tau_h$ fakes	shape	shape	–
fake factor W+jets contribution stat, dm $= 0$, $n_{\text{jet}} >= 1$	jet $\to \tau_h$ fakes	shape	shape	–
fake factor W+jets contribution stat, dm $= 1$, $n_{\text{jet}} = 0$	jet $\to \tau_h$ fakes	shape	shape	–
fake factor W+jets contribution stat, dm $= 1$, $n_{\text{jet}} >= 1$	jet $\to \tau_h$ fakes	shape	shape	–
fake factor $t\bar{t}$ contribution stat, dm $= 0$, $n_{\text{jet}} = 0$	jet $\to \tau_h$ fakes	shape	shape	–
fake factor $t\bar{t}$ contribution stat, dm $= 1$, $n_{\text{jet}} = 0$	jet $\to \tau_h$ fakes	shape	shape	–
fake factor QCD contribution syst	jet $\to \tau_h$ fakes	shape	shape	shape
fake factor W+jets contribution syst	jet $\to \tau_h$ fakes	shape	shape	shape
fake factor $t\bar{t}$ contribution syst	jet $\to \tau_h$ fakes	shape	shape	shape
fake factor Drell-Yan fraction syst	jet $\to \tau_h$ fakes	–	–	shape
fake factor W+jets fraction syst	jet $\to \tau_h$ fakes	–	–	shape
fake factor $t\bar{t}$ fraction syst	jet $\to \tau_h$ fakes	–	–	shape
fake factor normalisation, per channel	jet $\to \tau_h$ fakes	3.5–4 %	4.4–7.1 %	2.3–2.8 %
fake factor normalisation, per category	jet $\to \tau_h$ fakes	5.5–7.5 %	6.8–9.7 %	9.9–10 %
fake factor normalisation, sytematics	jet $\to \tau_h$ fakes	4 %	4 %	3 %

A.4.2 Pulls and constraints

(a) normalized to prior constraint   **(b)** normalized to post-fit constraint
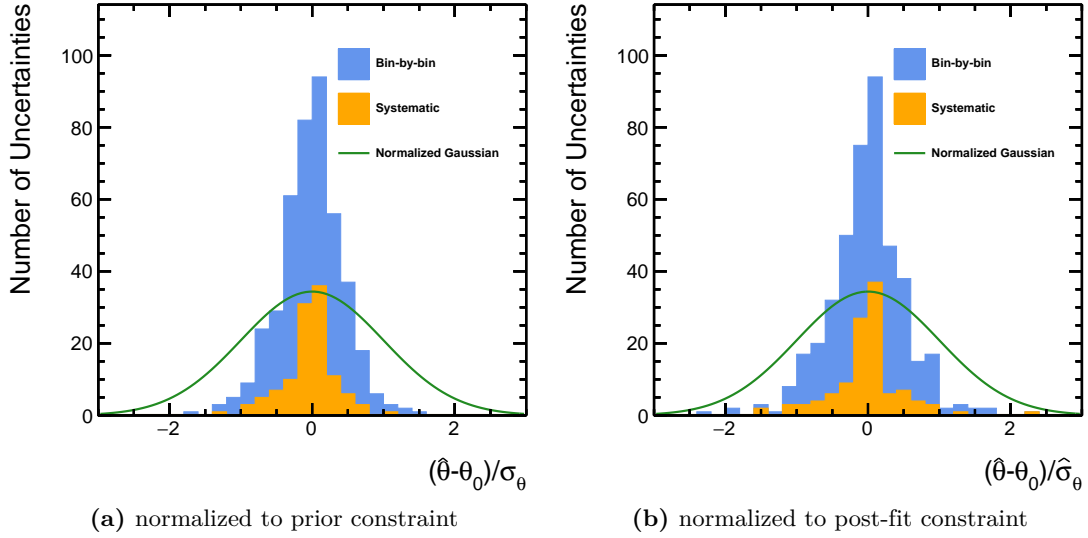
Figure A.30: Distribution of the pulls in the signal plus background fit of the nuisance parameters involved in the fit. The pulls are given normalized to the prior constraint (left) and post-fit constraint (right) of the nuisance parameters. The nuisance parameters are split into bin-by-bin uncertainties resembling the uncertainty due to the limited number of simulated events per process and other systematics. The pulls are expected to follow a Gaussian distribution, which is indicated by the magenta line.

Table A.7: Results of the fit of a Gaussian distribution to the poist-fit pulls and number of nuisance parameters of the respective type.

	bin-by-bin	other systematics	combination
number of nuisances	317	114	431
width	0.49 ± 0.03	0.38 ± 0.07	0.47 ± 0.03
mean	0.01 ± 0.03	-0.06 ± 0.05	0.00 ± 0.02

A.4.3 Goodness-of-fit test
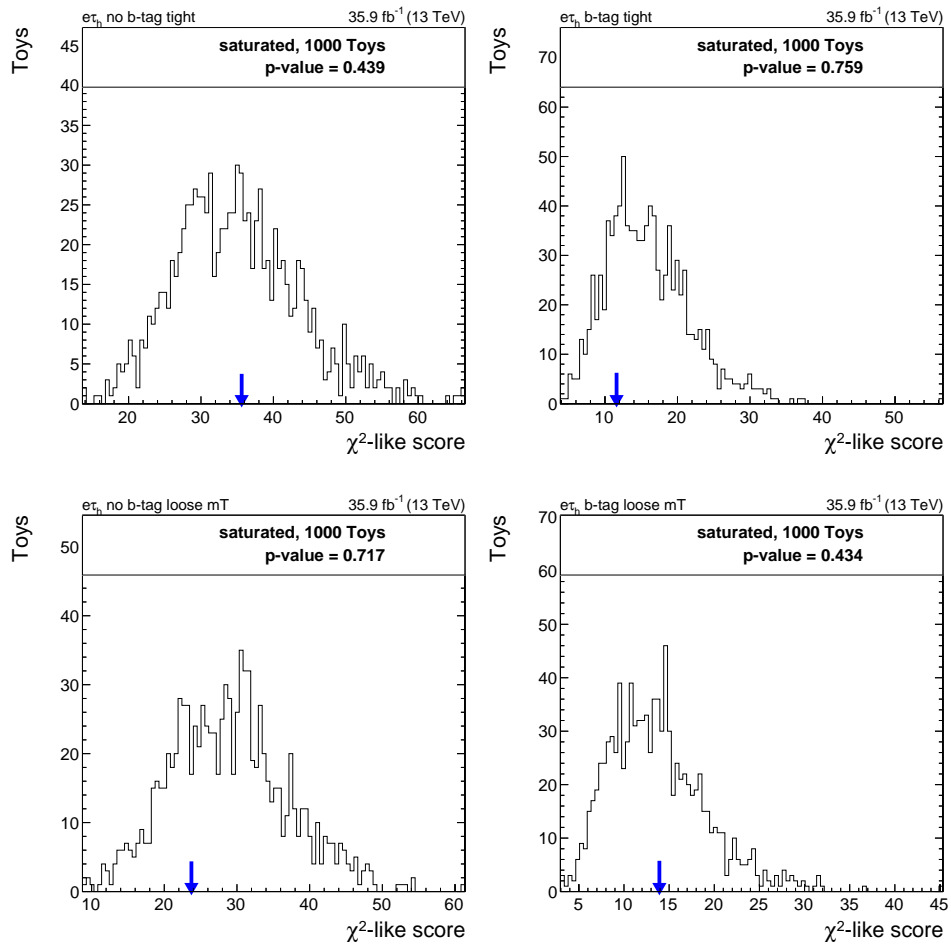
Figure A.31: Goodness of Fit in the $e\tau_\mathrm{h}$ channel using the fake factor method and the saturated approach.
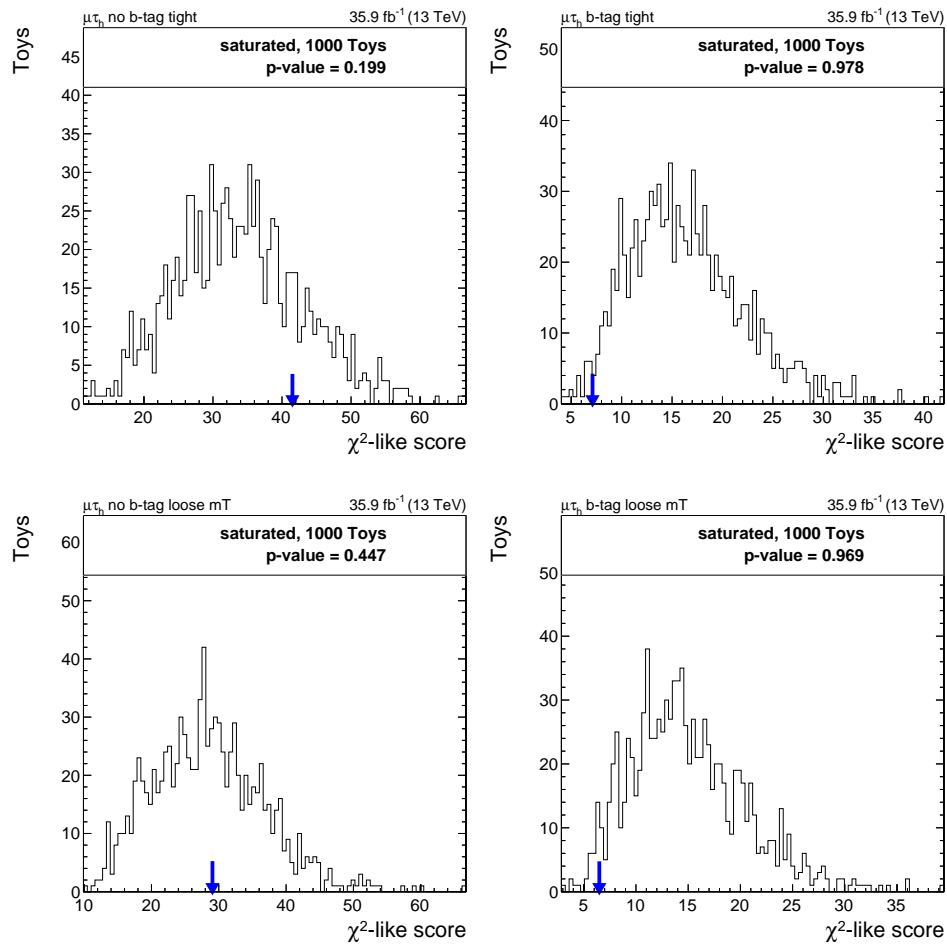
Figure A.32: Goodness of Fit in the $\mu\tau_\mathrm{h}$ channel using the fake factor method and the saturated approach.
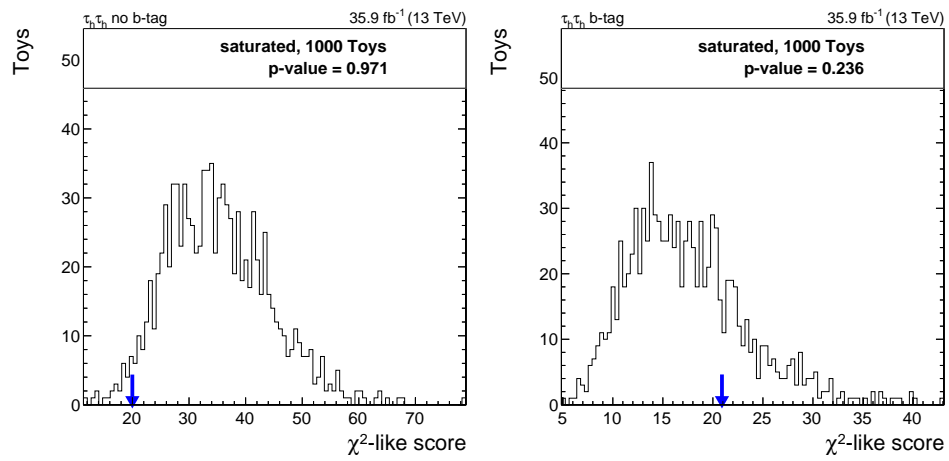
Figure A.33: Goodness of Fit in the $\tau_h\tau_h$ channel using the fake factor method and the saturated approach.

A.4.4 Prefit $m_\mathrm{T}^\mathrm{tot}$ distributions
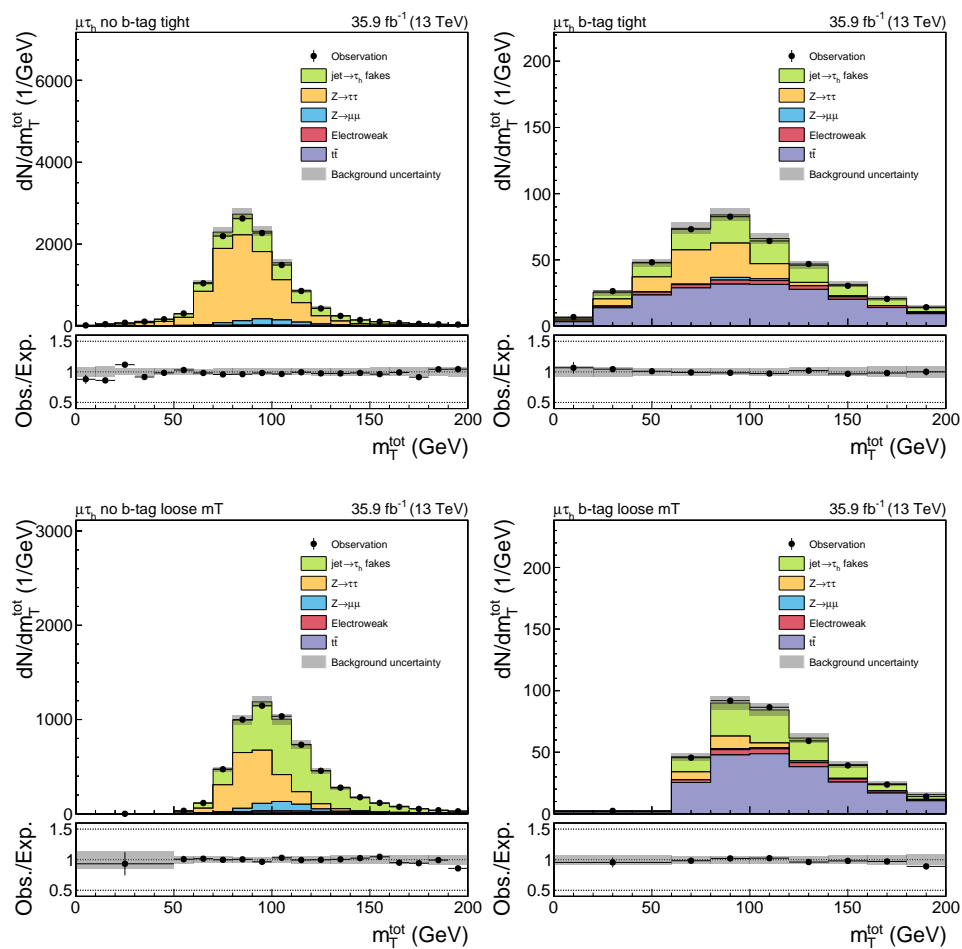
Figure A.34: Prefit distributions of $m_\mathrm{T}^\mathrm{tot}$ in the $\mu\tau_\mathrm{h}$ decay channel. The distributions are given for the $\mu\tau_\mathrm{h}$ no b-tag tight (top left), $\mu\tau_\mathrm{h}$ b-tag tight (top right), $\mu\tau_\mathrm{h}$ no b-tag loose mT (bottom left) and $\mu\tau_\mathrm{h}$ b-tag loose mT (bottom right) categories.
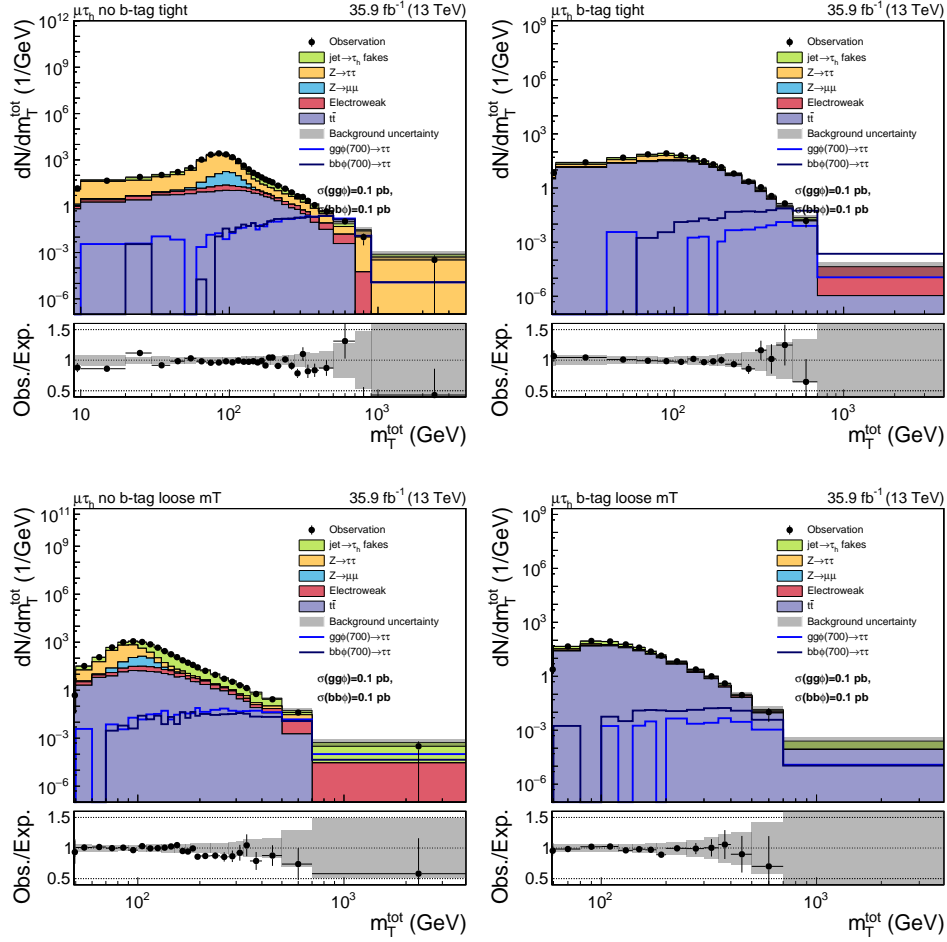
Figure A.35: Prefit distributions of $m_\mathrm{T}^\mathrm{tot}$ in the $\mu\tau_\mathrm{h}$ decay channel. The distributions are given for the $\mu\tau_\mathrm{h}$ no b-tag tight (top left), $\mu\tau_\mathrm{h}$ b-tag tight (top right), $\mu\tau_\mathrm{h}$ no b-tag loose mT (bottom left) and $\mu\tau_\mathrm{h}$ b-tag loose mT (bottom right) categories.
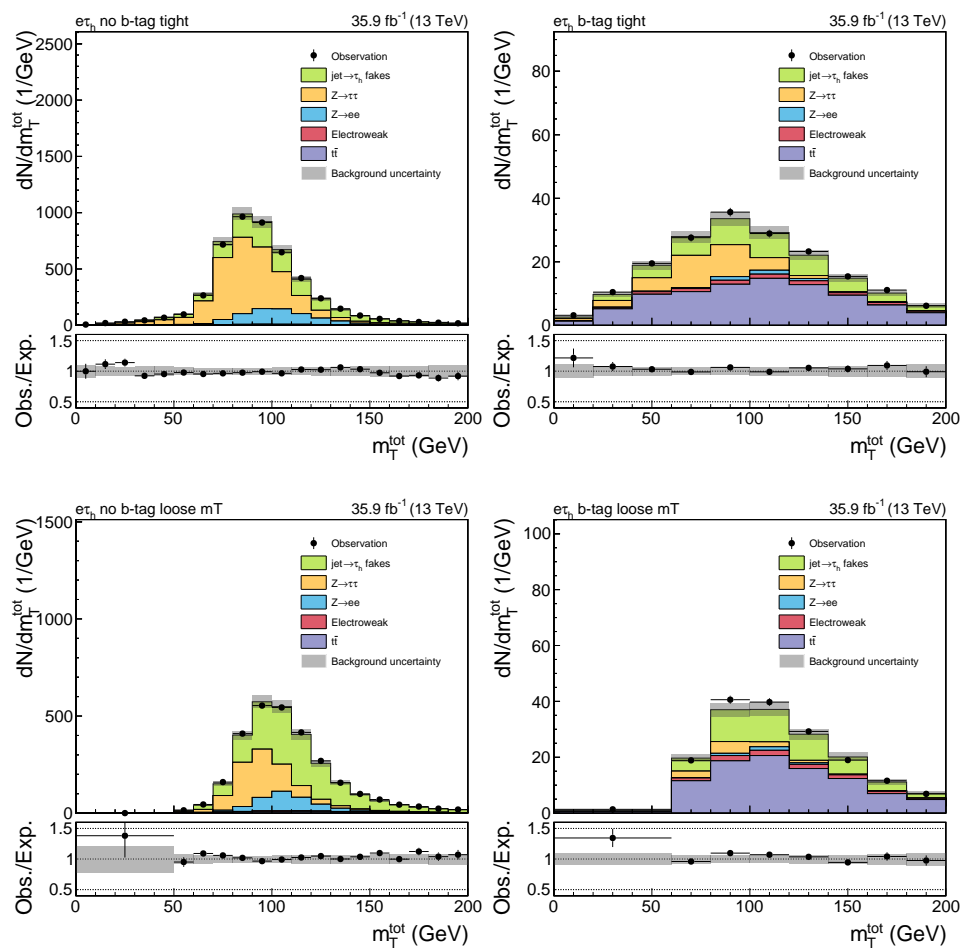
Figure A.36: Prefit distributions of m_T^{tot} in the $e\tau_h$ decay channel. The distributions are given for the $e\tau_h$ no b-tag tight (top left), $e\tau_h$ b-tag tight (top right), $e\tau_h$ no b-tag loose mT (bottom left) and $e\tau_h$ b-tag loose mT (bottom right) categories.
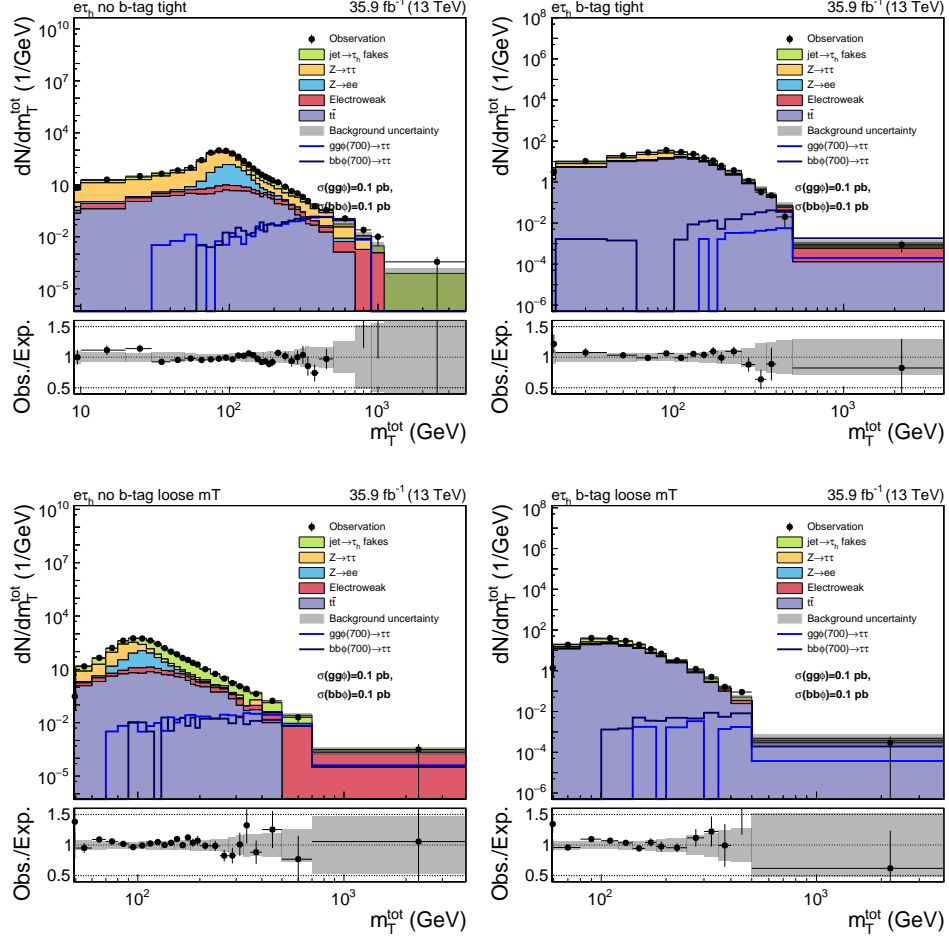
Figure A.37: Prefit distributions of m_T^{tot} in the $e\tau_h$ decay channel. The distributions are given for the $e\tau_h$ no b-tag tight (top left), $e\tau_h$ b-tag tight (top right), $e\tau_h$ no b-tag loose mT (bottom left) and $e\tau_h$ b-tag loose mT (bottom right) categories.
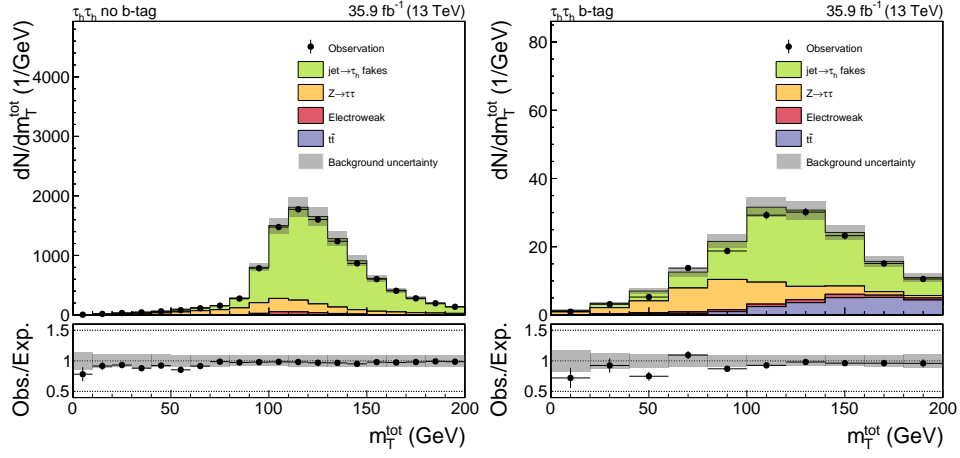
Figure A.38: Prefit distributions of m_T^{tot} in the $\tau_h\tau_h$ decay channel. The distributions are given for the $\tau_h\tau_h$ no b-tag (left) and $\tau_h\tau_h$ b-tag (right) categories.
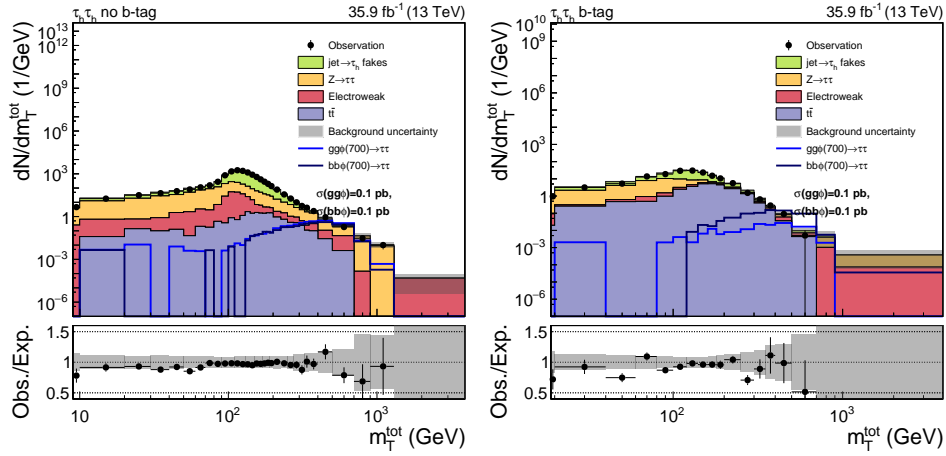
Figure A.39: Prefit distributions of m_T^{tot} in the $\tau_h\tau_h$ decay channel. The distributions are given for the $\tau_h\tau_h$ no b-tag (left) and $\tau_h\tau_h$ b-tag (right) categories.

A.4.5 Postfit $m_{\mathrm{T}}^{\mathrm{tot}}$ distributions
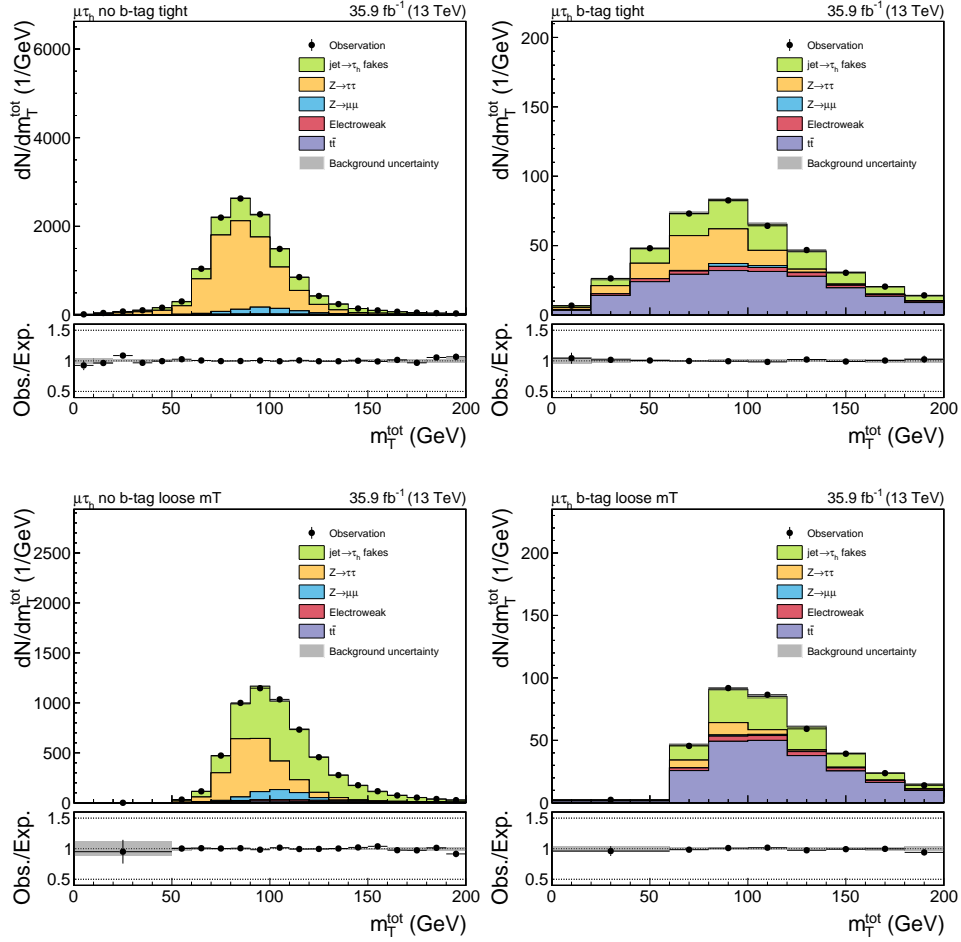
Figure A.40: Postfit distributions of $m_{\mathrm{T}}^{\mathrm{tot}}$ in the $\mu\tau_{\mathrm{h}}$ decay channel. The postfit distributions are evaluated based on the pulls of the nuisance parameters in the signal-plus-background fit. For the uncertainty bands the full uncertainty model is considered. The distributions are given for the $\mu\tau_{\mathrm{h}}$ no b-tag tight (top left), $\mu\tau_{\mathrm{h}}$ b-tag tight (top right), $\mu\tau_{\mathrm{h}}$ no b-tag loose mT (bottom left) and $\mu\tau_{\mathrm{h}}$ b-tag loose mT (bottom right) categories.
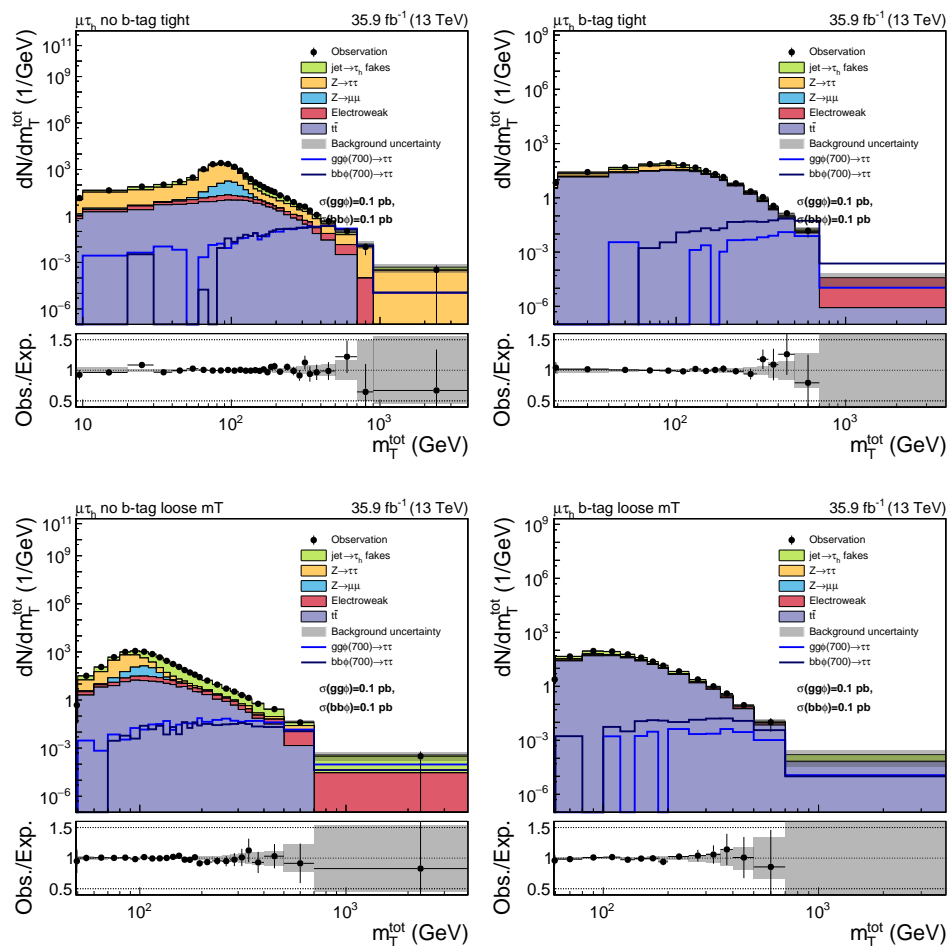
Figure A.41: Postfit distributions of $m_\mathrm{T}^\mathrm{tot}$ in the $\mu\tau_\mathrm{h}$ decay channel. The postfit distributions are evaluated based on the pulls of the nuisance parameters in the signal-plus-background fit. For the uncertainty bands the full uncertainty model is considered. The distributions are given for the $\mu\tau_\mathrm{h}$ no b-tag tight (top left), $\mu\tau_\mathrm{h}$ b-tag tight (top right), $\mu\tau_\mathrm{h}$ no b-tag loose mT (bottom left) and $\mu\tau_\mathrm{h}$ b-tag loose mT (bottom right) categories.
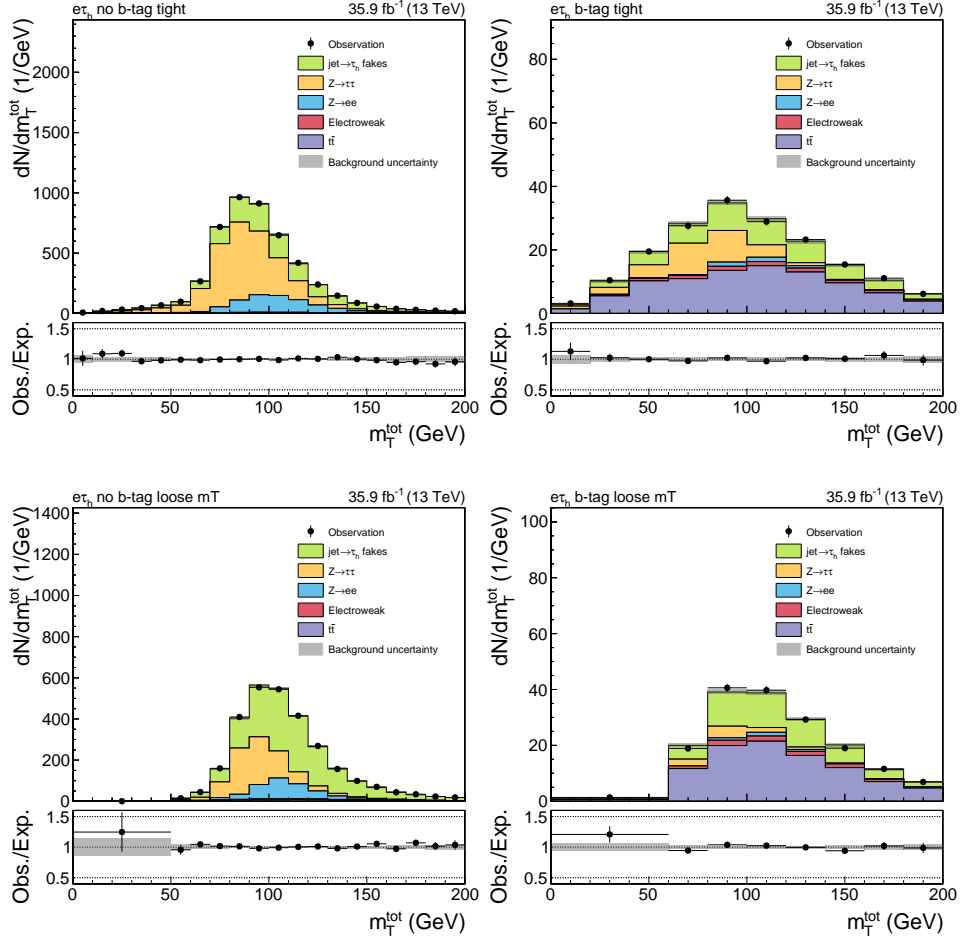
Figure A.42: Postfit distributions of m_T^{tot} in the $e\tau_h$ decay channel. The postfit distributions are evaluated based on the pulls of the nuisance parameters in the signal-plus-background fit. For the uncertainty bands the full uncertainty model is considered. The distributions are given for the $e\tau_h$ no b-tag tight (top left), $e\tau_h$ b-tag tight (top right), $e\tau_h$ no b-tag loose mT (bottom left) and $e\tau_h$ b-tag loose mT (bottom right) categories.
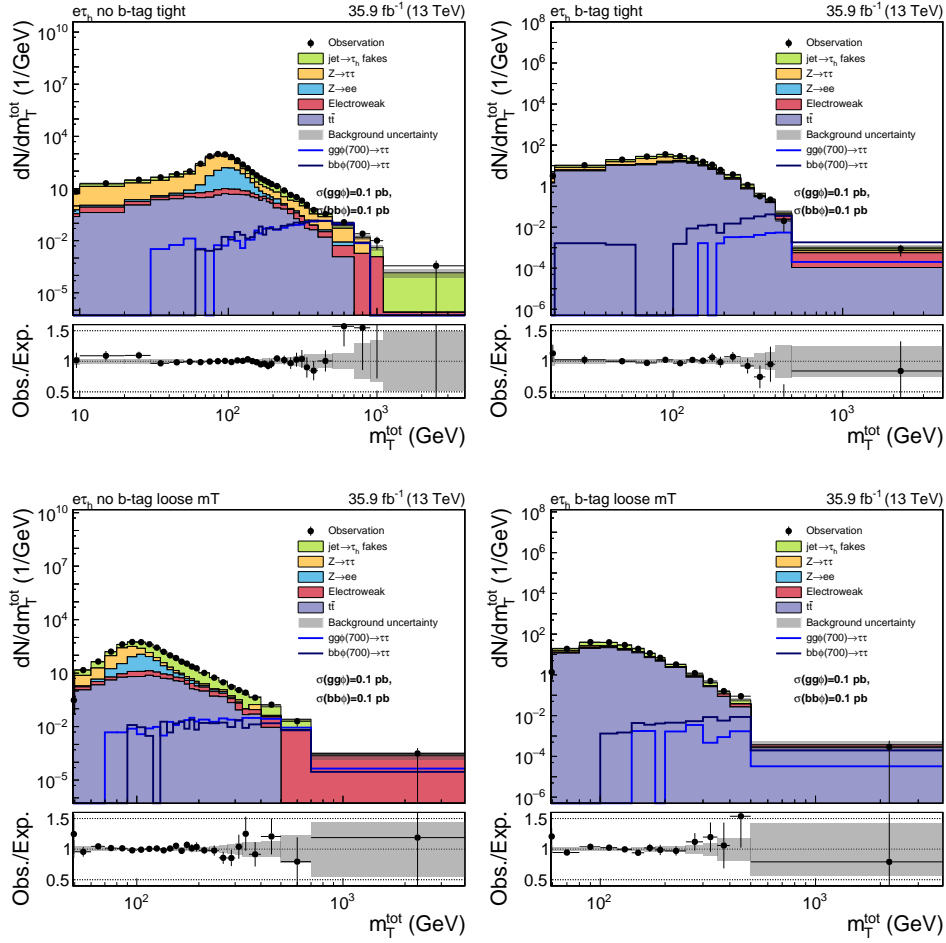
Figure A.43: Postfit distributions of m_T^{tot} in the $e\tau_h$ decay channel. The postfit distributions are evaluated based on the pulls of the nuisance parameters in the signal-plus-background fit. For the uncertainty bands the full uncertainty model is considered. The distributions are given for the $e\tau_h$ no b-tag tight (top left), $e\tau_h$ b-tag tight (top right), $e\tau_h$ no b-tag loose mT (bottom left) and $e\tau_h$ b-tag loose mT (bottom right) categories.
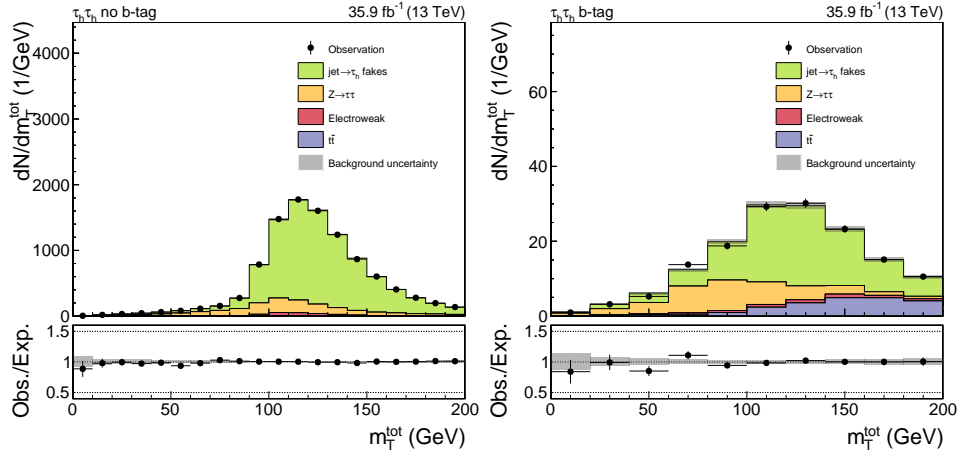
Figure A.44: Postfit distributions of $m_\mathrm{T}^\mathrm{tot}$ in the $\tau_\mathrm{h}\tau_\mathrm{h}$ decay channel. The postfit distributions are evaluated based on the pulls of the nuisance parameters in the signal-plus-background fit. For the uncertainty bands the full uncertainty model is considered. The distributions are given for the $\tau_\mathrm{h}\tau_\mathrm{h}$ no b-tag (left) and $\tau_\mathrm{h}\tau_\mathrm{h}$ b-tag (right) categories.
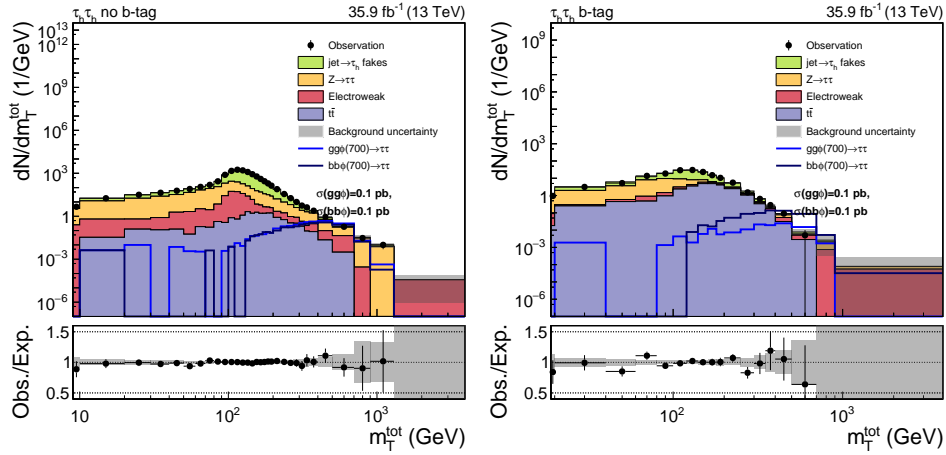
Figure A.45: Postfit distributions of $m_\mathrm{T}^\mathrm{tot}$ in the $\tau_\mathrm{h}\tau_\mathrm{h}$ decay channel. The postfit distributions are evaluated based on the pulls of the nuisance parameters in the signal-plus-background fit. For the uncertainty bands the full uncertainty model is considered. The distributions are given for the $\tau_\mathrm{h}\tau_\mathrm{h}$ no b-tag (left) and $\tau_\mathrm{h}\tau_\mathrm{h}$ b-tag (right) categories.

A.4.6 Exclusion limits
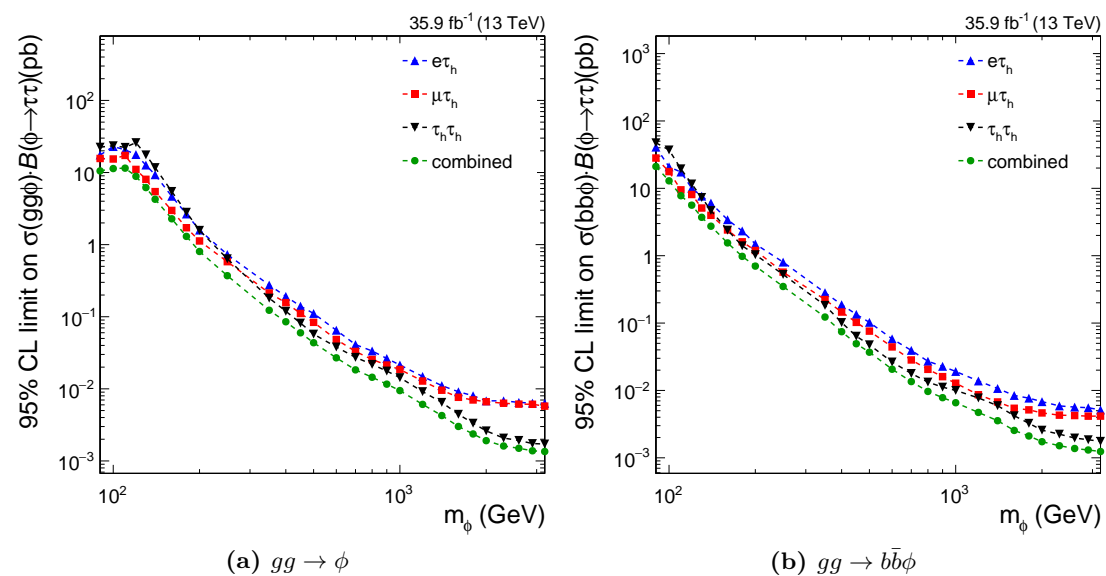
Figure A.46: Sensitivity of the searches in the individual decay channels $e\tau_{\mathrm{h}}$, $\mu\tau_{\mathrm{h}}$ and $\tau_{\mathrm{h}}\tau_{\mathrm{h}}$ as well as the combination of them to a single Higgs boson with a mass of m_{ϕ}. The sensitivity at high m_{ϕ} is mainly driven by the $\tau_{\mathrm{h}}\tau_{\mathrm{h}}$ decay channels while at low mass the semi-leptonic datasets

(a) $\mu\tau_{\mathrm{h}},\ gg \to \phi$

(b) $\mu\tau_{\mathrm{h}},\ gg \to b\bar{b}\phi$

(c) $e\tau_{\mathrm{h}},\ gg \to \phi$

(d) $e\tau_{\mathrm{h}},\ gg \to b\bar{b}\phi$
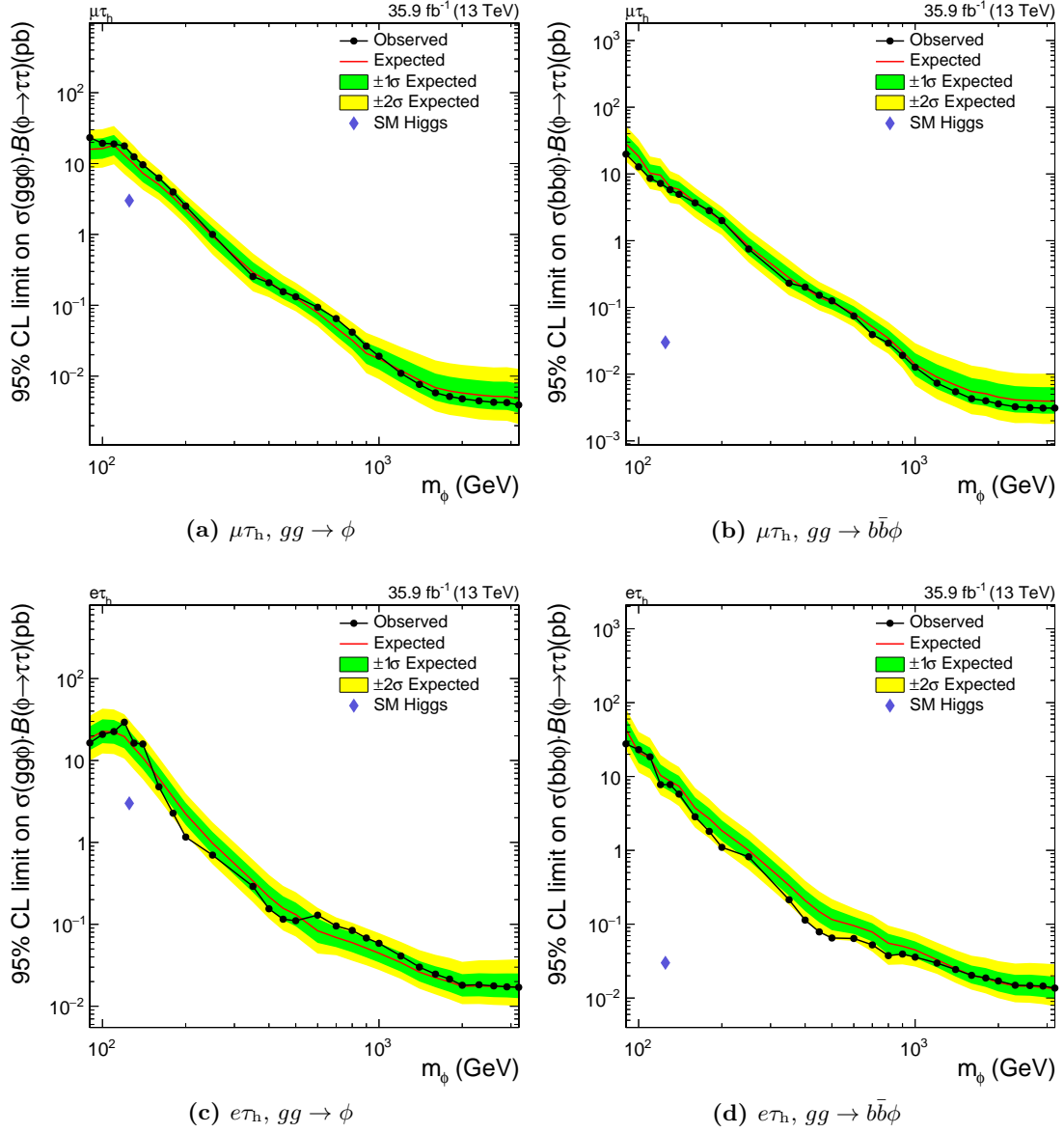
Figure A.47: Expected and observed exclusion limits at 95 % $\mathrm{CL_S}$ on the $\sigma\mathcal{B}$ for the $gg \to \phi$ (left) and $gg \to b\bar{b}\phi$ (right) production process. The exclusion limits are derived for the $\mu\tau_{\mathrm{h}}$ (top) and $e\tau_{\mathrm{h}}$ (bottom) decay channel. The cross section for the SM Higgs boson with a mass of 125 GeV is indicated by the blue marker. For the whole mass range no significant excess of the observation compared to the expectation is observed.

(a) $\tau_\mathrm{h}\tau_\mathrm{h}$, $gg \to \phi$

(b) $\tau_\mathrm{h}\tau_\mathrm{h}$, $gg \to b\bar{b}\phi$

(c) combined, $gg \to \phi$

(d) combined, $gg \to b\bar{b}\phi$
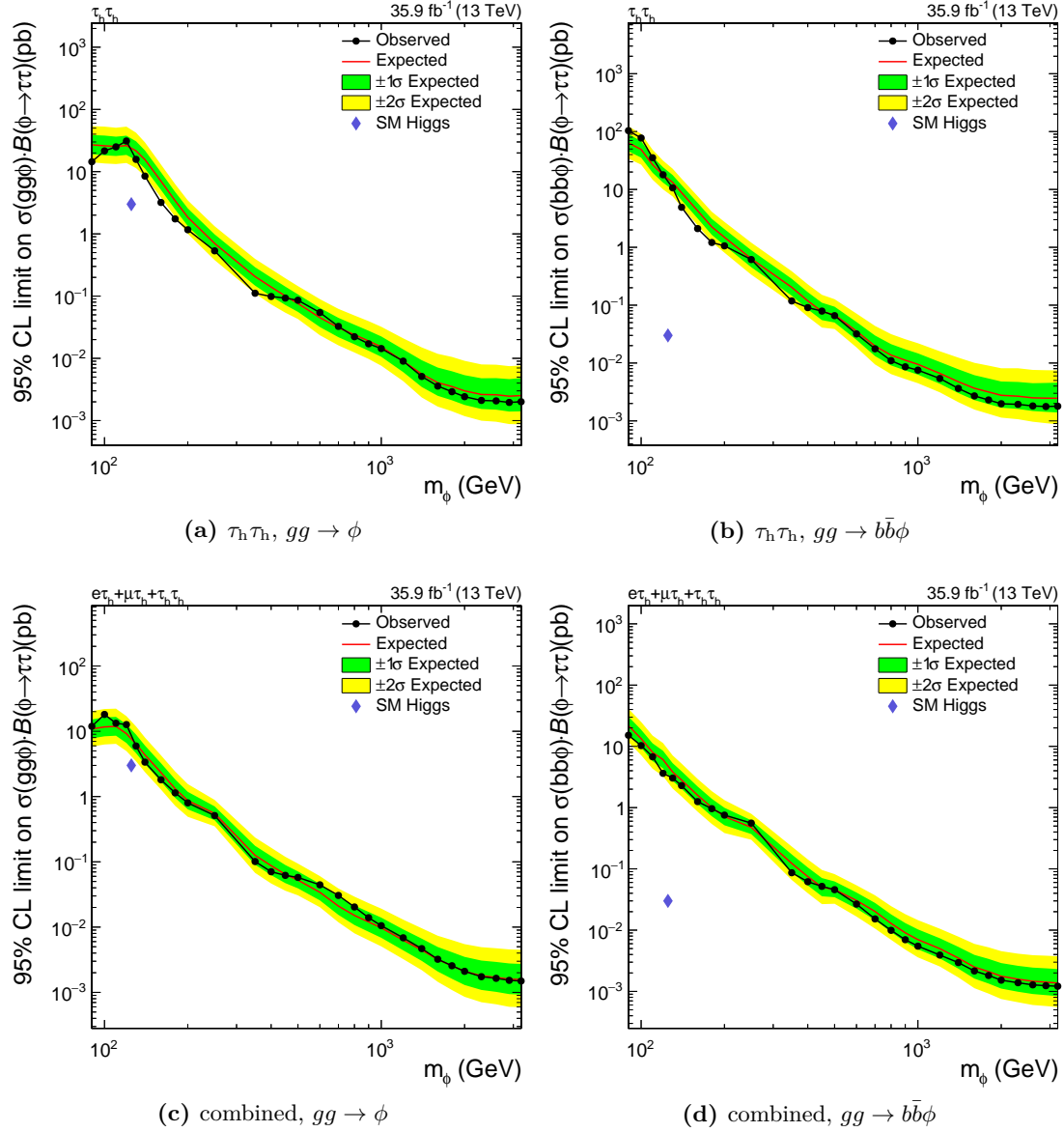
Figure A.48: Expected and observed exclusion limits at 95 % CL$_\mathrm{S}$ on the $\sigma\mathcal{B}$ for the $gg \to \phi$ (left) and $gg \to b\bar{b}\phi$ (right) production process. The exclusion limits are derived for the $\tau_\mathrm{h}\tau_\mathrm{h}$ (top) decay channel and the combination of the $\mu\tau_\mathrm{h}$, $e\tau_\mathrm{h}$ and $\tau_\mathrm{h}\tau_\mathrm{h}$ decay channel (bottom). The cross section for the SM Higgs boson with a mass of 125 GeV is indicated by the blue marker. For the whole mass range no significant excess of the observation compared to the expectation is observed.
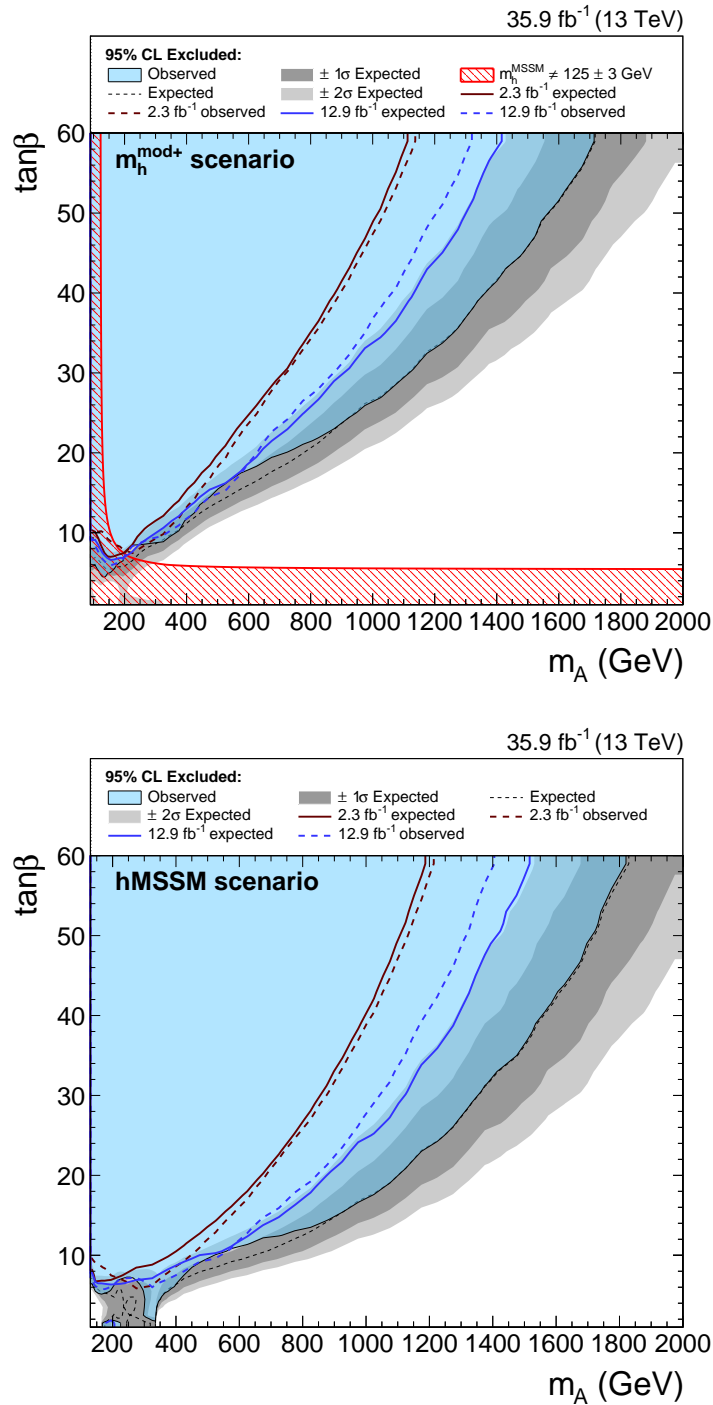
Figure A.49: Exclusion limits in the m_A-$\tan\beta$ plane for the $m_h^{\text{mod}+}$ (top) and hMSSM (bottom) scenarios. The exclusion limits derived in previous analyses using less data are also shown. The results for $2.3\,\text{fb}^{-1}$ are evaluated based on the results from [81] and for $12.9\,\text{fb}^{-1}$ from [5]. For both analyses the results are rederived using the asymptotic approach and limiting the analyzed channels to the $e\tau_h$, $\mu\tau_h$ and $\tau_h\tau_h$ decay channel.

A.4.7 Likelihood scan in *ggφ-bbφ* plane

(a) $m_\phi = 90\,\text{GeV}$

(b) $m_\phi = 100\,\text{GeV}$

(c) $m_\phi = 110\,\text{GeV}$
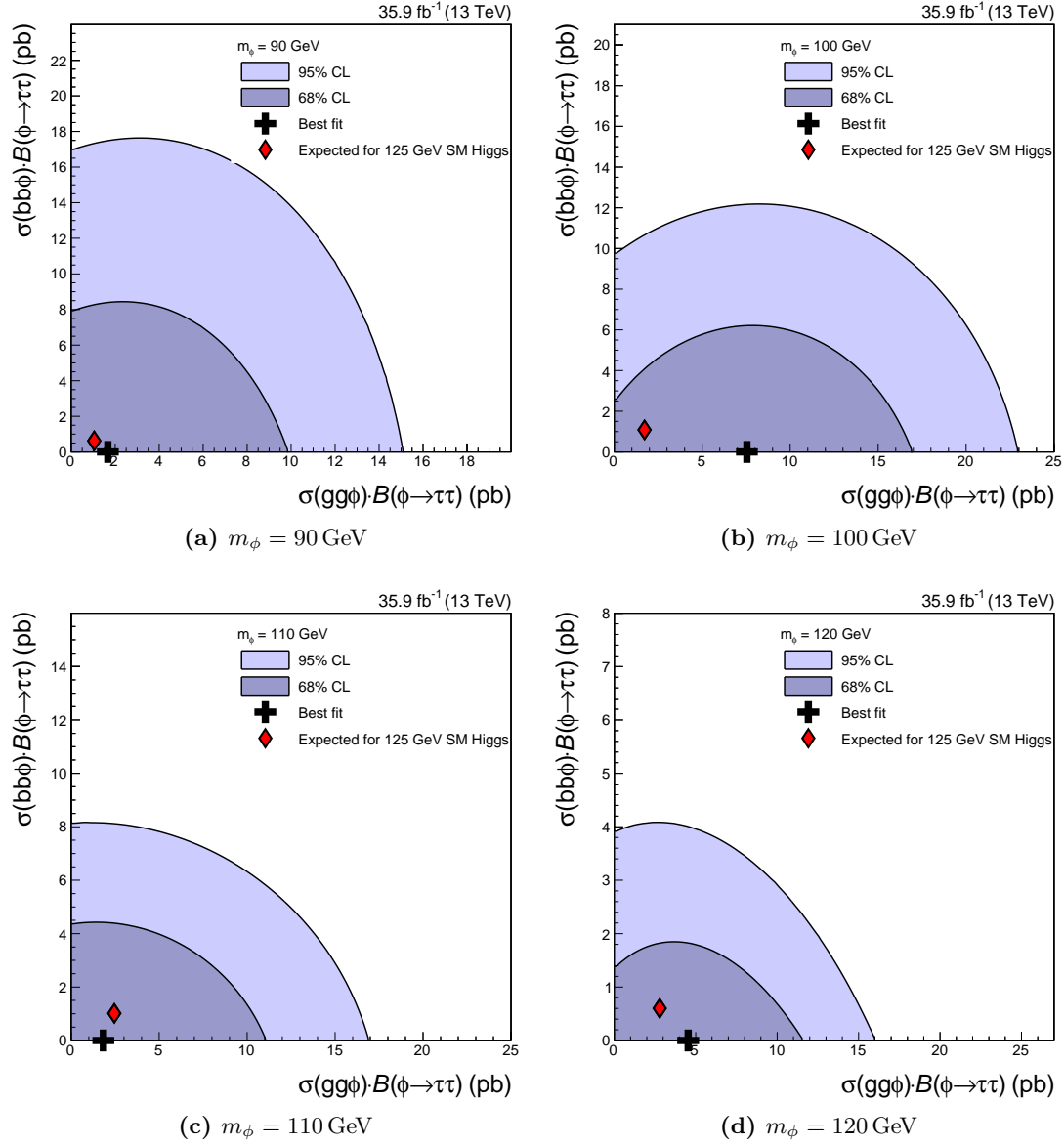
(d) $m_\phi = 120\,\text{GeV}$

Figure A.50: Likelihood scan in the *ggφ-bbφ* plane for four Higgs boson mass hypotheses $m_\phi = 90, 100, 110, 120\,\text{GeV}$. The expected best-fit point in case the observation is equal to the background and the Standard Model Higgs boson with a mass of $m_\text{H} = 125\,\text{GeV}$ is indicated. It is found to be within the 68 % confidence level for all masses. Likewise the origin indicating no Higgs boson with the given mass is observed is compatible within the 95 % confidence level for all masses.
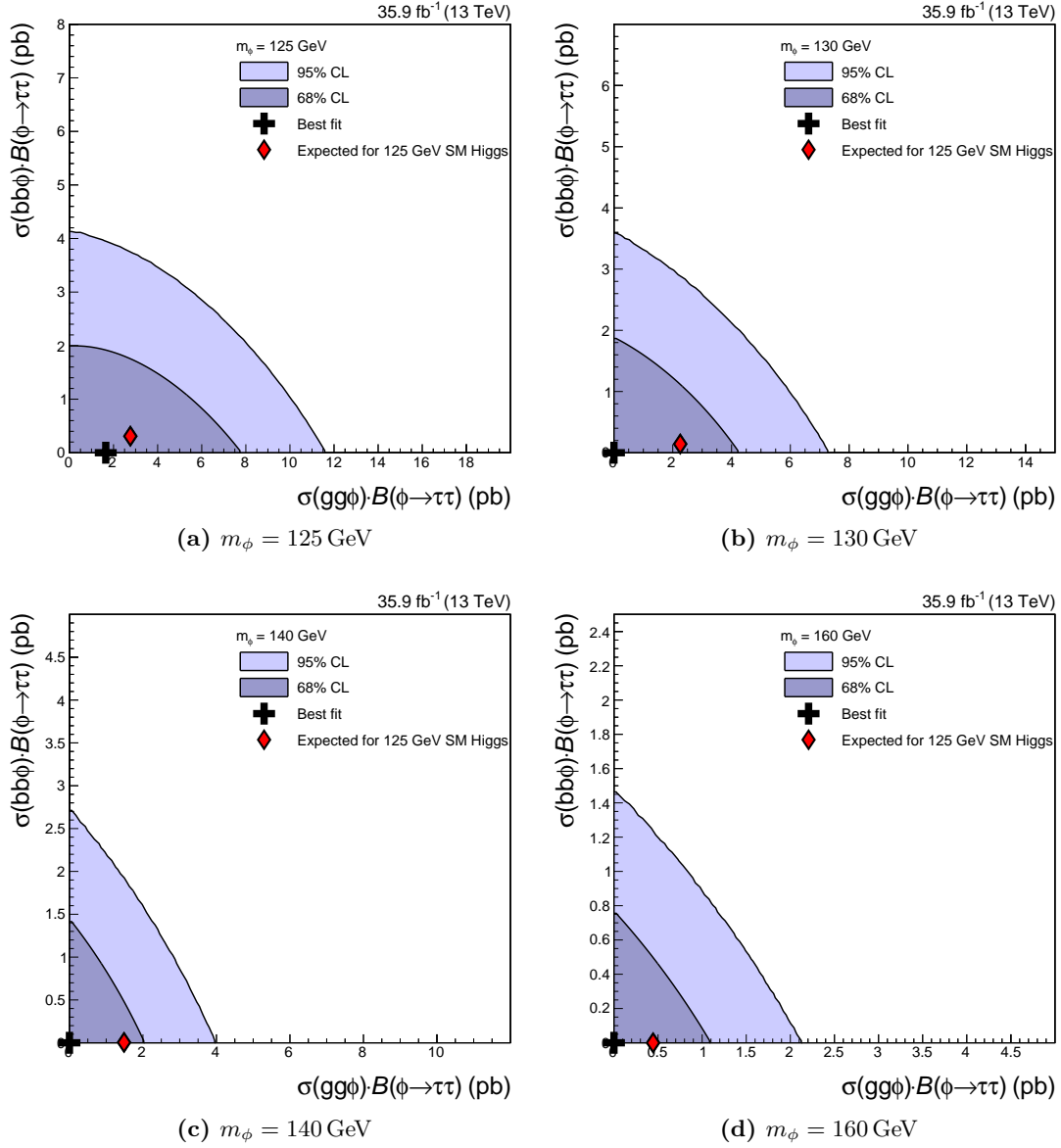
Figure A.51: Likelihood scan in the *ggφ-bbφ* plane for four Higgs boson mass hypotheses $m_\phi = 125, 130, 140, 160$ GeV. The expected best-fit point in case the observation is equal to the background and the Standard Model Higgs boson with a mass of $m_H = 125$ GeV is indicated. It is found to be within the 68 % confidence level for all masses. Likewise the origin indicating no Higgs boson with the given mass is observed is compatible within the 95 % confidence level for all masses.
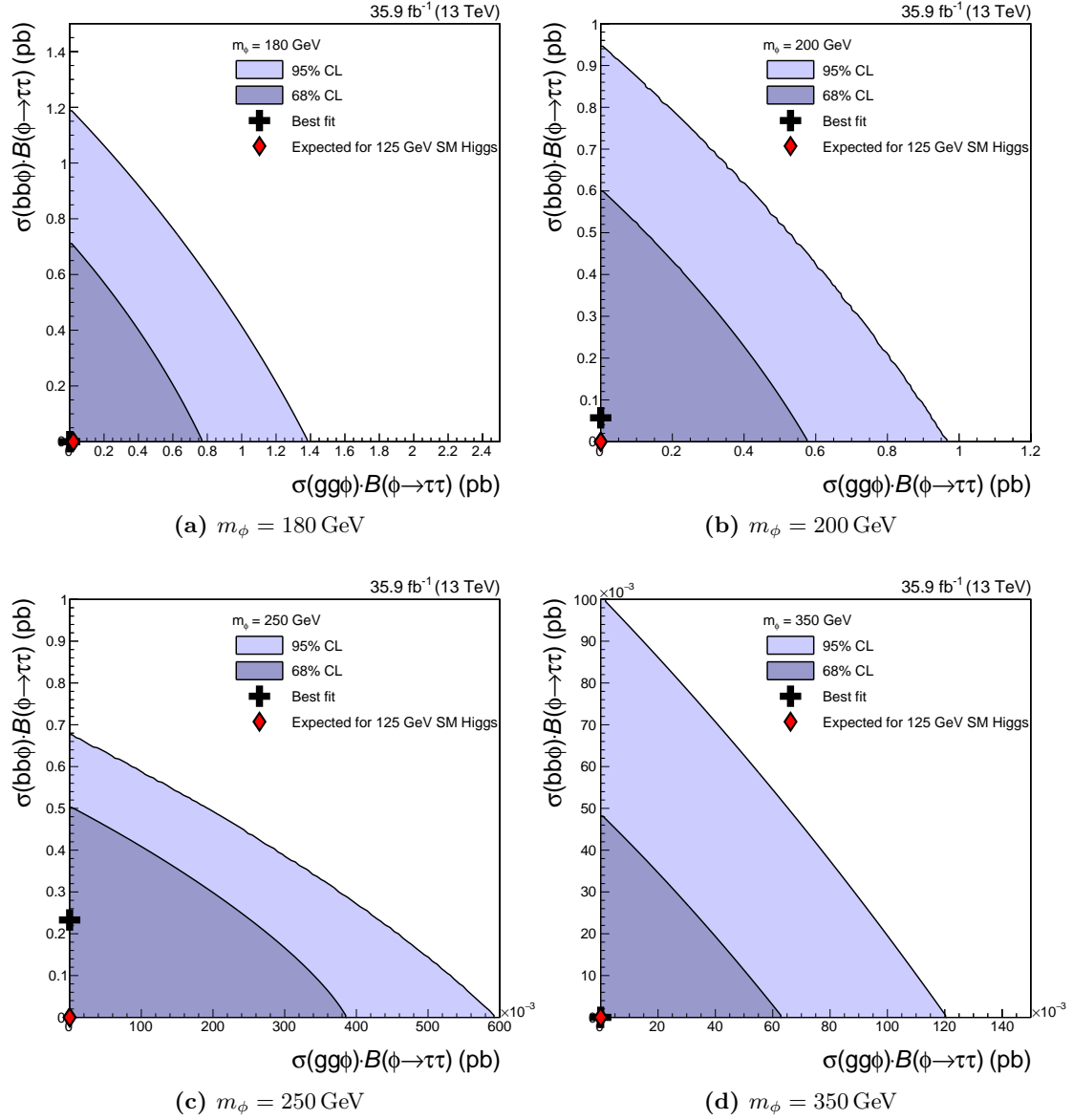
Figure A.52: Likelihood scan in the *ggφ-bbφ* plane for four Higgs boson mass hypotheses $m_\phi = 180, 200, 250, 350 \, \text{GeV}$. The expected best-fit point in case the observation is equal to the background and the Standard Model Higgs boson with a mass of $m_\text{H} = 125 \, \text{GeV}$ is indicated. It is found to be within the 68 % confidence level for all masses. Likewise the origin indicating no Higgs boson with the given mass is observed is compatible within the 95 % confidence level for all masses.
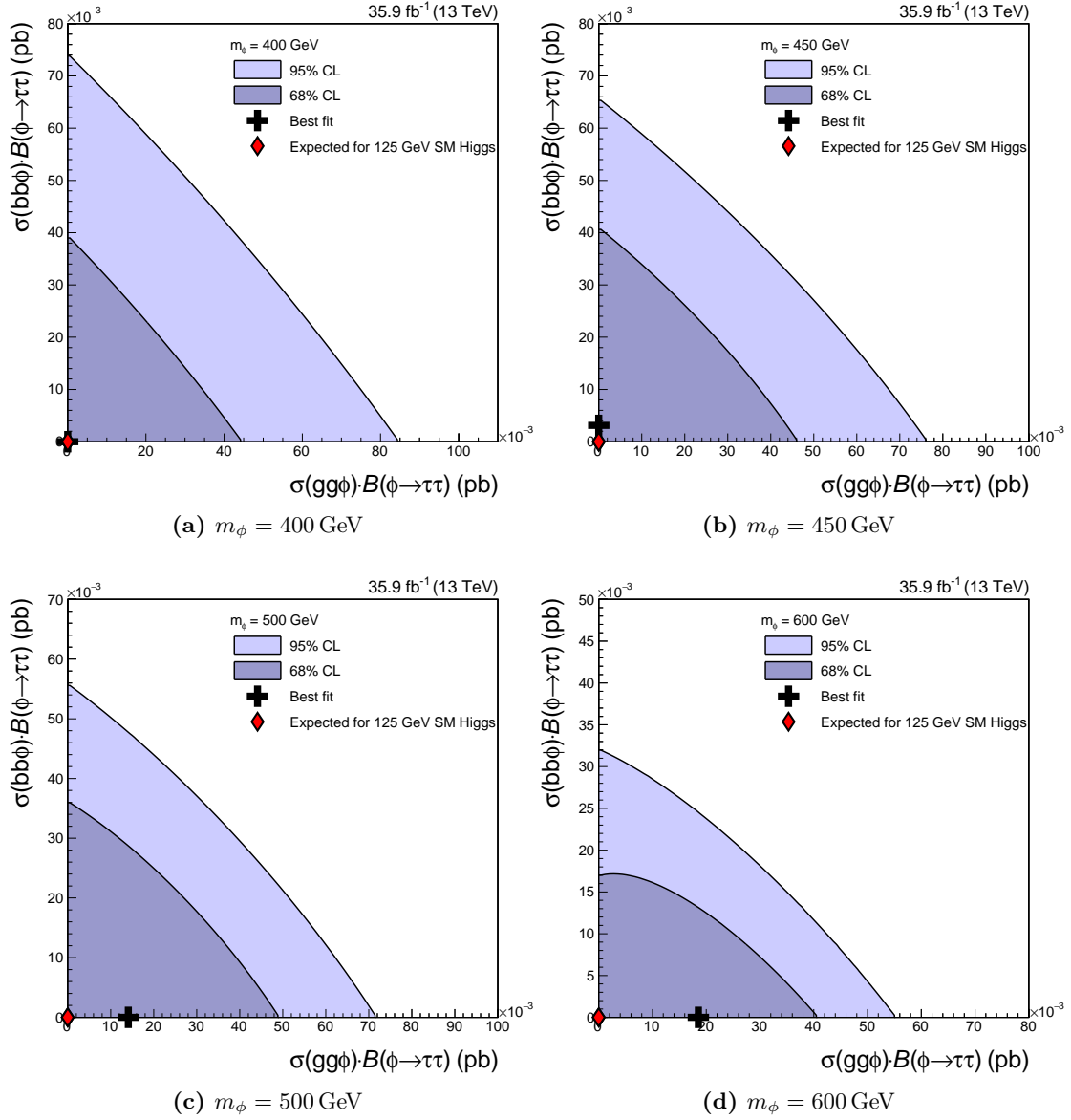
Figure A.53: Likelihood scan in the *ggϕ-bbϕ* plane for four Higgs boson mass hypotheses $m_\phi = 400, 450, 500, 600\,\mathrm{GeV}$. The expected best-fit point in case the observation is equal to the background and the Standard Model Higgs boson with a mass of $m_\mathrm{H} = 125\,\mathrm{GeV}$ is indicated. It is found to be within the 68 % confidence level for all masses. Likewise the origin indicating no Higgs boson with the given mass is observed is compatible within the 95 % confidence level for all masses.
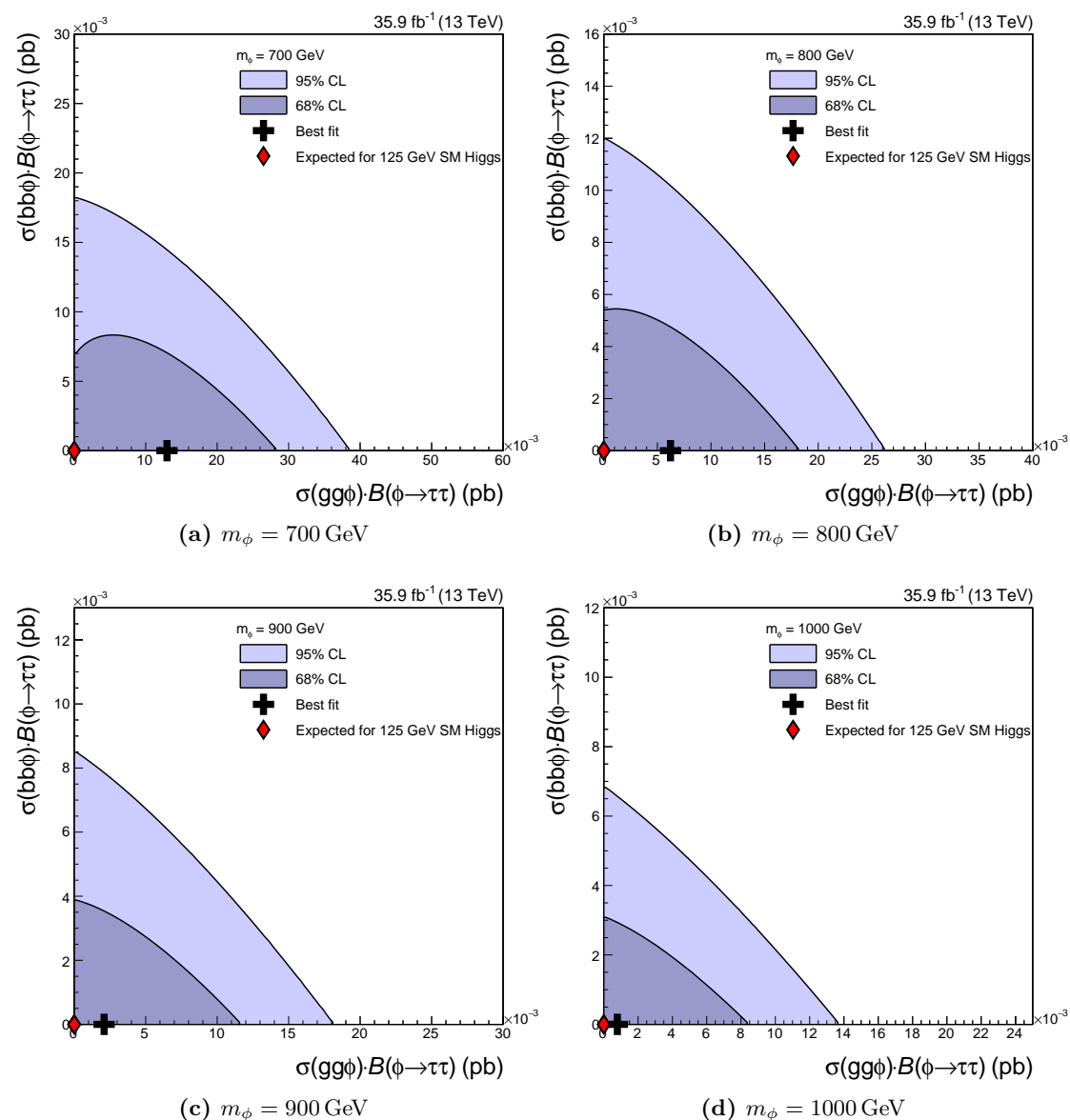
Figure A.54: Likelihood scan in the *ggφ-bbφ* plane for four Higgs boson mass hypotheses $m_\phi = 700, 800, 900, 1000$ GeV. The expected best-fit point in case the observation is equal to the background and the Standard Model Higgs boson with a mass of $m_H = 125$ GeV is indicated. It is found to be within the 68 % confidence level for all masses. Likewise the origin indicating no Higgs boson with the given mass is observed is compatible within the 95 % confidence level for all masses.
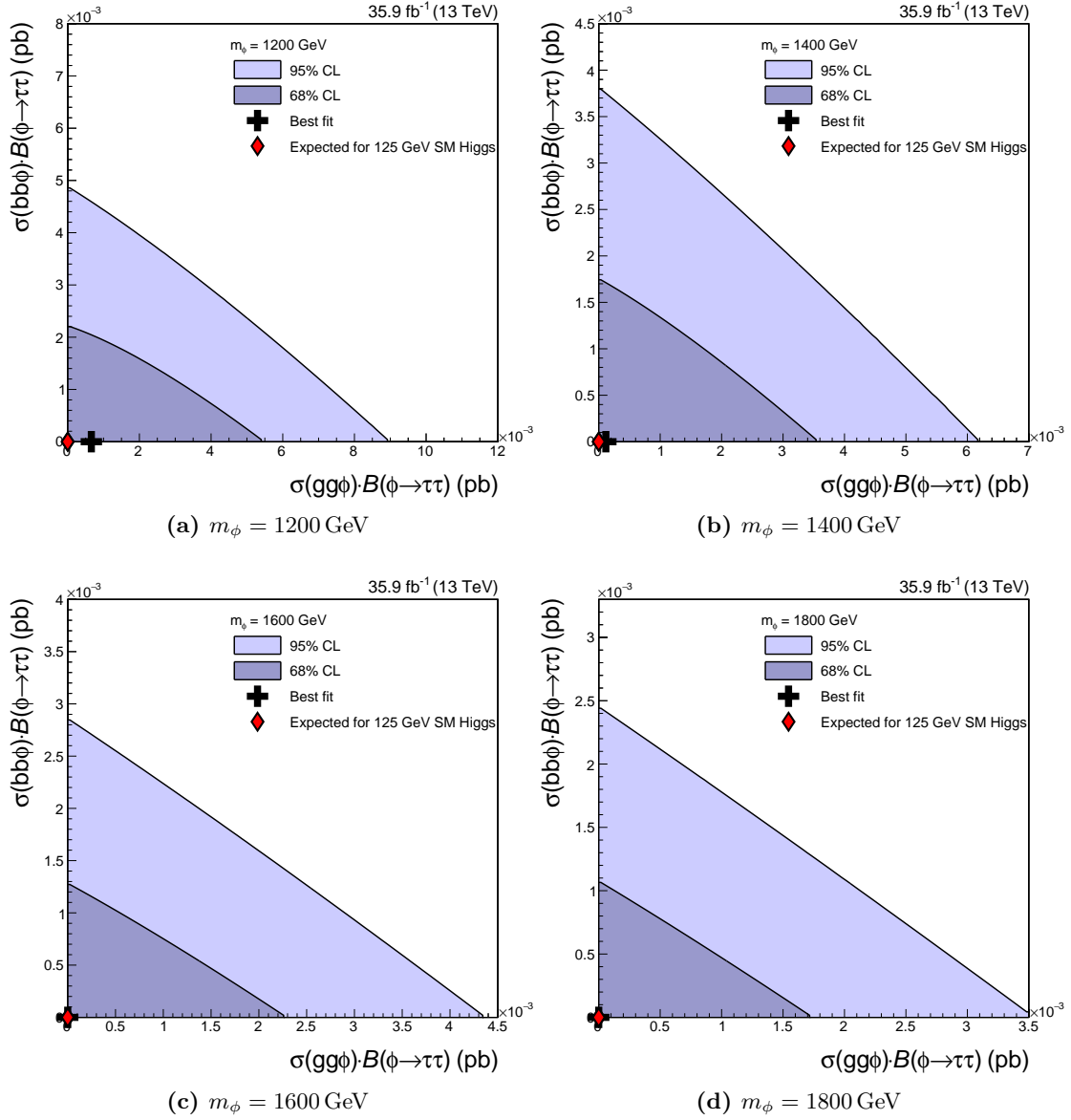
Figure A.55: Likelihood scan in the *ggφ-bbφ* plane for four Higgs boson mass hypotheses $m_\phi = 1200, 1400, 1600, 1800\,\mathrm{GeV}$. The expected best-fit point in case the observation is equal to the background and the Standard Model Higgs boson with a mass of $m_\mathrm{H} = 125\,\mathrm{GeV}$ is indicated. It is found to be within the 68 % confidence level for all masses. Likewise the origin indicating no Higgs boson with the given mass is observed is compatible within the 95 % confidence level for all masses.

(a) $m_\phi = 2000\,\mathrm{GeV}$

(b) $m_\phi = 2300\,\mathrm{GeV}$

(c) $m_\phi = 2600\,\mathrm{GeV}$
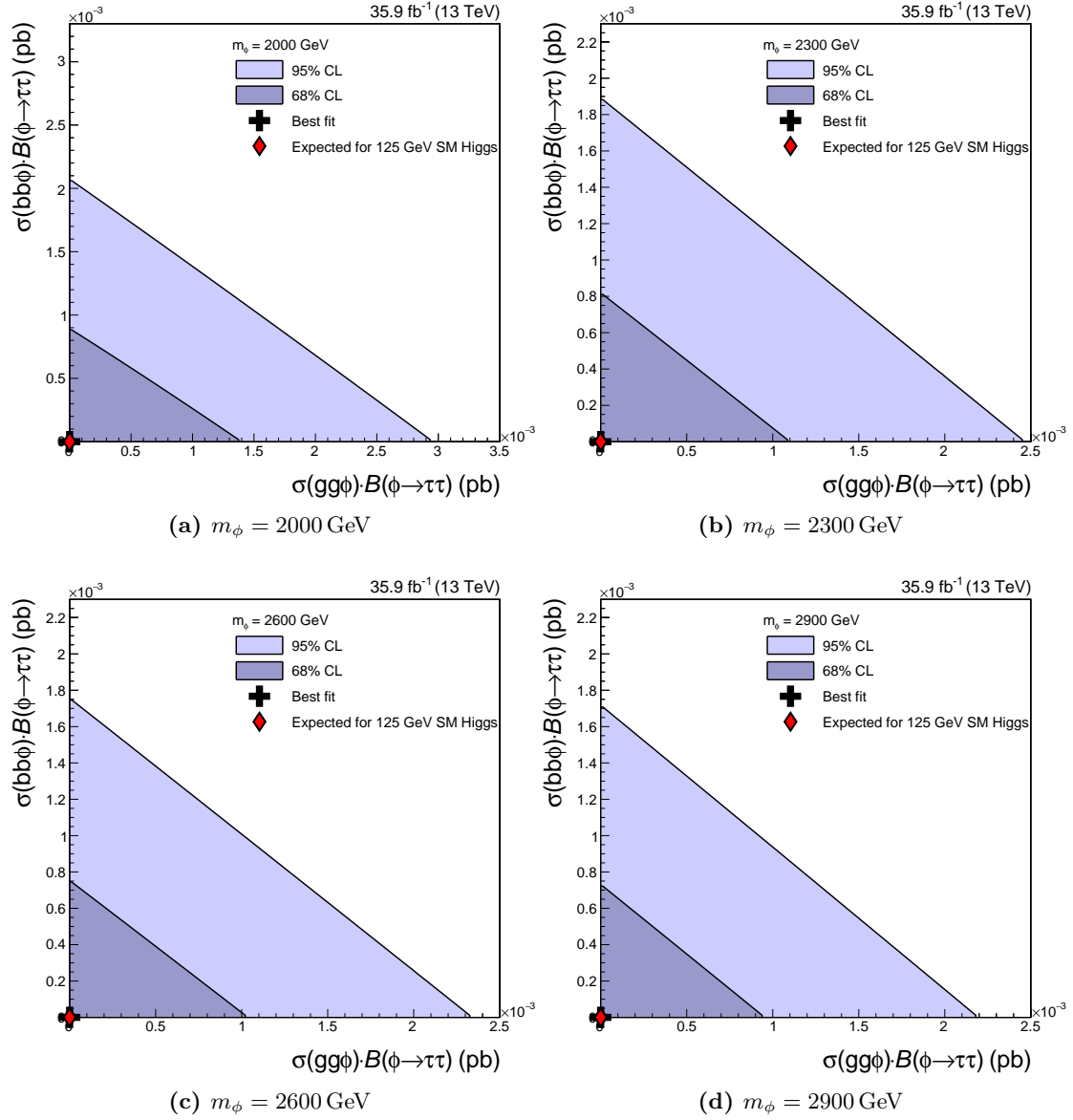
(d) $m_\phi = 2900\,\mathrm{GeV}$

Figure A.56: Likelihood scan in the *ggφ-bbφ* plane for four Higgs boson mass hypotheses $m_\phi = 2000, 2300, 2600, 2900\,\mathrm{GeV}$. The expected best-fit point in case the observation is equal to the background and the Standard Model Higgs boson with a mass of $m_\mathrm{H} = 125\,\mathrm{GeV}$ is indicated. It is found to be within the 68 % confidence level for all masses. Likewise the origin indicating no Higgs boson with the given mass is observed is compatible within the 95 % confidence level for all masses.

Bibliography

[1]   CMS Collaboration. "Search for a charged Higgs boson in pp collisions at $\sqrt{s} = 8$ TeV". *Journal of High Energy Physics* 11 (2015), p. 018.
DOI: 10.1007/JHEP11(2015)018. arXiv: 1508.07774 [hep-ex].

[2]   CMS Collaboration. "Search for charged Higgs bosons with the $H^{\pm} \to \tau^{\pm}\nu_{\tau}$ decay channel in the fully hadronic final state at $\sqrt{s} = 13$ TeV". Tech. rep. CMS-PAS-HIG-16-031. 2016. URL: http://cds.cern.ch/record/2223865.

[3]   CMS Collaboration. "Search for neutral MSSM Higgs bosons decaying to a pair of tau leptons in pp collisions". *Journal of High Energy Physics* 10 (2014), p. 160.
DOI: 10.1007/JHEP10(2014)160. arXiv: 1408.3316 [hep-ex].

[4]   CMS Collaboration. "Search for additional neutral Higgs bosons decaying to a pair of tau leptons in pp collisions at $\sqrt{s} = 7$ and 8 TeV". Tech. rep. CMS-PAS-HIG-14-029. Geneva: CERN, 2015. URL: http://cds.cern.ch/record/2041463.

[5]   CMS Collaboration. "Search for a neutral MSSM Higgs boson decaying into $\tau\tau$ with 12.9 fb^{-1} of data at $\sqrt{s} = 13$ TeV". Tech. rep. CMS-PAS-HIG-16-037. Geneva: CERN, 2016. URL: https://cds.cern.ch/record/2231507.

[6]   CMS Collaboration. "Summary results of high mass BSM Higgs searches using CMS run-I data". Tech. rep. CMS-PAS-HIG-16-007. Geneva: CERN, 2016. URL: https://cds.cern.ch/record/2142432.

[7]   Particle Data Group Collaboration. "Review of Particle Physics". *Chinese Physics C* 40.10 (2016), p. 100001.
DOI: 10.1088/1674-1137/40/10/100001.

[8]   UA1 Collaboration. "Experimental Observation of Isolated Large Transverse Energy Electrons with Associated Missing Energy at $\sqrt{s} = 540$ GeV". *Physics Letters* 122B (1983), pp. 103–116.
DOI: 10.1016/0370-2693(83)91177-2.

[9]   UA2 Collaboration. "Observation of Single Isolated Electrons of High Transverse Momentum in Events with Missing Transverse Energy at the CERN $\bar{p}p$ Collider". *Physics Letters* 122B (1983), pp. 476–485.
DOI: 10.1016/0370-2693(83)91605-2.

[10] UA1 Collaboration. "Experimental Observation of Lepton Pairs of Invariant Mass Around 95 GeV/c^2 at the CERN SPS Collider". *Physics Letters* 126B (1983), pp. 398–410.
DOI: 10.1016/0370-2693(83)90188-0.

[11] UA2 Collaboration. "Evidence for $Z^0 \rightarrow e^+e^-$ at the CERN $\bar{p}p$ Collider". *Physics Letters* 129B (1983), pp. 130–140.
DOI: 10.1016/0370-2693(83)90744-X.

[12] F. Englert and R. Brout. "Broken Symmetry and the Mass of Gauge Vector Mesons". *Physical Review Letters* 13 (1964), pp. 321–323.
DOI: 10.1103/PhysRevLett.13.321.

[13] Peter W. Higgs. "Broken symmetries, massless particles and gauge fields". *Physics Letters* 12 (1964), pp. 132–133.
DOI: 10.1016/0031-9163(64)91136-9.

[14] Peter W. Higgs. "Broken Symmetries and the Masses of Gauge Bosons". *Physical Review Letters* 13 (1964), pp. 508–509.
DOI: 10.1103/PhysRevLett.13.508.

[15] G.S. Guralnik, C.R. Hagen, and T.W.B. Kibble. "Global Conservation Laws and Massless Particles". *Physical Review Letters* 13 (1964), pp. 585–587.
DOI: 10.1103/PhysRevLett.13.585.

[16] T. W. B. Kibble. "Symmetry Breaking in Non-Abelian Gauge Theories". *Physical Review* 155 (1967), pp. 1554–1561.
DOI: 10.1103/PhysRev.155.1554.

[17] Peter W. Higgs. "Spontaneous Symmetry Breakdown without Massless Bosons". *Physical Review* 145 (1966), pp. 1156–1163.
DOI: 10.1103/PhysRev.145.1156.

[18] Abdelhak Djouadi. "The Anatomy of electro-weak symmetry breaking. I: The Higgs boson in the standard model". *Physics Reports* 457 (2008), pp. 1–216.
DOI: 10.1016/j.physrep.2007.10.004. arXiv: hep-ph/0503172 [hep-ph].

[19] Roger Wolf. "The Higgs Boson Discovery at the Large Hadron Collider". Springer Tracts in Modern Physics 264. Springer, 2015. ISBN: 978-331-91851-2-5.

[20] Sebastian Wozniewski. "Entwicklung multivariater Analysemethoden zur Steigerung der Sensitivität auf supersymmetrische Higgs-Bosonen im $H \rightarrow \tau\tau$ Zerfallskanal". MA thesis. Karlsruhe, 2017. URL: http://ekp-invenio.physik.uni-karlsruhe.de/record/48913.

[21] F. Zwicky. "Die Rotverschiebung von extragalaktischen Nebeln". *Helvetica Physica Acta* 6 (1933). [Gen. Rel. Grav.41,207(2009)], pp. 110–127.
DOI: 10.1007/s10714-008-0707-4.

[22] F. Zwicky. "On the Masses of Nebulae and of Clusters of Nebulae". *The Astrophysical Journal* 86 (1937), pp. 217–246.
DOI: 10.1086/143864.

[23] Virginia Trimble. "Existence and Nature of Dark Matter in the Universe". *Annual Review of Astronomy and Astrophysics* 25 (1987), pp. 425–472.
DOI: 10.1146/annurev.aa.25.090187.002233.

[24] P. J. E. Peebles and Bharat Ratra. "The Cosmological constant and dark energy". *Reviews of Modern Physics* 75 (2003), pp. 559–606.
DOI: 10.1103/RevModPhys.75.559. arXiv: astro-ph/0207347 [astro-ph].

[25] Abdelhak Djouadi. "The Anatomy of electro-weak symmetry breaking. II. The Higgs bosons in the minimal supersymmetric model". *Physics Reports* 459 (2008), pp. 1–241.
DOI: 10.1016/j.physrep.2007.10.005. arXiv: hep-ph/0503173 [hep-ph].

[26] OPAL Collaboration. "Search for the standard model Higgs boson at LEP". *Physics Letters* B565 (2003), pp. 61–75.
DOI: 10.1016/S0370-2693(03)00614-2. arXiv: hep-ex/0306033 [hep-ex].

[27] M. Carena et al. "MSSM Higgs boson searches at the LHC: benchmark scenarios after the discovery of a Higgs-like particle". *The European Physical Journal C* 73.9 (2013), p. 2552. ISSN: 1434-6052.
DOI: 10.1140/epjc/s10052-013-2552-1. arXiv: 1302.7033 [hep-ph].

[28] A. Djouadi et al. "The post-Higgs MSSM scenario: Habemus MSSM?" *The European Physical Journal C* 73 (2013), p. 2650.
DOI: 10.1140/epjc/s10052-013-2650-0. arXiv: 1307.5205 [hep-ph].

[29] S. Heinemeyer, W. Hollik, and G. Weiglein. "FeynHiggs: A Program for the calculation of the masses of the neutral CP even Higgs bosons in the MSSM". *Computer Physics Communications* 124 (2000), pp. 76–89.
DOI: 10.1016/S0010-4655(99)00364-1. arXiv: hep-ph/9812320 [hep-ph].

[30] S. Heinemeyer, W. Hollik, and G. Weiglein. "The Masses of the neutral CP-even Higgs bosons in the MSSM: Accurate analysis at the two loop level". *The European Physical Journal C* 9 (1999), pp. 343–366.
DOI: 10.1007/s100529900006. arXiv: hep-ph/9812472 [hep-ph].

[31] G. Degrassi et al. "Towards high precision predictions for the MSSM Higgs sector". *The European Physical Journal C* 28 (2003), pp. 133–143.
DOI: 10.1140/epjc/s2003-01152-2. arXiv: hep-ph/0212020 [hep-ph].

[32] M. Frank et al. "The Higgs Boson Masses and Mixings of the Complex MSSM in the Feynman-Diagrammatic Approach". *Journal of High Energy Physics* 02 (2007), p. 047.
DOI: 10.1088/1126-6708/2007/02/047. arXiv: hep-ph/0611326 [hep-ph].

[33] T. Hahn et al. "High-Precision Predictions for the Light CP -Even Higgs Boson Mass of the Minimal Supersymmetric Standard Model". *Physical Review Letters* 112.14 (2014), p. 141801.
DOI: 10.1103/PhysRevLett.112.141801. arXiv: 1312.4937 [hep-ph].

[34] Henning Bahl and Wolfgang Hollik. "Precise prediction for the light MSSM Higgs boson mass combining effective field theory and fixed-order calculations". *The European Physical Journal C* 76.9 (2016), p. 499.
DOI: 10.1140/epjc/s10052-016-4354-8. arXiv: 1608.01880 [hep-ph].

[35] "LHC Higgs Cross Section Working Group 3: MSSM Neutral Higgs". URL: https://twiki.cern.ch/twiki/bin/view/LHCPhysics/LHCHXSWGMSSMNeutral (visited on 09/05/2017).

[36] Glen Cowan. "Statistics for Searches at the LHC". *Proceedings, 69th Scottish Universities Summer School in Physics : LHC Phenomenology (SUSSP69): St.Andrews, Scotland, August 19-September 1, 2012.* 2013, pp. 321–355.
DOI: 10.1007/978-3-319-05362-2_9. arXiv: 1307.2487 [hep-ex]. URL: https://inspirehep.net/record/1242009/files/arXiv:1307.2487.pdf.

[37] Volker Blobel and Erich Lohrmann. "Statistische und numerische Methoden der Datenanalyse". 1st ed. Teubner Verlag, 1998. ISBN: 3519032430.

[38] A. L. Read. "Presentation of Search Results: the CLs Technique". *Journal of Physics G* 28.10, 2693 (2002).
DOI: 10.1088/0954-3899/28/10/313.

[39] Bernhard Mistlberger and Falko Dulat. "Limit Setting Procedures and Theoretical Uncertainties in Higgs Boson Searches" (2012). arXiv: 1204.3851 [hep-ph].

[40] Glen Cowan et al. "Asymptotic formulae for likelihood-based tests of new physics". *The European Physical Journal C* 71 (2011), p. 1554.
DOI: 10.1140/epjc/s10052-011-1554-0. arXiv: 1007.1727 [physics.data-an].

[41] Glen Cowan et al. "Erratum to: Asymptotic formulae for likelihood-based tests of new physics". *The European Physical Journal C* 73.7 (2013), p. 2501. ISSN: 1434-6052.
DOI: 10.1140/epjc/s10052-013-2501-z.

[42] Sara Algeri, Jan Conrad, and David A. van Dyk. "A method for comparing non-nested models with application to astrophysical searches for new physics". *Monthly Notices of the Royal Astronomical Society* 458.1 (2016), pp. L84–L88.
DOI: 10.1093/mnrasl/slw025. arXiv: 1509.01010 [physics.data-an].

[43] Dennis Roy. "Improved statistical methods for searches for supersymmetric Higgs bosons decaying into pairs of τ leptons". MA thesis. Karlsruhe, 2016. URL: http://ekp-invenio.physik.uni-karlsruhe.de/record/48863.

[44] Oliver Sim Brüning et al. "LHC Design Report". CERN Yellow Reports: Monographs. Geneva: CERN, 2004. URL: https://cds.cern.ch/record/782076.

[45] "LHC Guide". Mar. 2017. URL: https://cds.cern.ch/record/2255762.

[46] Esma Anais Mobs. "The CERN accelerator complex. Complexe des accélérateurs du CERN" (Oct. 2016). General Photo. URL: https://cds.cern.ch/record/2225847.

[47] CMS Collaboration. "CMS detector design". URL: http://cms.web.cern.ch/news/cms-detector-design (visited on 06/10/2017).

[48] "Interactive Slice of the CMS detector". URL: https://cms-docdb.cern.ch/cgi-bin/PublicDocDB/RetrieveFile?docid=4172 (visited on 03/01/2017).

[49] CMS Collaboration. "The CMS Experiment at the CERN LHC". *Journal of Instrumentation* 3, S08004 (2008).
DOI: 10.1088/1748-0221/3/08/S08004.

[50] CMS Collaboration. "CMS Physics: Technical Design Report, Volume 2: Physics Performance". *Journal of Physics G*. Technical Design Report CMS 34.6 (2007). CERN-LHCC-2006-021.
DOI: 10.1088/0954-3899/34/6/S01.

[51] CMS Collaboration. "The Muon Project: Technical Design Report". Tech. rep. CERN/LHCC 97-32. Geneva: CERN, 1998. URL: https://cds.cern.ch/record/343814.

[52] CMS Collaboration. "The Tracker Project: Technical Design Report". Tech. rep. CERN/LHCC 98-006. Geneva: CERN, Apr. 1998. URL: https://cds.cern.ch/record/368412.

[53] CMS Collaboration. "Energy Calibration and Resolution of the CMS Electromagnetic Calorimeter in pp Collisions at $\sqrt{s} = 7$ TeV". *Journal of Instrumentation* 8 (2013), P09009.
DOI: 10.1088/1748-0221/8/09/P09009. arXiv: 1306.2016 [hep-ex].

[54] "The Worldwide LHC Computing Grid". Accessed: 2017-07-20. URL: http://bist.eu/wp-content/uploads/2017/02/Hemmer.pdf (visited on 03/31/2017).

[55] CMS Collaboration. "Particle-flow reconstruction and global event description with the CMS detector" (2017). arXiv: 1706.04965 [physics.ins-det].

[56] Matteo Cacciari, Gavin P. Salam, and Gregory Soyez. "The Anti-k(t) jet clustering algorithm". *Journal of High Energy Physics* 04 (2008), p. 063.
DOI: 10.1088/1126-6708/2008/04/063. arXiv: 0802.1189 [hep-ph].

[57] CMS Collaboration Collaboration. "Identification of b quark jets at the CMS Experiment in the LHC Run 2". Tech. rep. CMS-PAS-BTV-15-001. Geneva: CERN, 2016. URL: https://cds.cern.ch/record/2138504.

[58] CMS Collaboration. "Reconstruction and identification of τ lepton decays to hadrons and ν_τ at CMS". *Journal of Instrumentation* 11 (2016), P01019.
DOI: 10.1088/1748-0221/11/01/P01019. arXiv: 1510.07488 [physics.ins-det].

[59] CMS Collaboration. "Performance of reconstruction and identification of tau leptons in their decays to hadrons and tau neutrino in LHC Run-2". Tech. rep. CMS-PAS-TAU-16-002. Geneva: CERN, 2016. URL: http://cds.cern.ch/record/2196972.

[60]   Fabio Colombo. "Packaging and assembly technologies for the pixel detector up-
       grade and measurement of $\tau\tau$ final states with the CMS experiment at the LHC".
       PhD thesis. Karlsruhe, 2016.
       DOI: `10.5445/IR/1000056204`.

[61]   CMS Collaboration Collaboration. "Performance of missing energy reconstruction
       in 13 TeV pp collision data using the CMS detector". Tech. rep. CMS-PAS-JME-
       16-004. Geneva: CERN, 2016. URL: `https://cds.cern.ch/record/2205284`.

[62]   CMS Collaboration. "Summaries of CMS cross section measurements". URL: `https:
       //twiki.cern.ch/twiki/bin/view/CMSPublic/PhysicsResultsCombined`
       (visited on 09/05/2017).

[63]   Torbjörn Sjöstrand, Stephen Mrenna, and Peter Skands. "A brief introduction to
       PYTHIA 8.1". *Computer Physics Communications* 178.11 (2008), pp. 852–867.
       ISSN: 0010-4655.
       DOI: `10.1016/j.cpc.2008.01.036`.

[64]   LHC Higgs Cross Section Working Group. "Handbook of LHC Higgs Cross Sections:
       4. Deciphering the Nature of the Higgs Sector" (2016).
       DOI: `10.23731/CYRM-2017-002`. arXiv: `1610.07922 [hep-ph]`.

[65]   Robert V. Harlander, Stefan Liebler, and Hendrik Mantler. "SusHi: A program for
       the calculation of Higgs production in gluon fusion and bottom-quark annihilation
       in the Standard Model and the MSSM". *Computer Physics Communications* 184
       (2013), pp. 1605–1617.
       DOI: `10.1016/j.cpc.2013.02.006`. arXiv: `1212.3249 [hep-ph]`.

[66]   Michael Spira. "HIGLU: A program for the calculation of the total Higgs production
       cross-section at hadron colliders via gluon fusion including QCD corrections" (1995).
       arXiv: `hep-ph/9510347 [hep-ph]`.

[67]   Robert V. Harlander and William B. Kilgore. "Higgs boson production in bot-
       tom quark fusion at next-to-next-to leading order". *Physics Review D* 68 (2003),
       p. 013001.
       DOI: `10.1103/PhysRevD.68.013001`. arXiv: `hep-ph/0304035 [hep-ph]`.

[68]   A. Djouadi, J. Kalinowski, and M. Spira. "HDECAY: A Program for Higgs boson
       decays in the standard model and its supersymmetric extension". *Computer Physics
       Communications* 108 (1998), pp. 56–74.
       DOI: `10.1016/S0010-4655(97)00123-9`. arXiv: `hep-ph/9704448 [hep-ph]`.

[69]   A. Djouadi, M. M. Muhlleitner, and M. Spira. "Decays of supersymmetric parti-
       cles: The Program SUSY-HIT (SUspect-SdecaY-Hdecay-InTerface)". *Acta Physica
       Polonica B* 38 (2007), pp. 635–644. arXiv: `hep-ph/0609292 [hep-ph]`.

[70]   Stefano Frixione, Paolo Nason, and Carlo Oleari. "Matching NLO QCD computa-
       tions with Parton Shower simulations: the POWHEG method". *Journal of High
       Energy Physics* 11 (2007), p. 070.
       DOI: `10.1088/1126-6708/2007/11/070`. arXiv: `0709.2092 [hep-ph]`.

[71] CDF Collaboration. "Observation of Top Quark Production in $\overline{p}p$ Collisions with the Collider Detector at Fermilab". *Physical Review Letters* 74 (1995), pp. 2626–2631.
DOI: 10.1103/PhysRevLett.74.2626.

[72] DØ Collaboration. "Observation of the Top Quark". *Physical Review Letters* 74 (1995), pp. 2632–2637.
DOI: 10.1103/PhysRevLett.74.2632.

[73] J. Alwall et al. "The automated computation of tree-level and next-to-leading order differential cross sections, and their matching to parton shower simulations". *Journal of High Energy Physics* 2014.7 (2014), p. 79. ISSN: 1029-8479.
DOI: 10.1007/JHEP07(2014)079. URL: http://dx.doi.org/10.1007/JHEP07(2014)079.

[74] CMS Collaboration. "Performance of Electron Reconstruction and Selection with the CMS Detector in Proton-Proton Collisions at $\sqrt{s} = 8$ TeV". *Journal of Instrumentation* 10.06 (2015), P06005.
DOI: 10.1088/1748-0221/10/06/P06005. arXiv: 1502.02701 [physics.ins-det].

[75] CMS Collaboration. "Performance of CMS muon reconstruction in pp collision events at $\sqrt{s} = 7$ TeV". *Journal of Instrumentation* 7 (2012), P10002.
DOI: 10.1088/1748-0221/7/10/P10002. arXiv: 1206.4071 [physics.ins-det].

[76] CMS Collaboration. "Search for additional neutral Higgs bosons in the di-τ final state in pp collisions" (2017). CMS-HIG-17-020, to be published.

[77] CMS Collaboration. "Identification of b-quark jets with the CMS experiment". *Journal of Instrumentation* 8 (2013), P04013.
DOI: 10.1088/1748-0221/8/04/P04013. arXiv: 1211.4462 [hep-ex].

[78] CMS Collaboration. "Measurement of the differential cross section for top quark pair production in pp collisions at $\sqrt{s} = 8\,\text{TeV}$". *The European Physical Journal C* 75.11 (2015), p. 542.
DOI: 10.1140/epjc/s10052-015-3709-x. arXiv: 1505.04480 [hep-ex].

[79] CMS Collaboration. "CMS Luminosity Measurements for the 2016 Data Taking Period". Tech. rep. CMS-PAS-LUM-17-001. Geneva: CERN, 2017. URL: http://cds.cern.ch/record/2257069.

[80] CMS Collaboration. "Jet energy scale and resolution in the CMS experiment in pp collisions at 8 TeV". *Journal of Instrumentation* 12.02 (2017), P02014.
DOI: 10.1088/1748-0221/12/02/P02014. arXiv: 1607.03663 [hep-ex].

[81] CMS Collaboration. "Search for a neutral MSSM Higgs boson decaying into tautau at 13 TeV". Tech. rep. CMS-PAS-HIG-16-006. Geneva: CERN, 2016. URL: https://cds.cern.ch/record/2160252.

[82] Robert D. Cousins. "Generalization of Chisquare Goodness-of-Fit Test for Binned Data Using Saturated Models, with Application to Histograms". Mar. 3, 2013. URL: http://www.physics.ucla.edu/~cousins/stats/cousins_saturated.pdf (visited on 07/12/2017).

[83] CMS Collaboration. "Search for a neutral MSSM Higgs boson decaying into $\tau\tau$ with 12.9 fb^{-1} of data at $\sqrt{s} = 13$ TeV". 2016. URL: http://cms-results.web.cern.ch/cms-results/public-results/preliminary-results/HIG-16-037/index.html (visited on 07/12/2017).

[84] Philip Bechtle et al. "HiggsBounds − 4: Improved Tests of Extended Higgs Sectors against Exclusion Bounds from LEP, the Tevatron and the LHC". *The European Physical Journal C* 74.3 (2014), p. 2693.
DOI: 10.1140/epjc/s10052-013-2693-2. arXiv: 1311.0055 [hep-ph].

[85] Philip Bechtle et al. "Applying Exclusion Likelihoods from LHC Searches to Extended Higgs Sectors". *The European Physical Journal C* 75.9 (2015), p. 421.
DOI: 10.1140/epjc/s10052-015-3650-z. arXiv: 1507.06706 [hep-ph].

[86] ATLAS Collaboration. "Observation of a New Particle in the Search for the Standard Model Higgs Boson with the ATLAS Detector at the LHC". *Physics Letters B* 716 (2012), pp. 1–29.
DOI: 10.1016/j.physletb.2012.08.020. arXiv: 1207.7214 [hep-ex].

[87] CMS Collaboration. "Observation of a New Boson at a Mass of 125 GeV with the CMS Experiment at the LHC". *Physics Letters B* 716 (2012), pp. 30–61.
DOI: 10.1016/j.physletb.2012.08.021. arXiv: 1207.7235 [hep-ex].

Danksagung

Danke auch an Bärbel Bräunling, die Sekräterin unseres Institutes die bei vielen der verwaltungstechnische Aufgaben die im Laufe der Zeit auftraten immer eine große Hilfe war. Der Graduierten Schule KSETA sowie dem Graduiertenkolleg 1694 „Elementarteilchenphysik bei höchster Energie und höchster Präzision" danke ich für die Unterstützung und Förderung während meiner Arbeit unter anderem in Form von Kolloquien, Seminaren und Workshops, sowie generell für die Förderung junger Wissenschaftler.

Für den Aufbau und Betrieb des bwForClusters NEMO, der für Teile der Ergebnisse dieser Arbeit genutzt wurde, danke ich dem Land Baden-Württemberg die diesen durch bwHPC fördert sowie der Deutschen Forschungsgemeinschaft die diesen durch INST 39/963-1 FUGG fördert.

Abschließend möchte ich meiner Familie für die nötige Unterstützung und den Rückhalt während meines Studiums und während der letzten Jahre danken. Ohne diese Unterstützung wäre die Arbeit in dieser Form nicht möglich gewesen.